Understanding Non-Plume Related Intraplate Volcanism

Sarah Elizabeth Mazza

Dissertation submitted to the faculty of Virginia Polytechnic Institute and State University in partial fulfillment of the requirement for the degree of

DOCTOR OF PHILOSOPHY
IN
GEOSCIENCES

Esteban Gazel, Chair
Elizabeth A. Johnson
Michael Bizimis
Robert J. Bodnar
Mark Caddick

November 29th, 2016
Blacksburg, VA

Key words: mantle geochemistry, isotope geochemistry, intraplate volcanism, lithospheric delamination, edge-driven convection

Copyright © 2016 Sarah Elizabeth Mazza

Understanding Non-Plume Related Intraplate Volcanism

Sarah E. Mazza

ABSTRACT

Intraplate volcanism is a worldwide phenomenon producing volcanoes away from active plate boundaries, a process that cannot yet be sufficiently explained by plate tectonic processes, and thus is still a missing piece in the understanding of the dynamics and evolution of our planet. Models for the formation of intraplate volcanism are dominated by mantle plumes, but alternative explanations, such as adiabatic decompression triggered by lithospheric delamination, and edge driven convection (EDC), could be responsible for magmatism. This dissertation explores intraplate volcanic locations that do not fit the mantle plume model, and presents geochemical evidence for lithospheric delamination and edge driven convection for the cause of volcanism.

I studied an Eocene volcanic swarm exposed in the Appalachian Valley and Ridge Province of Virginia and West Virginia, which are the youngest known igneous rocks along the Eastern North American Margin (ENAM). These magmas provide the only window into the most recent deep processes contributing to the post-rift evolution of this margin. This study presents the first high precision $^{40}Ar/^{39}Ar$ ages along with new geochemical data, and radiogenic isotopes that constrain the melting conditions and the timing of emplacement. Modeling of the melting conditions suggests that melting occurred under conditions slightly higher than average mantle beneath mid-ocean ridges. Asthenosphere upwelling related to localized lithospheric delamination is a possible process that can explain the intraplate signature of these magmas that lack evidence of a thermal anomaly.

The Virginia-West Virginia region of the ENAM also preserves a second post-rift magmatic event in the Late Jurassic. By studying both the Late Jurassic and Eocene magmatic events we can better understand the post-rift evolution of passive margins. This study presents a comprehensive set of geochemical data that includes new $^{40}Ar/^{39}Ar$ ages, major and trace-element compositions, and analysis of radiogenic isotopes to further constrain their magmatic history. Modeling suggests that the felsic volcanics from both the Late Jurassic and Eocene events are consistent with fractional crystallization. Lithospheric delamination is the best hypothesis for magmatism in Virginia/West Virginia, due to tectonic instabilities that are remnant from the long-term evolution of this margin, resulting in a "passive-aggressive" margin that records multiple magmatic events long after rifting ended.

Finally, Bermuda is an intraplate volcano that has been historically classified as mantle plume related but evidence to support the plume model is lacking. Instead, geophysics have argued that EDC is the best model to explain Bermuda volcanism. This study presents the first geochemical analysis of Bermuda volcanism, and found that Bermuda was built by two different magmatic processes: melting of carbonated peridotite to produce silica under-saturated, trace element enriched volcanics and melting of an enriched upper mantle component that produced silica saturated volcanics. We attribute the cyclicity of silica under-saturated and silica saturated volcanics to EDC melting.

Understanding Non-Plume Related Intraplate Volcanism

Sarah E. Mazza

GENERAL AUDIENCE ABSTRACT

Intraplate volcanoes are found away from active plate boundaries and cannot be explained by plate tectonics. Most introductory geology textbooks attribute intraplate volcanism to the mantle plume model, where hot material rises buoyantly through the Earth's mantle from depths near the core-mantle boundary. The associated volcanoes are then found in a linear track, due to plate motion over the stationary mantle plume. The mantle plume model is valid for some locations, such as Hawaii, but cannot explain all intraplate volcanoes. Other localized models such as lithospheric delamination and edge driven convection are needed to explain intraplate volcanism. Lithospheric delamination is a process where the base of the lithosphere (crust and upper mantle) pulls away from the top of the lithosphere due to density contrasts. The delamination of the base of the lithosphere allows for the warmer asthenosphere (mantle beneath the lithosphere) to upwell and produce melts by decompression. Edge driven convection is a process where temperature differences in thick, cold continental crust and thin, warm oceanic crust creates a localized convecting cell in the mantle. This convecting cell is associated with down-welling beneath the continental crust and upwelling beneath the oceanic crust, and associated volcanism would be found on the oceanic crust.

In Virginia-West Virginia there are two pulses of intraplate volcanic activity. Chapter 2 of this dissertation explores the geochemistry of the youngest volcanoes of Eastern North America, which are 48 million years old. Combining the geochemistry with the regional geophysics I proposed that lithospheric delamination is a plausible mechanism for these volcanic rocks. Chapter 3 further examines these volcanoes and adds a second pulse of magmatism that occurred 152 million years ago. Lithospheric delamination can also explain the 152 million year old volcanics.

Bermuda is an extinct volcanic island found in the Atlantic Ocean, and has been historically explain by the mantle plume model. However, there has been no geochemical data to support the mantle plume model and the geophysical evidence supports edge driven convection. I present the first geochemical analysis of Bermuda's volcanic pedestal and find that edge driven convection is a more plausible mechanism to account for volcanism.

Acknowledgements

To my advisor Esteban Gazel, thank you for bringing me to the "dark side" and providing me with the opportunities to explore my research interests. I am forever grateful for the support you gave me over the years, and I look forward to continuing to work with you as a colleague and collaborator.

To Liz Johnson, thank you for your invested interest in my research and for being a superb mentor these past few years, I greatly appreciate all of our conversations. To Michael Bizimis, thank you for all the analytical help, and for the providing insight with data interpretation. To Mark Caddick, thank you for your support, during both my MSc and PhD. To Robert Bodnar, thank you for asking the hard questions, I appreciate the challenge those questions poised.

I also want to thank and acknowledge Drew Coleman, who convinced that naive freshman back in the basement of Phillip Hall to enroll in his Minerology class. To Allen Glazner, thank you helping start my career as a research scientist and encouraging my research goals early on. A Roberto Braga, grazie per la pazienza e la guida che hai fornito nei miei primi anni come ricercatore. To Rick Law, thank you for much appreciated guidance and mentorship you offered over the years.

Thank you to the many collaborators, faculty, and research scientists that have provided technical expertise, mentorship, and guidance over the years: Jim Spotila, Ryan McAleer, Esther Schwarzenbach, Besim Dragovic, Claudia Adams, Bob Tracy, Berk Biryol, and Luca Fedele.

Many thanks to Pilar Madrigal, Jarek Trela, Denis Zamboni, Lisa Whalen, Ty Whalen, and Lowell Moore for your encouragement, conversation, and endless advice about life, graduate school, and research problems. Thank you to the staff and graduate students of the Geosciences Department at Virginia Tech. And many thanks to the support from all my friends scattered around the globe.

None of this would have been possible without the loving support of my husband, James Dale. Thank you for always believing in me and encouraging me to explore the world. To my parents, Ralph and Kate Mazza, thank you for always encouraging me to follow my dreams. Your support has always meant a lot. To my sister, Anne Mazza, thank you for the lifelong friendship and sisterhood we've shared, you inspire me to be the best I can be.

Attributions

Several co-authors contributed to the research and writing of the manuscripts included in this dissertation.

Chapter 2 was published as Mazza, S.E., Gazel, E., Johnson, E.A., Kunk, M.J., McAleer, R., Spotila, J.A., Bizimis, M., Coleman, D.S., 2014. Volcanoes of the passive margin: The youngest magmatic event in Eastern North America. Geology 42(6), 483-486. S.E. Mazza was responsible for sample analysis, project development, and writing the manuscript. E. Gazel helped with project conception, data analysis, and writing the manuscript. E.A. Johnson helped with project conception, sample collection, and writing the manuscript. M.J. Kunk and R. McAleer were responsible for the $^{40}Ar/^{39}Ar$ age dating of the samples. J.A. Spotila helped with regional data interpretation. M. Bizimis and D.S. Coleman aided with analytical work and manuscript revisions.

Chapter 3 was published as Mazza, S.E., Gazel, E., Johnson, E.A., Bizimis, M., McAleer, R., Biryol, C.B., accepted. Post-rift magmatic evolution of the eastern North American "passive-aggressive" margin. Geochemistry, Geophysics, Geosystems. S.E. Mazza was responsible for sample collection, data analysis and interpretation, modeling, and manuscript writing. E. Gazel and E.A. Johnson aided with samples collection, project conception, and manuscript revisions. M. Bizimis aided with analytical work and manuscript revisions. R. McAleer was responsible for $^{40}Ar/^{39}Ar$ age dating of the samples. C.B. Biryol was responsible for seismic tomography.

Chapter 4 is currently under preparation for submission. S.E. Mazza is responsible for project conception, sample collection, data analysis and interpretation, modeling, and manuscript writing. E. Gazel is responsible for project conception and data interpretation. M. Bizimis aided with analytical work and modeling. R. McAleer is responsible for $^{40}Ar/^{39}Ar$ age dating of the samples.

Table of Contents

Chapter 1: Introduction……....p. 1

Chapter 2: Volcanoes of the passive margin: The youngest magmatic event in Eastern North America……...…….p. 5

Abstract..……p. 6

Introduction ……..…….……....p. 6

Results ……...p. 8

Discussion …….……...….p. 9

Acknowledgements ……...p. 12

References Cited ……...p. 13

Figures ……..p. 18

Tables ……...…….……...p. 27

Supplementary Materials ……..….p. 36

Supplementary Figures ……p. 42

Chapter 3: Post rift magmatic evolution of the eastern North American "passive-aggressive" margin ……..p. 44

Key Points ……....p. 45

Abstract ……p. 45

Index Terms …….…….……p. 46

1. Introduction ……..……....p. 46
2. Geological background ……..…….……p. 47
3. Material and methods …….……p. 50
4. Results ……..……p. 53
    - 4.1 New geochronological constraints ……..……p. 53
    - 4.2 Geochemistry of the Late Jurassic magmatism … ….……...…….…p. 54
    - 4.3 Geochemistry of the Eocene magmatism ……..……..p. 55
5. Discussion ……..……p. 56

5.1 Petrological Modeling to Evaluate Magma Evolution …..……p. 56

5.2 Assessment of Crustal Interaction …….…….…p. 58

5.3 Contrasting the record of Late Jurassic and Eocene events in Virginia – West Virginia ……..…..…p. 60

5.4 Origin of co-genetic felsic rocks associated with the post-rift mafic pulses.....p. 62

5.5 Wide-spread alkaline magmatic pulses in the Late Jurassic along the ENAM……...……..…p. 66

5.6 Implications for the post-rift evolution of passive margins ….…..…p. 67

6. Conclusions ……..…...…...p. 70

Acknowledgements ……..……..…….....p. 72

References ……..…...…p. 72

Figures ……...…….....…p. 85

Tables ……...……..…p. 99

Supplementary Figures ……...…p. 120

Chapter 4: Solving the mystery of Bermuda ……..…….…p. 127

References ……..……p. 134

Methods ……..……p. 137

Figures ……..……..p. 140

Tables …….p. 146

Supplementary Figures …….…….p. 171

Appendix A: Contrasting sediment melt and fluid signatures for magma components in the Aeolian Arc: Implications for numerical modeling of subduction systems …….….p. 176

Appendix B: Laboratory Techniques in Geology: Embedding Analytical Methods into the Undergraduate Curriculum …….....……p. 177

List of Figures

Figure 2.1: Simplified geologic map showing sample locations of Eocene Magmas..……..p. 18

Figure 2.2: Geochemical results of the Eocene ENAM magmas compared with Atlantic oceanic basalt magmatism, CAMP, and North Atlantic MORB …….....p. 19

Figure 2.3: Age Spectra and isochrons for $^{40}Ar/^{39}Ar$ age dating ……...…p. 20

Figure 2.4: Radiogenic isotopic results for the Eocene ENAM magmas compared with CAMP, North Atlantic MORB, and Atlantic ocean basalt magmatism ……..……...…....p. 25

Figure 2.5: Temperature and pressure equilibration results for the Eocene Magmas ..…....p. 26

Supplementary Figure S2.1: Garnet in the Residue for the Eocene Magmas …….....p. 42

Supplementary Figure S2.2: Assessment of crustal interaction …….....p. 43

Figure 3.1: Simplified geological map showing sample locations of the Late Jurassic and Eocene volcanic rocks …….....p. 85

Figure 3.2: Total alkalis ($Na_2O + K_2O$) *vs*. SiO_2 for the Virginia – West Virginia Late Jurassic and Eocene volcanic pulses showing bimodal populations .....p. 86

Figure 3.3: Primitive Mantle normalized trace elements of the Virginia- West Virginia Post-Rift Magmas …….....p. 87

Figure 3.4: Trace element diagrams ……...p. 88

Figure 3.5: Radiogenic isotopic data for the Virginia – West Virginia Post-Rift Magmas ...p. 89

Figure 3.6: Fractional crystallization models …….……....p. 91

Figure 3.7: Assessment of crustal interaction …….....p. 92

Figure 3.8: Adakite discriminatory plots…….……....p. 94

Figure 3.9: Histogram showing magmatic events that have occurred on the ENAM…….....p. 96

Figure 3.10: Seismic tomography for Virginia – West Virginia ……....p. 97

Supplementary Figure 3.1: $^{40}Ar/^{39}Ar$ age spectrums for 14GBShelby ……..……..p. 120

Supplementary Figure 3.2: $^{40}Ar/^{39}Ar$ age spectrums for 14GBRt773. ……..……..p. 121

Supplementary Figure 3.3: $^{40}Ar/^{39}Ar$ age spectrums for 12DJHightownQuarry2……....p. 122

Supplementary Figure 3.4: $^{40}Ar/^{39}Ar$ age spectrums for TKColumn3 ……..……..p. 123

Supplementary Figure 3.5: $^{40}Ar/^{39}Ar$ age spectrums for MHXeno2 ……..……..p. 124

Supplementary Figure 3.6: Micrographs from the Late Jurassic volcanics ..…….....p. 125

Supplementary Figure 3.7: Micrographs from the Eocene volcanics..……..……..p. 126

Figure 4.1: Geologic Map and Core Log for Bermuda…… ……..……..p. 140

Figure 4.2: Bulk rock geochemistry for Bermuda ……..……..……. ……...p. 142

Figure 4.3: Radiogenic isotopic data for Bermuda ……..….p. 143

Figure 4.4: Schematic model to explain Bermuda volcanism as a product of edge driven convection ……..…….....p. 145

Supplementary Figure 4.1: Olivine chemistry ……..……..……..……...p. 171

Supplementary Figure 4.2: Results from Al-in-olivine thermometry for Bermuda plotted against Mg-number……..……...……....p. 172

Supplementary Figure 4.3: Radiogenic isotopic data for Bermuda plotted with other ocean island basalts ……..……....p. 173

Supplementary Figure 4.4: Models showing isotopic evolution from mixing Mid-Ocean Ridge Basalt and Black Shales …….p. 174

Supplementary Figure 4.5: Age projection of mid-ocean ridge basalt with high $^{206}Pb/^{204}Pb$ ……..…….……...……....p. 175

Chapter 1. Introduction

Intraplate magmatism is a global phenomenon producing oceanic and continental volcanoes away from active plate boundaries. This process cannot yet be explained by plate tectonics, and thus is still a missing piece in the understanding of the internal dynamics and evolution of our planet. Models for the formation of intraplate volcanism are dominated by active upwelling of thermal anomalies/mantle plumes relatively fixed in the deep mantle (i.e., the core-mantle boundary; Wilson, 1963; Morgan, 1971; Hofmann and White, 1982). The plume model has been used to explain locations such as the Hawaiian-Emperor chain, where massive hotspot volcanism is associated with a large swelling in seafloor topography that decays with distance from the hotspot. At such locations, a deep mantle plume is thought to produce an age-progressive chain of volcanoes on the overriding plate (Morgan, 1972). Chemical evidence for a deep mantle origin for plume activity comes from anomalously high mantle temperatures, as well as trace element and radiogenic isotope signatures (Hanan and Graham, 1996; Putirka et al., 2007; Herzberg et al., 2007). Global tomography also suggests that the mantle below some of these hotspot locations is characterized by slower S and P wave velocities compared to ambient mantle (interpreted as relatively hot material) extending through the 660 km discontinuity, deep into the lower mantle (e.g., Montelli et al., 2004). More recent work by French et al. (2013) and Romanowicz and French (2014) show that vertical low-velocity features in the lower mantle are associated with surficial hotspots.

While evidence for mantle plumes has been building over the years, it remains a subject of ongoing debate (e.g., Anderson, 2000; Anderson and Natland, 2014; Anderson and King, 2014). Not all locations that have been labeled as hotspots fit the model, particularly those with volumetrically minor volcanic activity, no clear age progression, and the lack of convincing

seismic or geochemical evidence to back up a deep-rooted thermal source. The ocean floor is carpeted by numerous seamounts of unknown origin, with current best estimates suggesting over 200,000 seamounts between 0.1 and 6.7 km high (Hillier and Watts, 2007). Many of these seamounts appear to be isolated or show no age progression whatsoever with adjacent volcanic edifices. These seamounts further add to the complexity of understanding intraplate volcanism and the mechanisms that produce melts in the upper mantle.

Alternative mechanisms to explain non-plume melting involve localized convective processes in the upper mantle, such as lithospheric delamination (Ducea and Saleeby, 1998; Lustrino, 2005), edge-driven convection (King and Anderson, 1998; King and Ritsema, 2000; King, 2007), shear-driven upwelling (Conrad et al., 2011), and a combination of edge-driven convection and shear-driven upwelling (Ballmer et al., 2015). Lithospheric delamination is a process where the base of the lithosphere (upper mantle with or without the lower crust) detaches and sinks into the asthenosphere due to Rayleigh-Taylor instabilities (Bird, 1978, 1979; Bird and Baumgartner, 1981; Elkins-Tanton, 2005; Lustrino, 2005). Basaltic magmatism is then produced due to the decompression of the asthenosphere (Kay et al., 1994; Farmer et al., 2002; Lustrino, 2005). Edge driven convection is a process where the thermal contrast between thick (cold) continental lithosphere and thin (warm) oceanic lithosphere creates small-scale convection cells that can produce melts (King and Anderson, 1998; King and Ritsema, 2000; King, 2007). Edge driven convection (EDC) has been used as a geodynamic model to explain several Atlantic Ocean volcanoes (Trindade, Fernando de Noronha, Vema Seamount, the Cameroon Line, Cape Verde, Canaries, and Bermuda) but to date no geochemical studies have tested for EDC. Shear-driven upwelling is a geodynamic model that solely uses asthenospheric shear flow and viscosity heterogeneities in the mantle to produce melts (Conrad et al., 2011). Ballmer et al. (2015) showed

that a combination of shear-driven upwelling and EDC can also explain melt generation in some intraplate settings.

This dissertation explores the geochemistry and petrology of intraplate volcanism in Virginia – West Virginia and Bermuda to test plume versus non-plume models to explain mantle melting.

Chapter 2, published in *Geology*, focuses on the youngest volcanoes of the eastern North American Margin (ENAM), an Eocene (48-47 Ma) basaltic-rhyolitic suite of dikes, sills, and diatremes found in Virginia – West Virginia. The Eocene magmas are typical intraplate volcanics, are found away from any active plate boundary and have geochemical signatures typical of Ocean Island Basalts (OIBs). Previous work used a limited dataset to suggest a variety of melting mechanisms to explain these volcanics, but none of those studies used geochemical and petrological data to support their hypotheses. Based on trace element enrichments, radiogenic Sr-Nd-Pb signatures, and geothermobarometric calculations, this study suggests that the Virginia – West Virginia Eocene volcanics are the produce of lithospheric delamination (Mazza et al., 2014).

Chapter 3, accepted at *Geochemistry, Geophysics, Geosystems*, presents a detailed analysis of post-rift magmatism in Virginia – West Virginia and the ENAM. Co-spatially located with the Eocene volcanics of Virginia – West Virginia are a series of Late Jurassic alkaline volcanics that have been minimally discussed in the literature. This study presents the first $^{40}Ar/^{39}Ar$ radiometric dates and radiogenic isotopic data (Sr-Nd-Pb), and a complete major and trace element geochemical analysis of the Late Jurassic (153-152 Ma) volcanics, which occurred approximately 50 million years after the last major tectonic event in the ENAM (the rifting of Pangea at 200 Ma). Mazza et al. (accepted) shows that lithospheric delamination can also explain the Late Jurassic

volcanics, and discusses the implications of post-rift magmatism and tectonic rejuvenation of post-rift passive margins.

Chapter 4, in preparation for *Nature Geoscience*, presents the first major and trace element bulk rock geochemistry, radiogenic isotopic data (Sr-Nd-Pb-Hf), mineral chemistry, and $^{40}Ar/^{39}Ar$ radiometric dates for Bermuda. In 1972 Dalhousie University drilled over 700 m into the volcanic root of Bermuda, but limited work has been done on these rare samples. Bermuda magmatism has been explained by EDC, but to date no geochemical studies have been done to give insight to the melting mechanism. This study presents the first geochemical evidence to support the geodynamic models Bermuda being the product of EDC. Bermuda has also proved to be an important location to understand mantle chemical heterogeneities, as it provides evidence for a new isotopic mantle end-member distinguished by a young, high ^{328}U source that is likely the result of recycling carbon rich sediments into the mantle.

Chapter 2: Volcanoes of the passive margin: The youngest magmatic event in Eastern North America

Sarah E. Mazza[1], Esteban Gazel[1], Elizabeth A. Johnson[2], Michael J. Kunk[3], Ryan McAleer[3], James A. Spotila[1], Michael Bizimis[4], and Drew S. Coleman[5]

[1]Department of Geosciences, Virginia Tech, 4044 Derring Hall (0420), Blacksburg, VA 24061
[2]Department of Geology and Environmental Science, James Madison University, MSC 6903 Memorial Hall, Harrisonburg, VA 22807
[3]United States Geologic Survey, 12201 Sunrise Valley Dr., MS 926A, Reston, VA 20192-0002
[4]Department of Earth and Ocean Sciences, University of South Carolina, 701 Sumter Street, EWS 617, Columbia, SC 29208
[5]Department of Geological Sciences, University of North Carolina Chapel Hill, CB#3315, Chapel Hill, NC 27599, USA

Published in June 2014 in *Geology*.

ABSTRACT

The rifted Eastern North American Margin (ENAM) provides important clues to the long-term evolution of continental margins. An Eocene volcanic swarm exposed in the Appalachian Valley and Ridge Province of Virginia and West Virginia contains the youngest known igneous rocks in the ENAM. These magmas provide the only window into the most recent deep processes contributing to the post-rift evolution of this margin. Here we present new $^{40}Ar/^{39}Ar$ ages, geochemical data, and radiogenic isotopes that constrain the melting conditions and the timing of emplacement. Modeling of the melting conditions on primitive basalts yielded an average temperature and pressure of 1412 ± 25 °C and 2.32 ± 0.31 GPa, corresponding to a mantle potential temperature of ~1410 °C, suggesting melting conditions slightly higher than average mantle temperatures beneath mid-ocean ridges. When compared with magmas from Atlantic hotspots, the Eocene ENAM samples share isotopic signatures with the Azores and Cape Verde. This similarity suggests the possibility of a large-scale dissemination of similar sources in the upper mantle left over from the opening of the Atlantic. Asthenosphere upwelling related to localized lithospheric delamination is a possible process that can explain the intraplate signature of these magmas that lack evidence of a thermal anomaly. This process can also explain the Cenozoic dynamic topography and rejuvenation of the Central Appalachians.

INTRODUCTION

Since the separation of Pangea and the widespread magmatism of the Central Atlantic Magmatic Province (CAMP) at ~200 Ma (Blackburn et al., 2013; Callegaro et al., 2013), the Eastern North American Margin (ENAM) evolved into a passive margin. Nevertheless, there is evidence of unsteady erosion and topographic disequilibrium during the late Cenozoic (Galen et al., 2013; Miller et al., 2013; Rowley et al., 2013), and localized Eocene volcanism (e.g.

Southworth et al., 1993; Tso and Surber, 2006; this study), which raise the question: Why are there pulses of geologic activity in a "dead" orogen?

Mid-Eocene, magmatic rocks in the ENAM are isolated in the Valley and Ridge Province (VA and WV) (Fig. 1), and serve as a case study to understand why there is a reactivation of magmatic activity in a "passive" orogenic setting. Before this study, the evidence for the Eocene magmatic activity in this region was restricted to paleomagnetic data and K/Ar ages (e.g. Ressetar and Martin, 1980; Southworth et al., 1993). The range of K/Ar ages has been controversial as three dikes in Augusta County, VA, were dated as Late Jurassic (~150 Ma, Zartman et al., 1967; Southworth et al., 1993), which do not correspond to either the Eocene volcanism or CAMP.

The Eocene volcanic rocks occur as dikes, sills, plugs, and diatremes, up to ~400 m in diameter, and at least 150 bodies have been described in the literature (e.g., Southworth et al., 1993; Tso and Surber, 2006). The volcanic rocks are well preserved, with fresh mafic crystals, some with visible glassy chilled margins, and some carrying lower crustal and mantle xenoliths. These Eocene magmatic rocks are the only window into the ENAM mantle. As such, they provide critical constraints on the structure and composition of the asthenosphere and lithosphere beneath the ENAM, and are critical in the interpretation of the ongoing geophysical initiatives in the region.

The ENAM Eocene magmatic event is an example of continental intraplate volcanism, a type of volcanism that is typically explained by either a mantle plume or lithospheric delamination. Evidence for plume-generated volcanism comes from anomalously high temperatures and geochemical signatures of deep melt sources, such as Hawaii (e.g., Herzberg et al., 2007). Intraplate magmas with similar geochemical signatures as plume-related magmas, but

with lower temperatures and pressures of melt generation, have been explained by lithospheric delamination (e.g., New Zealand; Hoernle et al., 2006). Here we present a new set of $^{40}Ar/^{39}Ar$ ages, geochemical data, and radiogenic isotopes of samples from the youngest magmatic event recorded in the ENAM, in order to constrain the processes that produced this magmatic pulse and possibly lead to the rejuvenation of the East North American passive margin.

RESULTS

Rock samples were collected from dikes, diatremes and other volcanic remnants in VA and WV (locations shown in Figure 2.1 and Table 1) for geochemical and geochronological studies. Detailed analytical methods, descriptions of step-heating $^{40}Ar/^{39}Ar$ experiments and spectra diagrams are reported in the Supplementary Materials.

New major and trace element data (Table 1) suggest that the Eocene pulse is bimodal in composition with co-existing alkaline mafic (basanite, basalt, trachybasalt) and felsic (trachydacite) magmas. This study focuses on the mafic magmas with the main goal of constraining the melting conditions of the Eocene event in the ENAM. The felsic rocks were used to help constrain the age of the event and will be discussed in future contributions. When plotted in multi-element spider diagrams, the mafic samples show enrichments in moderately to highly incompatible elements, with steep rare-earth element patterns (La/Yb>10), positive Nb, and Ta anomalies, and depletions in K, Pb, and Rb (Figure 2.2).

The new $^{40}Ar/^{39}Ar$ ages (from basalt and trachydacite samples) confirm the youngest magmatic pulse in the ENAM at 47.9 ± 0.2 to 47.0 ± 0.2 Ma (Figure 2.3, Tables 1 and 2). These new ages fall within the range of previously published, low precision K/Ar ages (e.g., 48–35 Ma, Southworth et al., 1993). However, resampling at Trimble Knob, a location originally dated at 35

Ma by K/Ar, yielded an $^{40}Ar/^{39}Ar$ age of ca. 48 Ma, restricting the range of Eocene magmatism to a narrow pulse.

New Pb-Sr-Nd radiogenic isotope ratios are reported in Table 1 and plotted in Figure 2.4. Measured ratios were corrected to initial (in) eruptive ratios and using the parent/daughter ratios reported in Table S1. The range of radiogenic isotopes for the Eocene samples is $^{87}Sr/^{86}Sr_{in}$ 0.70332–0.70513, $^{143}Nd/^{144}Nd_{in}$ 0.51257–0.51287, $^{206}Pb/^{204}Pb_{in}$ 19.089–19.858, $^{207}Pb/^{204}Pb_{in}$ 15.557–15.651, and $^{208}Pb/^{204}Pb_{in}$ 38.642–39.053.

DISCUSSION

The new $^{40}Ar/^{39}Ar$ ages presented here of 47.9–47.0 Ma confirm that the youngest magmatic event in the ENAM happened ~150 Ma after the opening of the Atlantic that was accompanied by the voluminous CAMP magmatism (Blackburn et al., 2013). Several models have been proposed to explain the origin of this magmatic event, including: emplacement along basement fracture zones near the 38th parallel (Zartman et al., 1967), opening of crustal conduits due to a reorganization of plate motion and a change in the orientation of the regional stress field (Southworth et al., 1993), and plume-related magmatism (Chu et al., 2013).

Although some degree of crustal contamination is possible during magma transport (Supplementary Materials, Section S4), the range of Mg# (molar Mg/Mg+Fe) of 0.6-0.7 for the mafic magmas from VA and WV, and their positive Nb, Ta anomalies and negative Pb, K anomalies are all indicative of limited crustal contamination (Figure 2.2). Additionally these samples have Ce/Pb (20–40) and Nb/U (30–60) typical of intraplate magmas (e.g., Hofmann et al., 1986; Jackson et al., 2008). Therefore, we are confident in the use of the chemical information recorded in these rocks to interpret the processes that produced the Eocene magmas in the ENAM.

The temperature and pressure of the melting region are recorded in the chemical composition of primitive mantle-derived magmas. We limit our temperature-pressure calculations to samples that are in agreement with the requirements of the Lee et al. (2009) geothermobarometer (Supplementary Materials, Section S3). The average equilibration temperature calculated was 1412 ± 25 °C at a pressure of 2.32 ± 0.31 GPa; these conditions plot close to or on the dry peridotite solidus at those pressures and are consistent with a mantle temperature of ~1410 °C (Figure 2.5A). The melting temperature expected from ambient mantle at the mid-ocean ridge system is 1350 ± 50 °C (e.g., McKenzie et al., 2005) and from a localized mantle thermal anomaly like a plume is >1500 °C (e.g., Herzberg et al., 2007). Thus, the temperatures from samples of the ENAM Eocene magmatic event are slightly higher than expected for ambient mantle but not as high as expected for plume-related activity.

The basalts from the Mole Hill location and the basanites have the lowest $^{87}Sr/^{86}Sr$ (0.70354) and highest $\varepsilon Nd_{(i)}$ (~5) potentially indicating an origin from a dominantly upper mantle source (Zindler and Hart, 1986). However, the elevated $^{206}Pb/^{204}Pb$ values (up to ~20) also suggest the presence of a HIMU component (Furman and Gittings 2003). When compared to other intraplate settings in the Atlantic, surprisingly, the Eocene ENAM samples share isotopic signatures with the Azores (especially the Faial island) and Cape Verde Atlantic hotspots (Figure 2.4). The elevated $^{87}Sr/^{86}Sr$ and $^{206}Pb/^{204}Pb$ trends observed in both Atlantic hotspots and ENAM Eocene magmas suggests the possibility of a large-scale upper mantle dissemination of similar sources left over from the opening of the Atlantic in the upper mantle.

A recent seismic study from North Carolina (Wagner et al., 2012) proposed the presence of a "doubled Moho", interpreted as an accreted eclogitic fossil slab under the Piedmont. However, seismic data from the TEENA Array (Benoit and Long, 2009) suggest a Moho depth

of ~40 km below the Shenandoah Valley where the Eocene magmas erupted, thus the eclogitic fossil slab is currently missing there. Models using seismic anisotropy suggest vertical mantle flow under the edge of the ENAM; however, further data from the arrival of the USArray will better constrain these models (e.g., Long et al., 2010) and their possible role in the recent evolution of the margin.

The Eocene magmas are often found near or along NE-trending Alleghenian fault zones and fold hinges (Southworth et al., 1993; Johnson et al., 2013), suggesting that pre-existing crustal structures served as conduits that reactivated as extensional features. This evidence together with $^{3}He/^{4}He$ with a mantle signature ($R/R_A > 1$) from a local thermal spring connects the crustal fracture systems into the mantle (Baedke and Silvis, 2009). Field evidence of a change of regional stress field in the Eocene (Southworth et al., 1993), reactivation of faults associated with magma emplacement, and the lack of a thick crust/fossil slab beneath the areas of Eocene magmatism suggest that the ENAM Eocene magmatism resulted from localized upwelling as a response to delamination of the eclogitized lower section of the lithosphere or left-over fossil slab segments (e.g., Nelson, 1992).

Asthenosphere upwelling related to localized delamination can explain the intraplate geochemical signature of the ENAM Eocene magmas and lack of evidence of a thermal anomaly recorded in the major element geochemistry (Figure 2.5B). Similar delamination scenarios have been proposed to explain small-volume intraplate magmatism in the Arabian Peninsula (Avigad and Gvirtzman, 2009), the Basin and Range, western U.S. (e.g, Gazel et al., 2012 and references therein), New Zealand (Hoernle et al., 2006) and Mediterranean (Duggen, et al. 2005) among other locations worldwide. A recent seismic study suggests that a “hidden” hotspot trail exists beneath the ENAM, and that the plume was active at ~60 Ma in the area of the VA/WV Eocene

magmatism (Chu et al., 2013). Not only is the timing of the Eocene magmatism off by ~10 Ma, but the calculated mantle potential temperature (~1400 °C) is too low for a plume environment. Because of these discrepancies, the lower velocities at shallow depths presented in Chu et al. (2013) could also be interpreted as a delaminated lithosphere.

Finally, if the intraplate magmatism was produced by localized mantle upwelling, it may have coincided with transient perturbation of the landscape. Density variations and flow in the mantle have the potential to produce long wavelength, low amplitude surface uplift (i.e. Lee, 2014). On slowly eroding, stable continents, this dynamic topography may rejuvenate the landscape with a geomorphic response in the form of elevated erosion, increase in sedimentation rates and alteration of drainage patterns (e.g. Braun, 2010). Mantle-driven epierogeny may be partly responsible for a well-documented Neogene landscape rejuvenation along the ENAM passive margin (Pazzaglia and Gardner, 2000; Galen et al., 2013; Miller et al., 2013; Rowley et al, 2013). Given that the Eocene event was magmatic, it may have had a greater thermal effect and therefore may have been associated with an even larger pulse of topographic disequilibrium. Unfortunately, diagnostic features of dynamic topography are ephemeral, and no indications of Eocene landscape rejuvenation have yet been identified in the ENAM geomorphic record. Nonetheless, the local petrologic imprint of what may have been a long-wavelength crustal disturbance associated with Eocene lithospheric delamination and asthenospheric upwelling adds to mounting evidence that the post-orogenic history of the ENAM has been highlighted by geodynamic and topographic unsteadiness.

ACKNOWLEDGEMENTS

This project was supported by GeoPrisms-NSF award EAR-1249412/1249438 to EG and EJ and OCE 1129280 to MB. We thank D. Doctor, of the USGS and R. Diecchio, GMU

for help in sample collection, and M. Bulas from JMU for sample collection and preparation. Reviews and comments by M. Jackson, D. Peate, and one anonymous reviewer significantly improved the original manuscript. We also thank the editorial handlings of R. Holdsworth.

REFERENCES CITED

Avigad, D., and Gvirtzman, Z., 2009, Late Neoproterozoic rise and fall of the northern Arabian–Nubian shield: The role of lithospheric mantle delamination and subsequent thermal subsidence: Tectonophysics, v. 477, no. 3–4, p. 217–228, doi:10.1016/j.tecto.2009.04.018.

Baedke, S.J., and Silvis, N.V., 2009, Determining the source of heat impacting thermal springs in the Warm Springs Valley of Bath and Allegheny Counties, Virginia: Geological Society of America Abstracts with Programs, v. 41, no. 7, p.448.

Benoit, M.H., and Long, M.D., 2009, The TEENA experiment: A pilot project to study the structure and dynamics of the eastern US continental margin: American Geophysical Union Fall Meeting Abstracts, v. 90, p. 53.

Blackburn, T.J., Olsen, P.E., Bowring, S.A., McLean, N.M., Kent, D.V., Puffer, J., McHone, G., Rasbury, E.T., and Et-Touhami, M., 2013, Zircon U-Pb geochronology links the end-Triassic extinction with the Central Atlantic Magmatic Province: Science, v. 340, no. 6135, p. 941–945, doi:10.1126/science.1234204.

Braun, J., 2010, The many surface expressions of mantle dynamics: Nature Geoscience, v. 3, p. 825–833, doi:10.1038/ngeo1020.

Callegaro, S., Marzoli, A., Bertrand, H., Chiaradia, M., Reisberg, L., Meyzen, C., Bellieni, G., Weems, R.E., and Merle, R., 2013, Upper and lower crust recycling in the source of CAMP basaltic dykes from southeastern North America: Earth and Planetary Science Letters, v. 376, p. 186–199, doi:10.1016/j.epsl.2013.06.023.

Chu, R., Leng, W., Helmberger, D.V., and Gurnis, M., 2013, Hidden hotspot track beneath the eastern United States: Nature Geoscience, v. 6, no. 11, p. 963–966, doi:10.1038/ngeo1949.

Dicken, C.L., 2005, Preliminary Integrated Geologic Map Databases for the United States: Delaware, Maryland, New York, Pennsylvania, and Virginia: US Geological Survey, scale 1:250 000.

Duggen, S., Hoernle, K., van den Bogaard, P., and Garbe-Schönberg, D., 2005, Post-collisional transition from subduction- to intraplate-type magmatism in the westernmost Mediterranean: Evidence for continental-edge delamination of subcontinental lithosphere: Journal of Petrology, v. 46, no. 6, p. 1155–1201, doi:10.1093/petrology/egi013.

Furman, T., and Gittings, H., 2003, Eocene basalt volcanism in Central Virginia: Implications for Cenozoic tectonism: Southeastern Geology, v. 42, no. 2, p. 111-122.

Galen, S.F., Wegmann, K.W., and Bohnenstiehl, D.R., 2013, Recent rejuvenation of topographic relief in the southern Appalachians: GSA Today, v.23, n.2, doi:10.1130/GSATG163A.1.

Gazel, E., Plank, T., Forsyth, D.W., Bendersky, C., Lee, C.T.A., and Hauri, E.H., 2012, Lithosphere versus asthenosphere mantle sources at the Big Pine Volcanic Field, California: Geochemistry Geophysics Geosystems, v. 13, no. 6, doi:10.1029/2012GC004060.

Herzberg, C., Asimow, P.D., Arndt, N., Niu, Y., Lesher, C.M., Fitton, J.G., Cheadle, M.J., and Saunders, A.D., 2007, Temperatures in ambient mantle and plumes: Constraints from basalts, picrites, and komatiites: Geochemistry Geophysics Geosystems, v. 8, no. 2, doi:10.1029/2006GC001390.

Hirschmann, M.M., 2000, Mantle solidus: Experimental constrains and the effects of peridotite composition: Geochemistry Geophysics Geosystems, v. 1, no. 10, doi:10.1029/2000GC000070.

Hirschmann, M. M. 2010, Partial melt in the oceanic low velocity zone: Physics of the Earth and Planetary Interiors, v. 179, n. 1-2, p. 60-71, doi:10.1016/j.pepi.2009.12.003.

Hoernle, K., White, J.D.L., van den Bogaard, P., Hauff, F., Coombs, D.S., Werner, R., Timm, C., Garbe-Schönberg, D., Reay, A., and Cooper, A.F., 2006, Cenozoic intraplate volcanism on New Zealand: Upwelling induced by lithospheric removal: Earth and Planetary Science Letters, v. 248, no. 1–2, p. 350–367, doi:10.1016/j.epsl.2006.06.001.

Hofmann, A.W., Jochum, K.P., Seufert, M., and White, W.M., 1986, Nb and Pb in oceanic basalts: New constraints on mantle evolution: Earth and Planetary Science Letters, v. 79, p. 33–45, doi:10.1016/0012-821X(86)90038-5.

Jackson, M.G., Hart, S.R., Saal, A.E., Shimizu, N., Kurz, M.D., Blusztajn, J.S., and Skovgaard, A.C., 2008, Globally elevated titanium, tantalum, and niobium (TITAN) in ocean island basalts with high $^{3}He/^{4}He$: Geochemistry Geophysics Geosystems, v. 9, no. 4, doi:10.1029/2007GC001876.

Janney, P. E., and Castillo, P.R., 2001, Geochemistry of the oldest Atlantic oceanic crust suggests mantle plume involvement in the early history of the central Atlantic Ocean: Earth and Planetary Science Letters, v. 192 no. 3, p. 291-302, doi:10.1016/S0012-821X(01)00452-6.

Johnson, E.A., Kiracofe, Z.A., Haynes, J.T., and Nashimoto, K., 2013, The origin of sandstone xenoliths in the mole hill basalt, Rockingham county, Virginia: Implications for magma ascent and crustal structure in the western Shenandoah valley: Southeastern Geology, v. 49, no. 3, p. 95–118.

Lee, C.T.A., 2014, The Physics and chemistry of recycling lower continental crust: Treatise of Geochemistry, 2nd edition, doi:10.1016/B978-0-08-095975-7.00314-4.

Lee, C.T.A., Luffi, P., Plank, T., Dalton, H., and Leeman, W.P., 2009, Constraints on the depths and temperatures of basaltic magma generation on Earth and other terrestrial planets using new thermobarometers for mafic magmas: Earth and Planetary Science Letters, v. 279, no. 1–2, p. 20–33, doi:10.1016/j.epsl.2008.12.020.

Long, M.D., Benoit, M.H., Chapman, M.C., and King, S.D., 2010, Upper mantle anisotropy and transition zone thickness beneath southeastern North America and implications for mantle dynamics: Geochemistry Geophysics Geosystems, v. 11, no. 10, doi:10.1029/2010GC0032427.

McKenzie, D., Jackson, J., and Priestley, K., 2005, Thermal structure of oceanic and continental lithosphere: Earth and Planetary Science Letters, v. 233, no. 3–4, p. 337–349, doi:10.1016/j.epsl.2005.02.005.

Miller, S.R., Sak, P.B., Kirby, E., and Bierman, P.R., 2013, Neogene rejuvenation of central Appalachian topography: Evidence for differential rock uplift from stream profiles and erosion rates: Earth and Planetary Science Letters, v. 369–370, p. 1–12, doi:10.1016/j.epsl.2013.04.007.

Nelson, K.D., 1992, Are crustal thickness variations in old mountain belts like the Applachians a consequence of lithospheric delamination?: Geology, v. 20, no. 6, p. 498-502, doi: 10.1130/0091-7613(1992)020<0498

Pazzaglia, F.J., and Gardner, T.W., 2000, Late Cenozoic landscape evolution of the US Atlantic passive margin: insights into a North American Great Escarpment, p.283-302.

Ressetar, R., and Martin, D.L., 1980, Paleomagnetism of Eocene igneous intrusions in the Valley and Ridge Province, Virginia and West Virginia: Canadian Journal of Earth Sciences, v. 17, no. 11, p. 1583–1588, doi:10.1139/e80-165.

Rowley, D.B., Forte, A. M., Moucha, R., Mitrovica, J., Simmons, N., Grand, S., 2013, Dynamic topography change of the Eastern United States since 3 Million years ago: Science, v. 340, p. 1560-1563, doi:10.1126/science.1229180.

Southworth, C.S., Gray, K., and Sutter, J.F., 1993, Middle Eocene Intrusive Igneous Rocks of the Central Appalachian Valley and Ridge Province: Setting, Chemistry and Implications for Crustal Structure: U.S. Geological Survey Bulletin, Report B1839-I, p. J1–J24.

McDonough, W.F., and Sun, S.S., 1995, The Composition of the Earth: Chemical geology, v. 120, n. 3, p. 223-253, doi:10.1016/0009-2541(94)00140-4

Tso, J.L., and Surber, J.D., 2006, Eocene igneous rocks near Monterey, Virginia; A field study: Virginia Minerals, v. 49, no. 3–4, p. 9–24.

Wagner, L.S., Stewart, K., and Metcalf, K., 2012, Crustal-scale shortening structures beneath the Blue Ridge Mountains, North Carolina, USA: Lithosphere, v. 4, no. 3, p. 242–256, doi:10.1130/L184.1.

Zartman, R., Brock, M., Heyl, A., and Thomas, H., 1967, K-Ar and Rb-Sr ages of some alkalic intrusive rocks from central and eastern United States: American Journal of Science, v. 265, no. 10, p. 848–870, doi:10.2475/ajs.265.10.848.

Zindler, A., and Hart, S., 1986, Chemical geodynamics: Annual Review of Earth and Planetary Sciences, v. 14, p. 493–571, doi:10.1146/annurev.ea.14.050186.002425.

[1]GSA Data Repository item 2014175, is available online at www.geosociety.org/pubs/ft2014.htm, or on request from editing@geosociety.org or Documents Secretary, GSA, P.O. Box 9140, Boulder, CO 80301, USA.

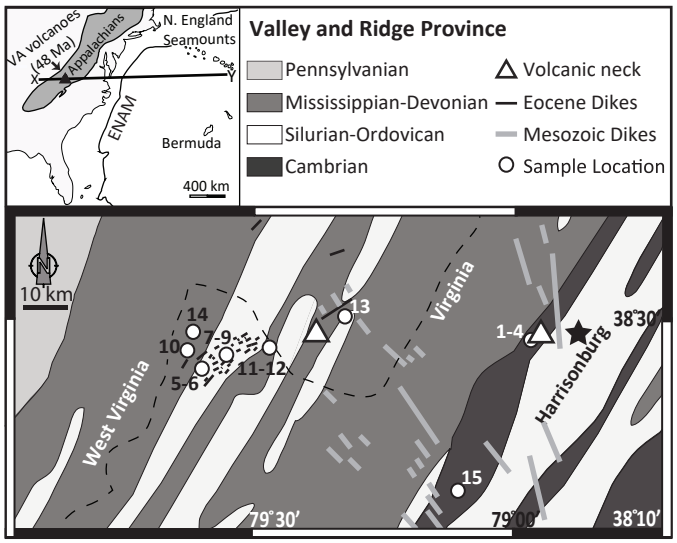

Figure 2.1: Simplified geologic map showing sample locations of Eocene magmas. Note the orientation of Mesozoic CAMP dikes toward the NW and the Eocene dikes toward the NE. Sample locations in Table 1. Cross-section XY shown in Figure 2.5b

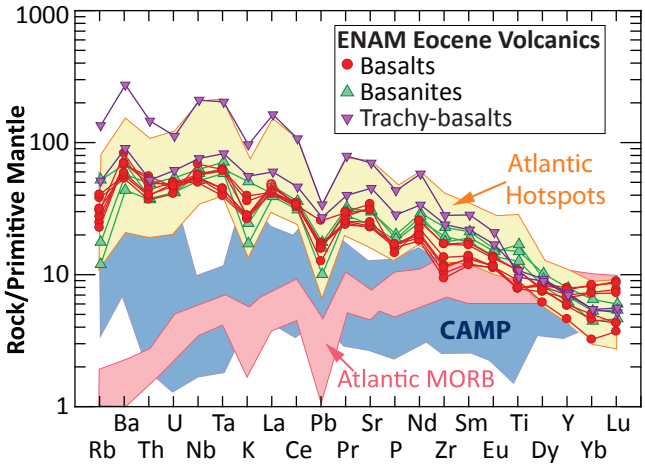

Figure 2.2: Geochemical results of the Eocene ENAM magmas compared with Atlantic oceanic basalt magmatism, CAMP, and North Atlantic MORB (23-33 ˚N, away from hotspot interactions). Primitive mantle reference from McDonough and Sun (1995). Additional data from Janney et al., 2001, Callegaro et al., 2013, and Georoc database (http://georoc.mpch-mainz.gqdg.de/georoc/).

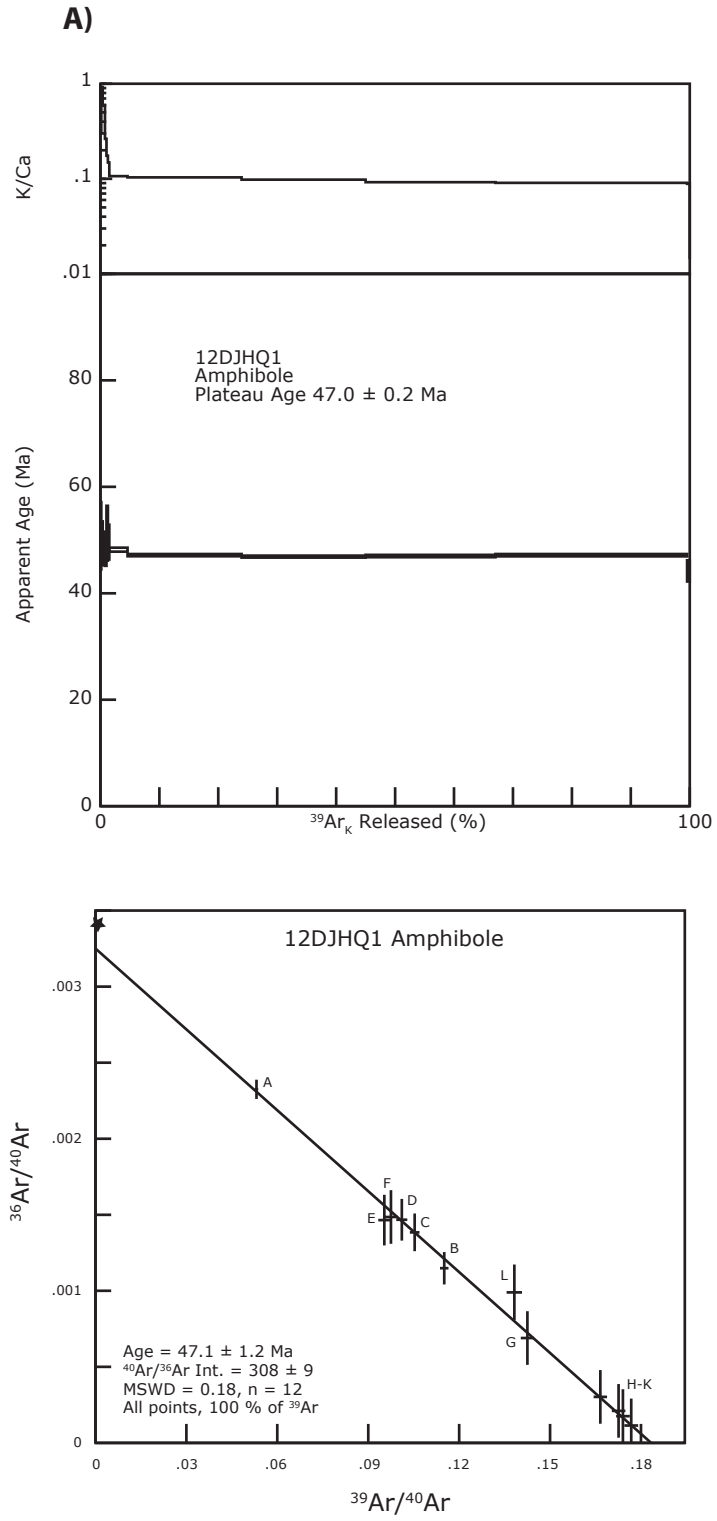

Figure 2.3: Age Spectra and isochrons for $^{40}Ar/^{39}Ar$ age dating. (A) 12DJHQ1 (B) DRBB-66 (C) 12DJ631D1 (D) 12DJ631C (E) Trimble Knob A.

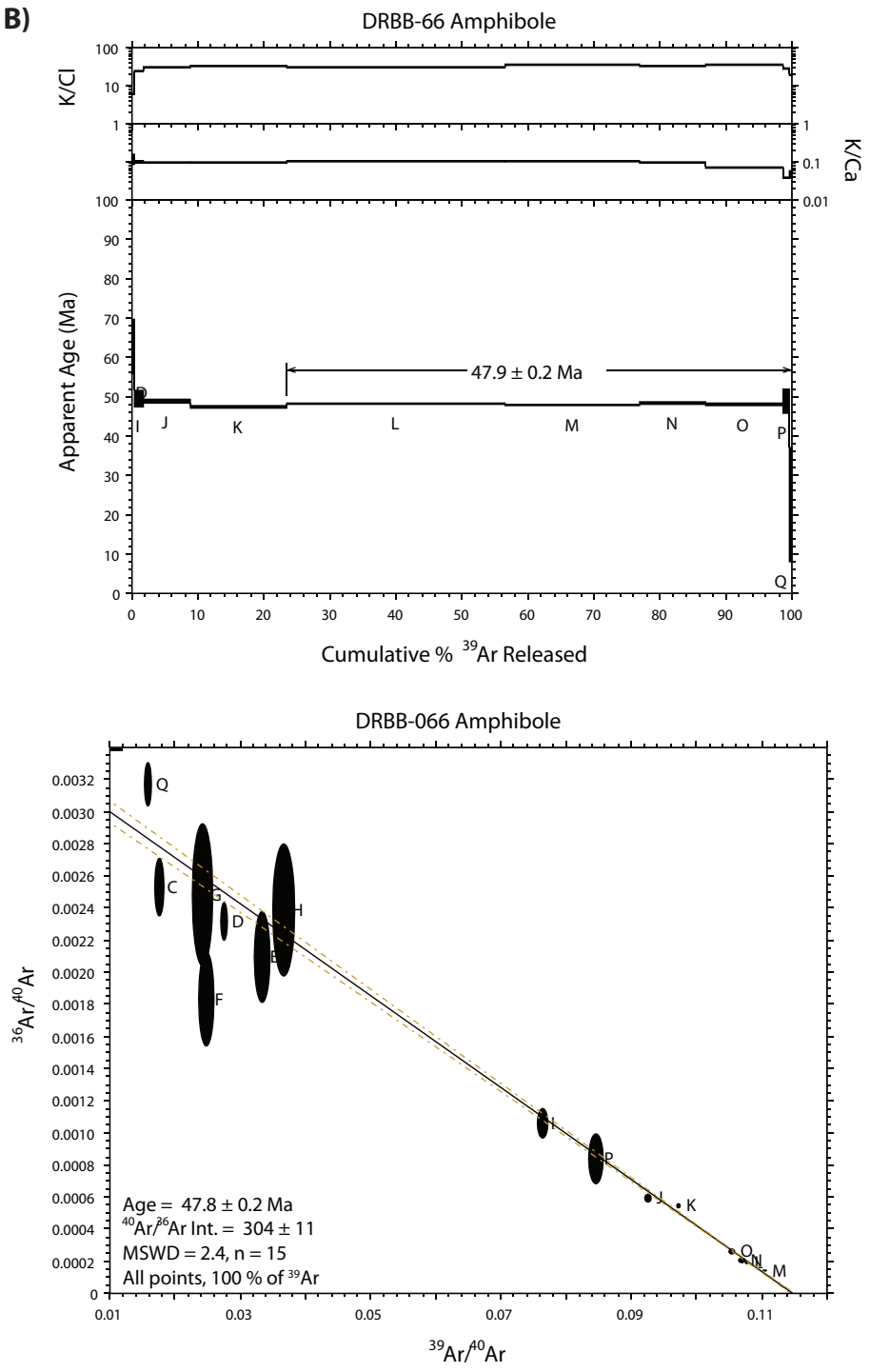

Figure 2.3: Age Spectra and isochrons for $^{40}Ar/^{39}Ar$ age dating. (A) 12DJHQ1 (B) DRBB-66 (C) 12DJ631D1 (D) 12DJ631C (E) Trimble Knob A.

C)

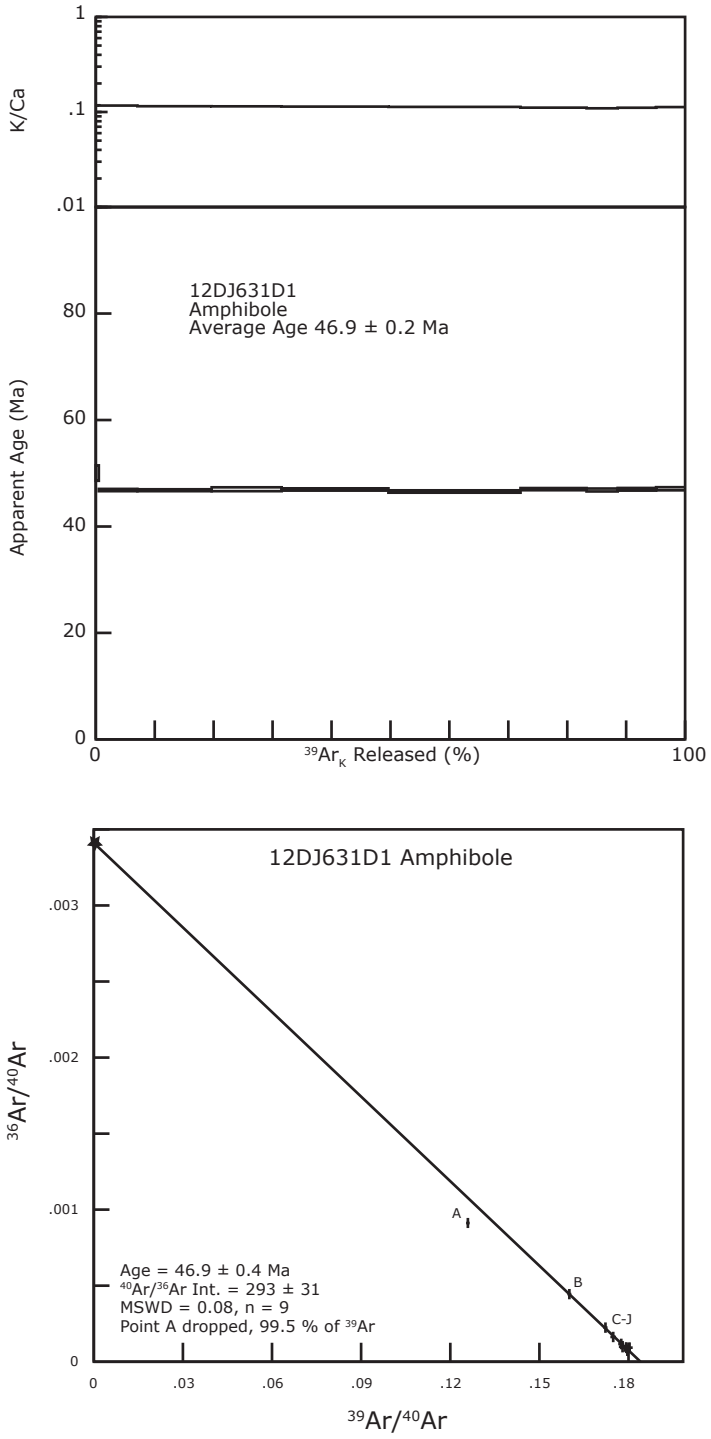

Figure 2.3: Age Spectra and isochrons for $^{40}Ar/^{39}Ar$ age dating. (A) 12DJHQ1 (B) DRBB-66 (C) 12DJ631D1 (D) 12DJ631C (E) Trimble Knob A.

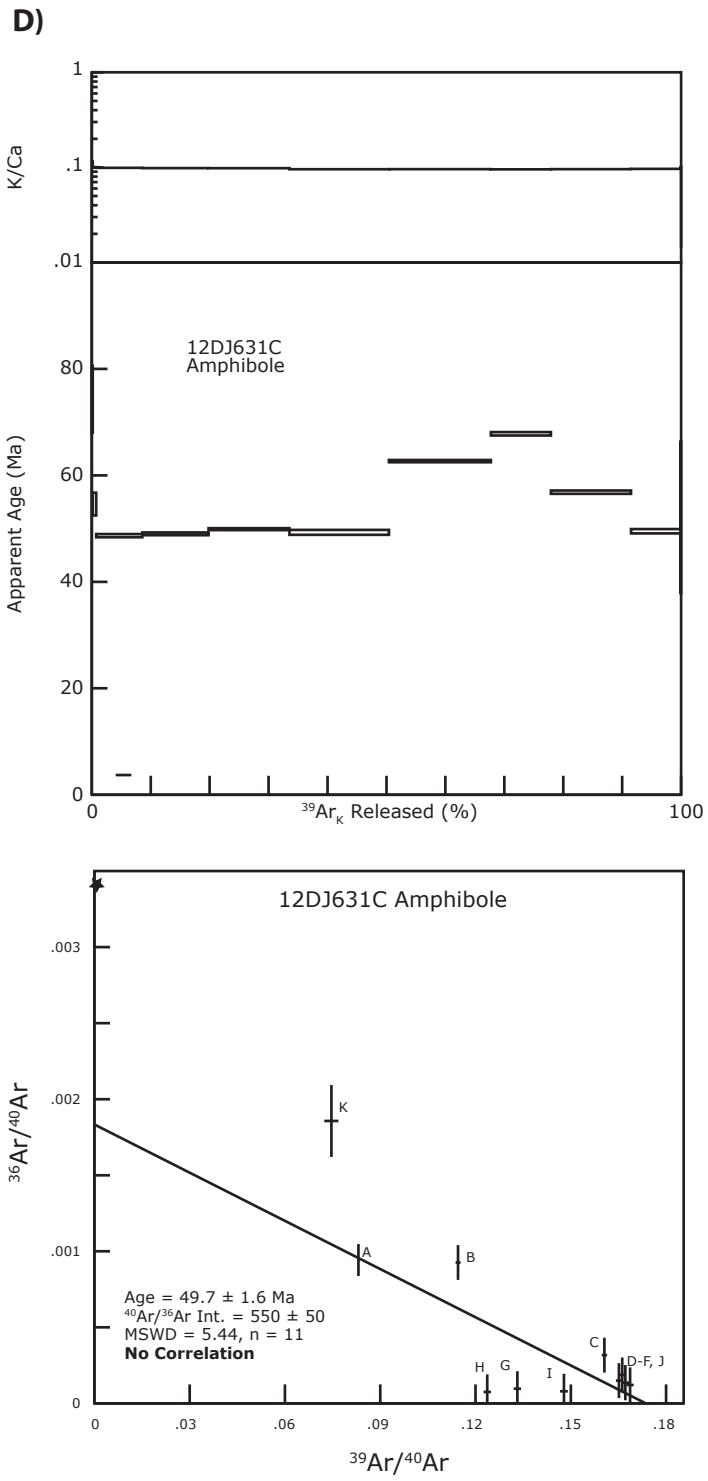

Figure 2.3: Age Spectra and isochrons for $^{40}Ar/^{39}Ar$ age dating. (A) 12DJHQ1 (B) DRBB-66 (C) 12DJ631D1 (D) 12DJ631C (E) Trimble Knob A.

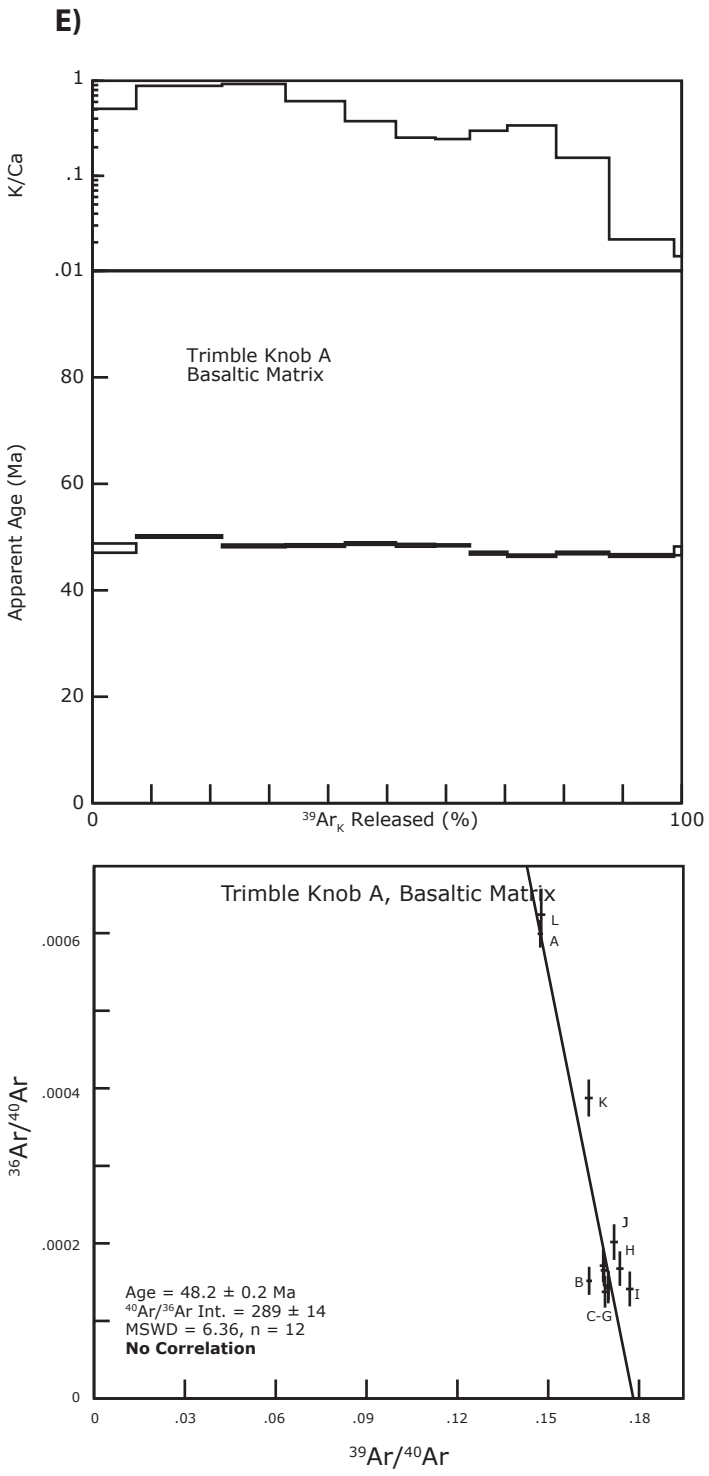

Figure 2.3: Age Spectra and isochrons for $^{40}Ar/^{39}Ar$ age dating. (A) 12DJHQ1 (B) DRBB-66 (C) 12DJ631D1 (D) 12DJ631C (E) Trimble Knob A.

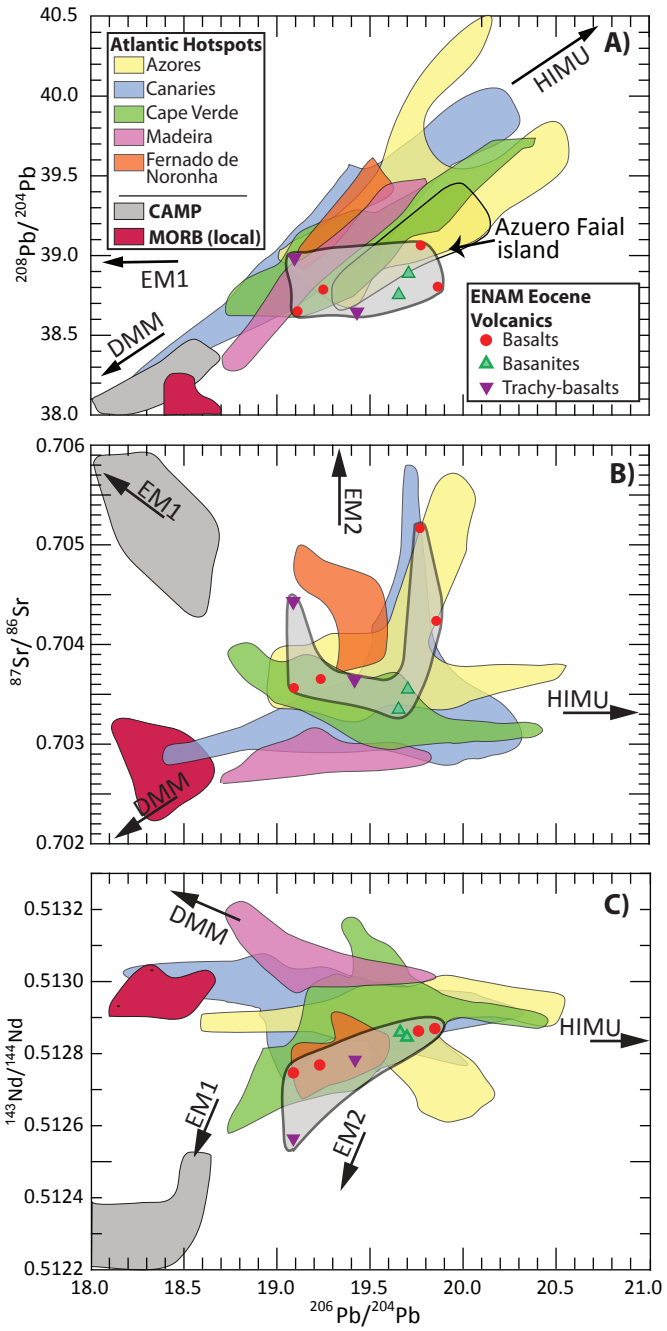

Figure 2.4: Radiogenic isotope results for the Eocene ENAM magmas compared with CAMP (Callegaro et al., 2013), North Atlantic MORB (samples offshore of Virginia from Janney et al., 2001), and Atlantic ocean basalt magmatism (Georoc database). Note how the ENAM magmas are in two trends resembling data from Cape Verde and the Faial component from the Azores. The Eocene ratios were age-corrected using an average age of 48 Ma.

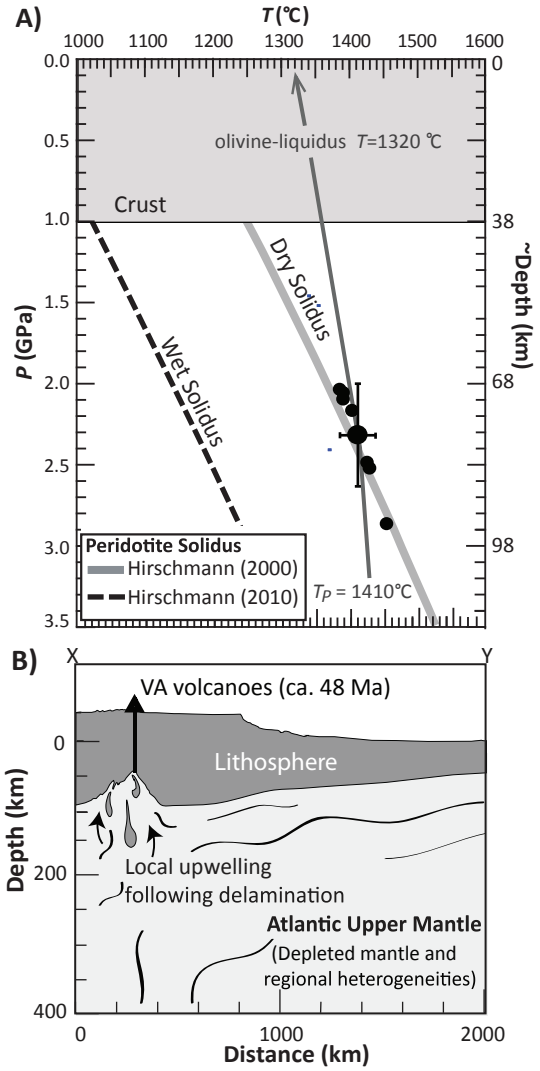

Figure 2.5: Temperature and pressure of equilibration results for the Eocene ENAM magmas. (A) Temperature as a function of pressure, the gray line with an arrow represents an adiabat consistent with the mantle potential temperature of ~1410 ˚C, that connects the average equilibration temperature and pressure (with error bars for one sigma standard deviation) to the average olivine-melt eruptive temperature of ~1320 ˚C and at the surface. The thickness of the crust is from Benoit and Long (2009). The wet solidus is for a source with 1000 ppm H2O, and the melting conditions for the ENAM magmas (Supplementary Materials). (B) Schematic model of the melting mechanism by lithospheric delamination and possible mantle sources of the VA volcanoes. Line of cross section shown in the inserted map in Figure 2.1.

Mazza et al., 2014

Table 1

Sample	Lat	Long	Age	error	SiO2	TiO2	Al2O3	Fe2O3	MnO	MgO	CaO	Na2O	K2O	P2O5	Totals
Eocene Magmas															
MH Summit	38.44814	-78.95275			45.69	1.59	15.04	11.43	0.21	9.65	11.79	2.51	0.78	0.35	99.04
MH Xeno 4	38.44892	-78.95130			45.69	1.58	14.92	11.81	0.21	9.57	11.47	2.42	0.79	0.35	98.81
MH 1.03	38.44908	-78.95206			45.55	1.57	15.10	11.26	0.20	9.49	11.92	2.42	0.76	0.33	98.60
MH 1.13	38.44947	-78.95072			45.80	1.59	14.94	11.41	0.20	9.34	11.81	2.44	0.81	0.35	98.69
12DJ613B	38.42307	-79.54177			43.55	1.82	10.27	11.07	0.18	13.79	14.15	1.50	0.81	0.30	97.43
TK5	38.40480	-79.58796	**48.20**	**0.20**	44.57	2.17	13.53	12.07	0.19	9.61	12.32	2.33	1.14	0.382	98.32
TK COLUMN 3	38.40481	-79.58808			44.48	2.18	13.49	12.19	0.20	9.83	11.93	2.37	1.04	0.382	98.09
VAFC03-6	38.43117	-79.45103			42.57	2.98	15.71	13.82	0.20	6.99	11.19	2.64	0.70	0.41	97.21
5 Hull Farm	38.43117	-79.45103			43.47	2.51	13.61	12.62	0.19	10.14	12.50	2.66	0.49	0.37	98.55
040 Hightown Dike	38.42931	-79.61675			41.09	3.36	13.74	14.48	0.20	8.18	11.60	2.37	1.45	0.38	96.85
12MB Wilfong 1	38.47419	-79.33241			47.13	2.17	16.26	12.25	0.20	4.10	8.26	3.83	1.62	0.59	96.41
VQ1	38.22028	-79.10198			43.65	1.93	13.92	10.54	0.19	7.94	10.96	2.40	2.81	0.90	95.25
12DJ631C	38.42274	-79.54174	**49.70**	**1.60**	65.42	0.41	16.40	2.47	0.05	0.42	1.44	5.00	3.85	0.07	95.53
12DJHightownQuarry2	38.45536	-79.60728	**47.00**	**0.20**	64.67	0.22	15.43	3.69	0.22	0.52	1.38	5.25	3.56	0.12	95.06
12DJ631D1	38.42373	-79.54297	**46.90**	**0.20**											
CAMP Dikes															
12DJ Mosque 1	38.44033	-78.84792			46.69	0.57	14.81	11.01	0.182	11.68	10.26	1.9	0.48	0.092	
042 SINGERS GLEN	38.5571	-78.9102			46.15	0.47	14.58	10.71	0.175	14.17	9.55	1.68	0.44	0.078	
Standard															
BHVO-2 from VT-XRF					49.41	2.69	13.3	11.98	0.172	7.17	11.11	2.36	0.54	0.252	

Mazza et al., 2014

Table 1

Sample	Sc	V	Cr	Co	Ni	Cu	Zn	Rb	Sr	Y	Zr	Nb	Mo	Sn	Cs
Eocene Magmas															
MH Summit	38.67	264.40	336.15	54.51	171.88	82.22	89.04	14.85	452.35	30.13	108.15	35.56	0.01	1.57	0.24
MH Xeno 4	31.20	234.06	292.71	49.41	174.85	83.75	81.64	16.50	465.11	34.09	122.71	35.94	0.01	1.41	0.19
MH 1.03	41.58	292.89	417.85	60.33	201.32	93.32	93.19	18.25	459.07	28.72	98.31	32.72	0.01	1.15	0.20
MH 1.13	30.35	237.24	353.70	49.16	158.59	59.80	79.42	13.59	496.52	32.92	118.30	35.20	0.01	1.12	0.14
12DJ613B	31.96	301.32	886.41	61.21	203.64	71.85	75.84	22.83	636.13	19.76	141.81	45.29	0.01	1.25	4.29
TK5	27.09	325.10	385.33	49.71	132.73	88.18	91.48	24.20	680.37	24.96	178.33	37.78	0.01	1.42	0.72
TK COLUMN 3	28.02	314.17	387.21	49.96	134.00	98.51	108.37	18.93	610.37	25.62	179.39	37.29	0.01	1.50	0.68
VAFC03-6	25.47	379.27	14.91	41.42	28.13	31.66	85.53	10.45	588.31	33.61	236.72	41.02	0.01	1.45	1.19
5 Hull Farm	31.71	334.12	431.54	55.78	118.31	73.74	89.16	7.10	464.62	26.38	201.57	33.66	0.01	1.63	1.53
040 Hightown Dike	31.07	367.03	23.29	44.55	30.90	33.30	73.92	31.00	601.15	28.93	183.89	38.09	0.01	1.90	0.28
12MB Wilfong 1	26.21	138.71	20.31	24.61	49.18	28.28	112.22	30.96	903.46	31.12	252.27	50.28	0.02	4.18	0.27
VQ1	24.78	171.08	385.84	36.36	111.64	44.30	81.88	81.51	######	30.34	297.06	139.18	0.03	1.41	16.75
12DJ631C	1.00	9.00	7.20	0.60	1.50	1.10	70.00	74.40	327.00	31.00	385.00	87.00			0.83
12DJHightownQuarry2	1.00	6.00	10.30	1.20	1.20	28.80	80.00	67.50	337.00	24.00	380.00	58.00			1.25
12DJ631D1															
CAMP Dikes															
12DJ Mosque 1	32.95	191.70	731.39	60.70	341.12	112.15	84.76	10.93	123.08	24.61	68.63	3.06	0.00	1.12	0.90
042 SINGERS GLEN	33.35	173.16	######	72.07	481.57	116.57	76.01	10.38	135.56	19.61	52.59	2.27	0.00	0.52	0.82

Mazza et al., 2014

Table 1

Sample	Ba	La	Ce	Pr	Nd	Sm	Eu	Gd	Tb	Dy	Ho	Er	Tm	Yb	Lu
Eocene Magmas															
MH Summit	462.93	29.52	58.51	6.24	23.69	4.92	1.72	5.44	0.81	5.52	1.06	3.14	0.43	3.24	0.52
MH Xeno 4	448.72	31.19	56.34	6.45	25.85	5.31	1.81	5.81	0.90	5.76	1.20	3.53	0.54	3.59	0.60
MH 1.03	547.53	27.72	57.19	6.05	22.57	4.79	1.75	5.21	0.81	4.99	1.05	3.00	0.43	3.17	0.49
MH 1.13	456.05	30.69	56.26	6.45	24.90	5.40	1.78	5.44	0.92	5.63	1.19	3.45	0.49	3.68	0.58
12DJ613B	352.10	26.63	54.46	7.03	28.01	5.63	1.77	5.76	0.80	4.14	0.81	1.89	0.23	1.42	0.25
TK5	370.94	27.30	58.26	7.60	32.11	7.10	2.11	6.54	0.95	5.26	0.95	2.42	0.31	2.01	0.29
TK COLUMN 3	389.36	27.17	56.38	7.48	31.76	6.78	2.05	6.54	0.95	5.11	0.94	2.60	0.31	2.21	0.29
VAFC03-6	373.43	29.87	59.70	8.13	36.11	8.49	2.38	8.42	1.20	6.79	1.29	3.18	0.40	2.83	0.40
5 Hull Farm	284.76	25.04	51.33	7.07	31.36	7.06	2.09	7.28	1.02	5.42	0.96	2.35	0.30	1.94	0.31
040 Hightown Dike	450.87	26.15	53.94	7.58	34.06	7.65	2.28	7.51	1.10	6.14	1.08	2.90	0.35	2.31	0.36
12MB Wilfong 1	602.38	39.15	77.87	10.21	42.46	8.92	2.62	8.26	1.19	6.27	1.12	2.90	0.37	2.42	0.35
VQ1	######	106.35	180.59	20.21	73.00	11.57	3.24	9.52	1.21	6.05	1.10	2.77	0.36	2.42	0.38
12DJ631C	######	95.30	104.00	17.00	57.60	8.70	2.60	6.70	1.00	5.50	1.10	3.20	0.50	3.30	0.50
12DJHightownQuarry2	######	63.80	125.00	13.10	46.10	7.40	1.80	5.40	0.80	4.40	0.90	2.60	0.40	2.90	0.50
12DJ631D1															
CAMP Dikes															
12DJ Mosque 1	170.85	7.10	14.78	1.96	8.42	2.23	0.75	2.95	0.58	4.01	0.92	2.58	0.38	2.83	0.46
042 SINGERS GLEN	130.13	5.40	12.41	1.52	6.73	1.78	0.56	2.28	0.48	3.03	0.71	2.12	0.32	2.29	0.36

Mazza et al., 2014

Table 1

Sample	Hf	Ta	Pb	Th	U
Eocene Magmas					
MH Summit	2.56	1.54	2.60	3.89	0.99
MH Xeno 4	3.06	1.66	2.44	4.41	0.94
MH 1.03	2.40	1.46	2.53	3.49	1.02
MH 1.13	2.93	1.66	2.45	4.19	0.92
12DJ613B	3.67	2.31	1.89	2.94	0.83
TK5	4.53	2.31	2.35	3.14	1.00
TK COLUMN 3	4.52	2.26	3.84	3.20	0.95
VAFC03-6	6.24	2.61	2.61	3.85	1.09
5 Hull Farm	5.02	2.14	1.49	2.91	0.85
040 Hightown Dike	5.03	2.30	2.36	2.98	0.84
12MB Wilfong 1	6.16	3.07	4.09	4.17	1.26
VQ1	6.07	7.57	5.11	11.69	2.29
12DJ631C	9.50	6.00	6.10	13.30	3.80
12DJHightownQuarry2	8.70	4.10	12.00	8.70	2.20
12DJ631D1					
CAMP Dikes					
12DJ Mosque 1	1.89	0.18	2.25	1.00	0.17
042 SINGERS GLEN	1.29	0.15	1.77	0.81	0.13

Mazza et al., 2014

Table 1

Sample	87Sr/86Sr	error	143Nd/144Nd	error	206Pb/204Pb	error	207Pb/204Pb	error	208Pb/204Pb	error
Eocene Magmas										
MH Summit	0.70361	0.00001	0.51279	0.00001	19.293	0.000	15.566	0.003	38.890	0.006
MH Xeno 4										
MH 1.03										
MH 1.13	0.70368	0.00001	0.51282	0.00000	19.430	0.000	15.628	0.000	39.067	0.001
12DJ613B	0.70520	0.00001	0.51290	0.00001	19.992	0.000	15.655	0.000	39.315	0.001
TK5	0.70428	0.00001	0.51291	0.00001	20.075	0.002	15.612	0.002	39.029	0.004
TK COLUMN 3										
VAFC03-6										
5 Hull Farm	0.70335	0.00001	0.51291	0.00001	19.943	0.004	15.628	0.004	39.077	0.006
040 Hightown Dike	0.70363	0.00001	0.51290	0.00000	19.886	0.001	15.660	0.000	39.091	0.001
12MB Wilfong 1	0.70368	0.00001	0.51283	0.00000	19.579	0.000	15.651	0.000	38.811	0.001
VQ1	0.70452	0.00001	0.51260	0.00000	19.316	0.000	15.596	0.000	39.360	0.001
12DJ631C										
12DJHightownQuarry2										
12DJ631D1										
CAMP Dikes										
12DJ Mosque 1										
042 SINGERS GLEN										

Mazza et al., 2014

Table 1

Sample	87Sr/86Sr_IN	143Nd/144Nd_IN	E0 ND	206Pb/204Pb_IN	207Pb/204Pb_IN	208Pb/204Pb_IN	T (˚C)	P (GPa)
Eocene Magmas								
MH Summit	0.70354	0.51275	2.89	19.102	15.557	38.642	1391	2.10
MH Xeno 4							1404	2.17
MH 1.03							1386	2.04
MH 1.13	0.70362	0.51277	3.47	19.240	15.619	38.783	1391	2.06
12DJ613B	0.70513	0.51286	5.04	19.766	15.644	39.053		
TK5	0.70421	0.51287	5.31	19.858	15.602	38.805	1426	2.49
TK COLUMN 3							1429	2.51
VAFC03-6								
5 Hull Farm	0.70332	0.51286	5.27	19.655	15.614	38.752	1454	2.87
040 Hightown Dike	0.70352	0.51285	5.09	19.705	15.651	38.879		
12MB Wilfong 1	0.70361	0.51279	3.78	19.423	15.643	38.642		
VQ1	0.70440	0.51257	-0.65	19.089	15.585	38.979		
12DJ631C								
12DJHightownQuarry2								
12DJ631D1								
CAMP Dikes								
12DJ Mosque 1							1354	1.52
042 SINGERS GLEN							1340	1.46

Step	Temperature	^{39}Ar	Radiogenic Yield	$^{39}Ar_k$	$^{40}Ar^*/^{39}Ar_k$	K/Ca	K/Cl	Age	Error
	(C)	*(% of total)*	*(%)*	*(moles)*				*(Ma)*	*(Ma)*
Sample:12DJHQ1 Amphibole 286KD57; J = 0.004846 ± 0.25 %, wt. = 0.1995 g									
A	700	0.1	31.3	2.27E-15	5.892	0.31	23	50.79	3.16
B	800	0.2	66.1	3.95E-15	5.740	0.93	48	49.50	2.01
C	900	0.4	59.1	6.43E-15	5.611	0.59	43	48.39	1.57
D	950	0.3	56.6	4.22E-15	5.604	0.26	22	48.34	1.59
E	1000	0.2	56.7	3.88E-15	5.950	0.18	14	51.28	2.57
F	1050	0.3	56.1	4.10E-15	5.754	0.15	12	49.61	1.64
G	1100	3.1	79.6	5.06E-14	5.587	0.11	9	48.19	0.19
H	1150	19.4	91.1	3.18E-13	5.467	0.10	10	47.17	0.11
I	1175	21.0	93.8	3.45E-13	5.433	0.10	11	46.88	0.09
J	1200	22.0	94.8	3.62E-13	5.447	0.09	12	47.00	0.11
K	1250	32.5	96.6	5.34E-13	5.465	0.09	12	47.16	0.11
L	1300	0.4	70.7	7.30E-15	5.119	0.09	11	44.20	0.99
Total Gas			93.3	1.64E-12	5.461	0.10	12	47.12	
95.0% gas released on plateau in steps H-K						Plateau Age = 47.0 ± 0.2			

Step	Temperature	^{39}Ar	Radiogenic Yield	$^{39}Ar_k$	$^{40}Ar^*/^{39}Ar_k$	K/Ca	K/Cl	Age	Error
	(C)	*(% of total)*	*(%)*	*(moles)*				*(Ma)*	*(Ma)*
DRBB-066 amphibole 121KD55; J = 0.003079 ± 0.25%, wt. = 0.0146 g									
C	900	0.2	25.4	1.68E-16	14.350	0.04	4	78.00	16.65
D	1000	0.4	31.6	4.41E-16	11.471	0.12	6	62.62	7.04
E	1050	0.2	38.2	1.93E-16	11.432	0.29	7	62.41	13.90
F	1100	0.1	46.0	1.41E-16	18.421	0.15	8	99.53	19.27
G	1125	0.1	26.8	8.64E-17	11.081	0.05	8	60.53	29.91
H	1150	0.1	29.5	1.47E-16	8.038	0.09	11	44.11	18.31
I	1175	1.4	68.9	1.36E-15	9.002	0.10	24	49.32	2.10
J	1200	7.1	82.6	7.04E-15	8.909	0.10	31	48.82	0.52
K	1225	14.6	83.9	1.44E-14	8.624	0.10	33	47.28	0.25
L	1250	33.1	94.5	3.27E-14	8.765	0.10	30	48.04	0.14
M	1275	20.4	96.0	2.02E-14	8.692	0.10	35	47.65	0.19
N	1300	9.8	94.1	9.72E-15	8.782	0.09	33	48.14	0.33
O	1350	11.9	92.3	1.17E-14	8.743	0.07	34	47.92	0.27
P	1450	0.9	75.3	9.32E-16	8.891	0.04	29	48.72	3.02
Q	1650	0.2	6.5	2.34E-16	4.070	0.05	19	22.47	14.43
Total Gas			90.7	9.94E-14	8.772	0.10	32	47.92	
76.4 % gas released on plateau in steps L-Q						Plateau Age = 47.9 ± 0.2			

Step	Temperature	^{39}Ar	Radiogenic Yield	$^{39}Ar_k$	$^{40}Ar^*/^{39}Ar_k$	K/Ca	K/Cl	Age	Error
	(C)	*(% of total)*	*(%)*	*(moles)*				*(Ma)*	*(Ma)*
DRBB-066 amphibole 121KD55; J = 0.003079 ± 0.25%, wt. = 0.0146 g									
C	900	0.2	25.4	1.68E-16	14.350	0.04	4	78.00	16.65
D	1000	0.4	31.6	4.41E-16	11.471	0.12	6	62.62	7.04
E	1050	0.2	38.2	1.93E-16	11.432	0.29	7	62.41	13.90
F	1100	0.1	46.0	1.41E-16	18.421	0.15	8	99.53	19.27
G	1125	0.1	26.8	8.64E-17	11.081	0.05	8	60.53	29.91

H	1150	0.1	29.5	1.47E-16	8.038	0.09	11	44.11	18.31
I	1175	1.4	68.9	1.36E-15	9.002	0.10	24	49.32	2.10
J	1200	7.1	82.6	7.04E-15	8.909	0.10	31	48.82	0.52
K	1225	14.6	83.9	1.44E-14	8.624	0.10	33	47.28	0.25
L	1250	33.1	94.5	3.27E-14	8.765	0.10	30	48.04	0.14
M	1275	20.4	96.0	2.02E-14	8.692	0.10	35	47.65	0.19
N	1300	9.8	94.1	9.72E-15	8.782	0.09	33	48.14	0.33
O	1350	11.9	92.3	1.17E-14	8.743	0.07	34	47.92	0.27
P	1450	0.9	75.3	9.32E-16	8.891	0.04	29	48.72	3.02
Q	1650	0.2	6.5	2.34E-16	4.070	0.05	19	22.47	14.43
Total Gas			90.7	9.94E-14	8.772	0.10	32	47.92	
76.4 % gas released on plateau in steps L-Q						Plateau Age = 47.9 ± 0.2			

Step	**Temperature**	**^{39}Ar**	**Radiogenic Yield**	**$^{39}Ar_k$**	**$^{40}Ar^*/^{39}Ar_k$**	**K/Ca**	**K/Cl**	**Age**	**Error**
	(C)	*(% of total)*	*(%)*	*(moles)*				*(Ma)*	*(Ma)*
Sample:12DJ631D1 Amphibole 270KD57; J = 0.004849 ± 0.25 %, wt. = 0.1951 g									
A	1050	0.5	73.0	1.13E-14	5.800	0.12	11	50.03	0.73
B	1075	6.6	86.9	1.44E-13	5.426	0.12	11	46.85	0.11
C	1100	12.6	93.4	2.76E-13	5.421	0.12	11	46.80	0.09
D	1125	11.9	95.2	2.61E-13	5.443	0.11	11	47.00	0.18
E	1150	18.1	96.5	3.97E-13	5.438	0.11	11	46.95	0.10
F	1175	22.4	97.3	4.92E-13	5.393	0.11	11	46.57	0.11
G	1200	11.2	97.8	2.45E-13	5.445	0.11	11	47.01	0.10
H	1225	5.3	97.3	1.16E-13	5.427	0.11	11	46.86	0.14
I	1250	6.5	97.8	1.43E-13	5.442	0.11	11	46.99	0.12
J	1350	4.9	97.1	1.08E-13	5.454	0.11	11	47.09	0.15
Total Gas			95.7	2.19E-12	5.429	0.11	11	46.87	
No Plateau									

Step	**Temperature**	**^{39}Ar**	**Radiogenic Yield**	**$^{39}Ar_k$**	**$^{40}Ar^*/^{39}Ar_k$**	**K/Ca**	**K/Cl**	**Age**	**Error**
	(C)	*(% of total)*	*(%)*	*(moles)*				*(Ma)*	*(Ma)*
Sample:12DJ631C Amphibole 272KD57; J = 0.004846 ± 0.25 %, wt. = 0.1950 g									
A	1050	0.2	72.1	2.99E-15	8.678	0.12	7	74.31	3.14
B	1075	0.6	72.6	1.07E-14	6.343	0.10	6	54.62	1.07
C	1100	7.8	90.6	1.42E-13	5.644	0.10	6	48.67	0.15
D	1125	11.2	94.5	2.04E-13	5.684	0.10	7	49.02	0.13
E	1150	13.7	95.6	2.49E-13	5.787	0.10	7	49.89	0.09
F	1175	16.9	96.4	3.07E-13	5.716	0.10	7	49.29	0.23
G	1200	17.3	97.2	3.14E-13	7.295	0.10	7	62.67	0.11
H	1225	10.2	97.8	1.85E-13	7.904	0.10	7	67.81	0.16
I	1250	13.6	97.7	2.47E-13	6.606	0.10	7	56.85	0.16
J	1350	8.4	96.0	1.53E-13	5.741	0.10	7	49.51	0.20
K	1450	0.1	45.1	1.87E-15	6.048	0.10	7	52.11	7.12
Total Gas			95.8	1.82E-12	6.344	0.10	7	54.63	
No Plateau									

Step	**Temperature**	**^{39}Ar**	**Radiogenic Yield**	**$^{39}Ar_k$**	**$^{40}Ar^*/^{39}Ar_k$**	**K/Ca**	**K/Cl**	**Age**	**Error**
	(C)	*(% of total)*	*(%)*	*(moles)*				*(Ma)*	*(Ma)*

Sample:Trimble Knob A Amphibole 278KD57; J = 0.004821 ± 0.25 %, wt. = 0.1900 g

A	700	7.4	82.3	1.69E-13	5.584	0.51	38	47.92	0.43
B	800	14.6	95.5	3.32E-13	5.842	0.88	68	50.10	0.11
C	850	10.8	95.7	2.46E-13	5.633	0.93	61	48.33	0.12
D	900	10.1	95.8	2.30E-13	5.641	0.61	49	48.41	0.11
E	950	8.7	95.9	1.97E-13	5.685	0.38	63	48.78	0.12
F	1000	6.7	95.1	1.52E-13	5.647	0.25	111	48.45	0.13
G	1050	5.9	94.9	1.34E-13	5.646	0.24	174	48.44	0.09
H	1100	6.4	95.1	1.45E-13	5.473	0.30	276	46.98	0.13
I	1150	8.3	95.8	1.89E-13	5.416	0.34	469	46.50	0.10
J	1200	9.0	94.0	2.05E-13	5.476	0.15	191	47.01	0.11
K	1250	11.0	88.6	2.51E-13	5.420	0.02	112	46.54	0.12
L	1350	1.3	81.6	2.97E-14	5.522	0.01	106	47.40	0.41
Total Gas			93.5	2.28E-12	5.600	0.45	135	48.05	
		No Plateau							

Chapter 2: Supplementary Materials

Volcanoes of the Passive Margin:
The youngest magmatic event in Eastern North America

S1. Methods

Rock samples were collected from dikes, plugs and diatremes in VA and WV (locations shown in Figure 2.1 and Table 1). $^{40}Ar/^{39}Ar$ ages were determined at the U.S. Geological Survey (USGS) in Reston, VA for four amphibole and one whole rock matrix samples. The amphibole samples were prepared using standard mineral separation techniques described by Kunk and McAleer (2011) to a purity of greater than 99.9 percent. The whole rock sample was processed using the same techniques to remove phenocrysts from the matrix and concentrate the ground mass. Samples were irradiated in two packages (KD55 & KD57) in the central thimble facility at the TRIGA reactor (GSTR) at the U.S.G.S., in Denver, CO. The monitor mineral used in both packages was FCT-3 sanidine with an age of 27.79 Ma (Kunk et al., 1985; Cebula et al., 1986) relative to MMhb-1 at 519.4 ± 2.5 Ma (Alexander et al., 1978; and Dalrymple et al., 1981). Following irradiation the samples were analyzed at the USGS in Reston, VA. The samples were heated in a small volume, molybdneum-lined, low-blank tantalum resistance furnace similar to that described by Staudacher (1978). After the gases from the samples were cleaned, the samples were then analyzed using a VG 1200B or a MAP 216 mass spectrometer. Data reduction was done using updated versions of the computer programs ArAr* (Haugerud and Kunk, 1988), and Mass spec (Deino, 2001) respectively. Plateau ages were determined using the definition of Fleck, et al. (1977) as modified by Haugerud and Kunk (1988). Inverse isotope correlation analysis of the analytical data to assess if non-atmospheric argon components were trapped in any samples and to calculate an inverse isochron age was done using the method of York (1969). All stated analytical uncertainties are 1σ. Uncertainties for the individual step ages do not include the uncertainties in the irradiation parameter "J", uncertainties for the production of interfering isotopes produced during neutron irradiation, or the uncertainty in the age of the monitor mineral. Only plateau and isochron ages include the uncertainty in the irradiation parameter "J". A more detailed description of the analytical and data reduction techniques can be found in Kunk and McAleer (2011), Hagarud and Kunk (1988), and Deino (2001)

Alteration-free rock chips of sample matrices (to exclude any xenocrysts or xenoliths) were selected under stereoscope microscope. These chips were powdered in an alumina mill and then fluxed into homogeneous glass disks with ultrapure $Li_2B_4O_7$ from Spex® (certified <<1 ppm blank for all trace elements) at the Petrology Lab at Virginia Tech for XRF and ICP-MS analyses. Major element geochemistry was collected with a Panalytical EDS-XRF with a silicon detector at the department of Geosciences at Virginia Tech. The accuracy for USGS standard BHVO-2g (run as an unknown) was better than 1.5% for most major elements but Na_2O, K_2O, and P_2O_5 that was better than 8% within reported values. The average RSD for 10 replicates of BHVO-2g were <1.6% for all major elements. Trace elements from fluxed glasses were collected with an Agilent 7500ce ICPMS coupled with a Geolas laser ablation system following the procedures detailed in Kelley et al. (2003) and Gazel (2012), with a He flow rate ~1 L/m – 5 Hz and an energy density on sample ~ 7 – 10 J/cm^2. Sample data were calibrated against fluxed glasses of USGS standards BHVO-2g, BCR-2g, and BIR-1g, using Ti from XRF as an internal standard and the standard

values from Kelley et al. (2003). The average relative accuracy for 10 replicates of BHVO-2g (run as an unknown) was better than 5% for most trace elements except Rb, Sr, Sn, Yb, and Th (better than 15%). The average precision for BHVO-2g was a RSD <5% for all elements with the exception of Ni, Cu, Gd, Yb, Lu, and Th (<7%,).

We measured radiogenic isotope ratios at the University of North Carolina (UNC) and at the Center for Elemental Mass Spectrometry (CEMS), University of South Carolina (USC). Isotopic ratios for Pb, Nd, and Sr were obtained on the VG Sector 54 thermal ionization mass spectrometer at UNC following procedures highlighted in Gray et al. (2008), and on a Neptune multi collector ICPMS at USC. Mass fractionation correction of 0.12%/amu as determined by replicate analyses of NBS-981 was used for Pb isotopic ratios on the TIMS. At CEMS/USC Pb isotope ratios were determined by the TI-addition technique (White et al., 2000). The NBS-981 was determined at $^{206}Pb/^{204}Pb = 16.936 \pm 0.001$, $^{207}Pb/^{204}Pb = 15.490 \pm 0.001$, $^{208}Pb/^{204}Pb = 36.694 \pm 0.003$ (2 standard deviations, = 13). Isotopic ratios for Nd were normalized to $^{146}Nd/^{144}Nd = 0.7219$ and the Nd standard JNdi was measured at $^{143}Nd/^{144}Nd = 0.5121$ and 0.512112 ± 0.000007 (n=6) at USC. Isotopic ratios for Sr were normalized to $^{86}Sr/^{88}Sr = 0.1194$ and replicate analyses of standard NBS-987 yielded $^{87}Sr/^{86}Sr = 0.710258$ at UNC and 0.710320 ± 0.000012 at USC. All Sr measurements are reported relative to NBS-987 $^{87}Sr/^{86}Sr = 0.710250$.

S2. Detailed description of $^{40}Ar/^{39}Ar$ Results

The age spectra from the four dated amphibole samples are of variable quality. Age spectra of samples 12DJHQ1 and DRBB-66 (Figure 2.3A & B and Table 2) both yielded plateau ages containing a large majority of gas (95 and 76 %) in each sample at 47.0 ± 0.2 and 47.9 ± 0.2 Ma respectively. Inverse isotope correlation analysis of the age spectrum data (Figure 2.3A & B) resulted in virtually identical ages (47.1 ± 1.2 and 47.8 ± 0.3 Ma) with acceptable MSWD (0.178 and 2.4) and atmospheric initial $^{40}Ar/^{36}Ar$ ratios (308 ± 9 and 304 ± 11). The age spectrum of sample 12DJ631D1 did not yielded an age plateau, but except for the first release step, the spectrum is essentially flat and has an average age of 46.9 ± 0.2 Ma. Inverse isotope correlation analysis of the age spectrum data (Figure 2.3C, Table 2) results in an apparent age of 46.9 ± 0.2 Ma with MSWD= 0.1 and an atmospheric initial $^{40}Ar/^{36}Ar$ ratio (293 ± 31). The age spectrum of amphibole sample 12DJ631C, did not yield an age plateau and is quite disturbed in the upper temperature steps climbing to ages as high as 68 Ma. Inverse isotope correlation analysis of the data from this sample did not produce a useful age (Figure 2.3D, Table 2).

The plateau ages of amphibole samples 12DJHQ1 and DRBB-66 give the most precise results of the samples analyzed and are interpreted to represent the time of dike emplacement. However, their ages are not the same within the limits of error when tested using the critical value test of Dalrymple and Lanphyre (1969, p. 120) suggesting that the emplacement of the Eocene dikes may have occurred over an interval of about 1 Ma from about 47.9 ± 0.2 Ma to 47.0 ± 0.2 Ma. The 46.9 ± 0.2 average and inverse isotope correlation of amphibole of sample 12DJ631D1 while of somewhat lesser quality strongly support the younger end of this age range. These ages fall within the range of previously published K/Ar data (Southworth et al., 1993), but are considerably more precise.

The age spectrum of basaltic matrix from sample Trimble Knob A was somewhat disturbed and did not yield an age plateau (Figure 2.3E, Table 2). Inverse isotope correlation analysis also failed to resolve an age for this sample. Nonetheless, the individual step ages for this sample range in age from 50.1 Ma to 46.4 Ma with a total gas age of 48.2 Ma. This age is the same as those of

three of the amphiboles discussed above, but is about 12-13 Ma older than a K/Ar age reported by Southworth et al., (1993) for a sample collected from the same outcrop. This large difference in age together with the lack of any other ages in the younger ~35 Ma range strongly suggests that the data for their sample from Trimble Knob is in error.

S3. Petrological modeling

Determining the source lithology of a suite of magmatic samples is not only important for the overall geotectonic interpretation of the magma genesis, but it is crucial to petrological modeling based on parameterization of experimental data and observations made on mantle peridotite sources. In recent years, the development of new petrological methods based on major element geochemistry (eg., Sobolev et al., 2005; Herzberg and Asimow, 2008; Dasgupta et al., 2007) provided new insights for the composition of magma source lithology. Finally, constraining magma oxidation state is fundamental to calculating primary compositions in equilibrium with the melting mantle source as the proportion of $Fe^{3+/}Fe^{2+}$, as only Fe^{2+} strongly affects olivine-melt equilibrium modeling.

In order to calculate the melting condition that produced the Eocene magmatic event in the ENAM, we used the thermobarometer developed by Lee et al. (2009) to produce primary magmas compositions and model the temperature and pressure of the melting regime. The thermometer in this model is based on olivine-melt Fe-Mg exchange, while the barometer is based on Si activity in melts in equilibrium with orthopyroxene+olivine. To use this thermobaromer, samples must be olivine controlled (as verified by major element geochemistry and petrographic studies). Olivine was then added by an incrementally calculation (using a constant $K_D = 0.3$ for the $Fe^{2+/}Mg$ exchange) until the melts reached equilibrium with mantle olivine (assumed to be Fo_{90}). For the H_2O content, we used 1 wt% H_2O from Sacco et al. (2011) and we assumed 0.15 Fe^{3+} as suggested by Kelley and Cottrell (2009) for samples with 1 wt% H_2O. An uncertainty of 1 wt% H_2O introduces a temperature uncertainty of 20°C; and 10% Fe^{3+}/Fe_T of 40°C and 0.3 GPa.

After this we used the CaO-MgO-SiO2 composition of the primary magmas following the model proposed by Herzberg (2010) and Gazel et al. (2011) to determine if the samples were produced by melting a peridotite source. Once the primary magmas from a peridotite source were determined, we calculated the mantle potential temperature in °C, with the following equation T_P=1463+12.74*MgO-2924/MgO (Herzberg and Asimow, 2008). The T_P uncertainty is ~60 °C (Herzberg and Gazel, 2009), making calculated T_Ps (reported in Table 1) within the range of ambient mantle or slightly elevated than ambient mantle (e.g. Putirka, 2005; McKenzie et al., 2005; Herzberg et al., 2007). Finally, for the set of samples used in this study we found negative correlation between Gd/Yb (ratio fractionated by garnet in the source during melting) and pressure of equilibration (Figure S2.1). This is consistent with an increase in the modal abundance of garnet in the mantle source with increasing pressure (e.g., Johnson, 1998), independently supporting the pressure estimates.

S4. Assessment of crustal interaction

In order to evaluate if the radiogenic signatures found in the Eocene VA intraplate magmas (Figure 2.4 main text, Table 1) are related to mantle sources and not crustal contamination, we produced an assessment of crustal interaction. To do this we compiled all the available isotopic

compositions for the local Blue Ridge crustal basement. The crustal end-members include gneisses, diorites-granites, and charnokites from Pettingill et al. (1984) and Sinha et al. (1996). These samples are corrected to the average eruptive age of the VA Eocene magmatism ~50Ma (Figure S2.2). To estimate the effect of depleted mantle sources we included local MORB samples, collected offshore from the VA Eocene magmas (Janney et al., 2001). Finally we produced assimilation-fractional crystallization modeling (AFC, DePaolo, 1981) with our end-member sample TK5 and a representative crustal end-member (Figure S2). For TK5, we used a modal composition of 30% olivine + 30% clinopyroxene + 40% plagioclase determined as CIPW norm of the primary magma composition in equilibrium with mantle (Fo_{90}) and the partition coefficients compiled by Rollinson (1993), and Pb from McKenzie and O'Nions (1991).

In terms of Pb isotopes the local Blue Ridge crust is surprisingly unradiogenic ($^{206}Pb/^{204}Pb$ < 17.6; $^{207}Pb/^{206}Pb$ 15.52-15.65; $^{208}Pb/^{204}Pb$ 36.5-37.5, Figure S2.3). This is clear evidence that the Pb isotopes signatures are not controlled by crustal contamination, and if anything, will produce less radiogenic magmas. AFC modeling failed to explain the Pb-data array of the Eocene magmas. Thus, the Pb-isotopes compositions are more consistent of mixing of MORB (Depleted Mantle) and HIMU sources (Figure S2.2 A and B). Although, Sr-isotopes from the VA samples may be controlled by crustal interaction by some degree, they are also within the range of expected mantle values from other Atlantic intraplate settings (Figure 4, main text), explained by mixing of MORB and HIMU sources (Figure S2.2 C). Finally, the Nd-isotopes from four of our VA Eocene samples can be explained by AFC modeling (Figure S2.2 D). Nevertheless, it is important to keep in mind that similar Nd-isotopes compositions have been found in the Cape Verde Archipelago (Figure 2.4, main text). The rest of the samples can be explained by mixing of MORB and HIMU sources, consistent with the results of Pb and Sr systems.

References

Alexander, E.C., Jr., Mickelson, G.M., and Lanphere, M.A., 1978, Mmhb-1: a new $^{40}Ar/^{39}Ar$ dating standard, in Zartman, R.E., ed., Short papers of the fourth international conference, geochronology, cosmochronology, and isotope geology 1978: U.S. Geological Survey Open-File Report 78-701, p. 6-8.

Cebula, G.T., Kunk, M.J., Mehnert, H.H, Naeseer, C.W., Obradovich, J.D., and Sutter, J.F., 1986, The Fish Canyon tuff, a potential standard for the $^{40}Ar/^{39}Ar$ and fission track dating methods: Terra Cognita, v.6, n. 2, p. 140.

Dalrymple, G.B., Alexander, E.C., Lanphere, M.A., and Kraker, G.P., 1981, Irradiation of samples for $^{40}Ar/^{39}Ar$ dating using the Geological Survey TRIGA reactor: U.S. Geol. Survey Prof. Paper 1176, 55 p.

Dalrymple, G.B. and Lanphere, M.A., 1969, Potassium-Argon dating principals techniques and applications to geochronology: W.H. Freeman and Company, 258 p.

Dasgupta, R., Hirschmann, M.M., and Smith, N.D., 2007, Partial melting experiments of peridotite+ CO2 at 3 GPa and genesis of alkalic ocean island basalts: Journal of Petrology, v. 48, n. 11, p. 2093-2124.

Deino, A.L., 2001, User's manual for Mass Spec v. 5.02: Berkeley Geochronology Center Special Publication 1a, 119p.

DePaolo, D., 1981, Trace element and isotopic effects of combined wallrock assimilation and fractional crystallization: Earth and planetary science letters, v. 53, n. 2, p. 189-202.

Fleck, R.J., Sutter, J.F., and Elliot, D.H., 1977, Interpretation of discordant $^{40}Ar/^{39}Ar$ age spectra of Mesozoic tholeiites from Antarctica: Geochim. Cosmochim. Acta, v. 41, p. 15-32.

Gazel, E., Hoernle, K., Carr, M. J., Herzberg, C., Saginor, I., den Bogaard, P. v., Hauff, F., Feigenson, M., and Swisher, C., 2011, Plume–subduction interaction in southern Central America: Mantle upwelling and slab melting: Lithos, v. 121, no. 1-4, p. 117-134.

Gazel, E., Plank, T., Forsyth, D. W., Bendersky, C., Lee, C. T. A., and Hauri, E. H., 2012, Lithosphere versus asthenosphere mantle sources at the Big Pine Volcanic Field, California: Geochemistry, Geophysics, Geosystems, v. 13, no. 6.

Gray, W., Glazner, A. F., Coleman, D. S., and Bartley, J. M., 2008, Long-term geochemical variability of the Late Cretaceous Tuolumne intrusive suite, central Sierra Nevada, California: Geological Society, London, Special Publications, v. 304, no. 1, p. 183-201.

Haugerud, R. A., and Kunk, M.J., 1988, ArAr*, a computer program for reduction of ^{40}Ar-^{39}Ar data: U.S. Geological Survey Open-File Report 88-261, 68 p.

Herzberg, C., 2010, Identification of Source Lithology in the Hawaiian and Canary Islands: Implications for Origins: Journal of Petrology, v. 52, no. 1, p. 113-146.

Herzberg, C., Asimow, P. D., Arndt, N., Niu, Y., Lesher, C. M., Fitton, J. G., Cheadle, M. J., and Saunders, A. D., 2007, Temperatures in ambient mantle and plumes: Constraints from basalts, picrites, and komatiites: Geochemistry, Geophysics, Geosystems, v. 8, no. 2.

Herzberg, C., Asimow, P.D., 2008, Petrology of some oceanic island basalts: PRIMELT2. XLS software for primary magma calculation: Geochemistry, Geophysics, Geosystems, v. 9, n. 9.

Janney, P., and Castillo, P., 2001, Geochemistry of the oldest Atlantic oceanic crust suggests mantle plume involvement in the early history of the central Atlantic Ocean: Earth and Planetary Science Letters, v. 192, n. 3, p. 291-302.

Johnson, K.T., 1998, Experimental determination of partition coefficients for rare earth and high-field-strength elements between clinopyroxene, garnet, and basaltic melt at high pressures: Contributions to Mineralogy and Petrology, v. 133, no- 1-2, p. 60-68, doi:10.1007/s004100050437.

Kelley, K.A., and Cottrell, E., 2009, Water and the oxidation state of subduction zone magmas: Science, v. 325, n. 5940, p. 605-607.

Kelley, K. A., Plank, T., Ludden, J., and Staudigel, H., 2003, Composition of altered oceanic crust at ODP Sites 801 and 1149: Geochemistry, Geophysics, Geosystems, v. 4, no. 6.

Kunk, M.J., and McAleer, R., 2011, $^{40}Ar/^{39}Ar$ Age-spectrum data for hornblende, biotite, white mica, and K-feldspar samples from metamorphic rocks in the Great Smokey Mountains of North Carolina and Tennessee: U.S. Geological Survey Open-File Report 2011-1250, 56 p.

Kunk, M. J., Sutter, J. F., and Naeser, C. W., 1985, High-precision $^{40}Ar/^{39}Ar$ Ages of Sanidine, Biotite, Hornblende, and Plagioclase From the Fish Canyon Tuff, San Juan Volcanic Field,

South-central Colorado: Geological Society of America Abstracts with Programs, v. 17, p. 636.

Lee, C.T.A., Luffi, P., Plank, T., Dalton, H., and Leeman, W.P., 2009, Constraints on the depths and temperatures of basaltic magma generation on Earth and other terrestrial planets using new thermobarometers for mafic magmas: Earth and Planetary Science Letters, v. 279, no. 1, p. 20-33.

McKenzie, D., Jackson, J., and Priestley, K., 2005, Thermal structure of oceanic and continental lithosphere: Earth and Planetary Science Letters, v. 233, no. 3, p. 337-349.

McKenzie, D., and O'nions, R.K., 1991, Partial melt distributions from inversion of rare earth element concentrations: Journal of Petrology, v. 32, n. 5, p. 1021-1091.

Pettingill, H.S., Sinha, A.K., and Tatsumoto, M., 1984, Age and origin of anorthosites, charnockites, and granulites in the Central Virginia Blue Ridge: Nd and Sr isotopic evidence: Contributions to Mineralogy and petrology, v. 85, p. 279-291.

Putirka, K.D., 2005, Mantle potential temperatures at Hawaii, Iceland, and the mid-ocean ridge system, as inferred from olivine phenocrysts: Evidence for thermally driven mantle plumes: Geochemistry, Geophysics, Geosystems, v. 6, no. 5.

Rollinson, H., 1993, Using geochemical data: evaluation, presentation, interpretation: New York, John Wiley & Sons, Inc. p. 52-61.

Sacco, B., Johnson, E.A., and Belkin, H.E., 2011, Depth and temperature of the mantle beneath Mole Hill, an Eocene basalt near Harrisonburg, VA: Geological Society of America Abstracts with Programs, v. 43, no. 5, p. 155.

Sinha, A.K., Hogan, J.P., and Parks, J., 1996, Lead isotope mapping of crustal reservoirs within the Grenville superterrane: I. Central and Southern Appalachians: Earth Processes: Reading the Isotopic Code, v. 95, p. 293-305.

Sobolev, A.V., Hofmann, A.W., Sobolev, S.V., and Nikogosian, I.K., 2005, An olivine-free mantle source of Hawaiian shield basalt: Nature, v. 434, n. 7033, p. 590-597.

Southworth, C. S., Gray, K., and Sutter, J. F., 1993, Middle Eocene Intrusive Igneous Rocks of the Central Appalachian Valley and Ridge Province: Setting, Chemistry and Implications for Crustal Structure.

Staudacher, T., Jessberger, E.K., Dorflinger, D., and Kilko, J., 1978, A refined ultrahigh-vacuum furnace for rare gas analysis: J. Phys. E: Sci. Instrum. v. 11, p. 781-784.

White, W.M., Albarede, F., and Telouk, P., 2000, High-precision analysis of Pb isotope ratios by multi-collector ICP-MS: Chemical Geology, v. 163, n. 3, p. 257-270.

York, D., 1969, Least squares fitting of a straight line with correlated errors: Earth and Planetary science Letters, v.5, p. 320-324.

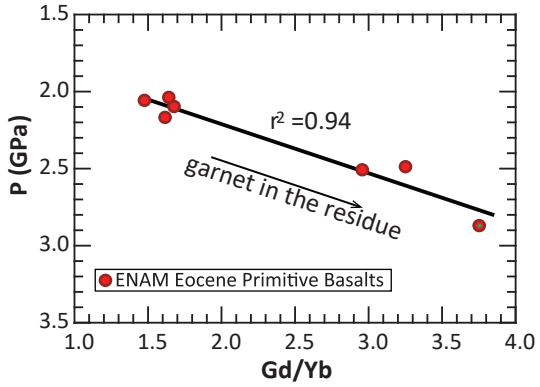

Figure S2.1: Garnet in the residue for the Eocene magmas. Gd/Yb (HREE fractionation) as a function of equilibration pressure (Section S3) suggesting an increase in modal garnet in the residue of the deeper equilibrated magmas.

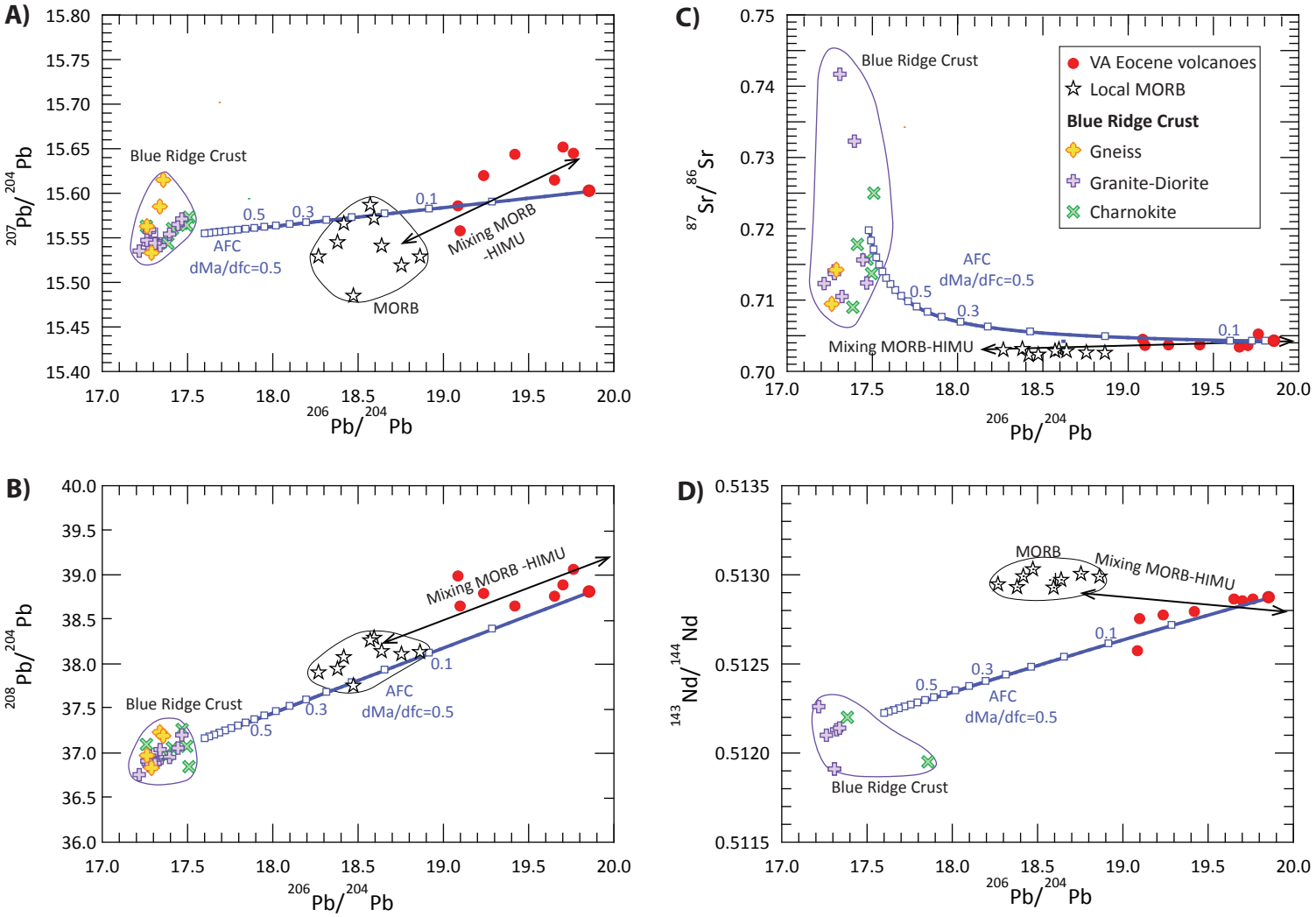

Figure S2.2: Assessment of crustal interaction. Blue Ridge crustal basement from Pettingill et al. (1984) and Sinha et al. (1996). Local MORB samples collected offshore of the VA Eocene magmas from Janney et al. (2001). All the samples are corrected to the average eruptive age of the VA Eocene magmatism, ~50Ma. The blue lines represent AFC modeling (DePaolo, 1981) of samples TK5 and a representative crustal end-member. Every tick mark represents F=0.1, for a maximum F=1. The rate or assimilation to crystallization (R=dMa/dFc) of 0.5. The black lines represent mixing between MORB and HIMU sources.

Chapter 3: Post-rift magmatic evolution of the eastern North American "passive-aggressive" margin

Sarah E. Mazza[1], Esteban Gazel[1*], Elizabeth A. Johnson[2], Michael Bizimis[3], Ryan McAleer[4], C. Berk Biryol[5]

[1]*Department of Geosciences, Virginia Tech, 4044 Derring Hall (0420), Blacksburg, VA 24061*
[2]*Department of Geology and Environmental Science, James Madison University, MSC 6903 Memorial Hall, Harrisonburg, VA 22807*
[3]*Department of Earth and Ocean Sciences, University of South Carolina, 701 Sumter Street, EWS 617, Columbia, SC 29208*
[4]*United States Geological Survey, 12201 Sunrise Valley Dr., MS 926A, Reston, VA 20192-0002*
[5]*Department of Geological Sciences, University of North Carolina at Chapel Hill, Mitchell Hall, 104 South Road, Chapel Hill, NC 27599-3315*

Accepted November, 2016 for publication in *Geochemistry, Geophysics, Geosystems*

Key Points

1) Bimodal late Jurassic volcanics in Virginia-West Virginia produced by tectonic instabilities remnant of the rifting of Pangea.

2) The Eastern North American passive margin is characterized by pulses of post-rift alkaline magmatic activity up to 150 Ma following rifting.

3) Pulses of magmatism and rejuvenation events in Eastern North American margin fail to fit the traditional passive-margin definition.

Abstract

Understanding the evolution of passive margins requires knowledge of temporal and chemical constraints on magmatism following the transition from super-continent to rifting, to post-rifting evolution. The Eastern North American Margin (ENAM) is an ideal study location as several magmatic pulses occurred in the 200 My following rifting. In particular, the Virginia-West Virginia region of the ENAM has experienced two post-rift magmatic pulses at ~152 Ma and 47 Ma, and thus provides a unique opportunity to study the long-term magmatic evolution of passive margins. Here we present a comprehensive set of geochemical data that includes new $^{40}Ar/^{39}Ar$ ages, major and trace-element compositions, and analysis of radiogenic isotopes to further constrain their magmatic history. The Late Jurassic volcanics are bi-modal, from basanites to phonolites, while the Eocene volcanics range from picrobasalt to rhyolite. Modeling suggests that the felsic volcanics from both the Late Jurassic and Eocene events are consistent with fractional crystallization. Sr-Nd-Pb systematics for the Late Jurassic event suggests HIMU and EMII components in the magma source that we interpret as upper mantle components rather

than crustal interaction. Lithospheric delamination is the best hypothesis for magmatism in Virginia/West Virginia, due to tectonic instabilities that are remnant from the long-term evolution of this margin, resulting in a "passive-aggressive" margin that records multiple magmatic events long after rifting ended.

Index Terms

1040 Radiogenic Isotope Geochemistry, 1065 Major and Trace Element Geochemistry, 1009 Geochemical Modeling, 1038 Mantle Processes, 8415 Intra-Plate Processes

1. Introduction

The Eastern North American Margin (ENAM) has been interpreted as a passive margin that developed after the rifting of Pangea and the subsequent opening of the Atlantic Ocean basin approximately 200 Mya [e.g. *Faill,* 1998; *Bradley,* 2008]. However, the ENAM has experienced tectonic rejuvenation post-rifting evident by topographic rejuvenation, ongoing seismic activity, and pulses of magmatic activity. Topographic rejuvenation is marked by increased erosion rates and unsteady sediment deposition [*Pazzaglia and Brandon,* 1996; *McKeon et al.,* 2013], and drainage reorganization [*Miller et al.,* 2013; *Prince and Spotila,* 2013] which have been linked to mantle-driven dynamic topography [*Rowley et al.,* 2013]. The 2011 Mineral, Virginia earthquake (M5.8) [*Horton et al.,* 2015] in the Central Virginia Seismic Zone and the 1886 Charleston, South Carolina earthquake (M6.9) [*Bakun and Hopper,* 2004] in the Charleston Seismic Zone are just two examples of strong earthquakes in the recent seismic record in the ENAM. Post-rift magmatism from the late Jurassic (152 Ma) [*Johnson et al.,* 1971] to Eocene (47 Ma) [*Johnson et al.,* 1971; *Southworth et al.,* 1993; *Mazza et al.,* 2014] is preserved from Virginia to Quebec

[*Eby*, 1984, 1985; *Foland et al.*, 1986]. These indicators of tectonic rejuvenation highlights the not-so-passive nature of the ENAM and suggests that passive margins are not as geologically stable as conventionally thought.

Incipient rift systems like the Red Sea-Gulf of Aden-East Africa rift system are useful for understanding the early development of passive margins [*Sahota et al.*, 1995; *Izzeldin*, 1987; *Pallister et al.*, 2010; *Korostelev et al.*, 2016; *Ebinger et al.*, 2010]. Yet, in order to understand the full evolution of passive margins we need to include areas that have been evolving for 10's of millions of years, such as ENAM. The ENAM is an ideal region to study the evolution of passive margins, and geochemical analysis of multiple magmatic events scattered throughout the ENAM can help to improve our knowledge of the processes that affect post-rift margins.

Here, we present a comprehensive set of new geochemical and geochronological data for the Late Jurassic and Eocene volcanics from the northern Valley and Ridge of Virginia and West Virginia, which includes new $^{40}Ar/^{39}Ar$ ages for the Late Jurassic magmatic pulse along with a complete whole-rock major and trace-element analysis of these alkaline volcanics, and the first Sr-Nd-Pb radiogenic isotopic data for these rocks. The Eocene samples included here are in addition to previously published samples [*Mazza et al.*, 2014], with additional $^{40}Ar/^{39}Ar$ ages that confirm Eocene magmatic activity, and the first discussion of the production of co-genetic felsic magmas. This comprehensive dataset will help understand Late Jurassic and Eocene magmatism and improve our understanding of processes associated with the post-rift magmatic activity in so-called passive margins.

2. Geological Background

The ENAM has enjoyed multiple orogenic events, locally known as Grenville (~1.2-0.9 Ga), Taconic (~470-440 Ma), Acadian (~420-360 Ma), and Alleghanian (~320-260 Ma) and super-continent break-up with Rodinia at ~570 Ma, and Pangea at ~200 Ma [*Tollo et al.,* 2004; *Hatcher*, 2002; 2010]. Starting in the Mesozoic, the ENAM has also experienced multiple magmatic events, not all clearly associated with tectonic events. The rifting of Pangea at ~200 Ma is related to the widespread magmatism of the Central Atlantic Magmatic Province (CAMP) [*Nomade et al.,* 2007; *Marzoli et al.,* 2011; *Blackburn et al.,* 2013; *Callegaro et al.,* 2013; *Whalen et al.,* 2015]. CAMP is preserved throughout the ENAM [*Whalen et al.,* 2015] and is located near Late Jurassic and Eocene volcanics of northwest Virginia - West Virginia (Figure 3.1) [*Johnson et al.,* 1971; *De Boer et al,* 1988; *Mazza et al.,* 2014]. CAMP has been associated with a possible super plume [e.g., *Wilson,* 1997], but Whalen et al. [2015] proposed that the breakup of Pangea, and the formation of CAMP, is related to a massive detachment of the low angle subducting Rheic plate which existed between the modified Laurentian margin (North America) and Gondwana prior to the Alleghenian orogeny. They found that the source of CAMP was significantly modified by subduction processes and melted at temperatures below what is expected from mantle plume activity.

Pangea rifting and CAMP magmatism initiated the ENAM's development into a passive margin [*Puffer,* 2001 & 2003; *Whalen et al.,* 2015], but the subsequent pulses of volcanic activity, plus recent mantle-influenced, dynamic topographic increase [e.g. *Rowley et al.,* 2013]. This suggests that the passive margin is in fact a dynamically active margin, meaning that even though traditional tectonic forces no longer effect the margin, it is still dynamically changing due to the structure of the mantle. Two magmatic events are recorded in the northern Valley and Ridge of Virginia - West Virginia: a Late Jurassic pulse that erupted approximately 50 My after

the initiation of rifting, followed by an Eocene pulse approximately 100 My later [*Johnson et al.*, 1971; *Mazza et al.*, 2014].

Post-rifting magmatism is not limited to Virginia - West Virginia. The ENAM experienced other Jurassic to Cretaceous magmatic events such as those recorded at the Monteregian Hills alkaline province in Quebec [*Eby*, 1984, 1985; *Foland et al.*, 1986; *Roulleau et al.*, 2013], the White Mountain Magma Series in New England, and the New England seamounts, all of which have been connected to the proposed Great Meteor hotspot (Figure 3.1) [*Crough*, 1981; *Duncan*, 1984; *McHone and Butler*, 1984; *Jansa and Pe-Piper*, 1988; *Klitgord et al.*, 1988; *McHone*, 1996]. Late Jurassic - Early Cretaceous kimberlitic magmatism in New York and Pennsylvania have been associated with the Great Meteor Hotspot [*Heaman and Kjarsgaard*, 2000; *Bikerman et al.*, 1997].

A series of Late Jurassic alkaline volcanics are found in the Valley and Ridge province of northern Virginia - West Virginia, alongside CAMP and Eocene volcanics [*Johnson et al.*, 1971; *Southworth et al.*, 1993]. K-Ar dating of a nepheline syenite from Augusta County, Virginia first constrained these alkaline units to the Late Jurassic (145 ± 7 Ma and 153 ± 8 Ma for biotite and amphibole, respectively) [*Zartman et al.*, 1967]. Johnson et al. [1971] gave the first detailed petrology for the Augusta County alkaline suite, and a recent study by Meyer and van Wijk [2015] presented detailed geochemistry for these Late Jurassic alkaline lavas, but limits Late Jurassic magmatism to a ~ 1000 km^2 elliptical area in Augusta County. Southworth et al. [1993] had Late Jurassic magmatism encompass a larger region that included Pendleton County, West Virginia, with a $^{40}Ar/^{39}Ar$ date of 147.0 ± 0.7 Ma from a mica pyroxenite. Meyer and van Wijk [2015] proposed that Late Jurassic volcanism were produced by lithospheric delamination

that resulted with the delaminated material interacting with the surrounding mantle lithosphere to trigger melting.

The youngest magmatic event in the ENAM is the Eocene (47.9 ± 0.2 to 47.0 ± 0.2 Ma [*Mazza et al.*, 2014]) suite of volcanics found in the Valley and Ridge province of northern Virginia - West Virginia (Figure 3.1) [*Southworth et al.*, 1993]. The Eocene volcanics occur as dikes, sills, plugs, and diatremes up to ~400 m in diameter in at least 150 documented locations [*Southworth et al.*, 1993; *Tso et al.*, 2004; *Tso and Surber*, 2006]. Several hypotheses have attempted to explain the Eocene volcanism: 1) a regional basement fracture zone along the 38th parallel linking volcanism in Kansas to Virginia [*Zartman et al.*, 1967; *Fullagar and Bottino*, 1969; *Dennison and Johnson*, 1971], 2) a still cooling magma chamber which also can account for regional uplift and local warm springs [*Dennison and Johnson*, 1971], 3) a shift in mid-plate stresses due to plate reorganization [*Vogt*, 1991] 4) a hidden hotspot [*Chu et al.*, 2013] and 5) delamination of an eclogized lower lithosphere or fossilized slab [*Mazza et al.*, 2014]. Lithospheric delamination remains the favored model for the production of the Eocene magmatic event, which can also explain the recent dynamic topographic uplift experienced in Virginia [*Pazzaglia and Gardner*, 1994; *Miller et al.*, 2013; *Rowley et al.*, 2013], that left a mantle scar, evident from slow-velocity anomalies under the Virginia – West Virginia Eocene volcanics [*Chu et al.*, 2013; *Schmandt and Lin*, 2014; *Biryol et al.*, 2016].

3. Materials and Methods

We collected and analyzed 29 new samples from Virginia and West Virginia that expand on previously published data [*Mazza et al.*, 2014]. We collected additional mafic and felsic volcanics assumed to belong to the Eocene magmatic pulse, and new mafic and felsic volcanics

assumed to belong to the Late Jurassic magmatic pulse. Latitude/longitude locations are reported in Table 1.

$^{40}Ar/^{39}Ar$ ages were determined at the New Mexico Geochronology Research Laboratory and at the U.S. Geological Survey (USGS) in Reston, Virginia. One biotite separate and 2 matrix concentrates were prepared for rocks expected to be Eocene in age. These samples were analyzed by the furnace-step heating method at the New Mexico Geochronology Research Laboratory on a Mass Analyzer Products Limited (MAP) 215-50 noble gas mass spectrometer following the standard procedure of this lab [e.g. *McDowell et al.,* 2005]. Biotite and amphibole separates were prepared for dikes presumably of Jurassic age. Aliquots of these mineral separates were irradiated in two packages (KD55 & KD57) in the central thimble facility at the TRIGA reactor (GSTR) at the USGS in Denver, Colorado. The monitor mineral used in both packages was FCT-3 sanidine with an age of 27.79 Ma [*Kunk et al.,* 1985; *Cebula et al.,* 1986] relative to MMhb-1 at 519.4 ± 2.5 Ma [*Alexander et al.,* 1978; *Dalrymple et al.,* 1981]. Following irradiation the samples were analyzed by the furnace-step heating methods on a MAP 216 mass spectrometer at the USGS in Reston, Virginia. Data reduction was completed following the techniques outlined in Kunk and McAleer [2011], Hagarud and Kunk [1988], and Deino [2001].

Alteration-free rock chips of sample matrices were selected under a stereoscope microscope, powdered in an alumina mill, and fluxed into homogeneous glass disks with ultrapure 34.83% $Li_2B_4O_7$ – 64.67% $LiBO_2$ – 0.5% LiBr flux from Spex® (certified <<1 ppm blank for all trace elements) in the Petrology Lab at Virginia Tech for EDS-XRF and Laser Ablation ICPMS analyses, following the protocols in Mazza et al. [2014]. Major element geochemistry was collected on a Panalytical EDS-XRF with a silicon detector at the Department of Geosciences at Virginia Tech. The accuracy for USGS standard BHVO-2 (run as an

unknown) was better than 1% for most major elements but Na_2O and P_2O_5 was only better than 8% within reported values. The average relative standard deviation for 10 replicates of BHVO-2 were <1% for all major elements except Na_2O and P_2O_5 which were <3%. Trace elements from fluxed glasses were collected with an Agilent 7500ce ICPMS coupled with a Geolas laser ablation system following the procedures detailed in Kelley et al. [2003] and Gazel et al. [2012], with a He flow rate ~1 L/m – 5 Hz and an energy density per sample of ~ 7 – 10 J/cm^2. LA-ICP-MS data was calibrated with fluxed glasses of USGS standards BHVO-2, BCR-2, BIR-1, and STM-1 using Ti from XRF as an internal standard. High precision trace element standard values are from He et al. [2015], Willbold and Jochum [2005], and Kelley et al. [2003] (standard values used reported in Table 1). The average relative accuracy for 10 replicates of BHVO-2 (run as an unknown) was better than 5% for most trace elements except Sc, Cr, Rb, Y, Zr, Nb, Sn, Ta, Pb, Th, and U (better than 15%). The average precision for BHVO-2 was better 4% for all elements with the exception of Sc, Zn, Sn, and Tm (<13 %,) (complete statistical analysis reported in Table 1).

Radiogenic isotope ratios were determined at the Center for Elemental Mass Spectrometry (CEMS), University of South Carolina (USC) following established procedure for this lab [*Bizimis et al.,* 2013; *Khanna et al.,* 2014]. Isotopic ratios for Pb, Nd, and Sr were obtained on a Neptune multi collector ICPMS at USC. Pb isotope ratios were determined by Tl-addition [*White et al.,* 2000]. Standard NBS-981 was determined at $^{206}Pb/^{204}Pb = 16.933 \pm 0.001$, $^{207}Pb/^{204}Pb = 15.486 \pm 0.001$, $^{208}Pb/^{204}Pb = 36.682 \pm 0.004$ (2σ, n=10). Isotopic ratios for Nd were normalized to $^{146}Nd/^{144}Nd = 0.7219$ and the Nd standard JNdi was measured at $^{143}Nd/^{144}Nd = 0.512094 \pm 0.000009$ (2σ, n=8). All Nd measurements are reported relative to JNdi $^{143}Nd/^{144}Nd = 0.512115$. Isotopic ratios for Sr were normalized to $^{86}Sr/^{88}Sr = 0.1194$ and replicate analyses of standard

NBS-987 yielded $^{87}Sr/^{86}Sr = 0.710316 \pm 0.000013$ (2σ, n=7). All Sr measurements are reported relative to NBS-987 $^{87}Sr/^{86}Sr = 0.710250$. USGS standards BCR-2 and BHVO-1 were run as unknowns and are presented in Table 2. Full procedural blanks ran at Pb < 38pg, Sr < 80pg, and Nd < 10 pg (Table 2).

4. Results

4.1 New geochronological constraints

$^{40}Ar/^{39}Ar$ ages from Augusta County, Virginia, confirm a Late Jurassic magmatic event ~50 Ma after the rifting of Pangea. High precision $^{40}Ar/^{39}Ar$ biotite and amphibole plateau ages from sample 39 (Figure 3.1) are 152.7 ± 0.4 Ma and 153.3 ± 0.4 Ma, respectively (Supplementary Figure 3.1a, b). These mineral separates yield integrated ages of 152.5 ± 0.5 Ma, and 152.2 ± 0.4 Ma, respectively. Biotite and amphibole were also dated from sample 35 and yielded slightly disturbed age spectra (Supplementary Figure 3.2a, b). However, these samples yield preferred ages of 153.4 ± 1.0 Ma and 152.9 ± 0.7 Ma, and suggest alkali magmatism occurred over a short period of time (<1 Ma) at 152-153 Ma.

$^{40}Ar/^{39}Ar$ analyses for the Eocene magmatic event include biotite dated from sample 22b which yields an age of 48.79 ± 0.07 Ma (Supplementary Figure 3.3) and is the location as 22a, which yields an age of 47.0 ± 0.2 Ma (amphibole) [*Mazza et al.*, 2014]. Matrix from sample 6 (basalt) yields an age of 48.6 ± 1.0 Ma (Supplementary Figure 3.4). Matrix from sample 2 (basalt) was also dated and yields slightly disturbed age spectra (Supplementary Figure 3.5) but the preferred ages of 48.78 ± 0.89 Ma and 47.39 ± 0.60 Ma are consistent with the other reported ages for the Eocene event [*Mazza et al.*, 2014].

4.2 Geochemistry of the Late Jurassic magmatism

There are two populations of samples, relatively low silica (SiO_2 44-47 wt%) and high silica (SiO_2 56-58 wt%). The low silica samples (Figure 3.2) have varying textures from porphyritic to aphanitic. Porphyritic samples are characterized by fine-grained matrix with phenocrysts of pyroxene + nepheline ± olivine ± amphibole ± biotite ± apatite. Amphibole and pyroxene phenocrysts are zoned with smooth, rounded edges, but show no other signs of reabsorption (Supplementary Figure 3.6a, b). Some pyroxenes have altered cores, and can be as large as 4 mm. Crustal xenoliths are common in the low silica samples. Like the Late Jurassic mafic suite, the high silica samples range from aphanitic with no phenocrysts to having abundant amphibole (0.7 - 2.5 mm) + biotite (< 0.6 mm) + nepheline ± K-feldspar phenocrysts (< 7 mm) (Supplementary Figure 3.6c). Amphibole phenocrysts in the high silica samples are defined by sharp crystal edges and range from (Supplementary Figure 3.6d). In some cases, K-feldspar phenocrysts exhibit tartan plaid twinning. Nepheline and feldspars in the groundmass generally form blades that are elongate to paleoflow direction. For more detailed petrographic descriptions for these samples, see Johnson et al. [1971].

Primitive mantle normalized spider diagrams show enrichments in Ba, but some show depletions in other fluid-mobile elements (Rb, K, and U) and a negative slope in the heavy rare earth elements (HREE) (Figure 3.3a). The Jurassic mafic samples are more enriched in high field strength elements (e.g., Nb 128-164 ppm, Ta 6-7ppm, Zr 168-297ppm) than average ocean island basalt (OIB) and plot in the upper end of the OIB field in the mantle array (Figure 3.4a) [*Pearce,* 2008]. Ce/Pb values straddle the canonical OIB values (~25), while Nb/U show greater variability, ranging from average OIB-concentrations to more enriched values (Figure 3.4b)

[*Hofmann et al.,* 1986]. These volcanics are also characterized by enrichments in Gd/Yb and La/Yb (Figure 3.4c).

The Late Jurassic felsic samples are predominantly classified as phonolites, with one tephriphonolite (Figure 3.2). These phonolites are extremely enriched in high field strength elements (e.g., Nb 239-710 ppm, Ta 11-41 ppm, Zr 444-1190 ppm) compared to the average non-subduction influenced phonolites. The general primitive normalized pattern for the Virginia – West Virginia phonolites shows depletions in Ba, Sr, P, and Ti, an enrichment in Pb, and a flat/slight positive slope in HREE (Figure 3.3b).

Sr-Nd-Pb isotopic analyses from one trachybasalt and four phonolites are plotted in Figure 3.5 (Table 2). The range of radiogenic isotopic ratios for the Late Jurassic event, age corrected to 150 Ma, are $(^{87}Sr/^{86}Sr)_i$ 0.704170 - 0.711616, $(^{143}Nd/^{144}Nd)_i$ 0.512459 - 0.512546, $(^{206}Pb/^{204}Pb)_i$ 18.630 – 22.646, $(^{207}Pb/^{204}Pb)_i$ 15.562 – 15.792, and $(^{208}Pb/^{204}Pb)_i$ 38.216 – 40.141.

It is important to note that sample 32, previously used in Mazza et al. [2014], has been re-grouped from the Eocene suite to the Jurassic suite, based on geographic location, trace element enrichments, and $^{144}Nd/^{143}Nd$ radiogenic isotopes.

4.3 Geochemistry of the Eocene magmatism

The Eocene mafic samples range from picrobasalt to basalt (41-48 wt%, Figure 3.2, Table 1). The mafic samples are generally porphyritic with fresh olivine (0.2 – 1 mm) + clinopyroxene (<7 mm) + spinel (< 0.1 mm) phenocrysts (Supplementary Figure 3.7a). Some samples also contain mantle clinopyroxene and olivine xenocrysts and plagioclase microphenocrysts [*Sacco et al.,* 2011]. The mafic units are generally better preserved in the field, found as dikes, sills, and volcanic plugs. The felsic samples are aphanitic to porphyritic with

fresh biotite (< 2 mm) ± amphibole (< 0.5 mm) and somewhat altered plagioclase and alkali feldspar phenocrysts (Supplementary Figure 3.7b, c). Amphibole and biotite generally have well defined crystal edges.

Trace elements normalized to primitive mantle show a typical intraplate signature (Figure 3.3c) that includes a steep slope in the HREE, with enrichments in Gd/Yb and La/Yb (Table 1, Figure 3.3c and 3.4c). Positive enrichments are found in high field strength elements (e.g., Nb 27-107 ppm, Ta 1-6 ppm, Zr 98-252 ppm) and depletions are found in fluid mobile elements (e.g. K and Pb). These mafic volcanics also fall within the OIB region of the mantle array (Figure 3.4a) [*Pearce,* 2008] and are close to canonical OIB Ce/Pb and Nb/U values (Figure 3.4b) [*Hofmann et al.,* 1986].

The felsic samples range in composition from trachyandesite to rhyolite (SiO_2 56-69 wt%, Figure 3.2). Like the mafic samples, high field strength elements are enriched (Figure 3.3d), but the HREE show a flat slope as also noted in samples from the Jurassic event. Dy/Yb ratios are also lower than the mafic volcanics, which is attributed to amphibole differentiation [*Davidson et al.,* 2007].

5. Discussion

5.1. Petrological Modeling to Evaluate Magma Evolution

The composition of the most primitive mafic volcanics is useful for understanding where the magmas equilibrated in the mantle, but to better understand mafic to felsic magma evolution we conducted geochemical modeling using rhyoliteMELTS [*Gualda et al.*, 2012]. Calculations were completed for crystal fractionation beginning from the liquidus and then cooling at 5 °C temperature intervals at constant pressure.

Ideally, the most primitive mafic composition should be the starting composition for fractional crystallization. However, the most primitive composition for the Late Jurassic volcanics failed to produce fractional crystallization models and thus we conducted our models with a range of starting compositions. The average composition of the mafic Late Jurassic volcanics produced melting models that best correspond to the compositions of the phonolites. For the Late Jurassic event a variety of starting pressures, water contents, and oxygen fugacities (fO_2, buffered with fayalite-magnetite-quartz, FMQ) were used in the models, with 10 kbar/35 km and 1 wt% H_2O producing the fractional crystallization paths that correspond with our data (Figure 3.6). While the water contents remain unknown for the Late Jurassic event, 1 wt% water is a reasonable estimate given the presence of hydrous phases such as amphibole and biotite, and the ability of phonolitic melts to contain 0.7-4.9 wt% water [*Carrol and Blank,* 1997; *Di Muro et al.,* 2006]. Using an fO_2 FMQ buffer, we produce models for fractional crystallization that best reproduce the evolution from basanite to phonolite (Figure 3.6a). As the biotite and K-feldspar were successfully crystallized in our models, but it failed to crystallize amphibole, which is a common limitation of rhyoliteMELTS [*Gualda et al.,* 2012]. Besides failing to crystalize amphibole, nepheline did not crystallize in these models which potentially is viable with the increase in Al_2O_3 that the phonolites exhibit but the models do not reproduce (Figure 3.6b). The other possibility to explain this difference in Al_2O_3 between the models and observed compositions is magmatic recharge. However, we do not see textural indicators of reabsorption in the samples.

For the Eocene event, we modeled a variety of starting compositions, pressures, water contents, and fO_2 values. The most primitive Eocene mafic sample (10) yielded models at 2 kbar/7 km and 1 wt% H_2O that best reproduced the data trends. Models with 1 wt% H_2O are

within the range of magmatic H_2O calculated for the Eocene magmas [*Sacco et al.*, 2011; *Soles et al.,* 2014]. FMQ best reproduced the majority of the fractionation trends of the felsic samples (Figure 3.6), especially MgO and FeO* (Figure 3.6d). However, in order to reproduce the alkali content of the trachydacites/rhyolites, the buffer FMQ +3 was necessary. This could be a limitation of the model because of its inability to produce thermodynamically complex phases, such as amphibole. Amphibole fractionation could explain the flat trend in Al_2O_3 *vs.* MgO space that the rhyoliteMELTS fails to reprodue (Figure 3.6b).

5.2. Assessment of Crustal Interaction

Crustal contamination has the potential to affect the trace element and isotopic compositions of the Late Jurassic and Eocene volcanics. Mazza et al. [2014] showed that the Eocene mafic volcanics were not affected by crustal contamination by conducting assimilation-fractional crystallization (AFC) model calculations [*DePaolo*, 1981]. To assess if any crustal material was assimilated during the evolution of the Late Jurassic event, we conduct similar AFC modeling. For the mafic end-member we used the most primitive sample with isotopic data, 32, which has a modal composition of 10% olivine, 30% clinopyroxene, and 60% plagioclase. We used the most primitive sample because we are interested in how these magmas evolve to more felsic compositions, and if the more felsic compositions share isotopic signatures with the regional basement. Using the modal compositions and parameters for bulk trace-element partition coefficients for Sr, Nd, and Pb [*Rollinson*, 1993; *McKenzie and O'Nions,* 1991], we calculated partition coefficients of 1.12 for Sr, 0.10 for Nd, and 0.22 for Pb. Trace element compositions for the Late Jurassic volcanics and the basement material used in the AFC models are similar (Table 3). A limited dataset of isotopic compositions for local Blue Ridge crustal

basement consisting of gneisses, diorite-granites, and charnokites was used for the assimilant composition [*Pettingill et al.,* 1984; *Sinha et al.,* 1996]. We modeled AFC for the extreme isotopic endmembers (RM1, lowest $^{87}Sr/^{86}Sr$; S-3-81, highest $^{87}Sr/^{86}Sr$; JP-92-36, most enriched Pb) and for the average composition of local Blue Ridge basement, from the Pedlar and Lovingston Massifs approximately 50 km to the southeast of the Late Jurassic volcanics, and the average regional Blue Ridge basement from Georgia, South Carolina, North Carolina, and Virginia [*Sinha et al.,* 1996; *Samson et al.,* 1995; *Carrigan et al.,* 2003].

The regional and local Blue Ridge basement is dominated by unradiogenic lead ($^{206}Pb/^{204}Pb < 17.6$ and $^{208}Pb/^{204}Pb < 37.5$) such that AFC fails to explain the trend for the Late Jurassic enriched composition ($^{206}Pb/^{204}Pb < 22.646$ and $^{208}Pb/^{204}Pb < 40.141$) (Figure 3.7a, b). Even when considering the isotopic endmembers, AFC fails to explain the enriched Pb compositions of the Late Jurassic volcanics (Figure 3.7a, b). Nd for the Late Jurassic volcanics is fairly consistent (average $^{143}Nd/^{144}Nd = 0.51250$) and generally more radiogenic than the local basement (average $^{143}Nd/^{144}Nd = 0.51221$). While a few basement samples are within the range of the Late Jurassic volcanics, AFC using the average basement composition cannot account for the radiogenic $^{143}Nd/^{144}Nd$ measured in the Late Jurassic volcanics (Figure 3.7c). The Late Jurassic volcanics share a similar range of $^{86}Sr/^{87}Sr$ as the Virginia basement material, and AFC modeling suggests up to 30% assimilation of basement material can influence the Sr compositions of these volcanics. However, when comparing Sr with the other isotopic systems, AFC cannot account for the trends of $^{87}Sr/^{86}Sr$ *vs.* $^{206}Pb/^{204}Pb$ (e.g. Figure 3.7d), $^{87}Sr/^{86}Sr$ *vs.* $^{207}Pb/^{204}Pb$, $^{87}Sr/^{86}Sr$ *vs.* $^{208}Pb/^{204}Pb$, or $^{87}Sr/^{86}Sr$ *vs.* $^{143}Nd/^{144}Nd$.

The evolution from the most primitive mafic sample with isotopic data to the most evolved phonolite does not seem to be controlled by interaction with the basement material, and

in fact plots in the opposite direction from crustal interaction. However, we must be careful with these interpretations for three reasons, a) the availability of complete Sr-Nd-Pb radiogenic isotopes plus trace element abundances for regional crustal basement is limited, and b) it is not certain that the lower crust beneath the Appalachians is the same as the basement massifs [*Pettingill et al.,* 1984; *Sinha et al.,* 1996], c) we cannot rule out AFC with carbonate crust, as this area of Virginia – West Virginia has abundant carbonates, but we cannot model AFC with these regional carbonates due to the lack of complete trace element and radiogenic isotopic data [e.g. *Samson,* 1996 which lacks trace element concentrations].

5.3 Contrasting the record of Late Jurassic and Eocene Events in Virginia- West Virginia

The Late Jurassic and Eocene magmatic events both range from mafic (basanite or picrobasalt) to felsic (phonolite or rhyolite) compositions (Figure 3.2). The mafic rocks from both events share intraplate signatures with enrichments in LILE and Nb/Yb and Th/Yb ratios. Heavy REE are good indicators of garnet in the residue, as seen by both the steep slope of HREE (Figure 3.3a and c) and high Gd/Yb ratios (Figure 3.4c). Therefore, both the Virginia-West Virginia Late Jurassic and Eocene mafic volcanics have HREE signatures indicative of melt originating at depths with residual garnet (>2.5-3 GPa, e.g., Johnson [1998] and Salters et al. [2002] for peridotite mantle and 1.8-5 GPa for pyroxenite mantle, e.g. Liu and Persnall, [2000]; Tuff et al. [2005]). The Late Jurassic mafic pulse has higher concentration of LREE than the Eocene pulse (La/Yb > 83 *vs.* 19, respectively), as well as high field strength elements (Nb/Yb > 73 *vs*. 32, respectively) suggesting that they resulted from lower degrees of partial melting or a more enriched source in incompatible elements. Ce/Pb and Nb/U values are close to the canonical OIB value (Figure 3.4b) [*Hofmann et al.,* 1986], suggesting an asthenospheric source

with limited interaction with the continental crust for both events. The enrichments of Nb/U are greater for the Late Jurassic event, which could suggest small melt fractions. Similarly, the Late Jurassic phonolites are also more enriched in LILE than the Eocene felsic rocks, and are characterized by depletions in Ba, Sr, P, and Ti. Depletions in Ba, Sr, and Eu are indicative of feldspar fractionation (Figure 3.3b) while lower P and Ti concentrations probably resulted from fractionation of apatite and Ti-oxides, respectively. The felsic volcanics from the Eocene event do not share the Ba and Eu depletions (Figure 3.3d). The rhyoliteMELTS models for the Late Jurassic volcanics produced K-feldspar during late stage fractionation, which agrees with the presence of K-feldspar phenocrysts and the trace element chemistry.

Radiogenic isotopic data show clear differences in the two pulses of magmatism in Virginia – West Virginia. We age-corrected Sr-Nd-Pb isotopes of the Late Jurassic volcanics to 150 Ma (Table 2, Figure 3.5). Additionally, the ENAM isotopic values are shown with global data for phonolites from continental intraplate, rift (East African Rift; EAR) and oceanic settings, kimberlites (Circum-Parana, Serbia, Canada, Baltic Shield, and New York), carbonatites, New England Seamounts, and Monteregian Hills, in order to elucidate processes that could have been responsible for volcanism. Radiogenic isotopes are indicators of melts derived from various mantle reservoirs, which have been defined as depleted mid-ocean ridge basalt mantle (DMM), enriched mantle I and II (EMI and EMII), and high μ (μ = $^{238}U/^{204}Pb$) mantle (HIMU) [*Zindler and Hart*, 1986]. The Late Jurassic alkaline volcanics cover a larger range of $(^{206}Pb/^{204}Pb)_i$ *vs* $(^{207}Pb/^{204}Pb)_i$ space than the Eocene pulse, with the phonolites extending towards radiogenic Pb-isotopes with HIMU affinities. The extent of radiogenic $(^{206}Pb/^{204}Pb)_i$ ratios is well beyond the typical range of silicate magmas. The only other locations with similar enrichments in $^{206}Pb/^{204}Pb$ are kimberlites from Circum-Parana and carbonatites from the EAR. The high

$^{206}Pb/^{204}Pb$ values from Circum-Parana have not been adequately explained, but the overall isotopic signatures suggest lithospheric mantle interaction common to kimberlites [*Araujo et al.*, 2001]. Enrichments in $^{208}Pb/^{204}Pb$ can be interpreted as interaction with an enriched mantle (EMII) component (Figure 3.5b). Kimberlites from the Baltic Shield and Serbia, and carbonatites and phonolites from the EAR have similar enrichments in $^{206}Pb/^{204}Pb$ and $^{208}Pb/^{204}Pb$ ratios. Overall, the variable enrichments in $^{208}Pb/^{204}Pb$ relative to $^{206}Pb/^{204}Pb$ suggest that the ENAM Late Jurassic alkaline volcanics contained EMII and HIMU components in their source, while the Eocene event suggests mixing between a HIMU and DMM component [*Mazza et al.*, 2014].

Late Jurassic alkaline volcanics in the ENAM have relatively uniform $(^{143}Nd/^{144}Nd)_i$ values, while $(^{87}Sr/^{86}Sr)_i$ covers a wide range from relatively unradiogenic to radiogenic (Figure 3.5c). These compositions are very similar to the New York kimberlites, which have been interpreted as derived from the asthenospheric mantle [*Bailey and Lupulescu*, 2015]. The enrichments in $^{87}Sr/^{86}Sr$ are potentially related to crustal interaction or calcite alteration.

As previously discussed, AFC cannot adequately explain the trends of Sr-Nd-Pb systematics for the Late Jurassic volcanics. Instead Sr-Nd-Pb systematics show an enrichment of radiogenic Pb with magma evolution, and $^{87}Sr/^{86}Sr$-$^{143}Nd/^{144}Nd$ compositions on par with volatile rich lithologies, e.g. kimberlites and carbonatites. We interpret these trends as the melting of an EMII influenced mantle source similar to the source of the New York kimberlites to the north, the interaction with an un-sampled high $^{206}Pb/^{204}Pb$ source potentially associated with metasomatism typical to kimberlite/carbonatite magmas.

5.4 Origin of co-genetic felsic rocks associated with the post-rift mafic pulses

A previous study interpreted these Late Jurassic volcanics as low and high silica adakites [*Meyer and van Wijk*, 2015]. Adakites were defined by Defant and Drummond [1990] as subduction related intermediate to felsic rocks, though further evidence also suggests that not all adakites are subduction related since partial melting of delaminated continental crust can also produce adakite compositions [*Xu et al*., 2002]. Adakites usually crystallize plagioclase, hornblende, and biotite, and have low Y and Yb (<18 ppm and 1.9 ppm, respectively), high Mg# (molar[MgO/(MgO+FeO)]*100)) of ~51, high $(La/Yb)_N > 10$ [*Martin*, 1999] and high Sr/Y [*Defant and Drummond*, 1990].

Some trace element signatures of Virginia - West Virginia Late Jurassic volcanics resemble adakites, as both the high silica and low silica rocks have high $(La/Yb)_N$ (Figure 3.8a) and high Sr/Y (Figure 3.8b), well within the range of global adakites. However, Yb_N and Y values are higher than the global adakite composition. In addition, the Mg# (Figure 3.8c) of the high silica volcanics is <20, thus significantly lower than the expected Mg# of adakites.

We instead interpret these rocks as phonolites, which are more enriched in Yb_N *vs*. $(La/Yb)_N$ (Figure 3.8a) and Y *vs*. Sr/Y (Figure 3.8b) than adakites. We restricted the geochemical data downloaded from GEOROC to high precision geochemistry that included the full range of trace elements (in particular Nb and Ta), and then subdivided the data to continental, rift (EAR), and oceanic phonolites. All three types of phonolites have high $(La/Yb)_N$ and high Sr/Y, similar to what is expected for adakites. However, Yb_N and Y are significantly more enriched in phonolites than in adakites. In general, the and high silica Late Jurassic volcanics predominantly correspond to phonolites from the EAR and ocean islands. The Mg# of these rift and intraplate phonolites is also within the range of the high silica Late Jurassic volcanics. Nb and Ta are potentially the most important elemental pair to help distinguish subduction *vs* non-subduction

magmas, due to the depletions of Nb and Ta in subduction related magmas. Arc-related adakites have strong depletions in Nb and Ta relative to other elements of similar compatibility [*Maury et al.*, 1996]. Meyer and van Wijk [2015] did not report any Nb or Ta data in their study, and thus could not use these elements to further help constrain their interpretation. As mentioned above, we found that Late Jurassic volcanics are highly enriched in Nb and Ta (Figure 3.3a and b), which is strong evidence for our reinterpretation of these rocks as non-subduction influenced phonolites. The alkali contents and mineral chemistry can also help determine adakites verses phonolite compositions, with the major element compositions of adakites being more similar to andesite-dacites whereas phonolites are enriched in alkalis (Figure 3.8d) [*Streckeisen,* 1979] and the preferred fractionation of feldspars in adakites and feldspathoids in phonolites. The Late Jurassic volcanics are enriched in Na_2O and K_2O and fractionated nepheline, both common features of phonolites.

Highly evolved alkaline lavas such as phonolites can be produced by several processes: fractional crystallization [e.g. *Panter et al.,* 1997], assimilation fractional crystallization (AFC) [e.g. *Wiesmaier et al.,* 2012], and variable degrees of partial melting [e.g. *Pelleter et al.*, 2014]. Fractional crystallization is most frequently evoked for producing phonolites in both rift and intraplate environments [e.g. *Panter et al.,* 1997; *Weaver*, 1990; *Le Roex et al.,* 1990; *Holm et al.,* 2005]. The EAR has phonolitic and carbonatitic magmas found within proximal to each other, including Oldoinyo Lengai, the only active carbonatitic volcano [*Bell and Simonetti,* 1996]. Phonolites in the EAR are characterized by depletions in Ba, P, Ti and enrichments in Nb, Y, Hf, Th and Ta [*Klaudius and Keller*, 2006; *Mana et al.*, 2012] and are suggested to have formed by crystal fractionation from nephelinite. Phonolites from Marie Byrd Land, the

continental rift in Antarctica, have also been explained by fractional crystallization of a basanitic magma source [*Panter et al.,* 1997; *LeMasurier et al.,* 2011].

Crystal fractionation has also been the proposed mechanism for the evolution of basanitic to phonolitic magmas in intraplate settings, such as seen in Trindade [*Weaver,* 1990; *Siebel et al.,* 2000], Tristan da Cunha [*Le Roex et al.*, 1990], Kerguelen [*Weis et al.*, 1993], and Cape Verde [*Holm et al.,* 2005]. Like rift phonolites, these evolved lavas have enrichments in Nb, Ta, Zr, and Hf and depletions in Ti. However, Tenerife in the Canary Islands and Mayotte in the Comoros Islands are two intraplate settings with evolved phonolites that cannot be adequately explained by fractional crystallization, where AFC and/or recycling of crustal material has been proposed [*Wiesmaier et al.,* 2012].

Based on our petrological modeling using rhyoliteMELTS (Figure 3.6), fractional crystallization from a basanitic magma source could have produced the Late Jurassic phonolites. The evolved nature of these phonolites makes constraining melting conditions difficult with traditional geothermobarometers. Nevertheless, one mafic sample can be used to estimate temperatures of melt equilibration with the Lee et al. [2009] thermobarometer, as it is based on olivine-melt Fe-Mg exchange for temperature calculations, and Si activity in melt in equilibrium with orthopyroxene + olivine for pressure calculations. Sample 31 was the only sample to crystallize olivine (sample 31) yielding melt equilibration conditions of 1351 °C and 2.09 GPa/70 km. Fractional crystallization models suggest that the phonolites equilibrated around 1 GPa, or approximately 35km depth. This places the final stages of fractional crystallization at the base of the crustal lithosphere, assuming an average crustal thickness of 40 km. Trace element signatures for the Late Jurassic phonolites agree with a shallow region of crystallization due to

the flat/slight positive slope in HREE (Figure 3.3b) and a low Dy/Yb ratio (Figure 3.4d), consistent with the presence of amphibole in cumulate phases [e.g. *Davidson et al.,* 2007].

Our models (Figure 3.6) show that the Eocene trachydacites and rhyolites are likely the result of crystal fractionation at shallow pressures. Modeling crystallization conditions suggest that these magmas differentiated at 0.2 GPa/ 6 km. HREE signatures confirms a shallow crystallization depth, seen by a flat slope in HREE (Figure 3.3d) that potentially obscured the original source-related signatures. Amphibole fractionation with an overall higher SiO_2 concentration also confirms crystallization at shallow depths (Figure 3.4d). This modeling exercise shows that the Eocene and Late Jurassic events fractionated at different depths, likely due to the difference in source compositions. The common association of phonolites with carbonatites, and the similarities of the Late Jurassic radiogenic isotopic data with volatile rich lithologies, e.g. carbonatites and kimberlites, suggests that carbonatite metasomatism could be responsible for composition of the Late Jurassic volcanics.

5.5 Wide-spread alkaline magmatic pulses in the Late Jurassic along the ENAM

New England and the adjacent Montréal region of Canada have also experienced multiple pulses of magmatic activity since the breakup of Pangea recorded by the White Mountain Magma Series (WMMS) from 200 - 90 Ma [*Foland and Faul*, 1977; *Hubacher and Foland,* 1991], the Monteregian Hills volcanic province in Montréal at 124 Ma [*Foland et al.,* 1986], and the New England Seamounts (NESM) with a clear west-east age progression from 103 Ma to 82 Ma [*Duncan,* 1984] (Figure 3.9). The multiple pulses of magmatism in New England have been linked to the movement of the Great Meteor hotspot [e.g. *Eby*, 1985], however all events except the NESM lack a clear age progression which argues against a common source.

Even if the WMMS, Monteregian Hills, and the NESM are not all the products of the Great Meteor hotspot, these volcanics and the Virginia- West Virginia volcanics can help elucidate processes involved with post-rift magmatism of the ENAM. Limited data exists for the post-rift New England volcanics, but what is available suggests an alkaline affinity. The Monteregian Hills range from alkali basalts to carbonatites (Oka carbonatite complex in the west) [*Eby,* 1985; *Roulleau et al.,* 2013], and the NESM consist of alkali basalts to basanites [*Houghton et al.,* 1979]. The Virginia- West Virginia Eocene event shares REE signatures with the NESM. The Late Jurassic event was more enriched in REE than the NESM and shares geochemical similarities with the NY kimberlites (elevated Gd/Yb, La/Yb, and Nb/Yb) (Figure 3.4).

The depletions of Zr and Hf relative to REE of similar compatibility in the upper mantle are often taken as indicators of carbonate metasomatism [*Dupuy et al.,* 1992; *Rudnick et al.,* 1993]. Virginia- West Virginia Eocene volcanics plot, on average, close to what is expected of OIBs, while Virginia – West Virginia Late Jurassic samples have increasingly larger Zr and Hf depletions relative to the REE (low Zr/Sm), pointing towards a source that may have been metasomatized by carbonate rich fluids (Figure 3.4e). The Late Jurassic volcanics are also more enriched in Sr (average 1983 ppm) than the Eocene volcanics (average 830 ppm), which can also be an indicator of carbonate metasomatism. The Monteregian Hills and NY kimberlites also have Zr and Hf depletions relative to the REE, and enrichments in Sr, that all trend towards a carbonatite-metasomatised source, consistent with the presence of carbonatites in the Monteregian Hills and the link between kimberlites and carbonate metasomatism.

5.6 Implications for the post-rift evolution of passive margins

Reactivation of a passive margin to a magmatically active margin would require processes that are associated with intraplate volcanism. Mantle plumes, thermochemical anomalies that originate deep within the earth (i.e., the core-mantle boundary) [*Morgan,* 1971; *Wilson,* 1973; *Hofmann and White,* 1982], are one mechanism that can account for post-rift magmatism. However, the mantle plume model cannot explain all non-tectonic, intraplate magmatism [*Anderson,* 2000; *Anderson and King,* 2014]. Alternative processes in the upper mantle, such as lithospheric delamination [*Ducea and Saleeby,* 1998; *Lustrino,* 2005] and shear-driven upwelling [*Conrad et al.,* 2011] can result in magmatic reactivation of passive margins without a deep mantle source. Lithospheric delamination results from gravitational instabilities in the lower lithosphere causing denser material to pull away and thus allowing warmer, more buoyant asthenospheric material to upwell and melt via decompression. Lithospheric instabilities in rift/post-rift settings have been suggested to form due to lateral variations of temperature and density formed during rifting processes [e.g., *Sleep,* 2007]. Such instabilities could allow for local delamination along post-rifted margins and associated magmatism [*Meyer and van Wijk,* 2015]. Shear-driven upwelling occurs in the asthenosphere as a result of relative motion of the mantle and a change in lithospheric thickness, such that the asthenosphere will upwell in the region of a lithospheric pocket, or scar during a delamination event [*Conrad et al.,* 2011]. Geodynamic modeling [*Meyer and van Wijk,* 2015] supports the idea that instabilities develop at the edges of rift zones, leading to delamination and associated decompression melting. They showed that the outer margins of rift zones, up to 600 km away from active rifting, could see a thinned mantle lithosphere (up to 25 km of lithospheric thinning), while the upper crust remains unchanged. The extension rate and width of the rift zone do not appear to affect the formation of these instabilities. The development of gravitational instabilities thus triggered delamination and

Meyer and van Wijk [2015] suggested that the delaminated material undergoes metamorphism, interacting with the surrounding mantle.

Lithospheric delimitation could be an appropriate model for the production of the Late Jurassic volcanics, as proposed by Meyer and van Wijk [2015]. While only one sample yielded a melt equilibration temperature, 1351 °C is too cold to invoke melting from a mantle plume [e.g. *Lee et al.,* 2009]. Based on the depths of melt equilibration for the mafic volcanics at 70 km and the felsic volcanics at 35 km, we suggest that delamination triggered initial melting with upwelling asthenosphere that incorporated lithospheric mantle during fractionation at shallower depths. Melting of other alkaline and volatile rich volcanics from along the ENAM between ~153 Ma and ~125 Ma, e.g. New York kimberlites and Monteregian Hills alkaline-carbonatite complex, are not the product of lithospheric delamination [e.g. *Roulleau et al.,* 2013; *Bailey and Lupulescu,* 2015], but nonetheless sample a similar, volatile rich, heterogeneous upper mantle as the Late Jurassic volcanics of Virginia – West Virginia.

Mazza et al. [2014] suggested that lithospheric delamination was the cause for the Eocene magmatic pulse by coupling geochemical data with seismic evidence for varying thicknesses of the lithosphere from North Carolina [*Wagner et al.,* 2012] and Virginia [*Benoit and Long,* 2009]. Since then, data from the EarthScope and USArray seismic network for the ENAM has confirmed that lithospheric delamination could be a plausible mechanism for Eocene volcanism [*Schmandt and Lin,* 2014; *Liu and Holt,* 2015; *Biryol et al.,* 2016; *Porter et al.,* 2016]. Schmandt and Lin [2014] reported a region of low seismic velocities termed the Central Appalachian anomalous zone, which includes our study area and the presence of a possible lithospheric scar. They suggest that lithospheric delamination could result in the present day anomaly. Schmandt and Lin [2014] also discussed the possibility of the fluids from the Farallon slab affecting the

rheology of the upper mantle and thus the low velocity anomaly. Biryol et al. [2016] expanded on these observations with additional data from the Southeastern Suture of the Appalachian Margin Experimental array. They suggest that delamination has been occurring in a piecemeal fashion, which also accounts for the rejuvenated tectonism seen in the ENAM. They suggest that a more recently removed piece of the lithosphere is visible as a fast velocity anomaly within the warmer asthenosphere (see F5 in Figure 3.10). Porter et al. [2016] also agrees that delamination is the most plausible mechanism to explain the observed low velocity anomaly.

Tomographic cross sections in the region of the Virginia-West Virginia volcanics shows a slow-velocity anomaly in the upper mantle (S2, Figure 3.10, tomography from Biryol et al. [2016]). The present day low-velocity anomaly corresponds to the depths of the Eocene melt equilibrium in Figure 3.10. Eocene mafic melts equilibrated between 2.0 and 3.0 GPa, based on calculations using the Lee et al. [2009] geothermobarometer and discussed in detail in Mazza et al. [2014]. It remains a possibility that partial melt still exists in this slow-velocity region beneath Virginia, and further geophysical work on the region can help clarify this. The possible ongoing presence of partial melts below Virginia could be due to a simultaneous change in the lithosphere-upper mantle asthenosphere flow due to the timing of the Farallon slab arriving to the ENAM [*Ren et al.,* 2007] coupled with the presence of instabilities remnant of rifting. Shear-driven convection [*Ballmer et al.,* 2015] cannot be excluded as a possibility for the ongoing presence of partial melts and more recent topographic rejuvenation events of the central Appalachians [e.g. *Pazzaglia and Garner,* 1994; *Rowley et al.,* 2013].

6. Conclusions

We conclude that lithospheric instabilities that lead to piecemeal foundering and thus delamination are probably the trigger that produced the volcanism and rejuvenation seen from Virginia to New England along the ENAM. The complex inheritance of the formation of the Appalachians by multiple collisions resulted in a "passive-aggressive" margin that continued its evolution 200 My after the opening of the Atlantic. We characterized two magmatic events in Virginia – West Virginia following the opening of the Atlantic Ocean basin, with a pulse at ~153 Ma and at ~47 Ma. The Late Jurassic pulse contains highly alkaline magmas, basanites and trachybasalts to phonolites, with the evolution of these magmas best explained by crystal fractionation at the base of a thinned lithosphere. Sr-Nd-Pb radiogenic isotopes suggest a heterogeneous source, with similar mantle reservoirs also sampled by kimberlites and carbonatites. The late Jurassic magmatic pulse are temporally equivalent with ~147 Ma kimberlites from NY and share isotopic similarities. This suggests that Late Jurassic magmatism was widespread across the ENAM, sampling a uniform upper mantle and was likely caused by tectonic instabilities inherited from rifting of Pangea [*Thomas,* 1977; *Thomas,* 2006].

Timing of the Eocene magmatism has been better constrained to 48-47 Ma. The felsic magmas resulted from crystal fractionation of basaltic magmas at shallow depths. Eocene magmas used preexisting shallow crustal features as melt conduits [*Johnson et al.,* 2013; *Shada et al.,* 2014]. Lithospheric delamination, as proposed by Mazza et al. [2014] remains the best model for magma production, and has been recently supported by geophysical evidence [e.g. *Schmandt and Lin, 2014*; *Biryol et al.,* 2016].

The ENAM records the evolution of continental rifting, from active supercontinent breakup to the development of a magmatically active margin that retains thermal instabilities up to 50 My after rift initiation. Later rejuvenation associated with the Eocene magmatic pulse and

more recent dynamic topography is not connected to the immediate post-rift evolution of the margin, but is likely due to ongoing lithospheric delamination.

Acknowledgements

Data for this study can be found in the supporting information section. This project was supported by GeoPrisms-NSF awards EAR-1249412 to EG and EAR-1249438 to EJ. We thank JMU undergraduate students B. Soles, G. Brennan, M. Bulas, D. Jones, N. Rossi, A. Wenger, and B. Sacco for sample collection help. This manuscript was improved by discussion with L. Wagner and B. Schmandt. We also thank J. Konter, K.S. Hughes, A. Merschat, and one anonymous reviewer for insightful comments and corrections, and T. Becker for editorial handling of this manuscript.

References

Alexander, E.C., Jr., G.M. Mickelson, and M.A. Lanphere (1978), Mmhb-1: a new 40Ar/39Ar dating standard, in Zartman, R.E., ed., *Short papers of the fourth international conference, geochronology, cosmochronology, and isotope geology 1978: U.S. Geological Survey Open-File Report 78-701*, 6-8.

Anderson, D. L. (2000), The thermal state of the upper mantle; no role for mantle plumes, *Geophysical Research Letters,* 27(22), 3623-3626. doi: 10.1029/2000GL011533

Anderson, D. L., and S. D. King (2014), Driving the Earth machine?, *Science,* 346(6214), 1184. doi:10.1126/science.1261831

Araujo, A., R. W. Carlson, J. C. Gaspar, and L. A. Bizzi (2001), Petrology of kamafugites and kimberlites from the Alto Paranaiba alkaline province, Minas Gerais, Brazil, *Contributions to Mineralogy and Petrology,* 142(2), 163-177. doi:10.1007/s004100100280

Bailey, D. G., and M. V. Lupulescu (2015), Spatial, temporal, mineralogical, and compositional variations in Mesozoic kimberlitic magmatism in New York State, *Lithos*, 212, 298-310. doi: 10.1016/j.lithos.2014.11.022

Bakun, W., and M. Hopper (2004), Magnitudes and locations of the 1811–1812 New Madrid, Missouri, and the 1886 Charleston, South Carolina, earthquakes, *Bulletin of the Seismological Society of America*, 94(1), 64-75. doi: 10.1785/0120020122

Ballmer, M. D., C. P. Conrad, E. I. Smith, and R. Johnsen (2015), Intraplate volcanism at the edges of the Colorado Plateau sustained by a combination of triggered edge-driven convection and shear-driven upwelling, *Geochemistry, Geophysics, Geosystems*, 16(2), 366-379. doi:10.1002/2014GC005641

Bell, K., and A. Simonetti (1996), Carbonatite magmatism and plume activity: implications from the Nd, Pb and Sr isotope systematics of Oldoinyo Lengai, *Journal of Petrology*, 37(6), 1321-1339.

Benoit, M., and M. Long (2009), The TEENA experiment: A pilot project to study the structure and dynamics of the eastern US continental margin, *paper presented at AGU Fall Meeting Abstracts*.

Bikerman, M., H. S. Prellwitz, J. Dembosky, A. Simonetti, and K. Bell (1997), New phlogopite K-Ar dates and the age of southwestern Pennsylvania kimberlite dikes, *Northeastern Geology and Environmental Sciences*, 19, 302-308.

Biryol, C. B., L. S. Wagner, K. M. Fischer, and R. B. Hawman (2016), Relationship between observed upper mantle structures and recent tectonic activity across the Southeastern United States, *Journal of Geophysical Research: Solid Earth*, 121(5), 3393-3414. doi: 10.1002/2015JB012698

Bizimis, M., V. J. Salters, M. O. Garcia, and M. D. Norman (2013), The composition and distribution of the rejuvenated component across the Hawaiian plume: Hf-Nd-Sr-Pb isotope systematics of Kaula lavas and pyroxenite xenoliths, *Geochemistry, Geophysics, Geosystems*, 14(10), 4458-4478. doi: 10.1002/ggge.20250

Blackburn, T. J., P. E. Olsen, S. A. Bowring, N. M. McLean, D. V. Kent, J. Puffer, G. McHone, E. T. Rasbury, and M. Et-Touhami (2013), Zircon U-Pb geochronology links the end-Triassic extinction with the Central Atlantic Magmatic Province, *Science*, 340(6135), 941-945. doi: 10.1126/science.1234204

Bradley, D. C. (2008), Passive margins through earth history, *Earth-Science Reviews*, 91(1), 1-26. doi: 10.1016/j.earscirev.2008.08.001

Callegaro, S., A. Marzoli, H. Bertrand, M. Chiaradia, L. Reisberg, C. Meyzen, G. Bellieni, R. E. Weems, and R. Merle (2013), Upper and lower crust recycling in the source of CAMP basaltic dykes from southeastern North America, *Earth and Planetary Science Letters*, 376, 186-199. doi: 10.1016/j.epsl.2013.06.023

Carrigan, C. W., C. F. Miller, P. D. Fullagar, B. R. Bream, R. D. Hatcher, and C. D. Coath (2003), Ion microprobe age and geochemistry of southern Appalachian basement, with

implications for Proterozoic and Paleozoic reconstructions, *Precambrian Research*, 120(1), 1-36. doi: 10.1016/S0301-9268(02)00113-4

Carroll, M. R., and J. G. Blank (1997), The solubility of H2O in phonolitic melts, *American Mineralogist*, 82(5-6), 549-556. doi: 10.2138/am-1997-5-615

Cebula, G.T., M.J. Kunk, H.H. Mehnert, C.W. Naeseer, J.D. Obradovich, and J.F. Sutter (1986) The Fish Canyon tuff, a potential standard for the 40Ar/39Ar and fission track dating methods, *Terra Cognita*, 6(2), 1-140

Conrad, C. P., T. A. Bianco, E. I. Smith, and P. Wessel (2011), Patterns of intraplate volcanism controlled by asthenospheric shear, Na*ture Geoscience*, 4(5), 317-321. doi: 10.1038/ngeo1111

Crough, S. T. (1981), Mesozoic hotspot epeirogeny in eastern North America, *Geology*, 9(1), 2-6. doi: : 10.1130/0091-7613(1981)9

Chu, R., W. Leng, D. V. Helmberger, and M. Gurnis (2013), Hidden hotspot track beneath the eastern United States, *Nature Geoscience*, 6(11), 963-966. doi: 10.1038/ngeo1949

Dalrymple, G.B., Alexander, E.C., Lanphere, M.A., and Kraker, G.P., 1981, Irradiation of samples for 40Ar/39Ar dating using the Geological Survey TRIGA reactor, *U.S. Geological Survey Profession Paper 1176*, 1-55.

Davidson, J., S. Turner, H. Handley, C. Macpherson, and A. Dosseto (2007), Amphibole "sponge" in arc crust?, *Geology*, 35(9), 787-790. doi: 10.1130/G23637A.1

De Boer, J., J. McHone, J. Puffer, P. Ragland, and D. Whittington (1988), Mesozoic and Cenozoic magmatism, *The Geology of North America*, 2, 217-241.

Defant, M. J., and M. S. Drummond (1990), Derivation of some modern arc magmas by melting of young subducted lithosphere, *Nature*, 347(6294), 662-665. doi: 10.1038/347662a0

Deino, A.L. (2001), User's manual for Mass Spec v. 5.02: Berkeley Geochronology Center Special Publication 1a, 1-119.

Dennison, J. M., and R. W. Johnson (1971), Tertiary intrusions and associated phenomena near the thirty-eighth parallel fracture zone in Virginia and West Virginia, *Geological Society of America Bulletin*, 82(2), 501-508. doi: 10.1130/0016-7606(1971)82[501:TIAAPN]2.0.CO;2

Di Muro, A., B. 1. Villemant, G. Montagnac, B. Scaillet, and B. Reynard (2006), Quantification of water content and speciation in natural silicic glasses (phonolite, dacite, rhyolite) by confocal microRaman spectrometry, *Geochimica et Cosmochimica Acta*, 70(11), 2868-2884. doi: 10.1016/j.gca.2006.02.016

DePaolo, D. J. (1981), Trace element and isotopic effects of combined wallrock assimilation and fractional crystallization, *Earth and Planetary Science Letters*, 53(2), 189-202. doi:10.1016/0012-821X(81)90153-9

Dicken, C. L., S. W. Nicholson, J. D. Horton, S. A. Kinney, G. Gunther, M. P. Foose, and J. A. Mueller (2005), Preliminary integrated geologic map databases for the United States: Delaware, Maryland, New York, Pennsylvania, and Virginia Rep. 2331-1258.

Ducea, M., and J. Saleeby (1998), A case for delamination of the deep batholithic crust beneath the Sierra Nevada, California, *International Geology Review*, 40(1), 78-93. doi: 10.1080/00206819809465199

Duncan, R. A. (1984), Age progressive volcanism in the New England seamounts and the opening of the central Atlantic Ocean, *Journal of Geophysical Research*, 89(B12), 9980-9990.

Dupuy, C., J. Liotard, and J. Dostal (1992), Zr/Hf fractionation in intraplate basaltic rocks: carbonate metasomatism in the mantle source, *Geochimica et Cosmochimica Acta*, 56(6), 2417-2423. doi: 10.1016/0016-7037(92)90198-R

Ebinger, C., A. Ayele, D. Keir, J. Rowland, G. Yirgu, T. Wright, M. Belachew, and I. Hamling (2010), Length and timescales of rift faulting and magma intrusion: the Afar rifting cycle from 2005 to present, *Annual Review of Earth and Planetary Sciences*, 38, 439-466. doi: 10.1146/annurev-earth-040809-152333

Eby, G. N. (1984), Geochronology of the Monteregian Hills alkaline igneous province, Quebec, *Geology*, 12(8), 468-470. doi:10. 1130/0091-7613(1984)

Eby, G. N. (1985), Age relations, chemistry, and petrogenesis of mafic alkaline dikes from the Monteregian Hills and younger White Mountain igneous provinces, *Canadian Journal of Earth Sciences*, 22(8), 1103-1111. doi: 10.1139/e85-112

Faill, R. T. (1998), A geologic history of the north-central Appalachians; Part 3, The Alleghany Orogeny, *American Journal of Science*, 298(2), 131-179. doi: 10.2475/ajs.298.2.131

Foland, K., and H. Faul (1977), Ages of the White Mountain intrusives; New Hampshire, Vermont, and Maine, USA, *American Journal of Science*, 277(7), 888-904. doi: 10.2475/ajs.277.7.888

Foland, K., L. A. Gilbert, C. A. Sebring, and C. Jiang-Feng (1986), 40Ar/39Ar ages for plutons of the Monteregian Hills, Quebec: Evidence for a single episode of Cretaceous magmatism, *Geological Society of America Bulletin*, 97(8), 966-974. doi: 10.1130/0016-7606(1986)97

Fullagar, P., and M. L. Bottino (1969), Tertiary felsite intrusions in the Valley and Ridge province, Virginia, *Geological Society of America Bulletin*, 80(9), 1853-1858. doi: 10.1130/0016-7606(1969)80[1853:TFIITV]2.0.CO;2

Gallen, S. F., K. W. Wegmann, and D. Bohnenstiehl (2013), Miocene rejuvenation of topographic relief in the southern Appalachians, *GSA Today*, 23(2), 4-10. doi: 10.1130/GSATG163A.1.

Gazel, E., T. Plank, D. W. Forsyth, C. Bendersky, C. T. A. Lee, and E. H. Hauri (2012), Lithosphere versus asthenosphere mantle sources at the Big Pine Volcanic Field, California, *Geochemistry, Geophysics, Geosystems*, 13(6). doi: 10.1029/2012GC004060

Ghiorso, M. S., and R. O. Sack (1995), Chemical mass transfer in magmatic processes IV. A revised and internally consistent thermodynamic model for the interpolation and extrapolation of liquid-solid equilibria in magmatic systems at elevated temperatures and pressures, *Contributions to Mineralogy and Petrology*, 119(2-3), 197-212. doi: 10.1007/BF00307281

Gualda, G. A., M. S. Ghiorso, R. V. Lemons, and T. L. Carley (2012), Rhyolite-MELTS: a modified calibration of MELTS optimized for silica-rich, fluid-bearing magmatic systems, *Journal of Petrology*, 53(5), 875-890. doi: 10.1093/petrology/egr080

Hatcher, R. D. (2002), Alleghanian (Appalachian) orogeny, a product of zipper tectonics: Rotational transpressive continent-continent collision and closing of ancient oceans along irregular margins, *Special paper-Geological Society of America*, (364), 199-208.

Hatcher, R. D. (2010), The Appalachian orogen: A brief summary, *Geological Society of America Memoirs*, 206, 1-19. doi: 10.1130/2010.1206(01)

Haugerud, R. A., and M.J. Kunk (1988), ArAr*, a computer program for reduction of 40Ar-39Ar data, *U.S. Geological Survey Open-File Report*, 88-261.

He, Z., F. Huang, H. Yu, Y. Xiao, F. Wang, Q. Li, Y. Xia, and X. Zhang (2015), A Flux-Free Fusion Technique for Rapid Determination of Major and Trace Elements in Silicate Rocks by LA-ICP-MS, *Geostandards and Geoanalytical Research*, 40(1), 5-21. doi: 10.1111/j.1751-908X.2015.00352.x

Heaman, L., and B. Kjarsgaard (2000), Timing of eastern North American kimberlite magmatism: continental extension of the Great Meteor hotspot track?, *Earth and Planetary Science Letters*, 178(3), 253-268. doi: 10.1016/S0012-821X(00)00079-0

Hofmann, A. W., and W. M. White (1982), Mantle plumes from ancient oceanic crust, *Earth and Planetary Science Letters*, 57(2), 421-436. doi: 10.1016/0012-821X(82)90161-3

Hofmann, A. W., K. Jochum, M. Seufert, and W. White (1986), Nb and Pb in oceanic basalts: new constraints on mantle evolution, *Earth and Planetary Science Letters*, 79(1-2), 33-45. doi:10.1016/0012-821X(86)90038-5

Holm, P. M., J. R. Wilson, B. P. Christensen, L. Hansen, S. L. Hansen, K. M. Hein, A. K. Mortensen, R. Pedersen, S. Plesner, and M. K. Runge (2005), Sampling the Cape Verde mantle

plume: evolution of melt compositions on Santo Antão, Cape Verde Islands, *Journal of Petrology*, 47(1), 145-189. doi: 10.1093/petrology/egi071

Horton, J. W., M. C. Chapman, and R. A. Green (2015), The 2011 Mineral, Virginia, earthquake, and its significance for seismic hazards in eastern North America—Overview and synthesis, *Geological Society of America Special Papers*, 509, 1-25. doi: 10.1130/2015.2509(01)

Houghton, R., J. Thomas, R. Diecchio, and A. Tagliacozzo (1979), Radiometric ages of basalts from DSDP Leg 43: sites 382 and 385 (New England seamounts), 384 (J Anomaly), 386 and 387 (central and western Bermuda Rise), *Initial reports of the Deep Sea Drilling Project*, Edited by BC Tucholke and PR Vogt, 43, 721-738.

Hubacher, F., and K. Foland (1991), 40Ar/39Ar ages for Cretaceous intrusions of the White Mountain magma series, northern New England, and their tectonic implications, *paper presented at Geological Society of America Abstract Programs*.

Izzeldin, A. (1987), Seismic, gravity and magnetic surveys in the central part of the Red Sea: their interpretation and implications for the structure and evolution of the Red Sea, *Tectonophysics*, 143(4), 269-306. doi: 10.1016/0040-1951(87)90214-9

Jansa, L. F., and G. Pe-Piper (1988), Middle Jurassic to Early Cretaceous igneous rocks along eastern North American continental margin, *AAPG Bulletin*, 72(3), 347-366.

Johnson, E.A., Z.A. Kiracofe, J.T. Haynes, K. Nashimoto (2013). The origin of sandstone xenoliths in the Mole Hill Basalt, Rockingham County, Virginia; implications for magma ascent and crustal structure in the Western Shenandoah Valley, Southeastern Geology, 49(3), 95-118.

Johnson, K. T. (1998), Experimental determination of partition coefficients for rare earth and high-field-strength elements between clinopyroxene, garnet, and basaltic melt at high pressures, *Contributions to Mineralogy and Petrology*, 133(1-2), 60-68. doi: 10.1007/s004100050437

Johnson, R. W., C. Milton, and J. M. Dennison (1971), Field trip to the igneous rocks of Augusta, Rockingham, Highland, and Bath counties, Virginia, *Virginia Division of Mineral Resources.*

Khanna, T. C., M. Bizimis, G. M. Yogodzinski, and S. Mallick (2014), Hafnium–neodymium isotope systematics of the 2.7 Ga Gadwal greenstone terrane, Eastern Dharwar craton, India: implications for the evolution of the Archean depleted mantle, *Geochimica et Cosmochimica Acta*, 127, 10-24. doi: 10.1016/j.gca.2013.11.024

Kelley, K. A., T. Plank, J. Ludden, and H. Staudigel (2003), Composition of altered oceanic crust at ODP Sites 801 and 1149, *Geochemistry, Geophysics, Geosystems*, 4(6). doi: 10.1029/2002GC000435

Klaudius, J., and J. Keller (2006), Peralkaline silicate lavas at Oldoinyo Lengai, Tanzania, *Lithos*, 91(1), 173-190. doi: 10.1016/j.lithos.2006.03.017

Klitgord, K. D., D. R. Hutchinson, and H. Schouten (1988), US Atlantic continental margin; structural and tectonic framework, *The Geology of North America*, 2, 19-55.

Korostelev, F., S. Leroy, D. Keir, C. Weemstra, L. Boschi, I. Molinari, A. Ahmed, G. W. Stuart, F. Rolandone, and K. Khanbari (2016), Magmatism at continental passive margins inferred from Ambient-Noise Phase-velocity in the Gulf of Aden, *Terra Nova*, 28(1), 19-26. doi: 10.1111/ter.12182

Kunk, M.J., and R. McAleer (2011), 40Ar/39Ar Age-spectrum data for hornblende, biotite, white mica, and K-feldspar samples from metamorphic rocks in the Great Smokey Mountains of North Carolina and Tennessee, *U.S. Geological Survey Open-File Report 2011-1250*, 1-56.

Kunk, M. J., J.F. Sutter, and C.W. Naeser (1985), High-precision 40Ar/39Ar Ages of Sanidine, Biotite, Hornblende, and Plagioclase from the Fish Canyon Tuff, San Juan Volcanic Field, South-central Colorado, *paper presented at Geological Society of America Abstract Programs*.

Lee, C.-T. A., P. Luffi, T. Plank, H. Dalton, and W. P. Leeman (2009), Constraints on the depths and temperatures of basaltic magma generation on Earth and other terrestrial planets using new thermobarometers for mafic magmas, *Earth and Planetary Science Letters*, 279(1), 20-33. doi: 10.1016/j.epsl.2008.12.020

LeMasurier, W. E., S. H. Choi, Y. Kawachi, S. B. Mukasa, and N. Rogers (2011), Evolution of pantellerite-trachyte-phonolite volcanoes by fractional crystallization of basanite magma in a continental rift setting, Marie Byrd Land, Antarctica, *Contributions to Mineralogy and Petrology*, 162(6), 1175-1199. doi: 10.1007/s00410-011-0646-z

Le Roex, A., R. Cliff, and B. Adair (1990), Tristan da Cunha, South Atlantic: geochemistry and petrogenesis of a basanite-phonolite lava series, *Journal of Petrology*, 31(4), 779-812. doi: 10.1093/petrology/31.4.779

Liu, Y., and W. E. Holt (2015), Wave gradiometry and its link with Helmholtz equation solutions applied to USArray in the eastern US, *Journal of Geophysical Research: Solid Earth*, 120(8), 5717-5746. doi: 10.1002/2015JB011982

Liu, T.-C., and D. Presnall (2000), Liquidus Phase Relations in the System CaO–MgO–Al2O3–SiO2 at 2· 0 GPa: Applications to Basalt Fractionation, Eclogites, and Igneous Sapphirine, *Journal of Petrology*, 41(1), 3-20. doi: 10.1093/petrology/41.1.3

Lustrino, M. (2005), How the delamination and detachment of lower crust can influence basaltic magmatism, *Earth-Science Reviews*, 72(1), 21-38. doi: 10.1016/j.earscirev.2005.03.004

Mana, S., T. Furman, M. Carr, G. Mollel, R. Mortlock, M. Feigenson, B. Turrin, and C. Swisher (2012), Geochronology and geochemistry of the Essimingor volcano: melting of metasomatized lithospheric mantle beneath the North Tanzanian Divergence zone (East African Rift), *Lithos*, 155, 310-325. doi: 10.1016/j.lithos.2012.09.009

Martin, H. (1999), Adakitic magmas: modern analogues of Archaean granitoids, *Lithos*, 46(3), 411-429. doi: 10.1016/S0024-4937(98)00076-0

Marzoli, A., F. Jourdan, J. H. Puffer, T. Cuppone, L. H. Tanner, R. E. Weems, H. Bertrand, S. Cirilli, G. Bellieni, and A. De Min (2011), Timing and duration of the Central Atlantic magmatic province in the Newark and Culpeper basins, eastern USA, *Lithos*, 122(3), 175-188. doi: 10.1016/j.lithos.2010.12.013

Maury, R. C., F. G. Sajona, M. Pubellier, H. Bellon, and M. J. Defant (1996), Fusion de la croute oceanique dans les zones de subduction/collision recentes; l'exemple de Mindanao (Philippines), *Bulletin de la Société géologique de France*, 167(5), 579-595.

Mazza, S. E., E. Gazel, E. A. Johnson, M. J. Kunk, R. McAleer, J. A. Spotila, M. Bizimis, and D. S. Coleman (2014), Volcanoes of the passive margin: The youngest magmatic event in eastern North America, *Geology*, 42(6), 483-486. doi: 10.1130/G35407.1

McDonough, W. F., and S.-S. Sun (1995), The composition of the Earth, *Chemical Geology*, 120(3), 223-253. doi: 10.1016/0009-2541(94)00140-4

McKeon, R. E., P. K. Zeitler, F. J. Pazzaglia, B. D. Idleman, and E. Enkelmann (2014), Decay of an old orogen: Inferences about Appalachian landscape evolution from low-temperature thermochronology, *Geological Society of America Bulletin*, 126(1-2), 31-46. doi: 10.1130/B30808.1

McHone, J. G., and J. R. Butler (1984), Mesozoic igneous provinces of New England and the opening of the North Atlantic Ocean, *Geological Society of America Bulletin*, 95(7), 757-765. doi: 10.1130/0016-7606(1984)95

McHone, J. G. (1996), Constraints on the mantle plume model for Mesozoic alkaline intrusions in northeastern North America, *Canadian Mineralogist*, 34, 325-334.

McKenzie, D., and R. O'nions (1991), Partial melt distributions from inversion of rare earth element concentrations, *Journal of Petrology*, 32(5), 1021-1091. doi: 10.1093/petrology/32.5.1021

Meyer, R., and J. van Wijk (2015), Post-breakup lithosphere recycling below the US East Coast: Evidence from adakitic rocks, *Geological Society of America Special Papers*, 514, 65-85. doi: 10.1130/2015.2514(06)

Miller, S. R., P. B. Sak, E. Kirby, and P. R. Bierman (2013), Neogene rejuvenation of central Appalachian topography: Evidence for differential rock uplift from stream profiles and erosion rates, *Earth and Planetary Science Letters*, 369, 1-12. doi: 10.1016/j.epsl.2013.04.007

Morgan, W. J. (1971), Convection plumes in the lower mantle, *Nature*, 230, 42-43. doi: 10.1038/230042a0

Nomade, S., K. Knight, E. Beutel, P. Renne, C. Verati, G. Féraud, A. Marzoli, N. Youbi, and H. Bertrand (2007), Chronology of the Central Atlantic Magmatic Province: implications for the Central Atlantic rifting processes and the Triassic–Jurassic biotic crisis, *Palaeogeography, Palaeoclimatology, Palaeoecology*, 244(1), 326-344. doi: 10.1016/j.palaeo.2006.06.034

Pallister, J. S., W. A. McCausland, S. Jónsson, Z. Lu, H. M. Zahran, S. El Hadidy, A. Aburukbah, I. C. Stewart, P. R. Lundgren, and R. A. White (2010), Broad accommodation of rift-related extension recorded by dyke intrusion in Saudi Arabia, *Nature Geoscience*, 3(10), 705-712. doi: 10.1038/ngeo966

Panter, K. S., P. R. Kyle, and J. L. Smellie (1997), Petrogenesis of a phonolite–trachyte succession at Mount Sidley, Marie Byrd Land, Antarctica, *Journal of Petrology*, 38(9), 1225-1253. doi: 10.1093/petroj/38.9.1225

Parrish, J. B., and P. M. Lavin (1982), Tectonic model for kimberlite emplacement in the Appalachian Plateau of Pennsylvania, *Geology*, 10(7), 344-347. doi: 10.1130/0091-7613(1982)10

Pazzaglia, F. J., and T. W. Gardner (1994), Late Cenozoic flexural deformation of the middle US Atlantic passive margin, *Journal of Geophysical Research: Solid Earth*, 99(B6), 12143-12157. doi: 10.1029/93JB03130

Pazzaglia, F. J., and M. T. Brandon (1996), Macrogeomorphic evolution of the post-Triassic Appalachian mountains determined by deconvolution of the offshore basin sedimentary record, *Basin Research*, 8(3), 255-278. doi: 10.1046/j.1365-2117.1996.00274.x

Pearce, J. A. (2008), Geochemical fingerprinting of oceanic basalts with applications to ophiolite classification and the search for Archean oceanic crust, *Lithos*, 100(1), 14-48. doi: 10.1016/j.lithos.2007.06.016

Pelleter, A.-A., M. Caroff, C. Cordier, P. Bachelery, P. Nehlig, D. Debeuf, and N. Arnaud (2014), Melilite-bearing lavas in Mayotte (France): An insight into the mantle source below the Comores, *Lithos*, 208, 281-297. doi: /10.1016/j.lithos.2014.09.012

Pe-Piper, G., and P. H. Reynolds (2000), Early Mesozoic alkaline mafic dykes, southwestern Nova Scotia, Canada, and their bearing on Triassic–Jurassic magmatism, *The Canadian Mineralogist*, 38(1), 217-232. doi: 10.2113/gscanmin.38.1.217

Pettingill, H. S., A. Sinha, and M. Tatsumoto (1984), Age and origin of anorthosites, charnockites, and granulites in the central Virginia Blue Ridge: Nd and Sr isotopic evidence, *Contributions to Mineralogy and Petrology*, 85(3), 279-291. doi: 10.1007/BF00378106

Porter, R., Y. Liu, and W. E. Holt (2016), Lithospheric records of orogeny within the continental US, *Geophysical Research Letters*, 43, 144-153. doi: 10.1002/2015GL066950

Prince, P. S., and J. A. Spotila (2013), Evidence of transient topographic disequilibrium in a landward passive margin river system: knickpoints and paleo-landscapes of the New River basin, southern Appalachians, *Earth Surface Processes and Landforms*, 38(14), 1685-1699. doi: 10.1002/esp.3406

Puffer, J. (2001), Contrasting high field strength element contents of continental flood basalts from plume versus reactivated-arc sources, *Geology*, 29(8), 675-678. doi: 10.1130/0091-7613(2001)029

Puffer, J. H. (2003), A Reactivated Back-Arc Source for CAMP Magma, The Central Atlantic Magmatic Province: Insights from Fragments of Pangea, 151-162. doi: 10.1029/136GM08

Ren, Y., E. Stutzmann, R. D. van Der Hilst, and J. Besse (2007), Understanding seismic heterogeneities in the lower mantle beneath the Americas from seismic tomography and plate tectonic history, *Journal of Geophysical Research: Solid Earth*, 112(B1). doi: 10.1029/2005JB004154

Rollinson, H. (1993), *Using Geochemical Data: Evaluation, Interpretation, Presentation*, edited, Longman, New York, p. 52-61.

Roulleau, E., R. Stevenson, and A. Polat (2013), Geochemical and isotopic (Nd–Sr–Hf–Pb) evidence for a lithospheric mantle source in the formation of the alkaline Monteregian Province (Quebec), *Canadian Journal of Earth Sciences*, 50(6), 650-666. doi: 10.1139/cjes-2012-0145

Ross, M. E. (2010), An Early Triassic 40Ar/39Ar age for a camptonite dyke in Cambridge, Massachusetts, USA, *Atlantic Geology*, 46(1), 127-135. doi: 10.4138/atlgeol.2010.007

Rowley, D. B., A. M. Forte, R. Moucha, J. X. Mitrovica, N. A. Simmons, and S. P. Grand (2013), Dynamic topography change of the eastern United States since 3 million years ago, *Science*, 340(6140), 1560-1563. doi: 10.1126/science.1229180

Rudnick, R. L., W. F. McDonough, and B. W. Chappell (1993), Carbonatite metasomatism in the northern Tanzanian mantle: petrographic and geochemical characteristics, *Earth and Planetary Science Letters*, 114(4), 463-475. doi:10.1016/0012-821X(93)90076-L

Sacco, B., E. A. Johnson, and H. E. Belkin (2011), Depth and temperature of the mantle beneath Mole Hill, an Eocene basalt near Harrisonburg, VA, *paper presented at 2011 GSA Annual Meeting in Minneapolis.*

Sahota, G., P. Styles, and K. Gerdes (1995), Evolution of the Gulf of Aden and implications for the development of the Red Sea, *Rift sedimentation and tectonics in the Red Sea-Gulf of Aden region.*

Salters, V. J., J. E. Longhi, and M. Bizimis (2002), Near mantle solidus trace element partitioning at pressures up to 3.4 GPa, *Geochemistry, Geophysics, Geosystems*, 3(7), 1-23. doi: 10.1029/2001GC000148

Samson, S. D., D. G. Coler, and J. A. Speer (1995), Geochemical and Nd Sr Pb isotopic composition of Alleghenian granites of the southern Appalachians: Origin, tectonic setting, and source characterization, *Earth and Planetary Science Letters*, 134(3), 359-376. doi: 10.1016/0012-821X(95)00124-U

Samson, S. D. (1996), 40Ar/39Ar and Nd-Sr isotopic characteristics of mid-Ordovician North American K-Bentonites: A test of early Paleozoic Laurentia-Gondwana interactions, *Tectonics*, 15(5), 1084-1092. doi: 10.1029/96TC00829.

Schmandt, B., and F. C. Lin (2014), P and S wave tomography of the mantle beneath the United States, *Geophysical Research Letters*, 41(18), 6342-6349. doi: 10.1002/2014GL061231

Shada, J.M., E.A. Johnson, S. Whitmeyer, and B. Cohick, (2014). Structural controls on the method of Eocene magmatic intrusion in Blue Grass Valley, Highland County, Virginia. *Presented at 63rd annual SE GSA meeting.*

Siebel, W., R. Becchio, F. Volker, M. Hansen, J. Viramonte, R. Trumbull, G. Haase, and M. Zimmer (2000), Trindade and Martín Vaz Islands, South Atlantic: Isotopic (Sr, Nd, Pb) and trace element constraints on plume related magmatism, *Journal of South American Earth Sciences*, 13(1), 79-103. doi: 10.1016/S0895-9811(00)00015-8

Sinha, A., J. Hogan, and J. Parks (1996), Lead isotope mapping of crustal reservoirs within the Grenville Superterrane: I. Central and Southern Appalachians, *Earth Processes: Reading the Isotopic Code*, 293-305.

Sleep, N. H. (2007), Edge-modulated stagnant-lid convection and volcanic passive margins, *Geochemistry, Geophysics, Geosystems*, 8(12). doi: 10.1029/2007GC001672

Streckeisen, A. (1979), Classification and nomenclature of volcanic rocks, lamprophyres, carbonatites, and melilitic rocks: Recommendations and suggestions of the IUGS Subcommission on the Systematics of Igneous Rocks, *Geology*, 7(7), 331-335. doi: 10.1130/0091-7613(1979)7

Soles, B., G. Brennan, E. Johnson, S. Mazza, and E. Gazel (2014), Variable Water Concentrations in the Asthenospheric and Lithospheric Mantle Underneath the Eastern United States, *paper presented at AGU Fall Meeting Abstracts.*

Southworth, C. S., K. J. Gray, and J. F. Sutter (1993), Middle Eocene intrusive igneous rocks of the central Appalachian Valley and Ridge province-setting, chemistry, and implications for crustal structure, *US Geological Survey Bulletin* 1839, 1-24.

Stracke, A., A. W. Hofmann, and S. R. Hart (2005), FOZO, HIMU, and the rest of the mantle zoo, *Geochemistry, Geophysics, Geosystems*, 6(5). doi: 10.1029/2004GC000824

Thomas, W. A. (1977), Evolution of Appalachian-Ouachita salients and recesses from reentrants and promontories in the continental margin, *American Journal of Science*, 277(10), 1233-1278. doi: 10.2475/ajs.277.10.1233

Thomas, W. A. (2006), Tectonic inheritance at a continental margin, *GSA today*, 16(2), 4-11. doi: 10.1130/1052-5173(2006)016<4:TIAACM>2.0.CO;2

Tollo, R. P., J. N. Aleinikoff, M. J. Bartholomew, and D. W. Rankin (2004), Neoproterozoic A-type granitoids of the central and southern Appalachians: intraplate magmatism associated with episodic rifting of the Rodinian supercontinent, *Precambrian Research*, 128(1), 3-38. doi: 10.1785/0120020122

Tso, J. L., R. R. McDowell, K. L. Avary, D. L. Matchen, and G. P. Wilkes (2004), Middle Eocene igneous rocks in the Valley and Ridge of Virginia and West Virginia, *US Geological Survey Circular*, 1624, 137-157.

Tso, J. L., and J. D. Surber (2006), Eocene igneous rocks near Monterey, Virginia: a field study, *Virginia Minerals*, 49(3-4), 9-24.

Tuff, J., E. Takahashi, and S. Gibson (2005), Experimental constraints on the role of garnet pyroxenite in the genesis of high-Fe mantle plume derived melts, *Journal of Petrology*, 46(10), 2023-2058. doi: 10.1093/petrology/egi046

Vogt, P. R. (1991), Bermuda and Appalachian-Labrador rises: Common non-hotspot processes?, *Geology*, 19(1), 41-44. doi: 10.1130/0091-7613(1991)019<0041:BAALRC>2.3.CO;2

Wagner, L. S., K. Stewart, and K. Metcalf (2012), Crustal-scale shortening structures beneath the Blue Ridge Mountains, North Carolina, USA, *Lithosphere*, 4(3), 242-256. doi: 10.1130/L184.1

Weaver, B. L. (1990), Geochemistry of highly-undersaturated ocean island basalt suites from the South Atlantic Ocean: Fernando de Noronha and Trindade islands, *Contributions to Mineralogy and Petrology*, 105(5), 502-515. doi: 10.1007/BF00302491

Weis, D., F. Frey, H. Leyrit, and I. Gautier (1993), Kerguelen Archipelago revisited: geochemical and isotopic study of the Southeast Province lavas, *Earth and Planetary Science Letters*, 118(1), 101-119. doi: 10.1016/0012-821X(93)90162-3

White, W. M., F. Albarède, and P. Télouk (2000), High-precision analysis of Pb isotope ratios by multi-collector ICP-MS, *Chemical Geology*, 167(3), 257-270. doi: 10.1016/S0009-2541(99)00182-5

Whalen, L., E. Gazel, C. Vidito, J. Puffer, M. Bizimis, W. Henika, and M. J. Caddick (2015), Supercontinental inheritance and its influence on supercontinental breakup: The Central Atlantic Magmatic Province and the breakup of Pangea, *Geochemistry, Geophysics, Geosystems*, 16(10), 3532-3554. doi: 10.1002/2015GC005885

Wiesmaier, S., V. R. Troll, J. C. Carracedo, R. M. Ellam, I. Bindeman, and J. A. Wolff (2012), Bimodality of Lavas in the Teide–Pico Viejo Succession in Tenerife—the Role of Crustal Melting in the Origin of Recent Phonolites, *Journal of Petrology*. doi: 10.1093/petrology/egs056

Willbold, M., and K. P. Jochum (2005), Multi-Element Isotope Dilution Sector Field ICP-MS: A Precise Technique for the Analysis of Geological Materials and its Application to Geological Reference Materials, *Geostandards and Geoanalytical Research*, 29(1), 63-82. doi: 10.1111/j.1751-908X.2005.tb00656.x

Wilson, J. T. (1973), Mantle plumes and plate motions, *Tectonophysics*, 19(2), 149-164. doi: 10.1016/0040-1951(73)90037-1

Wilson, M. (1997), Thermal evolution of the Central Atlantic passive margins: continental break-up above a Mesozoic super-plume, *Journal of the Geological Society*, 154(3), 491-495. doi: 10.1144/gsjgs.154.3.0491

Xu, J.-F., R. Shinjo, M. J. Defant, Q. Wang, and R. P. Rapp (2002), Origin of Mesozoic adakitic intrusive rocks in the Ningzhen area of east China: partial melting of delaminated lower continental crust?, *Geology*, 30(12), 1111-1114. doi: 10.1130/0091-7613(2002)030

Zartman, R., M. Brock, A. Heyl, and H. Thomas (1967), K-Ar and Rb-Sr ages of some alkalic intrusive rocks from central and eastern United States, *American Journal of Science*, 265(10), 848-870. doi: 10.2475/ajs.265.10.848

Zindler, A., and S. Hart (1986), Chemical geodynamics, *Annual Review of Earth and Planetary Sciences*, 14, 493-571. doi: 10.1146/annurev.ea.14.050186.002425

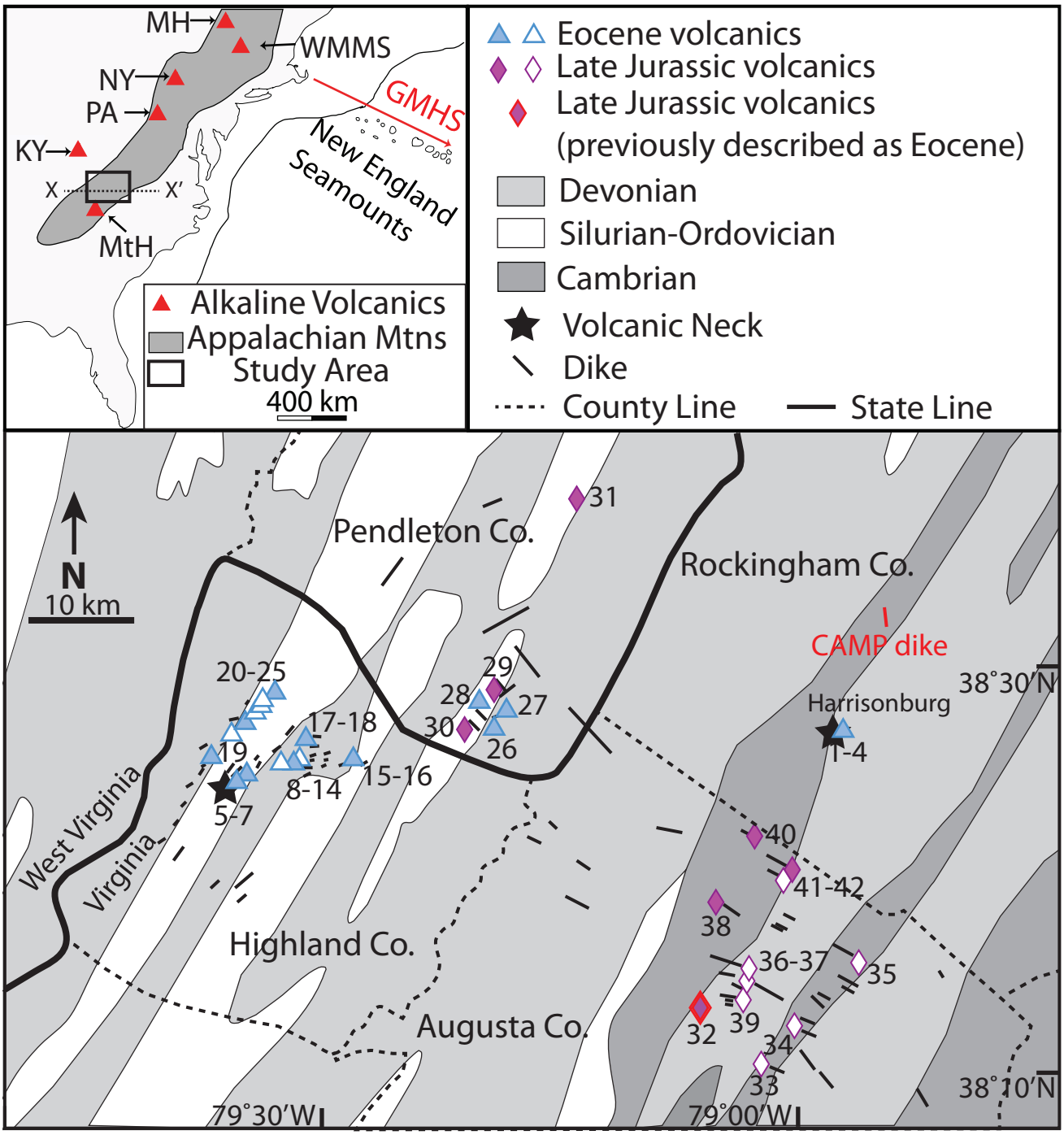

Figure 3.1: Simplified geological map showing sample locations of the Late Jurassic and Eocene volcanic rocks. Closed symbols representing samples of mafic (SiO_2 <50 wt%) composition and open symbols representing samples of felsic (SiO_2 >50 wt%) composition. The Late Jurassic dikes trend to the NW while the Eocene dikes trend to the NE. One NW trending dike in field area has been identified as belonging to the Central Atlantic Magmatic Province, shown in red and labeled on map [*Mazza et al.,* 2014]. GPS coordinates are provided in Table S1. Inset map shows other alkaline/kimberlitic volcanics found in the ENAM, MtH – Mount Horeb Kimberlite, Virginia, KY – Elliot County Kimberlite, Kentucky, PA – Masonville Kimberlite, Pennsylvania, NY – New York Kimberlites, New York, WMMS - White Mountain Magma Series, New Hampshire, MH – Monteregian Hills, Quebec, and the proposed trace of the Great Meteor Hot Spot (GMHS) with associated New England Seamounts. The Appalachian mountains (abbreviated Mtns) are shown in dark grey outline. Line X-X' corresponds to tomography of Biryol et al. [2016] in Figure 3.10.

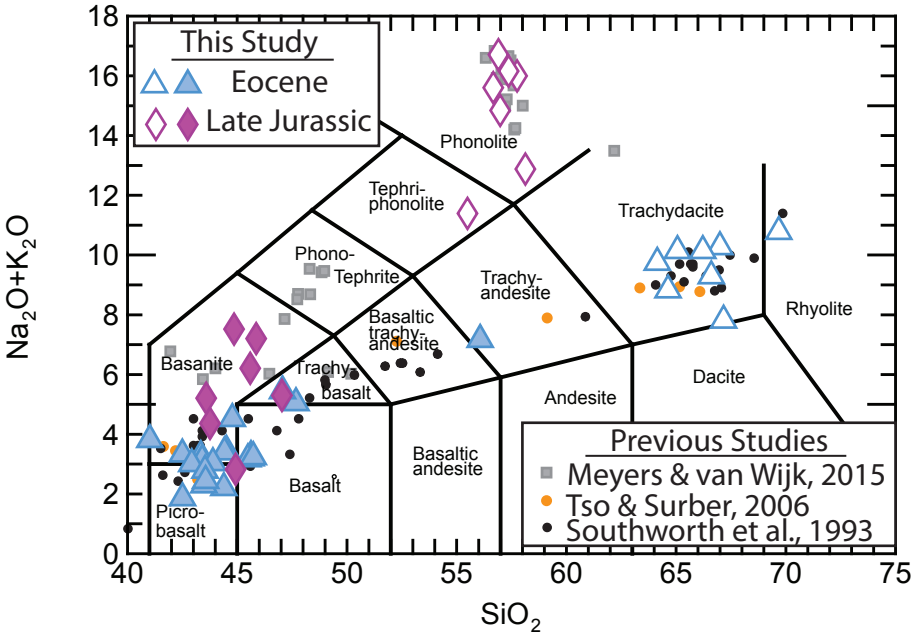

Figure 3.2: Total alkalis ($Na_2O + K_2O$) *vs.* SiO_2 for the Virginia-West Virginia Late Jurassic and Eocene volcanic pulses showing bimodal populations. Also plotted are Late Jurassic volcanics from Meyer and van Wijk [2015] and Eocene volcanics from Southworth et al. [1993] and Tso and Surber [2006]. Closed symbols representing samples of mafic (SiO_2 <50 wt%) composition and open symbols representing samples of felsic (SiO_2 >50 wt%) composition.

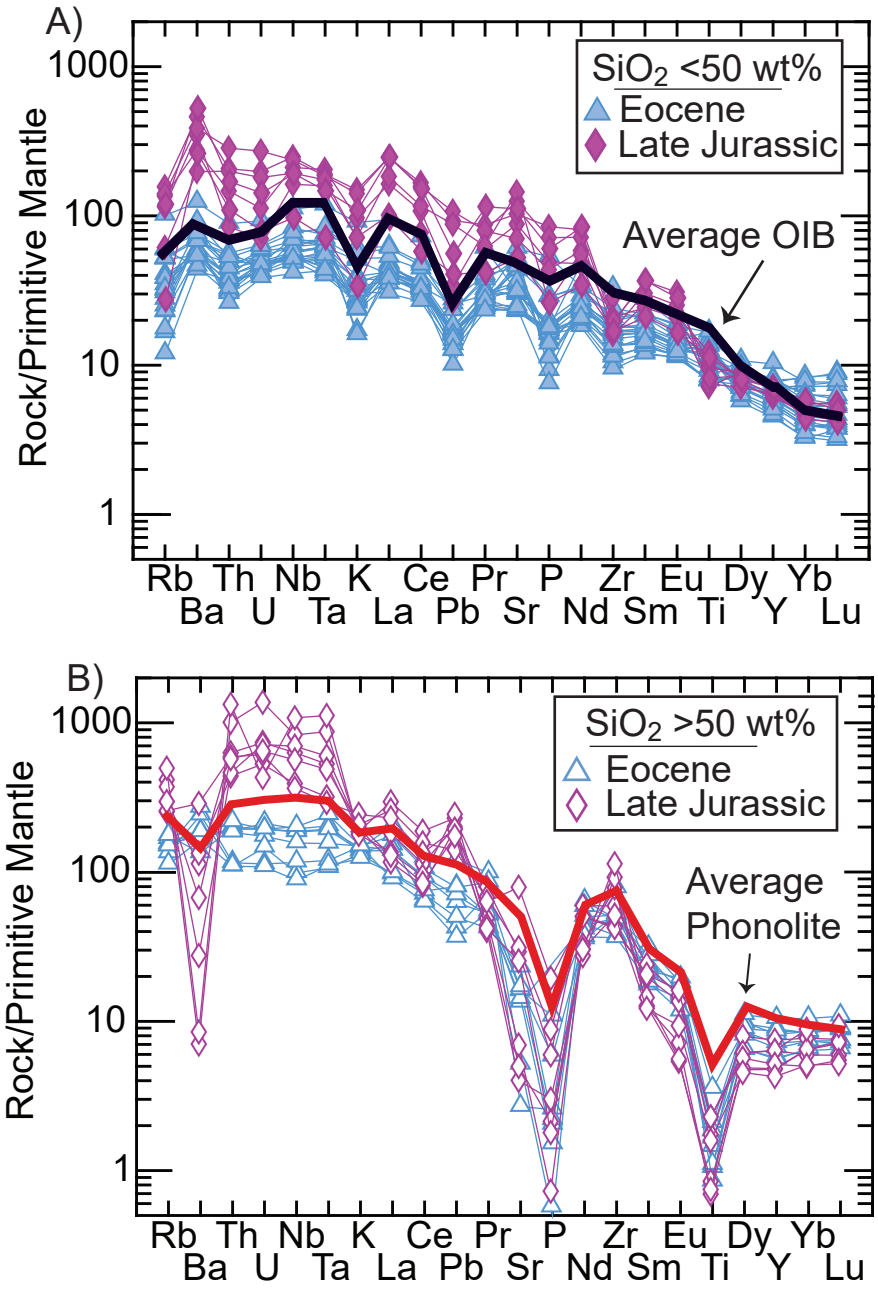

Figure 3.3: Primitive mantle normalized trace elements of the Virginia – West Virginia post-rift magmas. a) Eocene and Late Jurassic volcanics of mafic composition (SiO_2 <50 wt%) with average OIB calcuated from the GEOROC database, and b) Eocene and Late Jurassic volcanics of felsic composition (SiO_2 >50 wt%) with average global non-subduction influenced phonolites calculated from the GEOROC database.

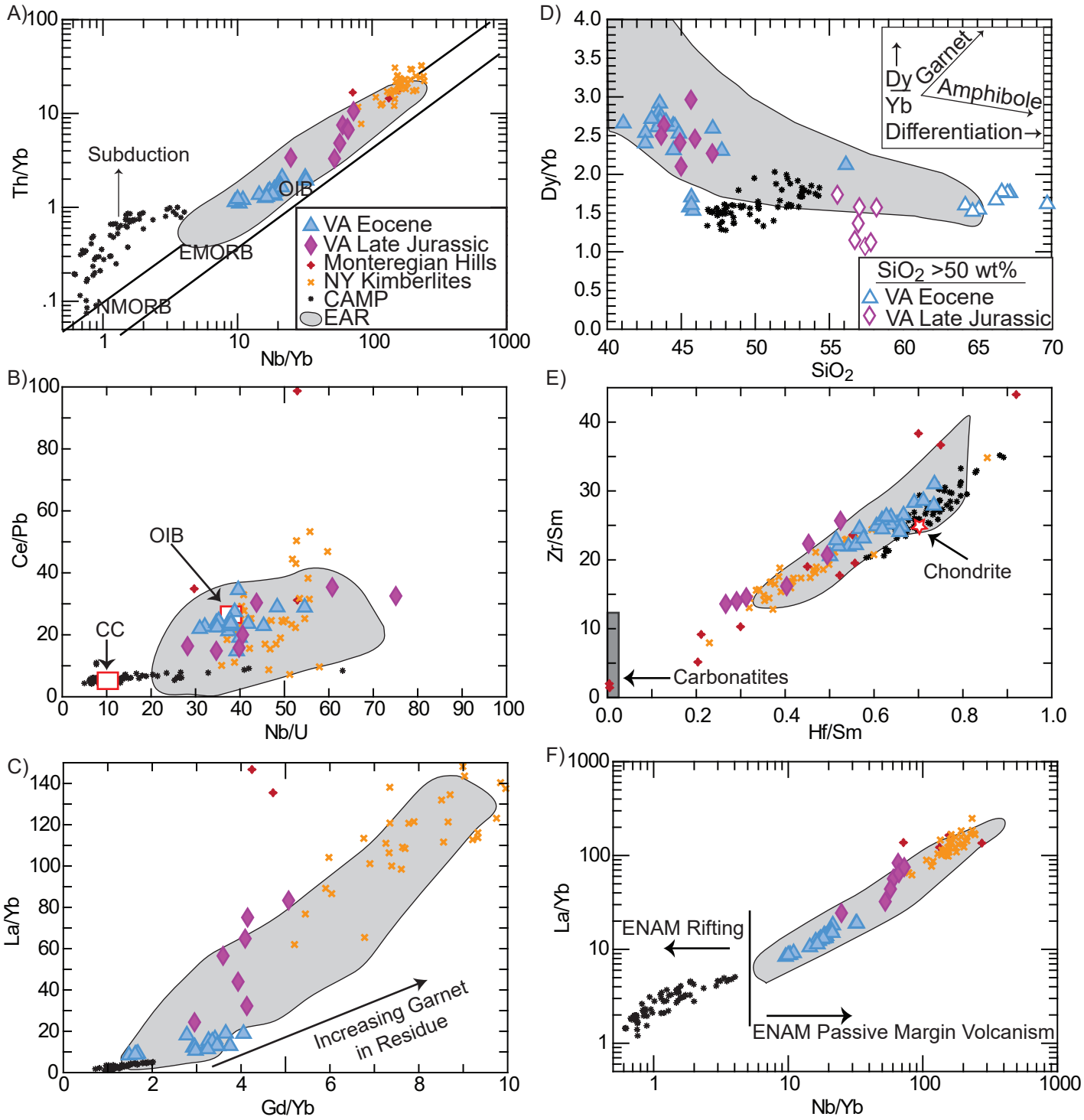

Figure 3.4: Trace element diagrams. A) Mantle array diagram from Pearce [2008] showing the regions for NMORB (Normal Mid Ocean Ridge Basalt), EMORB (Enriched Mid Ocean Ridge Basalt), OIB (Ocean Island Basalt), and subduction influence. B) Ce/Pb *vs.* Nb/U to show conical continental crust (CC) and OIB concentrations [*Hofmann et al.*, 1986]. C) La/Yb *vs.* Gd/Yb to show correlation of increasing Gd/Yb and increasing garnet in residue. D) Dy/Yb *vs.* SiO_2 to show amphibole fractionation [*Davidson et al.*, 2007] E) Zr/Sm *vs.* Hf/Sm modified from Dupuy et al. [1992] to show trends to carbonatite metasomatism. F) La/Yb *vs.* Nb/Yb shows differences in ENAM rifting and passive margin volcanics. The East African Rift volcanics (EAR) are shown in a field, whereas southeast Brazil, Central Atlantic Magmatic Province (CAMP), NY Kimberlities, and Monteregian Hills are shown individually.

Figure 3.5

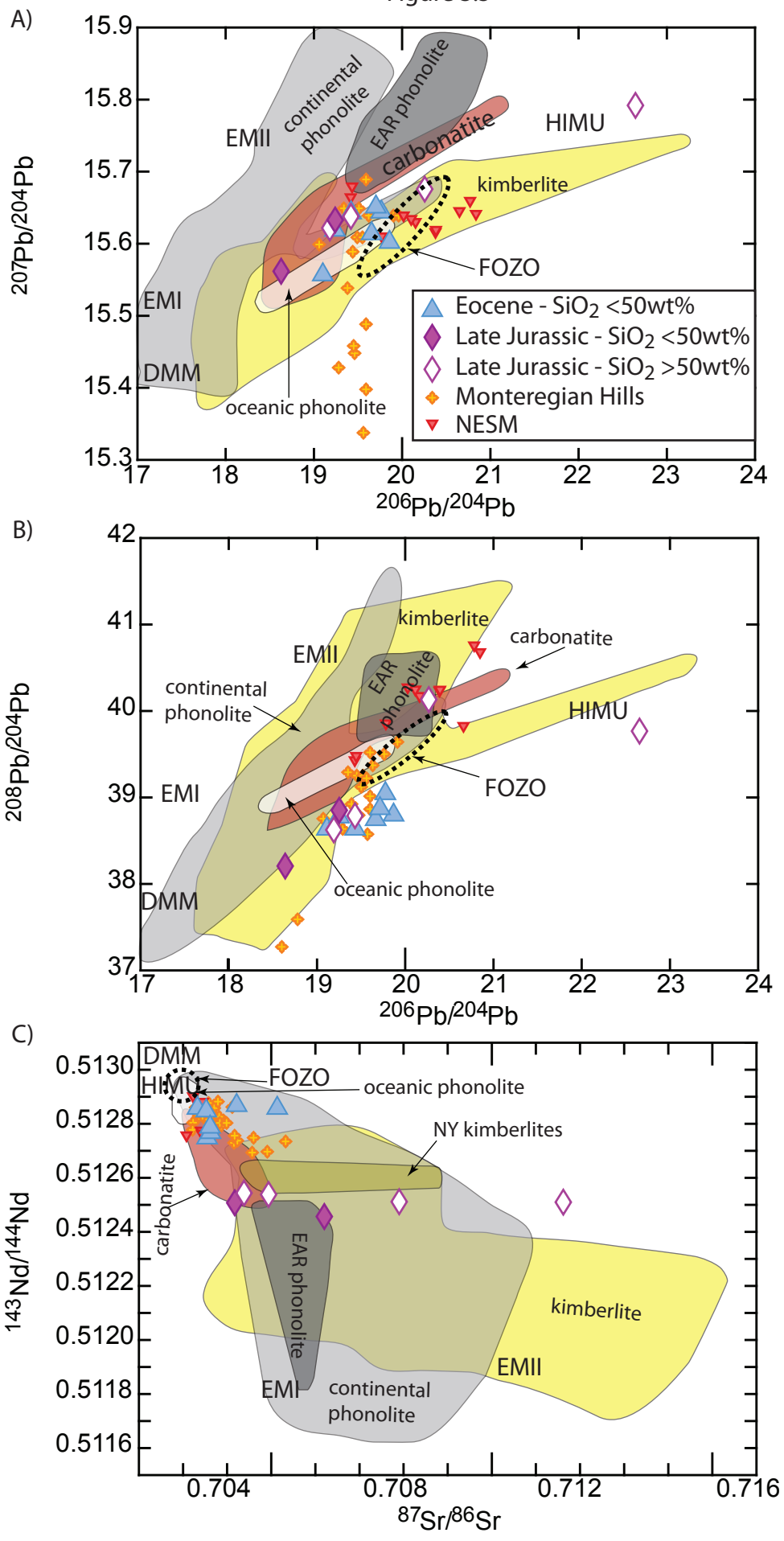
A)
15.9
15.8
15.7
15.6
15.5
15.4
15.3
17
18
19
20
21
22
23
24
$^{207}Pb/^{204}Pb$
$^{206}Pb/^{204}Pb$
EMII
continental phonolite
EAR phonolite
carbonatite
HIMU
kimberlite
FOZO
EMI
DMM
oceanic phonolite
Eocene - SiO_2 <50wt%
Late Jurassic - SiO_2 <50wt%
Late Jurassic - SiO_2 >50wt%
Monteregian Hills
NESM
B)
42
41
40
39
38
37
17
18
19
20
21
22
23
24
$^{208}Pb/^{204}Pb$
$^{206}Pb/^{204}Pb$
kimberlite
carbonatite
EMII
continental phonolite
EAR phonolite
HIMU
FOZO
EMI
oceanic phonolite
DMM
C)
0.5130
0.5128
0.5126
0.5124
0.5122
0.5120
0.5118
0.5116
0.704
0.708
0.712
0.716
$^{143}Nd/^{144}Nd$
$^{87}Sr/^{86}Sr$
DMM
HIMU
FOZO
oceanic phonolite
NY kimberlites
carbonatite
EAR phonolite
kimberlite
EMII
EMI
continental phonolite

Figure 3.5: (Previous Page) Radiogenic isotopic data for the Virginia – West Virginia post-rift magmas. ENAM volcanics are compared with East African Rift (EAR) phonolites, continental phonolites, oceanic phonolites, carbonatites, and kimberlites (data obtain from the GEOROC database; georoc.mpch-mainz.gqdq.de/georoc/). Virginia samples were age corrected to 150 Ma (late Jurassic) and 50 Ma (Eocene). DMM – depleted MORB mantle, EMI – enriched mantle I, EMII – enriched mantle II, HIMU – high μ, FOZO – Focus Zone [*Zindler and Hart,* 1986; *Stracke et al.,* 2005].

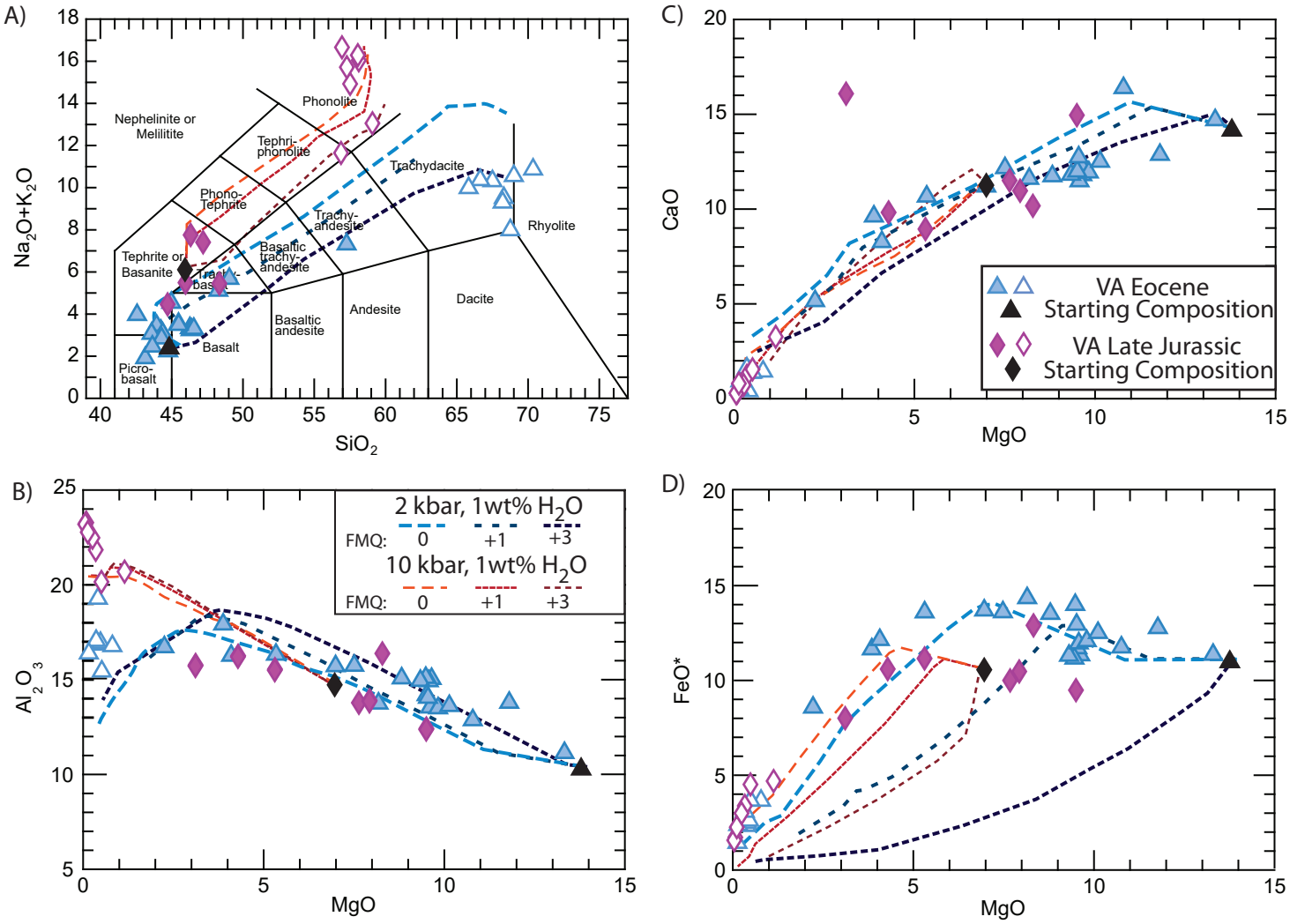

Figure 3.6: Fractional crystallization models. Made with rhyoliteMELTS [*Gualda et al.*, 2012], showing various fractional crystallization paths of the melt for both the Virginia Eocene and Late Jurassic magmas. The starting compositions are indicated by black diamond/triangle, with varying oxygen fugacity buffer conditions (fO_2 FMQ) indicated by variation of line texture.

Figure 3.7

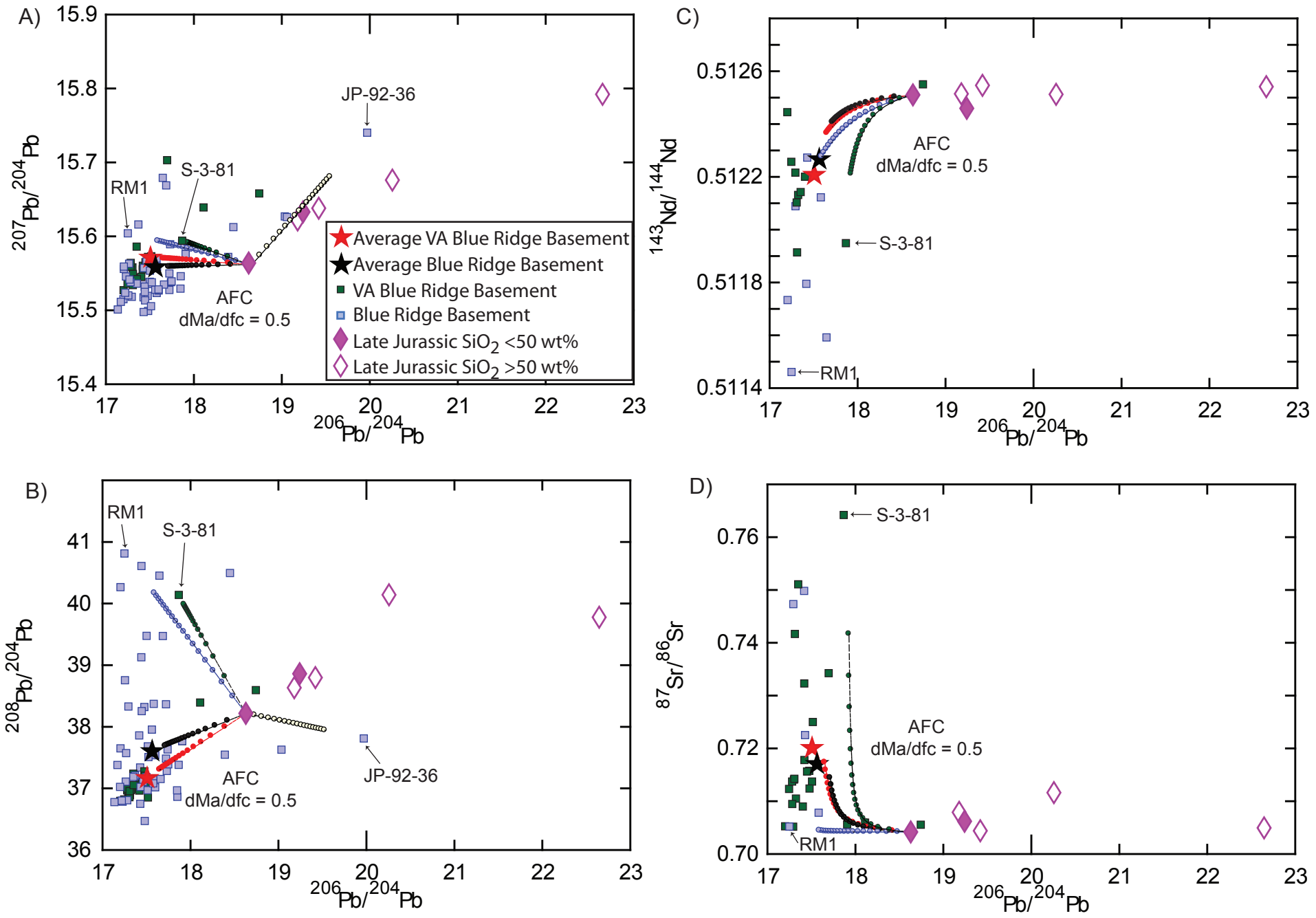
A)
B)
C)
D)
JP-92-36
S-3-81
RM1
AFC
dMa/dfc = 0.5
Average VA Blue Ridge Basement
Average Blue Ridge Basement
VA Blue Ridge Basement
Blue Ridge Basement
Late Jurassic SiO2 <50 wt%
Late Jurassic SiO2 >50 wt%
207Pb/204Pb
206Pb/204Pb
208Pb/204Pb
143Nd/144Nd
87Sr/86Sr

Figure 3.7:(Previous Page) Assessment of crustal interaction. Blue Ridge basement from Pettingill et al. [1984], Samson et al. [1995], Sinha et al. [1996], Carrigan et al. [2003]. Basement end-members are RM1 [*Carrigan et al.,* 2003], S-3-81 [*Pettingill et al.,* 1984], and JP-92-36 (Pb only) [*Sinha et al.,* 1996]. All samples are age corrected to average eruptive age of Virginia Late Jurassic magmatism (150 Ma). Every circle-tick mark represents dF=0.05 with a maximum dF=1. F = mass of assimilated material over initial mass. The rate of assimilation to crystallizaiton (R=dMa/dfc) is 0.5.

Figure 3.8

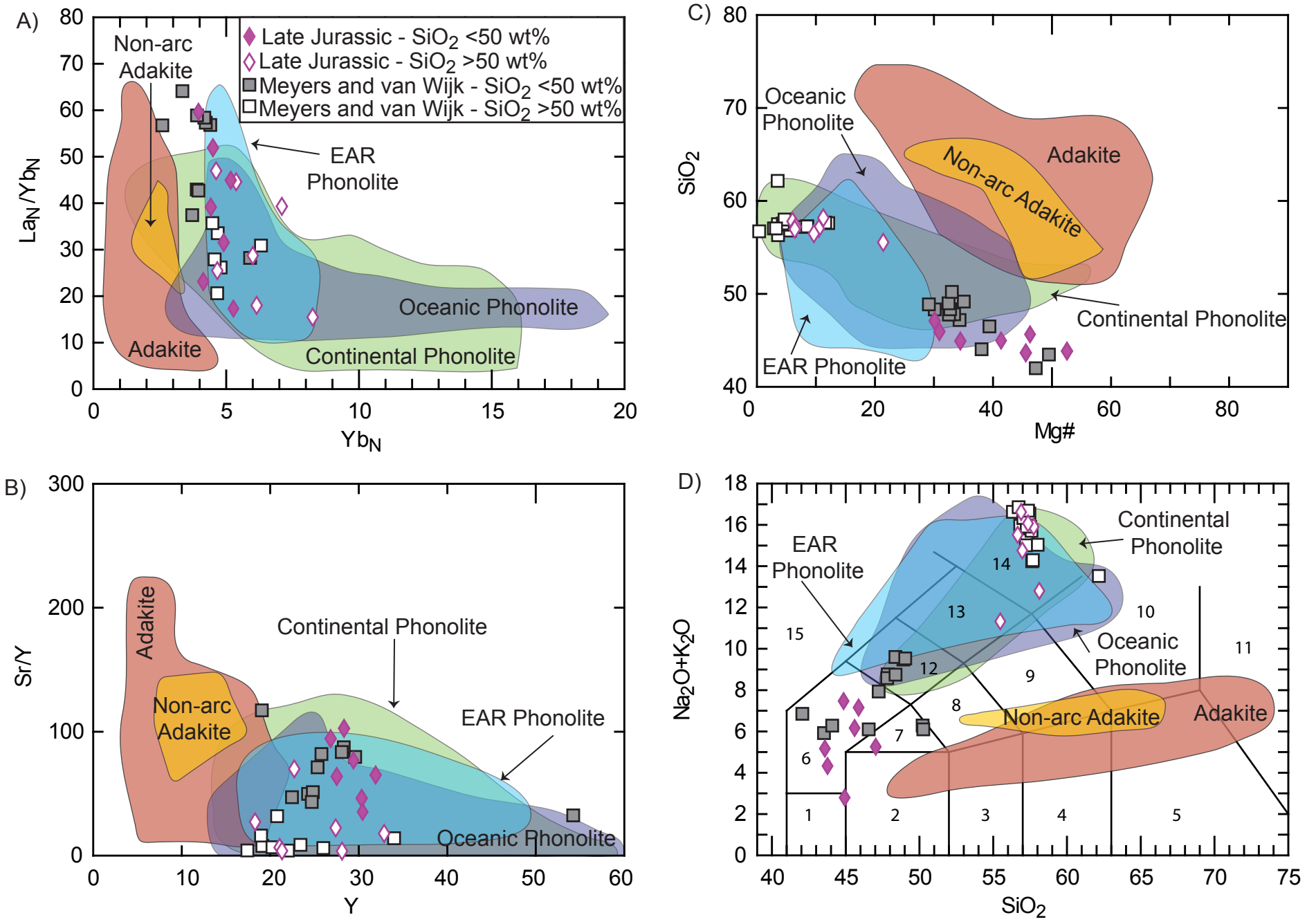
A)
Late Jurassic - SiO2 <50 wt%
Late Jurassic - SiO2 >50 wt%
Meyers and van Wijk - SiO2 <50 wt%
Meyers and van Wijk - SiO2 >50 wt%
Non-arc Adakite
EAR Phonolite
Oceanic Phonolite
Continental Phonolite
Adakite
LaN/YbN
YbN
B)
Adakite
Continental Phonolite
Non-arc Adakite
EAR Phonolite
Oceanic Phonolite
Sr/Y
Y
C)
Oceanic Phonolite
Adakite
Non-arc Adakite
Continental Phonolite
EAR Phonolite
SiO2
Mg#
D)
EAR Phonolite
Continental Phonolite
Oceanic Phonolite
Non-arc Adakite
Adakite
Na2O+K2O
SiO2

Figure 3.8: (Previous Page) Adakite discriminatory plots. Shown with global adakites, non-arc adakites, continental phonolites, East African Rift (EAR) phonolites, and oceanic phonolites from GEOROC database. A)Chondrite normalized La/Yb *vs.* Yb [*Martin*, 1999]. B) Sr/Y *vs.* Y [*Defant and Drummond*, 1990]. C) SiO_2 *vs.* Mg# where Mg# = molar MgO/(MgO+FeO)*100. D) Total alkalis ($Na_2O + K_2O$) *vs.* SiO_2 verse with rock types as 1: Picrobasalt, 2: Basalt, 3: Basaltic Andesite, 4: Andesite, 5: Dacite, 6: Basanite, 7: Trachybasalt, 8: Basaltic Trachyandesite, 9: Trachyandesite, 10: Trachydacite, 11: Rhyolite, 12: Phonotephrite, 13: Tephriphonolite, 14: Phonolite, 15: Melilitite.

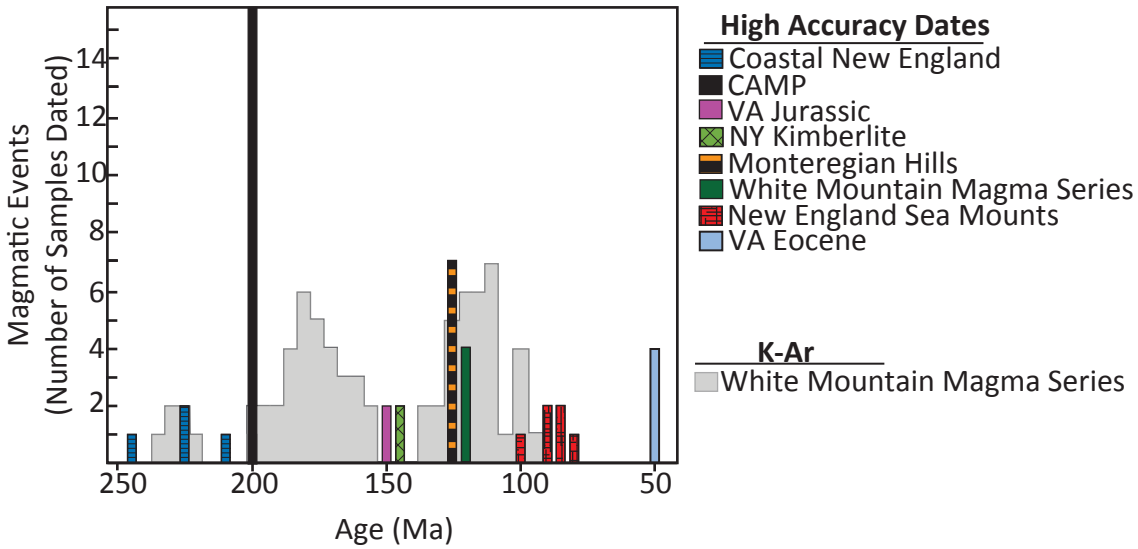

Figure 3.9: Histogram showing magmatic events that have occurred on the ENAM. Ages come from Pe-Piper and Reynolds [2000] and Ross [2010] (Coastal New England), Blackburn et al. [2013] (CAMP), Foland and Fowl [1977] and Hubacher and Foland [1991] (White Mountain Magma Series for K-Ar and Ar-Ar, respectively), Heaman and Kjarsgaard [2000] (NY Kimberlites), Foland et al. [1986] (Monteregian Hills), and Duncan [1984] (New England Seamounts).

Figure 3.10

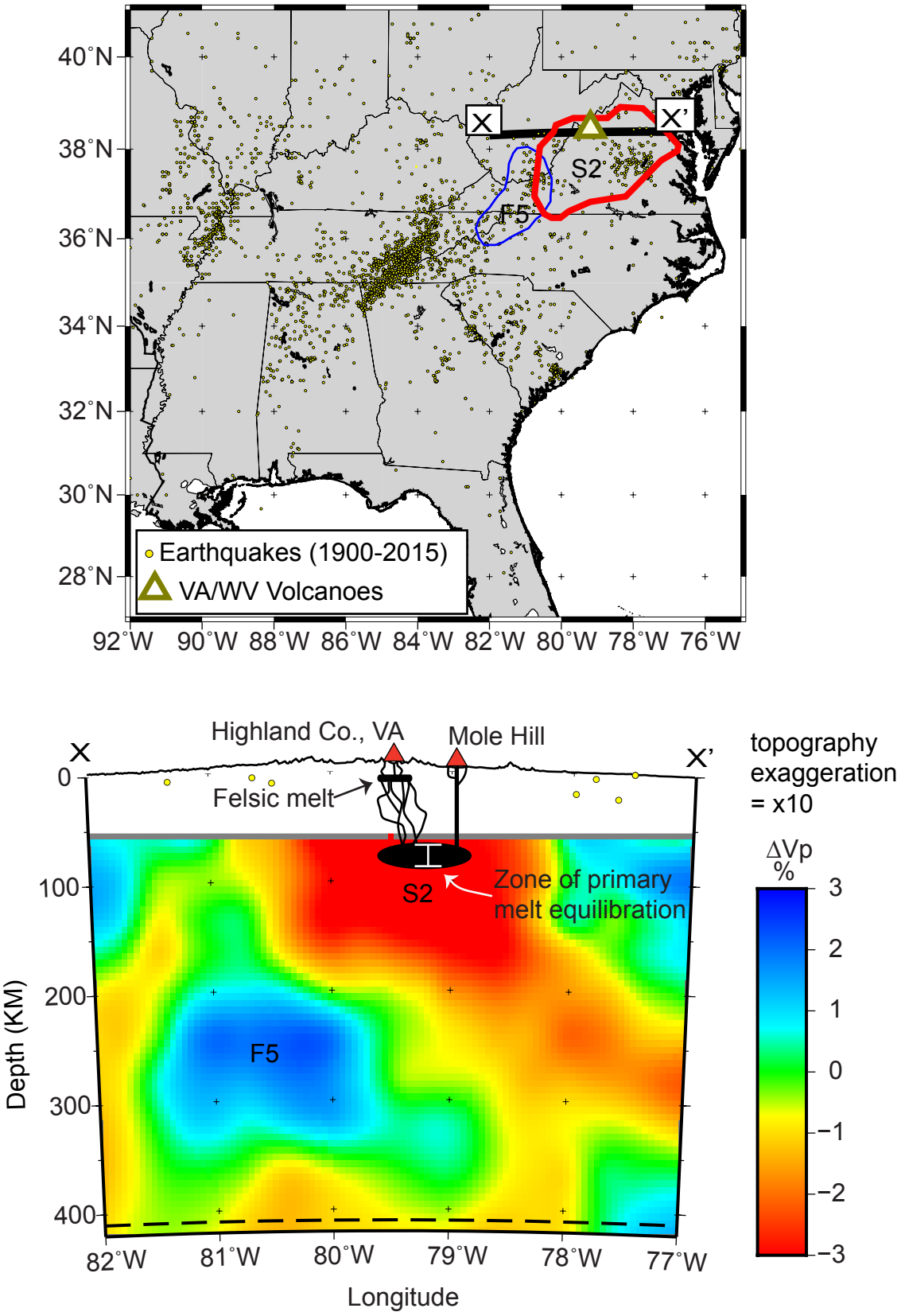
40˚N
38˚N
36˚N
34˚N
32˚N
30˚N
28˚N
92˚W
90˚W
88˚W
86˚W
84˚W
82˚W
80˚W
78˚W
76˚W
X
X'
S2
F5
Earthquakes (1900-2015)
VA/WV Volcanoes
Highland Co., VA
Mole Hill
Felsic melt
S2
Zone of primary
melt equilibration
F5
Depth (KM)
0
100
200
300
400
82˚W
81˚W
80˚W
79˚W
78˚W
77˚W
Longitude
topography
exaggeration
= x10
ΔVp
%
3
2
1
0
−1
−2
−3

Figure 3.10: (Previous Page) Seismic tomography for Virginia – West Virginia. Depths of equilibration and fractional crystallization for Eocene processes, shown in black, coupled with new tomographic results from Biryol et al. [2016] from the EarthScope Transportable Array experiment and the Southeastern Suture of the Appalachian Margin experiment across the ENAM. Top panel shows extent of seismic stations used for tomographic results, with X-X' representing the line of section shown in the bottom panel. F5 is a proposed recent piece of delaminated lithosphere, and S2 is the slow velocity anomaly possibly associated with upwelling and the Eocene melting event. Red S2 and Blue F5 shown on the top panel correspond to the regions in the cross section. For full methodology regarding this tomography, see Biryol et al. [2016]. Calculated mafic melt equilibrium zones [Mazza et al., 2014] and felsic melt fractional crystallization zone from rhyoliteMELTS.

Chapter 3

Table 1

Sample Name	Fig. 1 Location	Latitude (N)	Longitude (W)	Age (Ma)	SiO2 (wt%)	TiO2 (wt%)	Al2O3 (wt%)	Fe2O3 (wt%)
Eocene								
MH Summit*	1	38°26'53.3"	-078°57'09.9"		45.69	1.59	15.04	11.43
MH Xeno 4 *	2	38°26'56.1"	-078°57'04.7"	48.78 ± 0.89 [a]	45.69	1.58	14.92	11.81
MH 1.03*	3	38°26'56.7"	-078°57'07.4"		45.55	1.57	15.1	11.26
MH 1.13*	4	38°26'58.1"	-078°57'02.6"		45.8	1.59	14.94	11.41
TK5*	5	38°24'17.3"	-079°35'16.6"		44.57	2.17	13.53	12.07
TK COLUMN 3*	6	38°24'17.3"	-079°35'17.1"	48.6 ± 1 [a]	44.48	2.18	13.49	12.19
13LJMonterey	7	38°24'38.1"	-079°34'51.3"		67.2	0.29	19.27	2.34
12DJ631A	8	38°25'23.1"	-079°32'30.4"		44.46	1.91	11.13	11.46
12DJ631B*	9	38°25'23.1"	-079°32'30.4"		43.55	1.82	10.27	11.07
12DJ631C*	10	38°25'21.9"	-079°32'30.3"		66.64	0.42	16.85	2.5
14GBKahleB	11	38°25'32.6"	-079°31'40.8"		43.41	2.67	15.07	13.64
14GBKahleC	12	38°25'33.1"	-079°31'39.8"		67.03	0.21	16.23	2.39
14GBKahleE	13	38°25'27.6"	-079°31'35.0"		66.25	0.37	16.94	2.62
14GBKahleF	14	38°25'31.2"	-079°31'30.0"		42.58	2.28	12.86	11.85
5 Hull Farm*	15	38?25'35.8"	-079?28' 04.5"		43.47	2.51	13.61	12.62
VAFC03-6*	16	38?24' 50.9"	-079?31'58.6"		42.57	2.98	15.71	13.82
14SMRt624	17	38°26'31.8"	-079°31'00.2"		43.96	2.71	15.73	13.73
14SMRt624B	18	38°26'30.0"	-079°30'51.5"		43	2.74	14.18	14.12
040HightownDike*	19	38°25'45.5"	-079°37' 00.3"		41.09	3.36	13.74	14.48
13JSTrible2	20	38°26'43.6"	-079°37'16.5"		65.1	0.33	17.05	3.1
13BCTrible4	21	38°26'49.0"	-079°37'19.5"		43.6	2.49	14.05	13.06
12DJHighTownQuarry1	22	38°27'19.3"	-079°36' 25.3"		64.18	0.71	16.77	3.68
12DJHighTownQuarry2*	22	38°27'19.3"	-079°36' 25.3"	48.79 ± 0.07 [a]	64.67	0.22	15.43	3.69
13LJAnderson	23	38°27'51.6"	-079°35'51.5"		56.12	1.67	16.71	8.65
14BSTreeDike	24	38°28'18.7"	-079°35'28.1"		69.71	0.17	16.38	1.44
14SMRt637	25	38°28'51.4"	-079°34'33.3"		47.74	2.47	17.91	11.75
12MBBFTrib1	26	38°27'04.4"	-079°19'04.0"		43.63	2.52	13.78	12.88
13NRBillsMill	27	38°27'53.8"	-079°18'14.3"		44.84	3.33	16.32	13.72
12MB Wilfong 1*	28	38°28'27.1"	-079°19'56.7"		47.13	2.17	16.26	12.25

Chapter 3

Table 1

Sample Name	Fig. 1 Location	Latitude (N)	Longitude (W)	Age (Ma)	SiO2 (wt%)	TiO2 (wt%)	Al2O3 (wt%)	Fe2O3 (wt%)
Late Jurassic								
12MBSugarGrove1	29	38°28'54.0"	-079°19'06.0"		45.66	1.66	13.8	9.93
2-SUGAR GROVE	30	38°26'53.0"	-079°21'22.7"		44.99	2.28	16.39	13.16
14SMBrandywine	31	38°38'22.6"	-079°13'52.0"		43.83	2.46	12.43	9.54
VQ**	32	38°13'13.0"	-079°06'07.1"		43.65	1.93	13.92	10.54
13LJRt11A	33	38°10'30.6"	-079°02'10.3”		57.03	0.35	21.91	3.41
14GBVerona	34	38°12'24.3"	-079°00'13.5”		57.8	0.17	23.35	1.73
14GBRt773	35	38°15'38.9"	-078°56'05.4”	149.7 ± 0.4 [b]	58.18	0.46	20.22	4.55
13LJSpringHillA	36	38°15'12.5"	-079°03'05.9”		56.72	0.14	22.55	3.01
14LJSpringHillB	37	38°14'42.5"	-079°03'06.7”		57.42	0.15	23.26	1.58
14SMRt607	38	38°18'31.8"	-079°05'09.7”		45.93	1.44	16.27	10.67
14GBShelby	39	38°13'36.9"	-079°03'25.9”	152.5 ± 0.5 [b]	55.54	0.46	20.76	4.73
14SMRt613	40	38°21'44.5"	-079°02'34.5”		44.92	2.09	15.56	11.23
14GBRt699	41	38°20'00.2"	-079°00'20.9”		56.95	0.32	22.84	2.27
14GBArey	42	38°19'39.9"	-079°00'39.1”		47.1	1.51	15.78	8.05
USGS Standard								
BHVO-2 (n=10)					49.52	2.69	13.51	12.07
accuracy					0.8	1.5	0.1	1.9
Relative Standard Deviation					0.3	0.3	0.2	0.1

* in Mazza et al., 2014

** previously labeled as Eocene

[a] samples measured at the New Mexico Geochronology Research Laboratory

[b] samples measured at the USGS

Chapter 3
Table 1

Sample Name	MnO (wt%)	MgO (wt%)	CaO (wt%)	Na2O (wt%)	K2O (wt%)	P2O5 (wt%)	Total	LOI (wt%)	Sc (ppm)
Eocene									
MH Summit*	0.21	9.65	11.79	2.51	0.78	0.35	99.04	-	38.67
MH Xeno 4 *	0.21	9.57	11.47	2.42	0.79	0.35	98.81	-	31.2
MH 1.03*	0.2	9.49	11.92	2.42	0.76	0.33	98.6	-	41.58
MH 1.13*	0.2	9.34	11.81	2.44	0.81	0.35	98.69	-	30.35
TK5*	0.19	9.61	12.32	2.33	1.14	0.38	98.32	-	27.09
TK COLUMN 3*	0.2	9.83	11.93	2.37	1.04	0.38	98.09	-	28.02
13LJMonterey	0.017	0.41	0.4	3.61	4.19	0.053	97.78	5.41	32.69
12DJ631A	0.169	13.33	14.69	1.55	0.67	0.234	99.6	2.36	35.55
12DJ631B*	0.18	13.79	14.15	1.5	0.81	0.3	97.43	-	31.96
12DJ631C*	0.042	0.43	1.43	5.29	3.99	0.042	97.63	-	29.24
14GBKahleB	0.197	8.82	11.73	2.2	1.09	0.338	99.17	1.5	30.36
14GBKahleC	0.034	0.18	0.92	6.25	4	-0.044	97.2	1.12	30.14
14GBKahleE	0.037	0.48	1.36	5.8	4.32	0.031	98.21	1.5	28.32
14GBKahleF	0.176	10.79	16.38	1.13	0.75	0.189	98.99	3.05	30.79
5 Hull Farm*	0.19	10.14	12.5	2.66	0.49	0.37	98.55	-	31.71
VAFC03-6*	0.2	6.99	11.19	2.64	0.7	0.41	97.21	-	25.47
14SMRt624	0.189	7.51	12.16	2.59	0.46	0.355	99.39	2.04	29.74
14SMRt624B	0.182	9.51	11.98	2.34	0.68	0.229	98.96	1.88	28.88
040HightownDike*	0.2	8.18	11.6	2.37	1.45	0.38	96.85	-	31.07
13JSTrible2	0.047	0.36	1.6	6.29	3.83	0.045	97.75	0.72	28.63
13BCTrible4	0.183	9.55	12.73	1.84	0.96	0.284	98.75	2.56	29.6
12DJHighTownQuarry1	0.034	0.81	1.43	5.42	4.31	0.222	97.57	1.86	28.23
12DJHighTownQuarry2*	0.22	0.52	1.38	5.25	3.56	0.12	95.06	-	1
13LJAnderson	0.149	2.25	5.15	4.55	2.61	0.366	98.23	5.47	25.69
14BSTreeDike	0.025	0.16	0.47	6.45	4.31	0.004	99.12	1.09	31.34
14SMRt637	0.229	3.88	9.61	3.55	1.5	0.597	99.24	1.27	21.69
12MBBFTrib1	0.172	11.8	12.86	1.56	0.9	0.154	100.26	2.38	35.92
13NRBillsMill	0.219	5.34	10.66	2.74	1.78	1.096	100.05	3.98	23.09
12MB Wilfong 1*	0.2	4.1	8.26	3.83	1.62	0.59	96.41	-	26.21

Chapter 3

Table 1

Sample Name	MnO (wt%)	MgO (wt%)	CaO (wt%)	Na2O (wt%)	K2O (wt%)	P2O5 (wt%)	Total	LOI (wt%)	Sc (ppm)
Late Jurassic									
12MBSugarGrove1	0.187	7.67	11.46	3.03	3.18	1.254	97.83	3.61	-
2-SUGAR GROVE	0.218	8.32	10.12	1.85	0.99	0.543	98.86	7.27	-
14SMBrandywine	0.137	9.51	14.95	2.29	2.08	1.009	98.24	3.54	32.77
VQ**	0.19	7.94	10.96	2.4	2.81	0.9	95.25	-	24.78
13LJRt11A	0.237	0.36	1.2	9.42	5.38	0.123	99.42	4.62	24.53
14GBVerona	0.166	0.1	0.33	10.56	5.39	0.015	99.61	5.4	25.24
14GBRt773	0.209	0.52	1.55	6.85	6	0.182	98.72	3.27	25.46
13LJSpringHillA	0.22	0.27	0.72	9.83	5.73	0.062	99.25	5.54	25.85
14LJSpringHillB	0.1825	0.07	0.28	10.94	5.17	0.044	99.1	5.12	25.36
14SMRt607	0.205	4.3	9.82	2.87	4.33	1.752	97.59	5.31	24.36
14GBShelby	0.189	1.16	3.26	4.33	7.04	0.401	97.87	3.25	25.05
14SMRt613	0.182	5.32	8.94	3.42	4.09	1.477	97.23	3.92	25.19
14GBRt699	0.151	0.14	0.8	10.65	6.01	0.037	100.17	3.14	24.6
14GBArey	0.179	3.12	16.08	3.23	2.07	0.547	97.67	5.67	23.91
USGS Standard									
BHVO-2 (n=10)	0.164	7.31	11.25	2.05	0.51	0.256	99.33		29.53
accuracy	1.5	1.1	1.3	7.7	1.9	5.2			8
Relative Standard Deviation	0.6	0.4	0.2	1.8	0.9	2.9			13

* in Mazza et al., 2014

** previously labeled as Eocene

[a] samples measured at the New Mexico Geochronology Research Laboratory

[b] samples measured at the USGS

Chapter 3

Table 1

Sample Name	V (ppm)	Cr (ppm)	Co (ppm)	Ni (ppm)	Cu (ppm)	Zn (ppm)	Ga (ppm)	Rb (ppm)	Sr(ppm)	Y (ppm)
Eocene										
MH Summit*	264.4	336.15	54.51	171.88	82.22	89.04	-	14.85	452.35	30.13
MH Xeno 4 *	234.06	292.71	49.41	174.85	83.75	81.64	-	16.5	465.11	34.09
MH 1.03*	292.89	417.85	60.33	201.32	93.32	93.19	-	18.25	459.07	28.72
MH 1.13*	237.24	353.7	49.16	158.59	59.8	79.42	-	13.59	496.52	32.92
TK5*	325.1	385.33	49.71	132.73	88.18	91.48	-	24.2	680.37	24.96
TK COLUMN 3*	314.17	387.21	49.96	134	98.51	108.37	-	18.93	610.37	25.62
13LJMonterey	0.48	1.81	0.62	11.75	4.74	110.52	46.02	105.18	53.29	35.1
12DJ631A	330.8	937.69	66.24	219.7	79.63	87.12	24.79	20.65	849.48	19.22
12DJ631B*	301.32	886.41	61.21	203.64	71.85	75.84	-	22.83	636.13	19.76
12DJ631C*	4.25	3.58	0.57	4.37	3.58	73.98	52.25	100.18	317.9	38.41
14GBKahleB	361.87	223.71	56.16	93.36	63.55	109.18	26.98	30.6	853.56	24.57
14GBKahleC	1.57	0.69	0.28	1.93	2	72.56	40.07	92.56	265.94	30.75
14GBKahleE	1.21	0.55	0.21	3.06	1.88	75.27	41.67	89.39	281.59	28.43
14GBKahleF	350.76	493.19	53.58	123.27	72.25	100	25.77	9.84	3245.16	22.52
5 Hull Farm*	334.12	431.54	55.78	118.31	73.74	89.16	-	7.1	464.62	26.38
VAFC03-6*	379.27	14.91	41.42	28.13	31.66	85.53	-	10.45	588.31	33.61
14SMRt624	381.76	153.66	53	64.88	63.29	106.8	28.14	22.68	714.74	25.84
14SMRt624B	377.24	257.7	56.43	79.65	54.34	85.1	22.83	35.33	918.71	24.05
040HightownDike*	367.03	23.29	44.55	30.9	33.3	73.92	-	31	601.15	28.93
13JSTrible2	1.35	0.61	0.99	4.53	1.21	80.22	48.69	80.42	458	24.62
13BCTrible4	357.61	346.26	55.65	91.39	53.65	111.86	24.66	13.74	942.67	23.76
12DJHighTownQuarry1	6.02	0.61	1.37	2.26	1.62	105.52	72.03	89.57	322.43	36.88
12DJHighTownQuarry2*	6	10.3	1.2	1.2	28.8	80	-	67.5	337	24
13LJAnderson	136.31	2.59	14.41	12.64	11.25	107.55	39.89	60.34	616.69	43.83
14BSTreeDike	1.22	0.57	0.26	2.1	2.4	87.85	55.67	105.09	102.26	44.77
14SMRt637	120.36	1.48	19.35	8.19	4.08	95.68	27.31	31.29	1030.11	34.77
12MBBFTrib1	385.95	435.37	65.51	131.06	76.98	90.3	29.62	19.29	480.72	21.37
13NRBillsMill	180.97	3.06	25.89	18	11.53	93.57	27.05	36.02	1203.07	33.82
12MB Wilfong 1*	138.71	20.31	24.61	49.18	28.28	112.22	-	30.96	903.46	31.12

Chapter 3

Table 1

Sample Name	V (ppm)	Cr (ppm)	Co (ppm)	Ni (ppm)	Cu (ppm)	Zn (ppm)	Ga (ppm)	Rb (ppm)	Sr(ppm)	Y (ppm)
Late Jurassic										
12MBSugarGrove1	202.62	248	33.32	69.72	48.79	104.18	48.97	72.32	2236.61	29.39
2-SUGAR GROVE	274.54	65.77	45.02	65.53	58.75	99.1	28.04	16.61	1055.88	30.42
14SMBrandywine	252.25	576.88	41.78	129.87	35.16	77.98	82.31	69.4	1755.5	27.51
VQ**	171.08	385.84	36.36	111.64	44.3	81.88	-	81.51	1404.04	30.34
13LJRt11A	4.39	1.79	1.14	2.82	1.18	142.34	35.13	177.75	581.86	32.11
14GBVerona	2.25	0.47	0.07	2.92	3.12	81.82	22.5	249.6	137.95	20.51
14GBRt773	9.8	0.85	2.25	5.26	1.81	122.17	35.8	152	618.61	27.36
13LJSpringHillA	2.95	0.53	0.31	2.57	1.83	151.78	24.26	223.47	79.9	20.72
14LJSpringHillB	1.64	3	0.01	3.17	1.58	100.59	24.64	297.5	99.05	27.38
14SMRt607	128.38	4.39	24.31	18.19	21.95	111.15	80.89	94.18	2053.27	31.1
14GBShelby	19.24	0.91	3.96	3.07	2.93	105.99	56.75	154.43	1572.38	22.13
14SMRt613	193.23	37.19	31.62	37.15	34.71	103.72	67.17	84.21	2500.33	26.19
14GBRt699	10.21	0.31	0.51	1.82	2.63	104.75	29.19	178.04	504.9	18.31
14GBArey	78.9	4.02	14.88	15.45	14.53	89.06	42.64	36.84	2877.22	27.68
USGS Standard										
BHVO-2 (n=10)	320.42	270.53	43.23	119.95	135.76	107.26	21.08	9.79	407.07	25.39
accuracy	2	6	2	1	1	0	5	14	3	12
Relative Standard Deviation	1	3	2	2	4	7	1	1	0	1

* in Mazza et al., 2014

** previously labeled as Eocene

[a] samples measured at the New Mexico Geochronology Research Laboratory

[b] samples measured at the USGS

Chapter 3

Table 1

Sample Name	Zr (ppm)	Nb (ppm)	Mo (ppm)	Sn (ppm)	Cs (ppm)	Ba (ppm)	La (ppm)	Ce (ppm)	Pr (ppm)	Nd (ppm)
Eocene										
MH Summit*	108.15	35.56	0.01	1.57	0.24	462.93	29.52	58.51	6.24	23.69
MH Xeno 4 *	122.71	35.94	0.01	1.41	0.19	448.72	31.19	56.34	6.45	25.85
MH 1.03*	98.31	32.72	0.01	1.15	0.2	547.53	27.72	57.19	6.05	22.57
MH 1.13*	118.3	35.2	0.01	1.12	0.14	456.05	30.69	56.26	6.45	24.9
TK5*	178.33	37.78	0.01	1.42	0.72	370.94	27.3	58.26	7.6	32.11
TK COLUMN 3*	179.39	37.29	0.01	1.5	0.68	389.36	27.17	56.38	7.48	31.76
13LJMonterey	510.77	123.46	0.51	4.4	0.21	884.92	132.37	209.56	25.01	79.85
12DJ631A	137.03	46.93	0.5	1.42	1.99	373.98	27.41	59.19	7.27	29.38
12DJ631B*	141.81	45.29	0.01	1.25	4.29	352.1	26.63	54.46	7.03	28.01
12DJ631C*	538.95	128.31	0.5	3.49	0.15	1132.68	98.11	108.17	18.34	62.78
14GBKahleB	178.66	34.8	0.51	2.29	4.07	360.33	24.29	55.11	7.05	30.5
14GBKahleC	391.81	122.03	2.79	3.54	0.21	1156.32	90.54	153.77	13.36	56.24
14GBKahleE	516.55	103	1.74	3.12	0.11	1230.39	90.37	154.61	13.05	54.97
14GBKahleF	165.87	31.89	0.5	1.7	0.39	381.22	24.32	55.46	7.17	31.15
5 Hull Farm*	201.57	33.66	0.01	1.63	1.53	284.76	25.04	51.33	7.07	31.36
VAFC03-6*	236.72	41.02	0.01	1.45	1.19	373.43	29.87	59.7	8.13	36.11
14SMRt624	189.92	40.83	0.51	1.88	1.72	387.66	28.73	61.75	7.79	33.29
14SMRt624B	157.12	31.52	0.5	1.52	0.54	302.38	22.58	48.38	6.31	27.83
040HightownDike*	183.89	38.09	0.01	1.9	0.28	450.87	26.15	53.94	7.58	34.06
13JSTrible2	553.97	64.92	4.76	2.39	0.19	1587.47	62.74	118.53	10.68	44.46
13BCTrible4	171.29	33.45	0.5	1.72	0.17	352.34	24.28	53.7	6.83	29.66
12DJHighTownQuarry1	821.82	76.45	0.51	2.48	0.16	1782.97	58.04	104.75	13.89	51.73
12DJHighTownQuarry2*	380	58	-	-	1.25	1087	63.8	125	13.1	46.1
13LJAnderson	345.02	72.96	0.51	2.51	0.47	809.82	61.34	120.37	15.33	59.93
14BSTreeDike	508.63	132.5	0.5	3.65	0.14	1224.59	113.44	175.94	21.73	73.02
14SMRt637	218.19	44.88	0.51	1.77	0.27	471.33	34.02	73.44	9.41	40.89
12MBBFTrib1	142.68	27.08	0.5	3.68	2.07	442.15	19.56	44.6	5.83	25.62
13NRBillsMill	205.89	54.41	0.51	2.37	0.26	499.13	40.25	81.53	9.88	42.04
12MB Wilfong 1*	252.27	50.28	0.02	4.18	0.27	602.38	39.15	77.87	10.21	42.46

Chapter 3

Table 1

Sample Name	Zr (ppm)	Nb (ppm)	Mo (ppm)	Sn (ppm)	Cs (ppm)	Ba (ppm)	La (ppm)	Ce (ppm)	Pr (ppm)	Nd (ppm)
Late Jurassic										
12MBSugarGrove1	210.38	127.29	2.9	1.27	28.22	3500.99	161.71	255.98	29.4	106.14
2-SUGAR GROVE	178.32	64.51	1.63	1.68	1.47	1740.91	63.02	97.29	10.7	43.41
14SMBrandywine	168.98	107.39	0.51	1.11	19.8	2308.43	65.76	129.7	15.21	59.98
VQ**	297.06	139.18	0.03	1.41	16.75	1819.95	106.35	180.59	20.21	73
13LJRt11A	623.82	415.4	10.67	1.31	4.72	749.07	191.77	314.77	20.13	74.32
14GBVerona	822.01	545.99	12.85	1.44	1.34	46.42	118.36	189.65	12.43	40.49
14GBRt773	456.5	257.35	8.5	0.95	3.85	880.57	168.44	262.44	17.25	63.25
13LJSpringHillA	967.98	458.97	14.41	1.9	8.58	181.72	75.49	136	10.28	34.39
14LJSpringHillB	1190.87	709.92	4.13	2.03	3.61	55.93	87.61	156.67	11.18	38.12
14SMRt607	202.65	163.71	3.21	0.78	1.45	3050.01	159.49	279.43	22.17	101.45
14GBShelby	444.38	239.4	6.78	0.56	2.6	1899.74	149.12	225.57	16.08	62.73
14SMRt613	179.81	155.97	5.97	0.97	1.66	2562.74	160.64	263.75	20.29	90.06
14GBRt699	541.16	371.44	4.83	0.75	2.49	445.1	83.74	141.03	10.67	37.83
14GBArey	220.34	127.67	0.6	1.37	24.67	1309.97	119.22	195.56	15.96	68.86
USGS Standard										
BHVO-2 (n=10)	148.85	17.07	4.33	1.94		132.81	15.76	37.05	5.46	24.23
accuracy	13	6	324	8		1	3	1	3	1
Relative Standard Deviation	0	1	8	7		0	1	1	1	1

* in Mazza et al., 2014

** previously labeled as Eocene

[a] samples measured at the New Mexico Geochronology Research Laboratory

[b] samples measured at the USGS

Chapter 3

Table 1

Sample Name	Sm (ppm)	Eu (ppm)	Gd (ppm)	Tb (ppm)	Dy (ppm)	Ho (ppm)	Er (ppm)	Tm (ppm)	Yb (ppm)	Lu (ppm)
Eocene										
MH Summit*	4.92	1.72	5.44	0.81	5.52	1.06	3.14	0.43	3.24	0.52
MH Xeno 4 *	5.31	1.81	5.81	0.9	5.76	1.2	3.53	0.54	3.59	0.6
MH 1.03*	4.79	1.75	5.21	0.81	4.99	1.05	3	0.43	3.17	0.49
MH 1.13*	5.4	1.78	5.44	0.92	5.63	1.19	3.45	0.49	3.68	0.58
TK5*	7.1	2.11	6.54	0.95	5.26	0.95	2.42	0.31	2.01	0.29
TK COLUMN 3*	6.78	2.05	6.54	0.95	5.11	0.94	2.6	0.31	2.21	0.29
13LJMonterey	12.71	2.78	9.64	1.29	6.65	1.18	3.4	0.54	3.78	0.59
12DJ631A	6.19	1.87	5.3	0.74	3.81	0.65	1.7	0.22	1.45	0.21
12DJ631B*	5.63	1.77	5.76	0.8	4.14	0.81	1.89	0.23	1.42	0.25
12DJ631C*	9.58	2.82	8.02	1.16	6.5	1.2	3.49	0.57	3.67	0.6
14GBKahleB	6.83	2.13	6.15	0.86	4.8	0.84	2.19	0.29	1.84	0.26
14GBKahleC	9.27	2.3	7.01	1.08	5.73	1.14	3.18	0.54	3.26	0.5
14GBKahleE	8.58	2.42	7.06	0.98	5.41	1.03	3.05	0.48	3.25	0.48
14GBKahleF	6.67	2.06	5.91	0.84	4.36	0.78	2	0.28	1.72	0.27
5 Hull Farm*	7.06	2.09	7.28	1.02	5.42	0.96	2.35	0.3	1.94	0.31
VAFC03-6*	8.49	2.38	8.42	1.2	6.79	1.29	3.18	0.4	2.83	0.4
14SMRt624	7.23	2.24	6.44	0.94	5.14	0.88	2.29	0.32	1.92	0.28
14SMRt624B	6.43	1.93	5.99	0.87	4.7	0.83	2.09	0.29	1.73	0.26
040HightownDike*	7.65	2.28	7.51	1.1	6.14	1.08	2.9	0.35	2.31	0.36
13JSTrible2	7.09	2.18	5.98	0.78	4.34	0.83	2.51	0.39	2.81	0.44
13BCTrible4	6.65	2.06	5.8	0.86	4.7	0.85	2.12	0.3	1.75	0.25
12DJHighTownQuarry1	8.83	2.99	7.2	1.05	6	1.16	3.59	0.56	3.75	0.61
12DJHighTownQuarry2*	7.4	1.8	5.4	0.8	4.4	0.9	2.6	0.4	2.9	0.5
13LJAnderson	11.14	2.85	9.46	1.37	7.21	1.31	3.6	0.53	3.4	0.52
14BSTreeDike	11.11	2.36	9.2	1.29	7.45	1.38	4.26	0.7	4.61	0.73
14SMRt637	8.92	2.91	8.19	1.17	6.45	1.15	3.01	0.43	2.8	0.42
12MBBFTrib1	5.75	1.86	5.33	0.79	4.2	0.72	1.89	0.26	1.53	0.22
13NRBillsMill	9.01	2.82	8.53	1.23	6.59	1.17	3	0.42	2.61	0.37
12MB Wilfong 1*	8.92	2.62	8.26	1.19	6.27	1.12	2.9	0.37	2.42	0.35

Chapter 3

Table 1

Sample Name	Sm (ppm)	Eu (ppm)	Gd (ppm)	Tb (ppm)	Dy (ppm)	Ho (ppm)	Er (ppm)	Tm (ppm)	Yb (ppm)	Lu (ppm)
Late Jurassic										
12MBSugarGrove1	15.03	4.37	9.84	1.17	5.75	1.09	2.53	0.35	1.94	0.28
2-SUGAR GROVE	8.63	2.56	7.65	1.09	5.44	1.11	2.72	0.39	2.59	0.34
14SMBrandywine	10.46	3.31	8.43	1.05	5.37	0.95	2.44	0.34	2.04	0.29
VQ**	11.57	3.24	9.52	1.21	6.05	1.1	2.77	0.36	2.42	0.38
13LJRt11A	9.73	2.3	7.74	0.99	5.36	1.05	2.96	0.5	3.4	0.51
14GBVerona	5.16	0.83	5.13	0.59	3.19	0.65	2.03	0.36	2.84	0.48
14GBRt773	8.07	2.09	6.47	0.81	4.12	0.84	2.41	0.37	2.62	0.4
13LJSpringHillA	5.08	1.11	4.84	0.58	3.29	0.64	2.03	0.38	2.86	0.49
14LJSpringHillB	5.85	0.86	5.04	0.69	4.17	0.86	2.92	0.53	3.9	0.63
14SMRt607	14.91	4.76	10.07	1.29	6.05	1.09	2.79	0.4	2.46	0.37
14GBShelby	8.37	2.48	6.49	0.75	3.82	0.71	2.12	0.33	2.2	0.37
14SMRt613	12.35	3.89	8.88	1.13	5.16	0.94	2.41	0.3	2.14	0.29
14GBRt699	4.95	1.44	4.95	0.58	3.06	0.64	1.83	0.33	2.24	0.35
14GBArey	9.87	3.21	7.59	0.99	4.79	0.92	2.2	0.33	2.11	0.33
USGS Standard										
BHVO-2 (n=10)	6.31	2.15	6.21	0.97	5.18	0.94	2.45	0.32	1.95	0.27
accuracy	4	5	0	4	2	3	2	2	0	2
Relative Standard Deviation	2	3	1	2	3	3	2	6	2	4

* in Mazza et al., 2014

** previously labeled as Eocene

[a] samples measured at the New Mexico Geochronology Research Laboratory

[b] samples measured at the USGS

Chapter 3
Table 1

Sample Name	Hf (ppm)	Ta (ppm)	Pb (ppm)	Th (ppm)	U (ppm)
Eocene					
MH Summit*	2.56	1.54	2.6	3.89	0.99
MH Xeno 4 *	3.06	1.66	2.44	4.41	0.94
MH 1.03*	2.4	1.46	2.53	3.49	1.02
MH 1.13*	2.93	1.66	2.45	4.19	0.92
TK5*	4.53	2.31	2.35	3.14	1
TK COLUMN 3*	4.52	2.26	3.84	3.2	0.95
13LJMonterey	12.2	7.17	18.27	15.88	3.95
12DJ631A	3.46	2.37	2.05	2.8	0.97
12DJ631B*	3.67	2.31	1.89	2.94	0.83
12DJ631C*	12.56	7.53	6.3	14.99	4.3
14GBKahleB	4.36	2.02	2.42	2.45	0.93
14GBKahleC	11.25	7.07	9.34	15.41	3.93
14GBKahleE	12.77	5.75	10.5	14.66	3.51
14GBKahleF	4.04	1.97	2.53	2.5	1.03
5 Hull Farm*	5.02	2.14	1.49	2.91	0.85
VAFC03-6*	6.24	2.61	2.61	3.85	1.09
14SMRt624	4.54	2.41	2.76	3.15	1.17
14SMRt624B	3.98	1.91	2.05	2.39	0.83
040HightownDike*	5.03	2.3	2.36	2.98	0.84
13JSTrible2	12.53	3.95	7.43	8.69	2.97
13BCTrible4	4.11	1.99	2.2	2.58	0.95
12DJHighTownQuarry1	16	4.42	5.46	9.17	2.3
12DJHighTownQuarry2*	8.7	4.1	12	8.7	2.2
13LJAnderson	8.2	4.35	4.4	7.05	1.88
14BSTreeDike	12.48	8.94	11.85	17.21	3.93
14SMRt637	5.06	2.54	3.47	3.53	1.2
12MBBFTrib1	3.81	1.59	1.87	2.05	0.78
13NRBillsMill	4.64	2.78	3.46	4.48	1.3
12MB Wilfong 1*	6.16	3.07	4.09	4.17	1.26

Chapter 3

Table 1

Sample Name	Hf (ppm)	Ta (ppm)	Pb (ppm)	Th (ppm)	U (ppm)
Late Jurassic					
12MBSugarGrove1	4.37	5.48	8.44	13.55	2.91
2-SUGAR GROVE	4.27	2.67	6.15	8.77	1.62
14SMBrandywine	4.22	5.9	3.99	6.74	1.43
VQ**	6.07	7.57	5.11	11.69	2.29
13LJRt11A	11.73	19.58	34.47	50.08	14.98
14GBVerona	15.15	32.24	30.17	80.11	27.87
14GBRt773	8.67	11.81	21.12	34.99	10.74
13LJSpringHillA	16.3	22.15	29.01	36.9	14.51
14LJSpringHillB	21.93	41.35	36.6	105.37	8.75
14SMRt607	3.97	7.05	13.99	16.51	4.03
14GBShelby	7.96	10.81	29.1	47.04	12.46
14SMRt613	3.86	6.88	16.14	22.66	5.53
14GBRt699	9.53	18.03	26.13	45.63	13.12
14GBArey	4.47	6.47	13.21	15.86	3.68
USGS Standard					
BHVO-2 (n=10)	4.15	1.06	2.03	1.24	0.46
accuracy	1	6	13	10	14
Relative Standard Deviation	1	2	2	3	4

* in Mazza et al., 2014

** previously labeled as Eocene

[a] samples measured at the New Mexico Geochronology Research Laboratory

[b] samples measured at the USGS

Chapter 3

Table 2

Sample Name	$^{87}Sr/^{86}Sr$	2σ	$^{143}Nd/^{144}Nd$	2σ	$^{206}Pb/^{204}Pb$	2σ	$^{207}Pb/^{204}Pb$	2σ	$^{208}Pb/^{204}Pb$	2σ
Eocene										
MH Summit*	0.703610	0.00001	0.512786	0.000008	19.293	0.0005	15.566	0.0030	38.89	0.0060
MH 1.13*	0.703677	0.00001	0.512816	0.000004	19.43	0.0004	15.628	0.0003	39.067	0.0010
TK5*	0.704282	0.00001	0.512910	0.000009	20.075	0.0020	15.612	0.0020	39.029	0.0040
12DJ631B*	0.705202	0.00001	0.512896	0.000005	19.992	0.0005	15.655	0.0004	39.315	0.0012
5 Hull Farm*	0.703354	0.00001	0.512908	0.000011	19.943	0.0040	15.628	0.0040	39.077	0.0060
040HightownDike*	0.703627	0.00001	0.512899	0.000004	19.886	0.0005	15.66	0.0003	39.091	0.0015
12MB Wilfong 1*	0.703676	0.00001	0.512832	0.000003	19.579	0.0004	15.651	0.0004	38.811	0.0012
Late Jurassic										
VQ**	0.704523	0.000010	0.512605	0.000004	19.316	0.0005	15.596	0.0004	39.360	0.0012
13LJRt11A	0.713502	0.000006	0.512589	0.000005	20.952	0.0006	15.710	0.0006	40.900	0.0017
14GBRt773	0.709411	0.000005	0.512590	0.000005	19.968	0.0010	15.661	0.0010	39.471	0.0030
14GBShelby	0.704984	0.000009	0.512625	0.000003	20.086	0.0006	15.670	0.0005	39.619	0.0017
14GBRt699	0.707111	0.000009	0.512618	0.000004	23.473	0.0008	15.833	0.0000	40.716	0.0016
14GBArey	0.706276	0.000011	0.512544	0.000006	19.672	0.0006	15.654	0.0005	39.465	0.0016
USGS Standards										
BHVO-1 (isotopes only)	0.703603	0.000013	0.512994	0.000005	18.636	0.001	15.484	0.001	38.175	0.002
BCR-2 (isotopes only)	0.705133	0.000009	0.512651	0.000004	18.796	0.001	15.616	0.001	38.793	0.002
Blank (isotope only)	<80 pg		<10 pg		<38 pg					

NBS measured	16.9329354	15.4856171	36.6820234
Todt et al., 1996	16.9356	15.4891	36.7006
Difference	0.0027	0.0035	0.0186

* in Mazza et al., 2014

** previously labeled as Eocene

normalized to Todt et al., 1996

Chapter 3

Table 2

Sample Name	$(^{87}Sr/^{86}Sr)_i$	$(^{143}Nd/^{144}Nd)_i$	ΣNd0	ΣNdt	$(^{206}Pb/^{204}Pb)_i$	$(^{207}Pb/^{204}Pb)_i$	$(^{208}Pb/^{204}Pb)_i$
Eocene							
MH Summit*	0.703540	0.512750	3.34	2.89	19.102	15.557	38.642
MH 1.13*	0.703620	0.512770	3.89	3.47	19.240	15.619	38.783
TK5*	0.704210	0.512870	5.71	5.31	19.858	15.602	38.805
12DJ631B*	0.705130	0.512860	5.52	5.04	19.766	15.644	39.053
5 Hull Farm*	0.703320	0.512860	5.66	5.27	19.655	15.614	38.752
040HightownDike*	0.703520	0.512850	5.48	5.09	19.705	15.651	38.879
12MB Wilfong 1*	0.703610	0.512790	4.23	3.78	19.423	15.643	38.642
Late Jurassic							
VQ**	0.704170	0.512510	1.29	-0.65	18.630	15.562	38.216
13LJRt11A	0.711616	0.512512	1.31	-0.95	20.258	15.676	40.141
14GBRt773	0.707895	0.512514	1.35	-0.94	19.181	15.622	38.633
14GBShelby	0.704378	0.512546	1.97	-0.25	19.421	15.638	38.798
14GBRt699	0.704936	0.512541	1.87	-0.38	22.646	15.792	39.776
14GBArey	0.706197	0.512459	0.27	-1.84	19.242	15.633	38.860
USGS Standards							
BHVO-1 (isotopes only)							
BCR-2 (isotopes only)							
Blank (isotope only)							

Chapter 3

Table 2

Sample Name	$^{206}Pb/^{204}Pb^{\#}$	2σ	$^{207}Pb/^{204}Pb^{\#}$	2σ	$^{208}Pb/^{204}Pb^{\#}$	2σ
Eocene						
MH Summit*						
MH 1.13*						
TK5*						
12DJ631B*						
5 Hull Farm*						
040HightownDike*						
12MB Wilfong 1*						
Late Jurassic						
VQ**	19.319	0.0005	15.599	0.0004	39.379	0.0012
13LJRt11A	20.955	0.0006	15.713	0.0006	40.919	0.0017
14GBRt773	19.971	0.001	15.664	0.001	39.490	0.003
14GBShelby	20.089	0.0006	15.673	0.0005	39.638	0.0017
14GBRt699	23.476	0.0008	15.836	0.0005	40.735	0.0016
14GBArey	19.675	0.0006	15.657	0.0005	39.484	0.0016
USGS Standards						
BHVO-1 (isotopes only)	18.639	0.001	15.487	0.001	38.194	0.002
BCR-2 (isotopes only)	18.799	0.001	15.619	0.001	38.812	0.002
Blank (isotope only)						

Chapter 3

Table 3

Sample Name	Citation	Nd	Sm	$^{143}Nd/^{144}Nd$	$^{143}Nd/^{144}Nd_{(150Ma)}$	Σ Nd	Σ Nd_i	U	Th	Pb	$^{206}Pb/^{204}Pb$	$^{207}Pb/^{204}Pb$	$^{208}Pb/^{204}Pb$
Rm-1	a	19.1	2.8	0.511490	0.511461	-22.40	-22.39	0.5	11.0	12.2	17.271	15.605	40.961
NC-81	a	24.5	5.0	0.511773	0.511733	-16.90	-16.87	0.2	16.0	21.3	17.209	15.556	40.389
NC-28	a	20.1	3.0	0.511621	0.511592	-19.80	-19.84	1.0	1.0	23.1	17.669	15.680	40.458
WG-CS	a	44.8	9.1	0.512129	0.512089	-9.90	-9.93	1.6	23.7	45.4	17.312	15.519	38.412
SC-RC	a	117.4	17.0	0.511823	0.511795	-15.90	-15.90	1.2	6.6	18.5	17.449	15.539	37.916
SM-GC	a	40.6	9.7	0.512320	0.512273	-6.20	-6.20	1.3	5.2	17.7	17.464	15.519	37.384
SM-PM1	a	48.2	10.7	0.512166	0.512122	-9.20	-9.21	1.0	5.3	16.2	17.613	15.560	38.424
HP-25	b & c							0.5	2.0	26.4	17.477	15.566	37.275
HP-30	b & c							0.5	1.3	35.7	17.516	15.573	36.852
HP-32	b & c							0.9	1.5	33.1	17.508	15.565	37.082
75-273	b & c									36.2	17.421	15.560	37.068
76-96	b & c	100.4	20.3	0.512240	0.512200	2.58	-7.76	0.6	1.5	16.8	17.402	15.545	36.994
S-3-81	b & c	76.4	12.1	0.511980	0.511949	1.16	-12.84	0.8	5.3	46.5	17.867	15.594	40.138
S-4-81C	b	86.4	14.2	0.512060	0.512028	2.21	-11.28						
S-4-81M	b	208.0	38.3	0.512130	0.512094	1.92	-9.91						
S-5-81	b	50.8	10.5	0.512240	0.512199	2.16	-7.76						
H-22-81	b	1.3	0.2	0.511900	0.511874	1.30	-14.40						
HP-24	b & c	6.3	1.3	0.512590	0.512550	6.30	-0.94	0.2	0.1	30.3	18.744	15.658	38.593
H-18-81	b & c	2.8	0.8	0.512500	0.512445	2.80	-2.69	0.3	0.1	5.6	17.201	15.527	36.796
H-6-81	b & c	2.1	0.5	0.512260	0.512215	2.14	-7.37	0.1	0.1	4.5	17.293	15.540	36.920
76-92	b & c	45.0	9.4	0.512610	0.512569	44.96	-0.55						
76-242	b	5.0	1.8	0.512860	0.512788	4.96	4.33						
7902	b	180.7	33.4	0.512000	0.511964	180.70	-12.45						
H-5-81	b & c							0.2	1.0		17.906	15.576	37.767
H-2-81	b & c							0.4	1.7		18.111	15.639	38.393
H-9-81	b	9.2	1.2	0.511940	0.511914	9.23	-13.62	0.4	1.6	46.9	17.313	15.544	36.889
H-10-81	b							1.1	2.0	22.3	17.419	15.555	36.964
H-11-81	b	96.2	19.0	0.512180	0.512141	96.20	-8.93						
H-13-81	b	82.8	16.4	0.512170	0.512131	82.78	-9.13	0.1	8.0	17.1	17.325	15.542	36.969
H-14-81	b & c	26.3	5.8	0.512300	0.512257	26.32	-6.59	1.2	7.9	19.2	17.247	15.536	36.820
75-361	b & c							1.4	7.0	25.8	17.302	15.558	36.900
75-557	b & c							2.3	6.9	38.0	17.298	15.544	36.915
75-363	b & c							0.2	0.3	30.1	17.281	15.559	36.968
75-364	b & c							0.4	8.8	25.9	17.451	15.565	37.108

HP-21	b & c							0.7	0.2		17.480	15.572	37.203
75-408	b & c							0.7	0.7	27.1	17.350	15.586	37.237
HP-14	b & c							0.8	2.4	18.4	17.283	15.564	36.992
HP-23	b & c							0.6	0.9	25.1	17.697	15.703	34.329
Z-9	b & c	160.2	30.3	0.512140	0.512103	160.20	-9.71	1.2	3.5	12.3	17.308	15.549	36.954
H-5-81	c							0.2	1.0		17.906	15.576	37.767
JP-92-36	c							1.0	1.1	8.1	20.032	15.743	37.831
JP-92-35	c							1.0	3.0	20.8	17.375	15.537	37.209
JP-92-34	c							0.8	1.6	18.6	17.887	15.592	37.394
JP-92-24	c							1.1	0.7	10.2	17.280	15.548	36.793
JP-92-29	c							0.5	0.8	11.1	17.502	15.500	36.482
JP-92-28	c							1.1	2.0	17.2	17.460	15.499	36.768
JP-92-30	c							0.3	0.8	7.0	17.872	15.547	36.880
JP-92-25	c							0.3	1.2	1.8	17.928	15.533	37.073
JP-92-31	c							0.8	1.3	15.7	19.060	15.628	37.641
JP-92-32	c							1.2	3.2	6.9	18.476	15.576	37.621
S-23-82	c							0.6	2.1	17.5	17.594	15.524	37.178
S-25-82	c							1.2	0.7	26.3	17.303	15.539	36.811
S-26-82	c							0.7	2.1	13.2	17.488	15.567	37.132
S-27-82	c							1.7	3.3	22.1	17.768	15.591	37.306
JP-92-1	c							0.5	5.4	5.3	17.734	15.671	39.639
JP-92-6	c							0.3	1.0	2.3	17.267	15.562	37.717
CNE-88	c							1.0	4.8	15.2	17.532	15.540	37.232
CNE-90	c							0.7	3.2	24.9	17.183	15.512	37.400
CNE-124	c									23.9	17.256	15.520	38.755
CNE-265	c							0.9	9.9	38.1	17.281	15.542	37.612
TF-21	c							3.3	64.7	49.2	18.484	15.614	40.715
TF-23A	c							0.7	10.0	88.1	17.446	15.532	39.145
TF-879	c							2.6	30.0	48.6	17.749	15.551	38.465
TF-1028	c							0.4	6.9	41.3	17.448	15.525	40.636
S-88-30	c							1.4	25.0	44.2	17.462	15.514	38.343
S-88-32	c							2.2	26.0	41.2	17.587	15.529	38.053
S-88-33	c							3.6	20.0	40.8	17.790	15.541	37.468
S-88-29	c							0.6	1.9	14.1	17.619	15.529	37.039
S-88-31	c							1.0	2.3	14.1	17.547	15.507	36.995
JS-90-66	c							1.5	2.8	30.8	17.600	15.571	37.095

S-88-3	c							0.4	16.0	31.2	17.226	15.524	36.880
S-88-4	c							1.8	7.1	27.1	17.535	15.555	39.517
S-88-5	c							1.4	7.4	27.1	17.547	15.539	37.551
Lilesville	d	52.4	8.9	0.512498	0.512465	-2.70	-2.73						
Pee Dee Gabbro	d	39.3	8.8	0.512565	0.512521	-1.40	-1.42						
Pageland	d	54.4	9.4	0.512470	0.512436	-3.30	-3.28						
Pageland	d	39.3	6.5	0.512485	0.512453	-3.00	-2.98						
Liberty Hill	d	64.7	9.2	0.512084	0.512056	-10.80	-10.81						
Liberty Hill	d	56.3	10.2	0.512416	0.512380	-4.30	-4.33						
Liberty Hill	d	27.4	5.4	0.512429	0.512390	-4.10	-4.08						
Winnsboro	d	46.3	7.0	0.512290	0.512260	-6.80	-6.79						
Winnsboro	d	79.5	11.7	0.512137	0.512108	-9.80	-9.77						
Harbison	d	28.9	4.6	0.512463	0.512432	-3.40	-3.41						
Columbia	d	33.7	5.7	0.512549	0.512516	-1.70	-1.74						
Columbia	d	20.8	3.3	0.512527	0.512495	-2.10	-2.17						
Cuffytown	d	27.5	5.9	0.512486	0.512444	-3.00	-2.97						
Siloam	d	62.4	9.1	0.512236	0.512207	-7.80	-7.84						
Danburg	d	41.6	6.0	0.512412	0.512384	-5.80	-4.41						
Lowry	d	71.0	11.0	0.512412	0.512382	-4.40	-4.41						
Catawba	d	15.3	3.5	0.512589	0.512543	-1.00	-0.96						
York	d	20.8	3.2	0.512360	0.512330	-5.40	-5.42						
Clover	d	27.8	4.0	0.512345	0.512316	-5.70	-5.72						
Gastonia	d	40.1	5.3	0.512291	0.512265	-6.80	-6.77						
Landis	d	27.0	4.0	0.512353	0.512324	-5.60	-5.56						
Sims	d	31.1	5.2	0.512539	0.512506	-1.90	-1.93						
Sims	d	26.4	4.4	0.512511	0.512478	-2.50	-2.48						
Castilia	d	23.4	4.2	0.512588	0.512552	-1.00	-0.98						
Castilia	d	23.0	3.8	0.512518	0.512486	-2.30	-2.34						
Portsmouth	d	20.4	3.6	0.512432	0.512397	-4.00	-4.02						
CloudsCreek	d	44.8	9.2	0.512378	0.512338	-5.10	-5.07						
Graniteville	d	23.3	3.9	0.512552	0.512519	-1.70	-1.68						
Edgefield	d	15.0	3.3	0.512471	0.512427	-3.30	-3.26						
Appling	d	44.8	7.6	0.512480	0.512447	-3.10	-3.08						
Towncreek	d	42.3	6.6	0.512446	0.512415	-3.70	-3.75						
All Blue Ridge Avg		48.9	8.7	0.512302	0.512266	9.16	-6.55	0.9	6.0	23.5	17.582	15.559	37.633
VA Blue Ridge Avg		61.2	11.6	0.512248	0.512207	29.23	-7.62	0.7	2.8	26.1	17.508	15.571	37.168

Chapter 3

Table 3

Sample Name	$^{206}Pb/^{204}Pb_{(150\ Ma)}$	$^{207}Pb/^{204}Pb_{(150\ Ma)}$	$^{208}Pb/^{204}Pb_{(150\ Ma)}$	Sr	Rb	$^{87}Sr/^{86}Sr$	$^{87}Sr/^{86}Sr_{(150\ Ma)}$
Rm-1	17.250	15.604	40.812	39	254	0.718556	0.705199976
NC-81	17.204	15.556	40.266				
NC-28	17.647	15.679	40.451				
WG-CS	17.295	15.518	38.329	126	152	0.749799	0.747306
SC-RC	17.418	15.538	37.859	262	235	0.751664	0.749811
SM-GC	17.429	15.517	37.338	93	200	0.726917	0.722522
SM-PM1	17.583	15.559	38.371	90	361	0.716030	0.707813
HP-25	17.477	15.566	37.275	459	125	0.716290	0.715730
HP-30	17.516	15.573	36.852	349	172	0.726000	0.724985
HP-32	17.508	15.565	37.082	529	125	0.714190	0.713704
75-273	17.421	15.560	37.068	426	134	0.718440	0.717793
76-96	17.402	15.545	36.994	437	48	0.709220	0.708996
S-3-81	17.867	15.594	40.138	178	265	0.767260	0.764183
S-4-81C				182	216	0.738760	0.736314
S-4-81M				181	175	0.733720	0.731728
S-5-81				286	89	0.714020	0.713379
H-22-81				1173	9	0.705120	0.705105
HP-24	18.744	15.658	38.593	1100	29	0.705580	0.705525
H-18-81	17.201	15.527	36.796	855	14	0.705260	0.705226
H-6-81	17.293	15.540	36.920	793	17	0.705200	0.705156
76-92				3550	1	0.704830	0.704830
76-242				50	6	0.706510	0.706258
7902				22	0	0.705460	0.705452
H-5-81	17.906	15.576	37.767	217	1	0.705600	0.705594
H-2-81	18.111	15.639	38.393	323	8	0.706000	0.705947
H-9-81	17.313	15.544	36.889	279	234	0.743400	0.741670
H-10-81	17.419	15.555	36.964	286	195	0.733680	0.732275
H-11-81				248	157	0.732670	0.731366
H-13-81	17.325	15.542	36.969	571	69	0.710740	0.710492
H-14-81	17.247	15.536	36.820	509	88	0.712670	0.712314
75-361	17.302	15.558	36.900	539	126	0.714570	0.714089
75-557	17.298	15.544	36.915	111	198	0.777090	0.773400
75-363	17.281	15.559	36.968	525	113	0.714150	0.713707
75-364	17.451	15.565	37.108	441	96	0.716060	0.715610

HP-21	17.480	15.572	37.203	547	87	0.712720	0.712392
75-408	17.350	15.586	37.237	132	138	0.753210	0.751052
HP-14	17.283	15.564	36.992	501	65	0.709720	0.709452
HP-23	17.697	15.703	34.329	206	128	0.735530	0.734250
Z-9	17.308	15.549	36.954				
H-5-81	17.906	15.576	37.767				
JP-92-36	19.970	15.740	37.809				
JP-92-35	17.352	15.536	37.186				
JP-92-34	17.866	15.591	37.380				
JP-92-24	17.229	15.546	36.782				
JP-92-29	17.481	15.499	36.471				
JP-92-28	17.430	15.498	36.750				
JP-92-30	17.851	15.546	36.862				
JP-92-25	17.848	15.529	36.968				
JP-92-31	19.035	15.627	37.628				
JP-92-32	18.391	15.572	37.546				
S-23-82	17.578	15.523	37.159				
S-25-82	17.281	15.538	36.807				
S-26-82	17.463	15.566	37.107				
S-27-82	17.731	15.589	37.282				
JP-92-1	17.687	15.669	39.472				
JP-92-6	17.204	15.559	37.648				
CNE-88	17.500	15.539	37.182				
CNE-90	17.170	15.511	37.380				
CNE-124	17.256	15.520	38.755				
CNE-265	17.270	15.541	37.571				
TF-21	18.450	15.612	40.494				
TF-23A	17.442	15.532	39.127				
TF-879	17.723	15.550	38.366				
TF-1028	17.443	15.525	40.608				
S-88-30	17.447	15.513	38.253				
S-88-32	17.561	15.528	37.952				
S-88-33	17.747	15.539	37.390				
S-88-29	17.599	15.528	37.018				
S-88-31	17.513	15.505	36.969				
JS-90-66	17.577	15.570	37.081				

S-88-3	17.220	15.524	36.800				
S-88-4	17.502	15.553	39.474				
S-88-5	17.522	15.538	37.508				
Lilesville				277	133	0.711500	0.710513
Pee Dee Gabbro				605	32	0.704617	0.704508
Pageland				307	150	0.710567	0.709563
Pageland				166	172	0.717716	0.715585
Liberty Hill				212	267	0.722370	0.719778
Liberty Hill				307	123	0.710158	0.709334
Liberty Hill				218	155	0.713805	0.712343
Winnsboro				231	285	0.721220	0.718681
Winnsboro				209	259	0.722765	0.720215
Harbison				790	134	0.706586	0.706237
Columbia				280	172	0.711760	0.710497
Columbia				120	238	0.709923	0.705846
Cuffytown							
Siloam				291	241	0.715952	0.714249
Danburg				199	252	0.720697	0.718091
Lowry				1513	111	0.705420	0.705269
Catawba				231	260	0.719187	0.716871
York				263	169	0.712972	0.711651
Clover				713	131	0.706569	0.706191
Gastonia				522	148	0.708447	0.707864
Landis				712	115	0.706405	0.706073
Sims				248	209	0.714098	0.712365
Sims				219	269	0.719668	0.717141
Castilia				325	127	0.709408	0.708605
Castilia				270	174	0.711837	0.710512
Portsmouth				219	303	0.723182	0.720335
CloudsCreek				202	144	0.719543	0.718076
Graniteville				216	153	0.712955	0.711499
Edgefield						0.722090	
Appling				278	150	0.710971	0.709862
Towncreek				339	12	0.710338	0.710265
All Blue Ridge Avg	17.565	15.558	37.602	418	144	0.718567	0.717014
VA Blue Ridge Avg	17.508	15.571	37.168	515	100	0.720884	0.720069

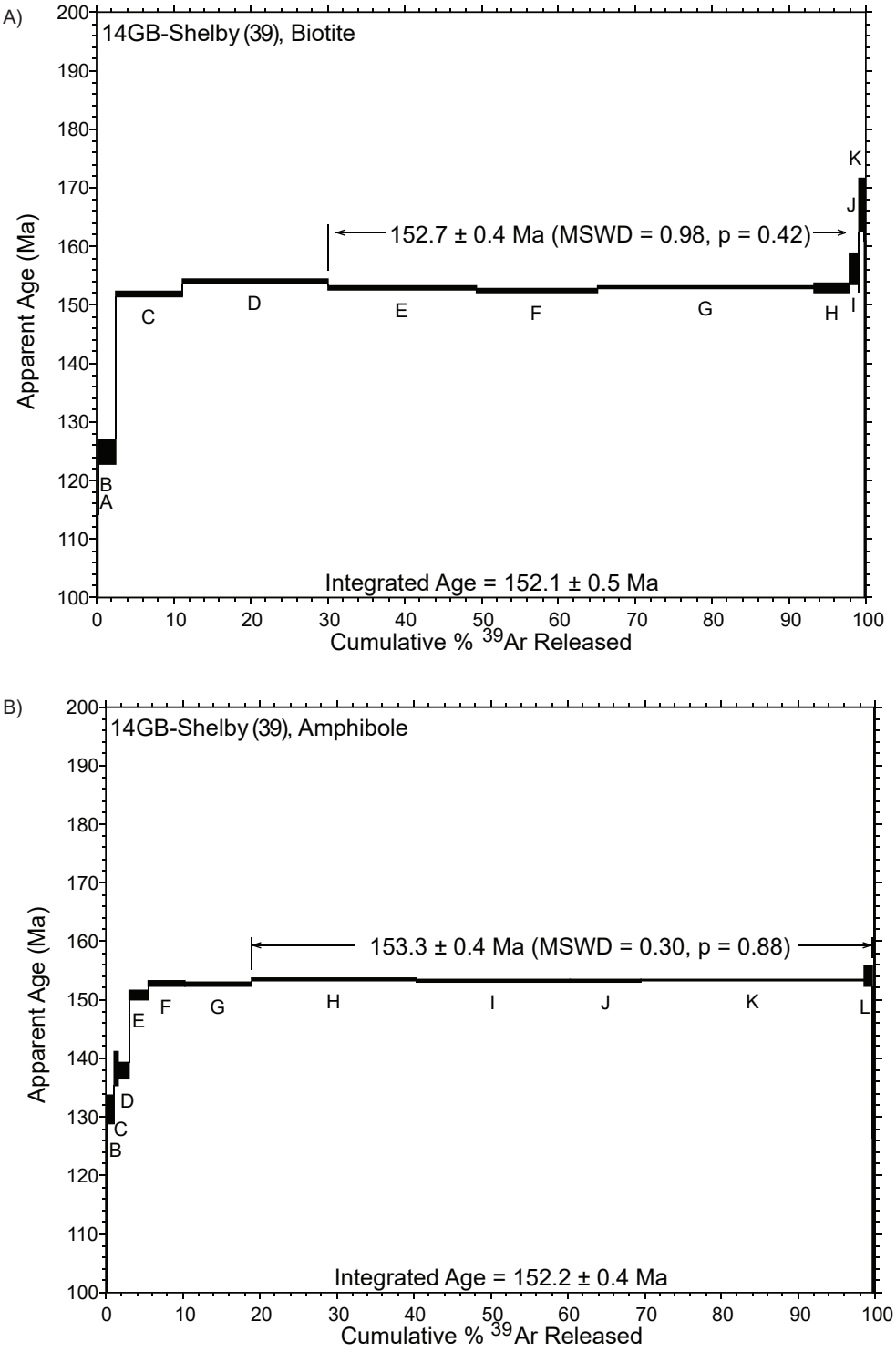

Supplementary Figure 3.1: $^{40}Ar/^{39}Ar$ age spectrums for 14GBShelby. A) Biotite from location A39, degassed in 11 steps with a flat age spectrum and an integrated age of 152.1 Ma. Steps E-I meet the statistical definition of a plateau and yield an age of 152.7 ± 0.4 Ma. B) Amphibole from location A39, degassed in 16 steps with a flat age spectrum and an integrated age of 152.2 Ma. Steps H-L meet the statistical definition of a plateau and yield an age of 153 ± 0.4 Ma.

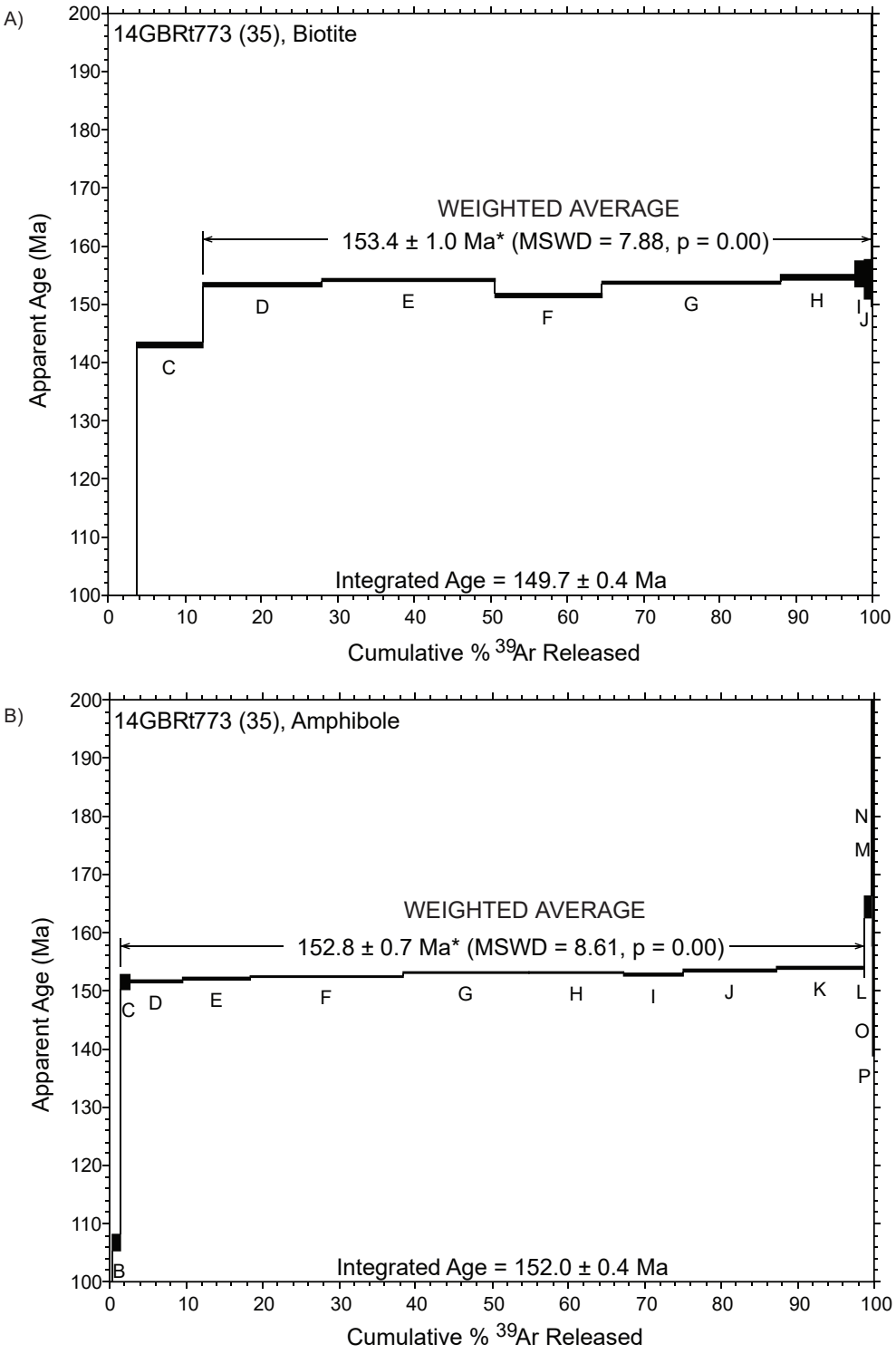

Supplementary Figure 3.2: $^{40}Ar/^{39}Ar$ age spectrums for 14GBRt773. A) Biotite from location A35, degassed in 11 steps with a flat age spectrum and an integrated age of 149.7 Ma. The first two steps are anomalously young, possibly due to inclusions or minor chloritization. Steps D-J range from 151.4 to 155.1 Ma in age, with a weighted average of 153.4 ± 1.0 Ma. This is our preferred age. B) Amphibole from A35 degassed in 15 steps the step ages climb slightly across the entire spectrum. Steps C-K have a fairly uniform K/Ca ratio and a weighted average of these steps yields an age of 152.8 ± 0.7 Ma and is our preferred age.

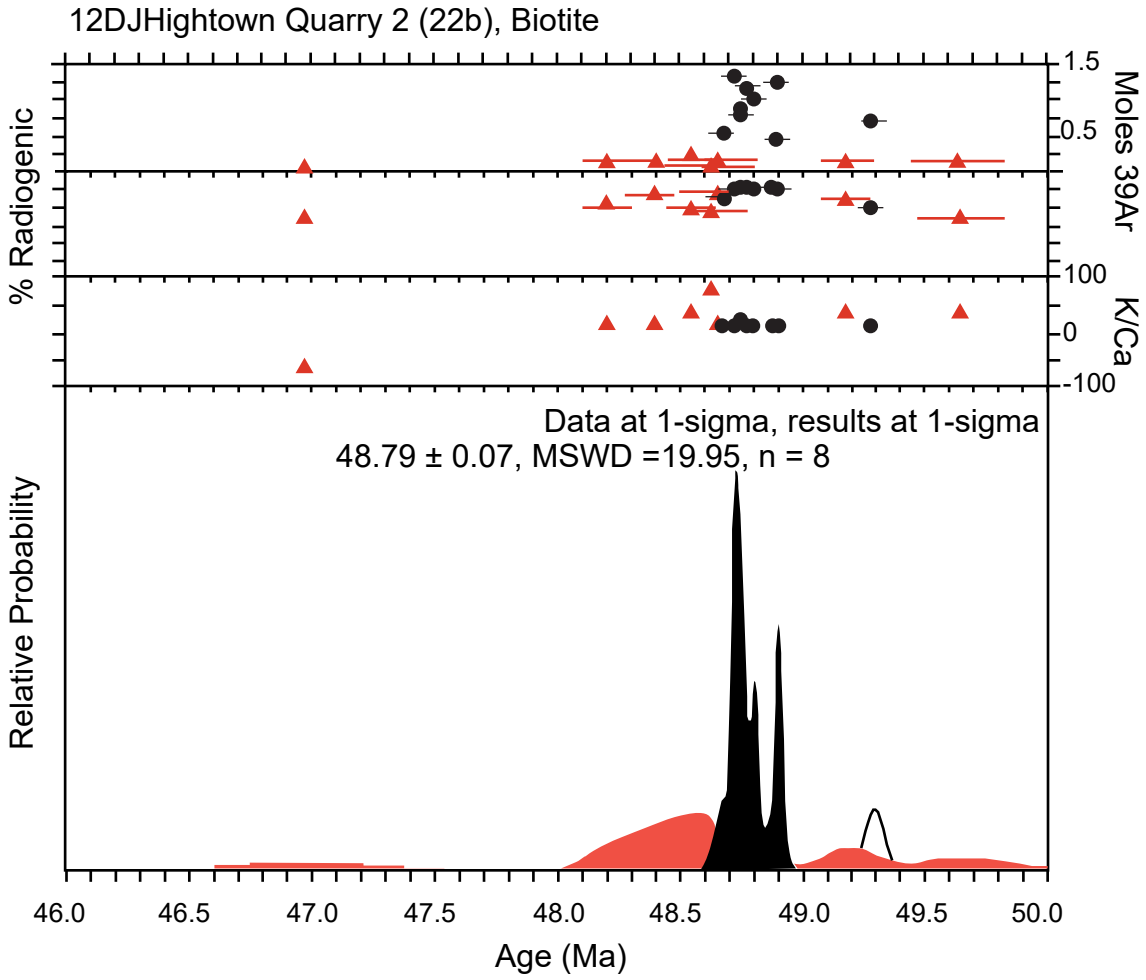

Supplementary Figure 3.3: $^{40}Ar/^{39}Ar$ age spectrums for 12DJHightownQuarry2. Biotite from location H22b, with Moles ^{39}Ar, K/Ca and relative probability of age yielding an age of 48.795 ± 0.073 Ma.

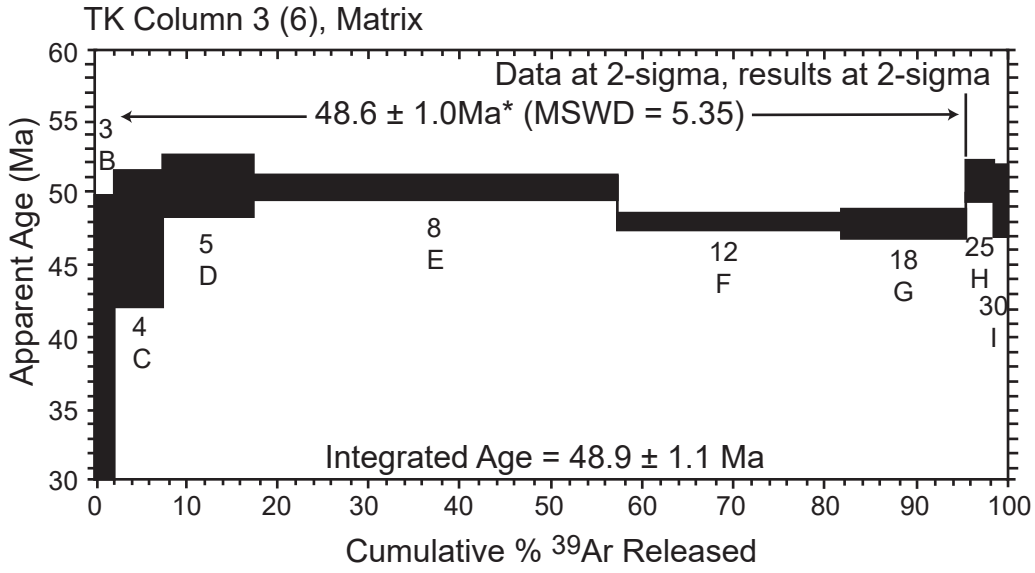

Supplementary Figure 3.4: $^{40}Ar/^{39}Ar$ age spectrums for TKColumn3. Matrix from location H6, degassed in 8 steps with a flat age spectrum and an integrated age of 48.9 ± 1.1 Ma. Steps C-G yield an average age of 48.6 ± 1.0 Ma.

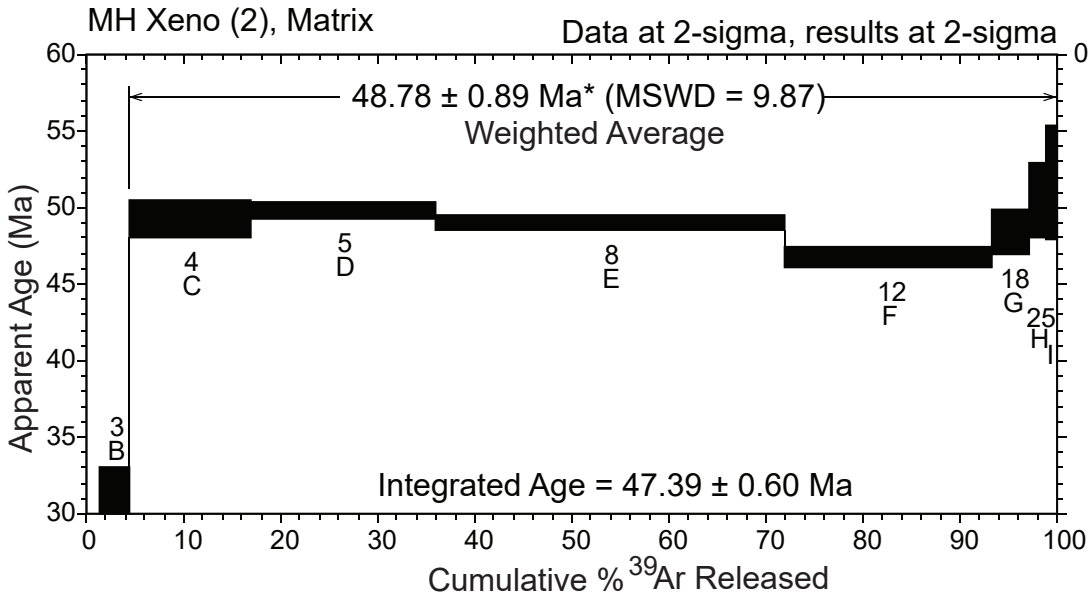

Supplementary Figure 3.5: $^{40}Ar/^{39}Ar$ age spectrums for MHXeno2. Matrix from location R2, degassed in 8 steps with a flat age spectrum and an integrated age of 47.39 ± 0.6 Ma. Steps C-G yield an average age of 48.78 ± 0.89 Ma.

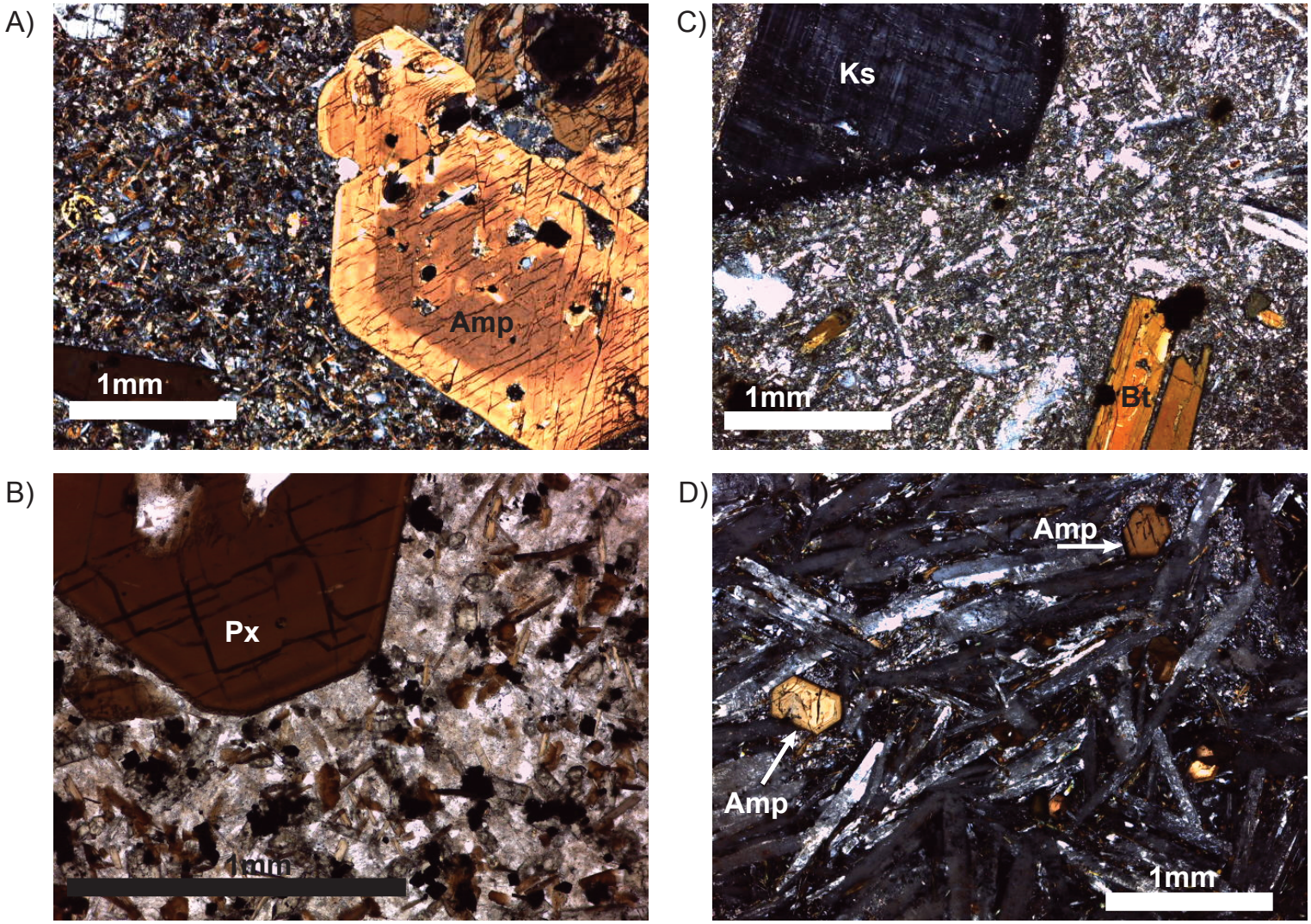

Supplementary Figure 3.6:
Micrographs from the Late Jurassic volcanics showing A) zoned amphibole with rounded crystal edges in basanite (sample 40, cross polarized light) B) pyroxene with rounded crystal edges in basanite (sample 40, plain polarized light) C) K-feldspar with tartan plaid twinning and biotite phenocrysts in phonolite (sample 39, cross polarized light), and D) amphibole phenocrysts with sharp crystal edges in nepheline groundmass in phonolite (sample 35, cross polarized light). Amp = amphibole, Px = pyroxene, Ks = K-feldspar, and Bt = biotite.

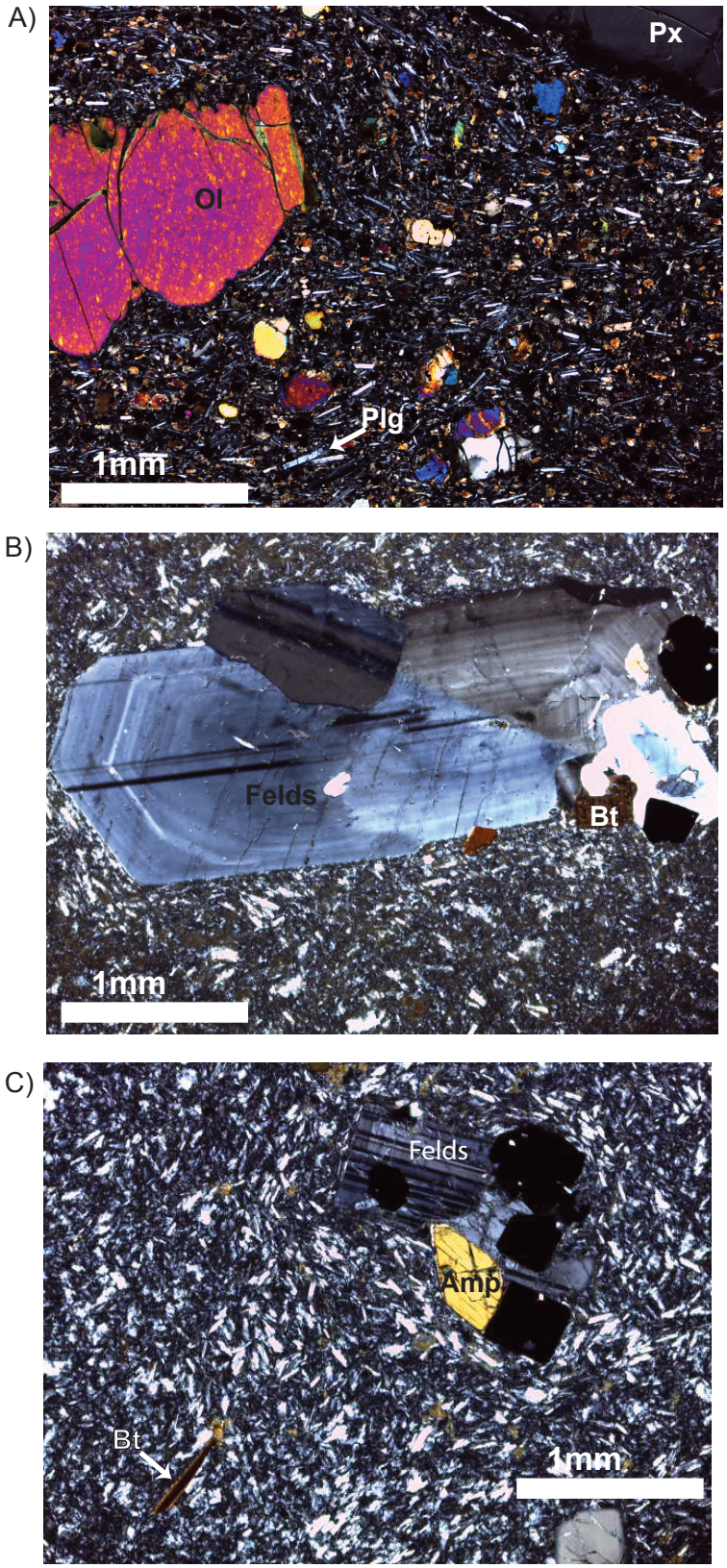

Supplementary Figure 3.7:
Micrographs from the Eocene volcanics showing A) fresh olivine phenocrysts with plagioclase matrix in picrobasalt (sample 18, cross polarized light) B) oscillatory zoning in feldspar phenocrysts with biotite in trachydacite (sample 20, cross polarized light) C) Alkali feldspar, amphibole, and biotite phenocrysts in trachdacite (sample 12, cross polarized light). Ol = olivine, Plg = plagioclase Px = pyroxene, Felds = alkali feldspar, Bt = biotite, Amp = amphibole.

Chapter 4: Solving the mystery of Bermuda: Evidence for a young, carbonated mantle

Sarah E. Mazza[1], Esteban Gazel[1], Michael Bizimis[2], Ryan McAleer[3]

[1]Department of Geosciences, Virginia Tech, 4044 Derring Hall (0420), Blacksburg, VA 24061
[2]Department of Earth and Ocean Sciences, University of South Carolina, 701 Sumter Street, EWS 617, Columbia, SC 29208
[3]United States Geological Survey, 12201 Sunrise Valley Dr., MS 926A, Reston, VA 20192-0002

Prepared for Submission to *Nature Geoscience*

Intraplate magmatism, typically associated with melting from buoyant upwelling in mantle plumes[1], provides direct evidence that the Earth's mantle is compositionally heterogeneous[2-4]. However, not all intraplate volcanoes can be explained by the mantle plume model[5], thus other models of melting such as lithospheric delamination[6] and edge driven convection (EDC)[7] must also be considered. Many of the chemical heterogeneities in the mantle are attributed to recycling during subduction, which allows for the addition of volatiles and incompatible elements (elements non-compatible in the mantle) into the mantle. In particular, radiogenic isotopes highlight the heterogeneous nature of the mantle, with several unique chemical end-members: enriched mantle I and II (EMI and EMII), depleted mantle (DM), and high $^{238}U/^{204}Pb$ (HIMU). Here we present new evidence from Bermuda for a fifth mantle end-member that is characterized as an extremely young HIMU (named HIMU-2) due to the recycling of carbon-rich units into the mantle. Silica under-saturated magmas from Bermuda record the most radiogenic $^{206}Pb/^{204}Pb$ isotopes in the Atlantic, coupled with low $^{207}Pb/^{204}Pb$. We thus interpret Bermuda as a young HIMU mantle reservoir which is the result of carbon triggered metasomatism of peridotite, due to EDC driven melting.

Bermuda is the surficial expression of the 1500 km long, NE-SW trending swell that rises 1 km above 110-140 Ma oceanic crust[8,9]. Like many ocean volcanic islands, Bermuda has been historically classified as mantle plume-derived[10-12]; however, evidence that supports the plume model is not conclusive. A first-order problem is the lack of a hotspot track associated with Bermuda[13-15]. Bermuda is the only visible volcanic feature in the proximity of the proposed hotspot trails, there is no evidence for volcanism at the proposed current location of the hotspot (~650 km southeast of Bermuda), and the Bermuda Rise trends perpendicular to the predicted plume trace (Figure 4.1). More recent geodynamic models use EDC, small-scale convection

associated with the thermal contrast between thick (cold) continental lithosphere and thin (warm) oceanic lithosphere to explain Bermuda[7,16]. The transition zone beneath Bermuda is ~25 km thinner than the global average, due to the combined effects of a depressed 410 km discontinuity and a depressed 660 km discontinuity. This has been used as evidence to argue against the mantle plume model for Bermuda[16].

Bermuda has remained a chemical enigma due to the inaccessibility of the igneous rocks by the carbonate cover. Nonetheless, the Deep Drill 1972 borehole recovered a continuous 767 m record of igneous activity[17] (Figure 4.1). Since 1972, only very limited geochronology and paleomagnetic results have been published[17-19]. We present the first comprehensive geochemical data for Bermuda, and find that Bermuda is composed of two main lithologies: two mineralogically unique silica under-saturated (BSU) alkaline units ranging from foidite to basanite with Ti-augite + nepheline + Ti-spinel ± phlogopite ± apatite ± perovskite and plagioclase + olivine + Ti-augite + spinel and silica saturated units (BSS) ranging from basalt to trachyandesite (Figure 4.2a; Supplementary Table 1).

Phlogopite separates from BSU yield $^{40}Ar/^{39}Ar$ ages between 34 and 30 Ma. BSU are generally fresh with alteration limited to small calcite veins, while BSS are prone to heavy calcite and hematite alteration. Ba and Sr are fluid mobile elements[20], and their general lack of enrichment (positive anomalies in the multi-element diagram Figure 4.2b) in BSU suggests that these samples are unaltered from a geochemical perspective. The BSS are enriched (Figure 4.2b) relative to the surrounding local mid-ocean ridge basalt (MORB)[21]. The BSU have characteristic patterns of ocean island basalts (OIB). These lavas are highly enriched in incompatible elements with positive Nb and Ta anomalies, and depletions in K and Pb (Figure 4.2b), and are more

enriched than other Atlantic intraplate locations (including: Canaries, Azores, Cape Verde, Madeira, and Fernando de Nornoha).

Olivine Mg# (molar Mg/(Mg+Fe)*100) ranges from 84-88 and most likely crystallized from a peridotite melt due to high Ni, Fe/Mn, and low Ca[22] (Supplementary Figure 4.1 and Supplementary Table 2). Due to silica under-saturation of BSU, traditional geothermobarometers cannot be used to estimate pressure-temperature conditions of melt equilibrium[23-25]. Instead, we can estimate minimum crystallization temperatures of olivine via olivine-spinel thermometry based on the exchange of Al_2O_3 between forsterite-rich olivine and Cr-rich spinels[26,27]. We estimate minimum olivine crystallization temperatures of 1260 °C, which is relatively cool compared to olivines crystallized in Large Igneous Provinces (1353 °C to 1485 °C) (Supplementary Figure 4.2).

Silica under-saturated, alkaline magmas, like BSU, cannot be produced by simple peridotite mantle melting, and thus CO_2 from carbonatites, carbonate minerals, or CO_2 fluid is needed[28]. A variety of experiments over the past two decades have attempted to constrain the relationship of CO_2 and silica under-saturated magmas[29-34], and have found that the onset of carbonated silicate melting is lower than the solidus from volatile-free peridotite in the sample pressure conditions[35], which is further depressed with the presence of H_2O[36]. The decompression of carbonated peridotite would produce a highly mobile carbonatitic melt near the solidus, which is extracted from the parent and that ascending melt will act as a metasomatic fluid and produce carbonated silicate melts[37,38]. The depression of the solidus with the addition of volatiles suggests that intraplate magmatism can be generated under cooler conditions. Carbon may be able to induce melting at depths close to the mantle transition zone by the partial melting of volatile (CO_2 and H_2O) rich subducted material[31,39-41].

Bermuda is best explained by melting a carbonated peridotite. There are similarities of major elements from the CO_2 enriched experimental melts with BSU, especially high CaO and low Al_2O_3 with low SiO_2 (Figure 4.2c)[35]. Garnet stability is enhanced in carbonated systems, and thus lower Al_2O_3 in the melt[42], and the presence of garnet in the residue material is evident from the steep slope in heavy rare earth elements (Figure 4.2b). The presence of phases such as apatite, phlogopite, Ti-augite, and perovskite further suggests melting from a carbon-metasomatized source[43].

Magmatic water concentrations are typically highest in arc basalts (~ 4 wt%)[44], while MORB and OIB have lower water contents (0.03 – 1 wt%)[45,46]. Magmatic water from BSU with Ol+Cpx yield the highest magmatic water concentrations (1.73-2.99 wt%, Supplementary Table 3), while BSU with phlogopite are lower (0.62-1.84 wt% H_2O)[47,48]. This is an important distinction because OH in Cpx has not been calibrated for magmas with hydrous phases, thus it is likely that even the phlogopite bearing units have more than 1.84 wt% H_2O. Nonetheless, Bermuda is derived from a volatile rich source, with up to 3 wt% water and CO_2.

Like with the major and trace element data, radiogenic Pb-Sr-Nd-Hf identifies two different mantle sources for Bermuda. BSS trends toward DM (Figure 4.3), with less radiogenic $^{206}Pb/^{204}Pb$, $^{207}Pb/^{204}Pb$, and $^{208}Pb/^{204}Pb$, and radiogenic $^{143}Nd/^{144}Nd$ and $^{176}Hf/^{177}Hf$. BSU shows similarities with HIMU, seen in highly radiogenic $^{206}Pb/^{204}Pb$, and $^{208}Pb/^{204}Pb$, and less radiogenic $^{87}Sr/^{86}Sr$, $^{143}Nd/^{144}Nd$, and $^{176}Hf/^{177}Hf$. $^{206}Pb/^{204}Pb$ is more enriched than St. Helena, the Atlantic HIMU end-member, and on par with values from Mangaia, the Pacific HIMU end-member. However, the $^{207}Pb/^{204}Pb$ values are significantly lower, resulting in a shallow, young geochron of 179 ± 140 Ma. While the error on the $^{206}Pb/^{207}Pb$ geochron is very large, it suggests that the mantle source for Bermuda is related to the newly formed Atlantic lithosphere.

Compared with the classic HIMU end-members, ΣNd_0 of BSU is within the same range (4.02-4.64, Figure 4.3d). However, ΣHf is more radiogenic than HIMU (average ΣHf of 3.68 for Mangaia and 3.59 for St. Helena versus 6.98 for BSU), falling much closer to the Nd-Hf mantle array[49]. $^{87}Sr/^{86}Sr$ for BSU is slightly more radiogenic than the classic HIMU composition (Figure 3).

Pb isotopes in the classic HIMU mantle are too radiogenic to come from an undifferentiated mantle or typical mantle peridotite[38], due to incompatibility of U and yet the high U/Pb (μ) ratio in the HIMU mantle. Thus HIMU has been best explained by recycling oceanic crust[2]. The recycling of incompatible elements is key for producing HIMU compositions, and a new hypothesis suggests that the HIMU signature comes from the binary mixing of carbonatitic silicate melts and DM[50]. These carbonatitic silicate melts are small degree melts from subducted oceanic lithosphere that incorporated marine carbonates and are then stored in the Transition Zone[50,51]. These incompatible element enriched carbonated silicate melts interact with peridotite mantle and produces silica under-saturated, alkali melts with metasomatic phases such as clinopyroxene and phlogopite[51]. Globally, OIBs trending towards the classic HIMU mantle are the most silica under-saturated, and the highest $^{206}Pb/^{204}Pb$ from Mangaia melt inclusions are associated with carbonate "globules", suggesting a link between CO_2 in the mantle source and the HIMU composition[43,51,52].

The most distinguishing feature of Bermuda is the high $^{206}Pb/^{204}Pb$ with low $^{207}Pb/^{204}Pb$ (Figure 4.3), and determining what can account for this potential shallow geochron is important for potentially defining Bermuda as a new mantle end-member, HIMU-2. First, there is no correlation between the trend of $^{206}Pb/^{204}Pb$ with $^{143}Nd/^{144}Nd$, $^{176}Hf/^{177}Hf$, or $^{87}Sr/^{88}Sr$, which does not support the Bermuda 206/207 trend being the product of mantle mixing. To test the plausibility of a young, enriched source we "aged" the lowest $^{206}Pb/^{204}Pb$ composition (19.965) for 200 Ma,

and were able to produce a $^{206}Pb/^{204}Pb$ value of 21.8 with a μ of 60 and a U/Pb ratio of 0.9. While the needed μ to get the highly radiogenic $^{206}Pb/^{204}Pb$ is high, it is not unreasonable. BSU has a range of μ of 35-52, with an average μ of 42. Compared to the classic HIMU, Bermuda is more enriched, as Mangaia has an average μ of 34 and St. Helena has a μ of 39 (Supplementary Figure 4.3). Not only that, Bermuda is more enriched with Pb and U than the HIMU end-members (average of 5 ppm Pb and 3 ppm U for Bermuda versus an average of 2 ppm Pb and 1 ppm U for Mangaia and St. Helena). If the source of Bermuda is approximately 200 Ma, then the average isotopic composition of the source would be $^{206}Pb/^{204}Pb$ 19.241, $^{207}Pb/^{204}Pb$ 15.574, $^{208}Pb/^{204}Pb$ 38.500, $^{176}Hf/^{177}Hf$ 0.28296, $^{143}Nd/^{144}Nd$ 0.51273, $^{87}Sr/^{88}Sr$ 0.70300.

Determining the source for our newly defined HIMU-2 remains difficult. CO_2 is necessary to produce silica under-saturation, and the recycled material needs to be enriched in U. Recycling black shales are rich in U and C and thus could partially explain the isotopic signatures of Bermuda. Mixing average black shale and MORB compositions can produce U and Pb compositions needed for the new HIMU-2 (Supplementary Figure 4.4), however such a mixture cannot adequately explain the $^{143}Nd/^{144}Nd$ and $^{176}Hf/^{177}Hf$ compositions of Bermuda. Modeling the recycling of other high U sources can also produce the $^{206}Pb/^{207}Pb$ signatures of Bermuda in a short, 200 Ma storage time, but still fail to produce the $^{143}Nd/^{144}Nd$ and $^{176}Hf/^{177}Hf$ compositions. We aged Atlantic MORB with high μ, as well as a variety of enriched peridotites, and while we could not reproduce all of the isotopic systems, we determined that the distinguishing feature of Bermuda is a young, high μ source.

Bermuda is likely the product of the recent recycling of U and C rich sediments, such as carbonates or black shales, which is stored in the upper-transition zone and/or lower portion of the upper mantle. These recycled materials aided in the production of carbon rich metasomatic fluids

that interacted with the peridotite mantle. Even though CO_2 can significantly decrease the solidus, olivine crystallization temperatures suggest that the thermal source of Bermuda was not a mantle plume. Geophysical evidence suggest Bermuda melting was triggered by EDC, and our geochemical data support this. Not only were these magmas the product of cool temperatures in the upper mantle, the 4 My of melting is not recorded in a particular stratigraphic order in the core. The association of alternating BSU and BSS could be the product of the convecting cell sampling various chemical domains in the mantle, such that the BSU sample deeper, carbonated HIMU-2 source lithologies, and BSS sample upper mantle DM (Figure 4.4).

Bermuda proves to be an important location in the Atlantic. The geochemistry and stratigraphy of Bermuda is the first location that supports the geophysical evidence for EDC. The convecting cell samples a new mantle end-member, HIMU-2, which is likely the product of CO_2-metasomatism from young, recycled sediments. This further suggests that the heterogeneous nature of the mantle is constantly being refreshed with the input of subducted material.

References

1 Wilson, J. T. Mantle plumes and plate motions. *Tectonophysics* **19**, 149-164 (1973).
2 Hofmann, A. Sampling mantle heterogeneity through oceanic basalts: isotopes and trace elements. *Treatise on geochemistry* **2**, 568 (2003).
3 Hofmann, A. W. & White, W. M. Mantle plumes from ancient oceanic crust. *Earth and Planetary Science Letters* **57**, 421-436 (1982).
4 Hart, S. R. Heterogeneous mantle domains: signatures, genesis and mixing chronologies. *Earth and Planetary Science Letters* **90**, 273-296 (1988).
5 Anderson, D. L. & King, S. D. Driving the Earth machine? *Science* **346**, 1184-1185 (2014).
6 Lustrino, M. How the delamination and detachment of lower crust can influence basaltic magmatism. *Earth-Science Reviews* **72**, 21-38 (2005).
7 King, S. D. & Anderson, D. L. Edge-driven convection. *Earth and Planetary Science Letters* **160**, 289-296 (1998).
8 Vogt, P. R. Bermuda and Appalachian-Labrador rises: Common non-hotspot processes? *Geology* **19**, 41-44 (1991).
9 Vogt, P. R. & Jung, W.-Y. Origin of the Bermuda volcanoes and the Bermuda Rise: history, observations, models, and puzzles. *Geological Society of America Special Papers* **430**, 553-591 (2007).

10 Morgan, W. & Crough, S. Bermuda hotspot and the Cape Fear Arch. *Eos Trans. AGU* **60**, 392-393 (1979).
11 Davies, G. F. Ocean bathymetry and mantle convection: 1. Large-scale flow and hotspots. *Journal of Geophysical Research: Solid Earth* **93**, 10467-10480 (1988).
12 Sleep, N. H. Monteregian hotspot track: A long-lived mantle plume. *Journal of Geophysical Research: Solid Earth* **95**, 21983-21990 (1990).
13 Morgan, W. J. Hotspot tracks and the early rifting of the Atlantic. *Tectonophysics* **94**, 123-139 (1983).
14 Duncan, R. A. Age progressive volcanism in the New England seamounts and the opening of the central Atlantic Ocean. *Journal of Geophysical Research* **89**, 9980-9990 (1984).
15 Müller, R. D., Royer, J.-Y. & Lawver, L. A. Revised plate motions relative to the hotspots from combined Atlantic and Indian Ocean hotspot tracks. *Geology* **21**, 275-278 (1993).
16 Benoit, M. H., Long, M. D. & King, S. D. Anomalously thin transition zone and apparently isotropic upper mantle beneath Bermuda: Evidence for upwelling. *Geochemistry, Geophysics, Geosystems* **14**, 4282-4291 (2013).
17 Rice, P. D., Hall, J. M. & Opdyke, N. D. Deep Drill 1972: a paleomagnetic study of the Bermuda Seamount. *Canadian Journal of Earth Sciences* **17**, 232-243 (1980).
18 Reynolds, P. & Aumento, F. Deep Drill 1972. Potassium-argon dating of the Bermuda drill core. *Canadian Journal of Earth Sciences* **11**, 1269-1273 (1974).
19 Williamson, M., Villeneuve, M. & Blasco, S. in *AGU Fall Meeting Abstracts.* 0646.
20 Pearce, J. A. & Peate, D. W. Tectonic implications of the composition of volcanic arc magmas. *Annual Review of Earth and Planetary Sciences* **23**, 251-286 (1995).
21 Janney, P. E. & Castillo, P. R. Geochemistry of the oldest Atlantic oceanic crust suggests mantle plume involvement in the early history of the central Atlantic Ocean. *Earth and Planetary Science Letters* **192**, 291-302 (2001).
22 Sobolev, A. V. *et al.* The amount of recycled crust in sources of mantle-derived melts. *Science* **316**, 412-417 (2007).
23 Putirka, K. D., Perfit, M., Ryerson, F. & Jackson, M. G. Ambient and excess mantle temperatures, olivine thermometry, and active vs. passive upwelling. *Chemical Geology* **241**, 177-206 (2007).
24 Herzberg, C. & Asimow, P. D. Petrology of some oceanic island basalts: PRIMELT2. XLS software for primary magma calculation. *Geochemistry, Geophysics, Geosystems* **9** (2008).
25 Lee, C.-T. A., Luffi, P., Plank, T., Dalton, H. & Leeman, W. P. Constraints on the depths and temperatures of basaltic magma generation on Earth and other terrestrial planets using new thermobarometers for mafic magmas. *Earth and Planetary Science Letters* **279**, 20-33 (2009).
26 Wan, Z., Coogan, L. A. & Canil, D. Experimental calibration of aluminum partitioning between olivine and spinel as a geothermometer. *American Mineralogist* **93**, 1142-1147 (2008).
27 Coogan, L., Saunders, A. & Wilson, R. Aluminum-in-olivine thermometry of primitive basalts: Evidence of an anomalously hot mantle source for large igneous provinces. *Chemical Geology* **368**, 1-10 (2014).
28 Dasgupta, R., Hirschmann, M. M. & Smith, N. D. Partial melting experiments of peridotite+ CO2 at 3 GPa and genesis of alkalic ocean island basalts. *Journal of Petrology* **48**, 2093-2124 (2007).

29 Eggler, D. H. The effect of CO< 2) upon partial melting of peridotite in the system Na< 2) O-CaO-Al< 2) O< 3)-MgO-SiO< 2)-CO< 2) to 35 kb, with an analysis of melting in a peridotite-H< 2) O-CO< 2) system. *American Journal of Science* **278**, 305-343 (1978).
30 Hirose, K. Partial melt compositions of carbonated peridotite at 3 GPa and role of CO~ 2 in alkali-basalt magma generation. *Geophysical Research Letters* **24**, 2837-2840 (1997).
31 Dasgupta, R., Hirschmann, M. M. & Withers, A. C. Deep global cycling of carbon constrained by the solidus of anhydrous, carbonated eclogite under upper mantle conditions. *Earth and Planetary Science Letters* **227**, 73-85 (2004).
32 Kogiso, T., Hirose, K. & Takahashi, E. Melting experiments on homogeneous mixtures of peridotite and basalt: application to the genesis of ocean island basalts. *Earth and Planetary Science Letters* **162**, 45-61 (1998).
33 Yaxley, G. M., Green, D. H. & Kamenetsky, V. Carbonatite metasomatism in the southeastern Australian lithosphere. *Journal of Petrology* **39**, 1917-1930 (1998).
34 Kogiso, T., Hirschmann, M. M. & Frost, D. J. High-pressure partial melting of garnet pyroxenite: possible mafic lithologies in the source of ocean island basalts. *Earth and Planetary Science Letters* **216**, 603-617 (2003).
35 Dasgupta, R. *et al.* Carbon-dioxide-rich silicate melt in the Earth/'s upper mantle. *Nature* **493**, 211-215 (2013).
36 Foley, S. *et al.* The composition of near-solidus melts of peridotite in the presence of CO 2 and H 2 O between 40 and 60 kbar. *Lithos* **112**, 274-283 (2009).
37 Mallik, A. & Dasgupta, R. Reactive infiltration of MORB-eclogite-derived carbonated silicate melt into fertile peridotite at 3 GPa and genesis of alkalic magmas. *Journal of Petrology* **54**, 2267-2300 (2013).
38 Dasgupta, R. & Hirschmann, M. M. The deep carbon cycle and melting in Earth's interior. *Earth and Planetary Science Letters* **298**, 1-13 (2010).
39 Kerrick, D. & Connolly, J. Metamorphic devolatilization of subducted oceanic metabasalts: implications for seismicity, arc magmatism and volatile recycling. *Earth and Planetary Science Letters* **189**, 19-29 (2001).
40 Thomsen, T. B. & Schmidt, M. W. Melting of carbonated pelites at 2.5–5.0 GPa, silicate–carbonatite liquid immiscibility, and potassium–carbon metasomatism of the mantle. *Earth and Planetary Science Letters* **267**, 17-31 (2008).
41 Karato, S. I., Bercovici, D., Leahy, G., Richard, G. & Jing, Z. The Transition-Zone Water Filter Model for Global Material Circulation: Where Do We stand? *Earth's Deep Water Cycle*, 289-313 (2006).
42 Dasgupta, R., Hirschmann, M. M. & Dellas, N. The effect of bulk composition on the solidus of carbonated eclogite from partial melting experiments at 3 GPa. *Contributions to Mineralogy and Petrology* **149**, 288-305 (2005).
43 Saal, A., Hart, S., Shimizu, N., Hauri, E. & Layne, G. Pb isotopic variability in melt inclusions from oceanic island basalts, Polynesia. *Science* **282**, 1481-1484 (1998).
44 Plank, T., Kelley, K. A., Zimmer, M. M., Hauri, E. H. & Wallace, P. J. Why do mafic arc magmas contain~ 4wt% water on average? *Earth and Planetary Science Letters* **364**, 168-179 (2013).
45 Sobolev, A. V. & Chaussidon, M. H 2 O concentrations in primary melts from supra-subduction zones and mid-ocean ridges: implications for H 2 O storage and recycling in the mantle. *Earth and Planetary Science Letters* **137**, 45-55 (1996).

46 Hauri, E. SIMS analysis of volatiles in silicate glasses, 2: isotopes and abundances in Hawaiian melt inclusions. *Chemical Geology* **183**, 115-141 (2002).
47 Wade, J. A. *et al.* Prediction of magmatic water contents via measurement of H2O in clinopyroxene phenocrysts. *Geology* **36**, 799-802 (2008).
48 O'Leary, J. A., Gaetani, G. A. & Hauri, E. H. The effect of tetrahedral Al 3+ on the partitioning of water between clinopyroxene and silicate melt. *Earth and Planetary Science Letters* **297**, 111-120 (2010).
49 Vervoort, J. D., Patchett, P. J., Blichert-Toft, J. & Albarède, F. Relationships between Lu–Hf and Sm–Nd isotopic systems in the global sedimentary system. *Earth and Planetary Science Letters* **168**, 79-99 (1999).
50 Castillo, P. R. A proposed new approach and unified solution to old Pb paradoxes. *Lithos* **252**, 32-40 (2016).
51 Castillo, P. R. The recycling of marine carbonates and sources of HIMU and FOZO ocean island basalts. *Lithos* **216**, 254-263 (2015).
52 Jackson, M. G. & Dasgupta, R. Compositions of HIMU, EM1, and EM2 from global trends between radiogenic isotopes and major elements in ocean island basalts. *Earth and Planetary Science Letters* **276**, 175-186 (2008).
53 Kunk, M. J. & McAleer, R. 40 Ar/39 Ar age-spectrum data for hornblende, biotite, white mica, and K-feldspar samples from metamorphic rocks in the Great Smoky Mountains of North Carolina and Tennessee. Report No. 2331-1258, (US Geological Survey, 2011).
54 Mazza, S. E. *et al.* Volcanoes of the passive margin: The youngest magmatic event in eastern North America. *Geology* **42**, 483-486 (2014).
55 Gazel, E. *et al.* Lithosphere versus asthenosphere mantle sources at the Big Pine Volcanic Field, California. *Geochemistry, Geophysics, Geosystems* **13** (2012).
56 White, W. M., Albarède, F. & Télouk, P. High-precision analysis of Pb isotope ratios by multi-collector ICP-MS. *Chemical Geology* **167**, 257-270 (2000).
57 Batanova, V. G., Sobolev, A. V. & Kuzmin, D. V. Trace element analysis of olivine: high precision analytical method for JEOL JXA-8230 electron probe microanalyser. *Chemical Geology* **419**, 149-157 (2015).

Methods

$^{40}Ar/^{39}Ar$ ages were determined at the U.S. Geological Survey (USGS) in Reston, Virginia. Four phlogopite separates were prepared for rocks expected to be Eocene in age. Aliquots of these mineral separates were irradiated in the central thimble facility at the TRIGA reactor (GSTR) at the USGS in Denver, Colorado. The monitor mineral used in both packages was FCT-3 sanidine with an age of 27.79 Ma relative to MMhb-1 at 519.4 ± 2.5 Ma. Following irradiation the samples

were analyzed by the furnace-step heating methods on a MAP 216 mass spectrometer at the USGS in Reston, Virginia[53].

Alteration-free rock chips of sample matrices were selected under a stereoscope microscope, powdered in an alumina mill, and fluxed into homogeneous glass disks with ultrapure 34.83% $Li_2B_4O_7$ – 64.67% $LiBO_2$ – 0.5% LiBr flux from Spex® (certified <<1 ppm blank for all trace elements) in the Petrology Lab at Virginia Tech for EDS-XRF and Laser Ablation ICPMS analyses. Major element geochemistry was collected on a Panalytical EDS-XRF with a silicon detector at the Department of Geosciences at Virginia Tech[54]. The accuracy for USGS standard BHVO-2 (run as an unknown) was better than 1% for most major elements but Na_2O and P_2O_5 was only better than 8% within reported values. The average relative standard deviation for 10 replicates of BHVO-2 were <1% for all major elements except Na_2O and P_2O_5 which were <3%. Trace elements from fluxed glasses were collected with an Agilent 7500ce ICPMS coupled with a Geolas laser ablation system[55], with a He flow rate ~1 L/m – 5 Hz and an energy density per sample of ~ 7 – 10 J/cm2. LA-ICP-MS data was calibrated with fluxed glasses of USGS standards BHVO-2, BCR-2, BIR-1, and STM-1 using Ti from XRF as an internal standard. The average relative accuracy for 10 replicates of BHVO-2 (run as an unknown) was better than 5% for most trace elements except Sc, Cr, Rb, Y, Zr, Nb, Sn, Ta, Pb, Th, and U (better than 15%). The average precision for BHVO-2 was better 4% for all elements with the exception of Sc, Zn, Sn, and Tm (<13 %,).

Radiogenic isotope ratios were determined at the Center for Elemental Mass Spectrometry (CEMS), University of South Carolina (USC). Sample powders from the same aliquots used for major and trace elements were digested in sub-boiling Teflon-distilled 3:1 HF:HNO_3 (v/V) mixture, and the isotopes were analyzed on aliquots of a single digestion. Pb was separated on an

anion resin with HBr and HNO_3 acids. Sr and REE were separated from bulk rock washes of the Pb chemistry on a cation resin in HCl. Sr was further separated on Sr-spec resin and Nd on Ln-resin. A second round of Pb chemistry was conducted on samples digested in 6N HCl. Isotopic ratios for Pb, Nd, and Sr were obtained on a Neptune multi collector ICPMS at USC. Pb isotope ratios were determined by Tl-addition[56]. Standard NBS-981 was determined at $^{206}Pb/^{204}Pb$ = 16.933 ± 0.001, $^{207}Pb/^{204}Pb$ = 15.486 ± 0.001, $^{208}Pb/^{204}Pb$ = 36.682 ± 0.004 (2σ, n=10). Isotopic ratios for Nd were normalized to $^{146}Nd/^{144}Nd$ = 0.7219 and the Nd standard JNdi was measured at $^{143}Nd/^{144}Nd$ = 0.512094 ± 0.000009 (2σ, n=8). All Nd measurements are reported relative to JNdi $^{143}Nd/^{144}Nd$ = 0.512115. Isotopic ratios for Sr were normalized to $^{86}Sr/^{88}Sr$ = 0.1194 and replicate analyses of standard NBS-987 yielded $^{87}Sr/^{86}Sr$ = 0.710316 ± 0.000013 (2σ, n=7). All Sr measurements are reported relative to NBS-987 $^{87}Sr/^{86}Sr$ = 0.710250. USGS standards BCR-2 and BHVO-1 were run as unknowns. Full procedural blanks ran at Pb < 38pg, Sr < 80pg, and Nd < 10 pg. All radiogenic isotope ratios were age corrected to initial eruptive values at 30 Ma.

High precision olivine and spinel mineral chemistry was collected at the University of Joseph Fourier, Grenoble France on a JEOL JXA-8230 Superprobe using a focused beam (~1 μm) of 25 kV and 900 nA[57]. We analyzed the San Carlos olivine standard at regular intervals during each analysis to correct for instrumental drift. Clinopyroxene phenocrysts were analyzed at Virginia Tech on a Cameca SX-50 Electron Microprobe with a beam strength of 20 nA and 15 kV. Double polished clinopyroxene grains were analyzed for OH concentrations on a Magna IR Spectrometer at James Madison University.

Figure 4.1

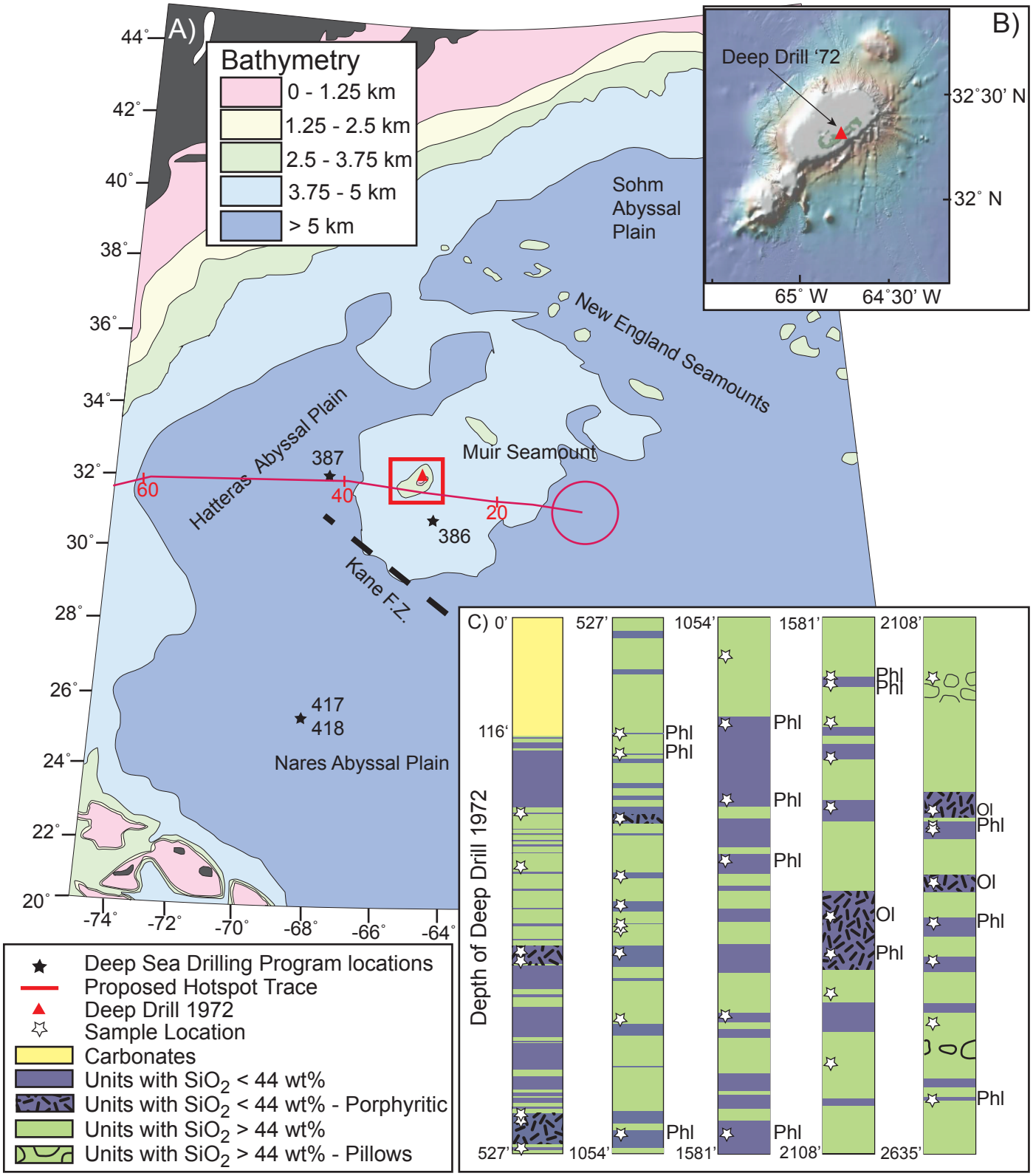
A)
Bathymetry
0 - 1.25 km
1.25 - 2.5 km
2.5 - 3.75 km
3.75 - 5 km
> 5 km
Sohm Abyssal Plain
New England Seamounts
Hatteras Abyssal Plain
Muir Seamount
Kane F.Z.
Nares Abyssal Plain
387
386
417
418
60
40
20
44˚
42˚
40˚
38˚
36˚
34˚
32˚
30˚
28˚
26˚
24˚
22˚
20˚
-74˚
-72˚
-70˚
-68˚
-66˚
-64˚
B)
Deep Drill '72
32˚30' N
32˚ N
65˚ W
64˚30' W
C)
Depth of Deep Drill 1972
0'
116'
527'
1054'
1581'
2108'
2635'
Phl
Ol
Deep Sea Drilling Program locations
Proposed Hotspot Trace
Deep Drill 1972
Sample Location
Carbonates
Units with SiO2 < 44 wt%
Units with SiO2 < 44 wt% - Porphyritic
Units with SiO2 > 44 wt%
Units with SiO2 > 44 wt% - Pillows

Figure 4.1: (Previous Page) Geologic map and core log for Bermuda. A) Bathymetric map of the northwestern Atlantic Ocean based on Vogt and Jung (2007) highlighting Bermuda and the Bermuda Rise. The Bermuda platform is outlined in red, shown in detail in B). The predicted W-E hotspot track[14] is shown as a red line. B) Detailed bathymetry of the Bermuda Rise and the location of the Deep Drill 1972. C) Sketch of the Bermuda core stratigraphy, based on core log from Dalhouise University. Original core log corresponds to physical markings on the core, all given in inches and feet (i.e., B1873 was collected at 1873' depth). Locations where olivine and phlogopite phenocrysts have been currently observed are marked.

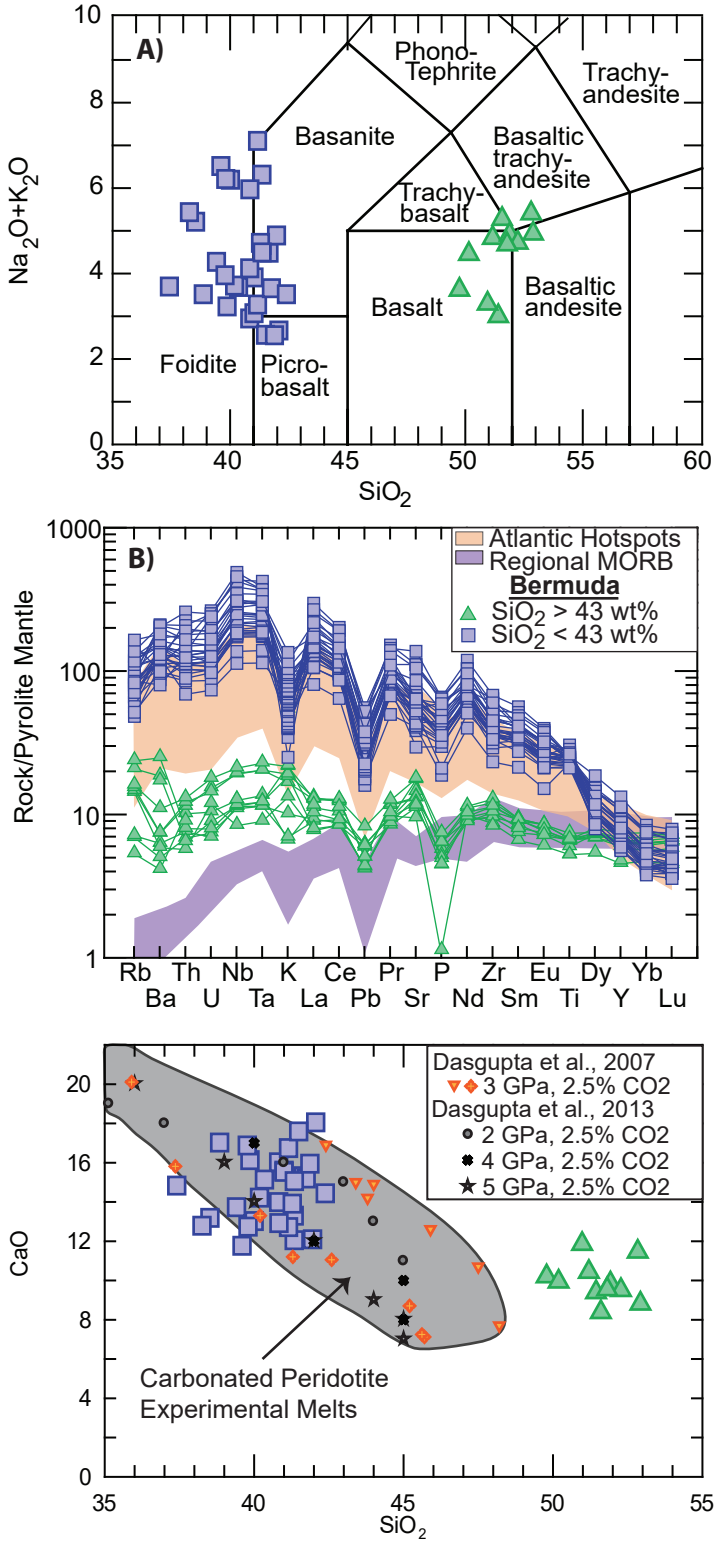

Figure 4.2: Bulk rock geochemistry for Bermuda. A) TAS diagram showing silica under-saturated alkaline units and silica saturated units. B) Primitive mantle[53] normalized trace element compositions for Bermuda compared with Atlantic Ocean Island basalt (OIB) magmatism (from GEOROC database) and local MORB (23º-33ºN)[21]. C) Comparison of CaO and SiO_2 compositions from Bermuda, with experimental data from melting of carbonated peridotite[28,35].

Figure 4.3

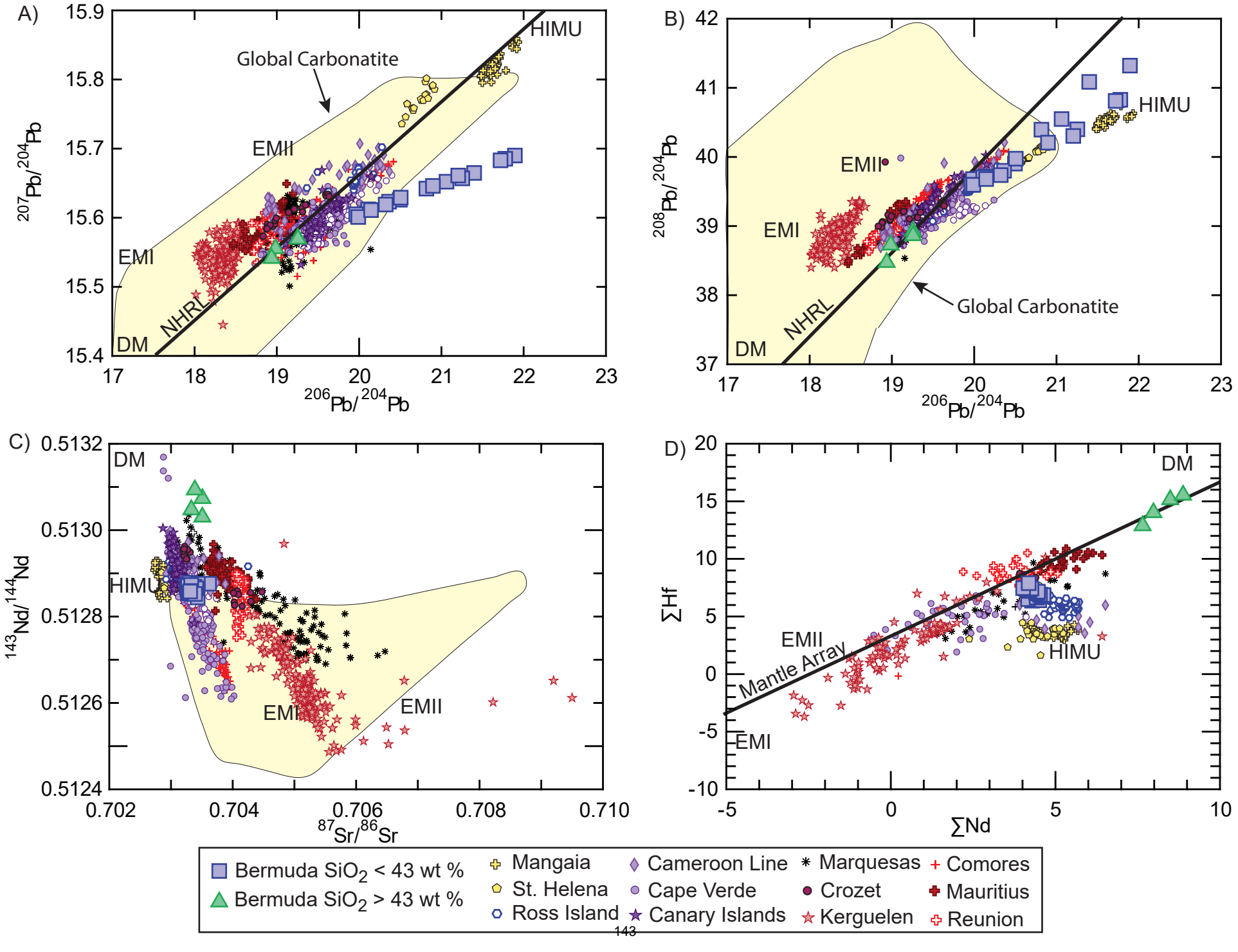
A)
HIMU
Global Carbonatite
EMII
EMI
NHRL
DM
$^{207}Pb/^{204}Pb$
$^{206}Pb/^{204}Pb$
B)
HIMU
EMII
EMI
NHRL
DM
Global Carbonatite
$^{208}Pb/^{204}Pb$
$^{206}Pb/^{204}Pb$
C)
DM
HIMU
EMI
EMII
$^{143}Nd/^{144}Nd$
$^{87}Sr/^{86}Sr$
D)
DM
EMII
Mantle Array
HIMU
EMI
ΣHf
ΣNd
Bermuda SiO_2 < 43 wt %
Bermuda SiO_2 > 43 wt %
Mangaia
St. Helena
Ross Island
Cameroon Line
Cape Verde
Canary Islands
Marquesas
Crozet
Kerguelen
Comores
Mauritius
Reunion

Figure 4.3: (Previous Page) Radiogenic isotopic data for Bermuda. Compared with Mangaia, St. Helena, Ross Island, Cameroon Line, Cape Verde, Canary Islands, Marquesas, Crozet, Kerguelen, Comores, Mauritius, and Reunion OIBs, data obtained from the GEOROC database. A) $^{207}Pb/^{204}Pb$ vs. $^{206}Pb/^{204}Pb$ showing shallow slope for BSU, with $^{206}Pb/^{204}Pb$ on par with Mangaia and St. Helena. B) $^{208}Pb/^{204}Pb$ vs. $^{206}Pb/^{204}Pb$ showing enriched $^{208}Pb/^{204}Pb$ for the high μ BSU samples. C) $^{143}Nd/^{144}Nd$ vs. $^{87}Sr/^{88}Sr$ showing near consistent $^{87}Sr/^{88}Sr$ for Bermuda with BSS having more radiogenic Nd. D) ΣHf vs. ΣNd showing BSU with radiogenic Hf plotting close to the mantle array[49]. NHRL = Northern Hemisphere Reference Line, EMI/II = Enriched Mantle I/II, DM = Depleted Mantle, HIMU = Classic definition of high $^{238}U/^{204}Pb$, HIMU-2 = new end-member as defined by this study, or young HIMU.

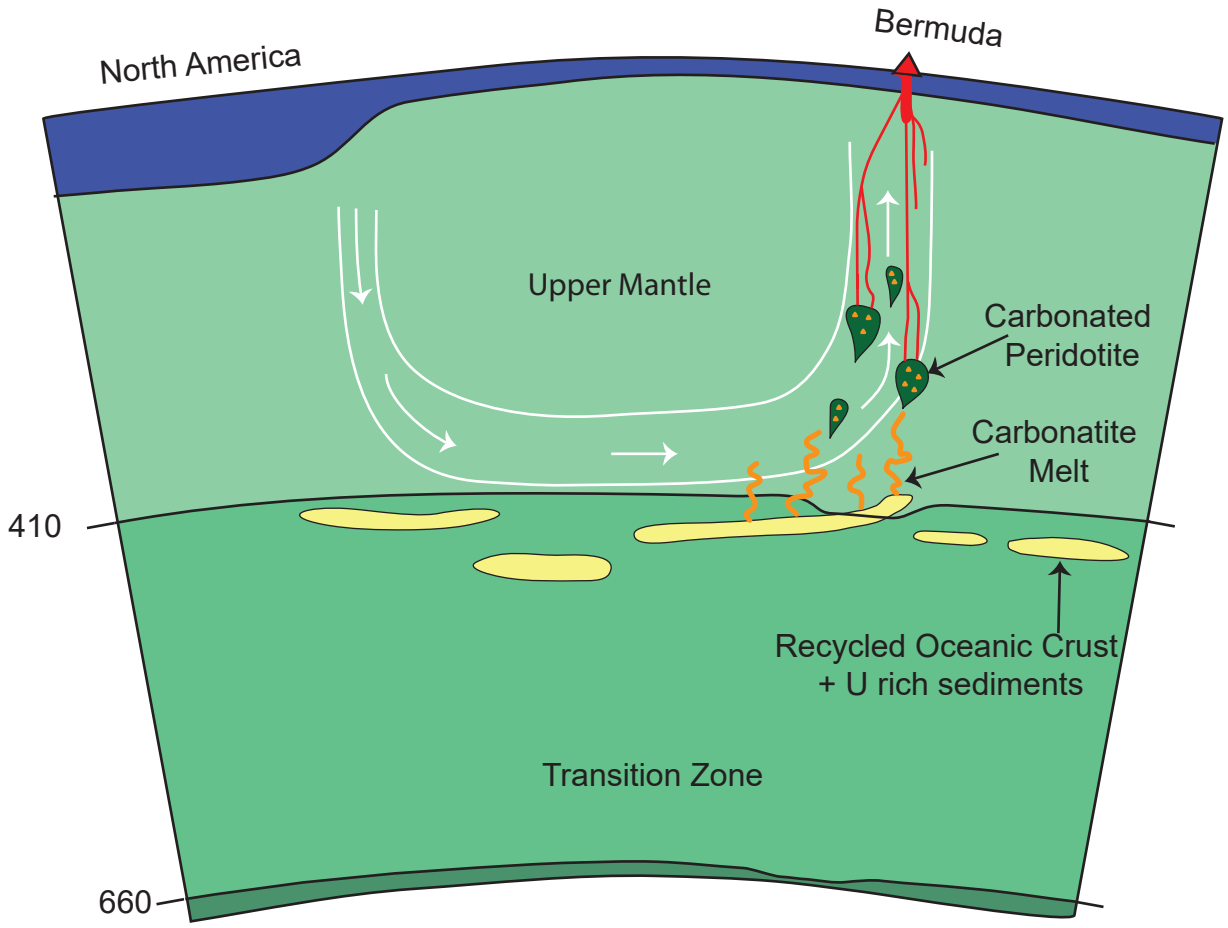

Figure 4.4: Schematic model to explain Bermuda volcanism as a produce of edge driven convection[7]. White lines and arrows represent convecting cell from EDC, which samples both the carbonated peridotite and depleted upper mantle. Carbonated peridotite is the product of recycled oceanic crust plus sediments melting to a carbonatitic metasomatized fluid that interacts with the peridotite. Depressions in the 410 km and 660 km are not drawn to scale, but approximate the observations from Benoit et al.[16].

Chapter 4

Table 1

SampleID	Depth	Phenocrysts	Age (Ma)	SiO2	TiO2	Al2O3	Fe2O3	MnO	MgO
B193	193			40.82	4.81	9.94	13.08	0.162	9.8
B259	259			51.54	1.48	16.52	7.43	0.151	7.8
B322	322			42.06	4.54	9.42	11.72	0.182	10.74
B328	328	Clinopyroxene		41	4.93	11.23	13.02	0.205	8.07
B486	486	Clinopyroxene		41.64	4.71	12.2	12.8	0.215	7.8
B490	490			41.34	4.93	11.68	13.46	0.162	8.25
B518	518	Clinopyroxene		40.35	4.68	11.05	13.83	0.171	9.42
B661	661	Phlogopite		40.18	5.48	13.29	14.73	0.219	5.98
B703	703	Phlogopite, apatite, clinopyroxene	30	41.34	4.83	15.3	11.27	0.273	4.69
B720	720	Clinopyroxene		39.86	5.05	11.63	13.84	0.197	7.52
B781	781			39.41	5.12	12.51	14.1	0.247	7.41
B815	815			41	4.96	12.07	13.25	0.192	7.34
B830	830	Clinopyroxene		41.15	5	11.92	13.69	0.201	7.75
B831	831			51.14	1.3	15.89	8.96	0.146	5.58
B854	854			49.73	1.34	15.95	10.08	0.156	7.46
B926	926			51.86	1.31	15.83	9.2	0.149	6.11
B1036	1036	Phlogopite	34	37.41	6.1	11.84	14.89	0.2	7.57
B1081	1081			50.13	1.33	16.19	9.47	0.173	7.03
B1160	1160	Phlogopite		38.52	5.7	12.95	14.9	0.203	7.32
B1236	1236	Phlogopite		39.77	4.54	9.18	13.01	0.184	10.74
B1297	1297	Phlogopite, clinopyroxene		40.82	5.26	10.93	14.84	0.157	8.27
B1445	1445	Clinopyroxene		41.49	4.56	10.28	11.91	0.176	10.81
B1568	1568	Phlogopite		39.6	5.27	13.22	12.9	0.335	6.33
B1641	1641	Phlogopite, apatite, clinopyroxene	30	41.15	4.81	14.2	12.11	0.297	4.66
B1644	1644	Phlogopite, apatite, clinopyroxene		40	5.1	14.31	12.03	0.276	5.18
B1687	1687			51.38	1.05	15.51	7.55	0.137	9.52
B1720	1720			41.96	4.58	13.76	12.2	0.167	7.69
B1768	1768			41.28	4.72	12.86	12.87	0.22	7.32
B1873	1873	Olivine, clinopyroxene		41.74	4.44	10.45	13.15	0.208	9.76
B1908	1908	Phlogopite, apatite, clinopyroxene	30.37	39.8	5.05	14.24	12.26	0.271	5.19
B1943	1943			52.86	1.12	15.16	8.02	0.134	8
B2032	2032			52.21	1.36	15.78	8.78	0.139	6.93
B2166	2166			52.77	1.04	15.24	6.21	0.115	6.25

Chapter 4

Table 1

SampleID	Depth	Phenocrysts	Age (Ma)	SiO2	TiO2	Al2O3	Fe2O3	MnO	MgO
B2299	2299	Olivine, clinopyroxene		41.87	4.33	9.63	12.82	0.182	11.97
B2318	2318	Phlogopite, clinopyroxene		41.35	4.21	9.99	12.59	0.207	10.83
B2319	2319	Clinopyroxene		40.83	4.98	13.6	13.11	0.232	5.57
B2364	2364			44.61	3.09	5.96	13.66	0.163	20.28
B2406	2406	Phlogopite		38.26	5.39	12.08	14.33	0.221	7.23
B2443	2443			42.38	4.34	10.28	12.66	0.171	9.86
B2520	2520			50.92	1.19	16.37	8.69	0.149	7.03
B2580	2580	Phlogopite		38.85	5	13.54	13.76	0.272	6.34
B1644_6N HCl									
B1873_6N HCl									
B1908_6N HCl									
B703_6N HCl									

Chapter 4

Table 1

SampleID	CaO	Na2O	K2O	P2O5	Total	LOI	Sc	V	Cr	Co	Ni	Cu
B193	16.02	1.08	1.89	0.691	98.29	7.12	36.05	396.44	368.44	53.72	110.64	107.29
B259	8.43	4.65	0.62	0.152	98.773		38.12	243.46	339.66	41.14	124.69	48.13
B322	18.05	0.62	2.07	0.685	100.09	2.83	39.47	381.98	648.69	48.75	101.8	88.56
B328	15.59	2.38	1.54	0.816	98.78	3.5	30.24	416.36	210.82	49.51	85.14	131.93
B486	15.31	2.8	1.69	0.739	99.904		29.24	395.14	218.2	46.18	76.88	129.61
B490	13.3	2.41	2.26	0.766	98.56	4.26	28.97	395.05	252.01	51.44	104	122.77
B518	15.14	2.31	1.39	0.82	99.16	4.15	31.16	417.74	371.5	55.62	103.99	137.74
B661	14.22	1.14	2.59	0.921	98.75		23.45	381.14	3.01	41.67	27.28	36.21
B703	12.05	5.31	0.99	1.249	97.3	4.64	19.92	392.84	5.84	28.62	30.62	19.95
B720	16.13	1.41	1.84	0.897	98.37	4.69	26.65	440.2	129.12	59.15	250.27	146.6
B781	13.73	3.56	0.72	1.237	98.04	5.86	25.69	438.67	92.25	51.91	102.87	113.15
B815	15.53	1.59	1.5	0.91	98.34	4.52	26.45	429.15	131.04	50.02	93.2	157.82
B830	16.74	0.57	2.72	0.73	100.471		28.85	419.88	152.04	49.69	80.11	119.5
B831	10.48	4.54	0.29	0.117	98.44	3.25	37.23	237.77	274.14	40.29	118.75	53.85
B854	10.25	3	0.63	0.091	98.69	2.88	38.31	248.48	296.92	43.34	136.41	76.6
B926	9.89	4.38	0.53	0.101	99.36		38.39	237.41	288.01	42.34	114.33	69.62
B1036	14.83	2.57	1.14	0.69	97.24	7.32	28.97	475.76	50.97	53.32	113.42	114.23
B1081	9.98	4.26	0.2	0.133	98.9	3.25	37.03	246.89	299.29	41.79	110.83	87.58
B1160	13.19	2.22	2.99	0.968	98.961		23.42	446.57	13.44	47.8	60.58	68.32
B1236	16.87	1.56	2.41	0.816	99.08	5.93	29.41	390.58	495.82	56.54	165.33	127.82
B1297	13.99	2.45	1.68	0.611	99.008		31.17	409.7	263.29	52.94	110.76	162.7
B1445	17.59	1.42	1.17	0.675	100.08	2.72	31.45	372.9	484.82	55.04	210.99	91.91
B1568	11.77	2.61	3.89	1.215	97.14		24.56	412.59	4.79	42.07	41.8	134.93
B1641	12.72	5.33	1.75	1.089	98.116		20.02	427.97	2.43	31.49	19.82	52
B1644	13.02	5.02	1.16	1.353	97.45	4.65	17.45	431.66	9.6	33.26	27.47	71.26
B1687	9.44	2.83	0.19	0.012	97.62	5.93	29.33	207.76	553.6	40.21	223.52	56.4
B1720	12.1	2.89	2	0.385	97.73	6.51	25.36	408.96	216.21	51.89	116.8	100.72
B1768	13.91	3.1	1.62	0.952	98.85		29.26	467.23	153.62	47.32	77.97	74.46
B1873	15.19	2.01	1.66	0.808	99.416		32.08	373.14	509.34	52.82	128.97	115.1
B1908	12.74	4.9	1.3	1.312	97.06	4.82	16.69	450.76	7.47	44.91	272.69	64.85
B1943	8.86	4.51	0.42	0.073	99.16		35.78	264.47	645.11	47.87	207.53	65.66
B2032	9.55	4.17	0.55	0.131	99.6		37.5	220.68	331.45	37.57	116.47	70.23
B2166	11.51	3.84	1.56	0.092	98.63	3.45	28.22	215.37	505.07	29.8	127.28	54.65

Chapter 4

Table 1

SampleID	CaO	Na2O	K2O	P2O5	Total	LOI	Sc	V	Cr	Co	Ni	Cu
B2299	15.95	1.35	1.23	0.63	99.96	1.56	26.95	379.01	715.31	61.33	236.13	148.19
B2318	15.06	1.7	2.8	0.432	99.169		32.85	340.29	611.31	54.77	150.13	104.76
B2319	12.92	4.19	1.77	1.006	98.208		22.57	431.7	19.67	42.99	42.15	87
B2364	10.89	0.22	0.73	0.384	99.99		35.49	290.71	1241.06	94.7	525.29	77.24
B2406	12.79	2.09	3.34	1.104	96.84	6.88	20.06	430.67	42.33	51.9	143.89	98.33
B2443	14.44	1.42	2.11	0.655	98.32	3.81	25.05	366.72	520.9	54.58	183.73	127.09
B2520	11.9	2.93	0.38	0.106	99.67	2.94	28.79	222.35	344.1	46.4	276.93	74.23
B2580	17.02	2.34	1.19	1.338	99.7		22.66	435.01	6.73	43.3	45.97	94.99
B1644_6N HCl												
B1873_6N HCl												
B1908_6N HCl												
B703_6N HCl												

Chapter 4

Table 1

SampleID	Zn	Ge	Rb	Sr	Y	Zr	Nb	Mo	Sn	Ba	La
B193	119.44	2.45	33.78	828.06	29.47	360.82	118.59	0.03	1.11	838.34	83.36
B259	66.74	-	9.54	351.83	28.05	133.47	13.78	0.5	1.17	71.95	8.3
B322	106.54	2.36	42.34	1062.87	28.09	362.93	125.44	0.01	1.11	802.48	87.94
B328	120.29	2.34	47.74	1469.28	32.08	412.67	160.56	0	1.12	942.36	108.45
B486	98.54	-	71.22	1155.16	29.72	382.63	164.44	0.5	3.02	980.24	93.45
B490	129.04	2.03	60.69	1038.67	31.42	383.64	138.78	0.04	1.21	977.18	93.69
B518	119.78	1.9	48.00	1009.50	29.47	329.37	115.03	0.02	1.06	855.58	81.37
B661	129.12	-	50.76	858.54	36.71	508.88	182.17	0.5	3.72	526.17	97.73
B703	163.32	2.03	52.09	2206.25	45.34	669.27	319.41	0.01	1.59	1317.39	151.39
B720	129.05	2.2	36.08	1216.06	31.86	399.21	152.6	0.01	15.05	953.58	104.25
B781	145.44	2.35	39.51	1084.02	38.7	488.9	208.52	0.01	1.19	852.24	136.04
B815	122.3	2.44	28.82	1278.60	35.3	435.25	169.56	0.03	3.14	721.41	117.86
B830	102.76	-	49.42	1003.69	32.04	409.55	164.4	0.5	3.14	857.69	94.92
B831	81.08	1.56	4.24	285.22	29.45	109.48	7.45	0.01	1	41.24	5.97
B854	71.29	1.4	14.14	236.93	31.82	119.08	7.64	0	0.77	163.25	6.59
B926	69.98	-	12.44	260.95	28.07	108.35	7.5	0.5	0.63	121.57	5.11
B1036	120.77	2.18	39.55	912.46	28.52	417.92	141.93	0.03	3.17	959.36	89.08
B1081	81.14	2.01	4.12	345.62	27.13	101.13	7.18	0.01	0.54	32.8	5.78
B1160	119.42	-	70.00	1198.69	37.05	484.28	192.72	0.5	3.59	1069.43	109.34
B1236	118.24	2.68	66.35	955.97	30.18	392.07	125.35	-	-	805.82	99.91
B1297	112.91	-	47.32	583.88	29.96	384.65	127.74	0.5	3.73	788.29	75.12
B1445	107.14	2.71	45.56	1171.14	26.58	361.64	113.16	-	-	691.21	84.67
B1568	115.37	-	98.35	1261.92	34.38	471.18	202.84	0.51	3.5	1191.54	111.49
B1641	132.71	-	75.47	1702.68	48.29	626.39	298.67	0.5	3.09	981.96	133.32
B1644	145.57	3.02	58.26	2198.03	56.67	708.62	282.52	-	-	1331.36	191.57
B1687	69.69	1.21	3.17	187.25	19.45	90.31	8.21	-	-	27.1	7.2
B1720	109.77	2.05	63.76	804.30	23.91	242.88	74.09	-	-	816.68	52.01
B1768	147.59	1.57	62.63	1588.34	34.31	401.44	180.04	1.1	1.56	926.59	113.43
B1873	99.67	-	48.72	1209.35	29.21	368.17	140.74	0.5	2.69	742.86	81.99
B1908	167.74	2.9	56.90	2072.66	47.67	620.32	277.41	-	-	1383.79	172.99
B1943	87.83	2.42	7.24	381.62	27.44	118.04	10.91	-	-	52.88	8.55
B2032	72.62	-	9.18	259.51	27.68	126.32	12.68	0.5	1.6	48.8	8.49
B2166	64.5	2.2	22.97	228.90	20.2	86.45	8.29	-	-	112.29	7.47

Chapter 4

Table 1

SampleID	Zn	Ge	Rb	Sr	Y	Zr	Nb	Mo	Sn	Ba	La
B2299	111.51	2.37	38.60	759.86	24.25	304.3	89.84	-	-	624.04	67.91
B2318	93.06	-	91.82	1044.01	25.34	348.24	120.58	0.51	2.94	651.24	68.35
B2319	112.91	-	75.20	1335.78	37.9	473.85	227.32	0.5	3.31	1116.22	124.41
B2364	115.16	1.8	28.83	331.45	17.91	220.16	73.39	1.09	0.97	429.88	50.27
B2406	150.68	2.74	82.10	1272.32	37.66	523.01	200.39	-	-	1362.43	140.52
B2443	112.47	2.31	30.84	824.42	28.02	374.35	120.05	-	-	571.86	88.35
B2520	66.24	1.58	8.51	221.62	26.92	99.89	5.48	-	-	38.55	4.97
B2580	120.75	-	53.99	2722.34	45.12	554.12	252.57	0.5	3.34	751.28	162.07
B1644_6N HCl											
B1873_6N HCl											
B1908_6N HCl											
B703_6N HCl											

Chapter 4

Table 1

SampleID	Ce	Pr	Nd	Sm	Eu	Gd	Dy	Ho	Er	Tm	Yb
B193	158.92	19.32	73.21	13.32	3.78	10.5	6.85	1.16	2.57	0.32	1.92
B259	21.19	3.17	14.19	3.78	1.3	4.83	5.02	1.05	2.83	0.4	2.77
B322	165.45	20.06	75.69	13.29	3.66	10.33	6.49	1.12	2.32	0.28	1.8
B328	199.76	23.48	88.18	14.88	4.15	11.5	7.12	1.23	2.84	0.36	2.32
B486	193.82	22.26	80.89	13.55	4.02	11.34	6.77	1.14	2.59	0.34	2.03
B490	179.39	21.44	80.29	13.69	3.92	10.61	6.61	1.2	2.78	0.36	1.98
B518	158.84	19.27	73.33	13.22	3.91	10.62	6.55	1.15	2.6	0.33	1.92
B661	202.81	24.36	92.15	15.96	4.68	13.32	8.32	1.4	3.27	0.4	2.39
B703	257.68	28.16	99.00	16.75	4.97	13.83	9.65	1.7	3.95	0.57	3.32
B720	194.65	23.02	86.25	14.88	4.25	11.34	7.19	1.28	2.8	0.36	2.22
B781	248.71	28.73	104.45	17.34	4.88	13.41	8.97	1.49	3.34	0.43	2.7
B815	210.38	24.98	95.11	15.97	4.23	12.58	7.74	1.42	3.06	0.4	2.51
B830	192.39	22.42	83.84	14.03	4.21	12.02	7.09	1.19	2.98	0.37	2.07
B831	14.59	2.37	11.84	3.71	1.2	4.13	5.06	1.06	2.9	0.43	3.02
B854	15.25	2.41	12.08	3.71	1.18	4.84	5.4	1.13	3.06	0.49	3.26
B926	14	2.21	11.05	3.26	1.14	4.38	4.84	1.05	3.02	0.41	2.9
B1036	173.14	20.66	79.84	13.59	3.87	10.69	6.67	1.13	2.41	0.32	1.91
B1081	15.34	2.36	11.37	3.44	1.09	3.92	4.58	1	2.66	0.4	2.79
B1160	222.55	26.02	96.70	16.41	4.78	13.72	8.11	1.37	3.34	0.41	2.47
B1236	202.63	23.53	92.96	14.63	3.91	9.45	7.27	1.19	2.8	0.33	1.87
B1297	160.28	19	72.15	12.84	3.79	10.95	6.94	1.15	2.68	0.34	1.9
B1445	173.53	20.51	80.04	13.26	3.58	8.18	6.16	1.04	2.48	0.29	1.79
B1568	241.51	27.79	100.28	16.70	4.91	13.39	7.87	1.3	3.15	0.38	2.34
B1641	236.41	25.68	91.39	16.13	4.95	14.26	9.74	1.76	4.33	0.52	3.3
B1644	336.34	38.46	148.13	22.80	6.1	15.88	12.48	2.13	5.07	0.58	3.69
B1687	17.31	2.47	12.34	2.66	0.92	2.6	3.59	0.7	2.11	0.3	2.07
B1720	107.35	12.59	49.81	8.63	2.32	6.13	5.32	0.91	2.37	0.29	1.86
B1768	228.41	25.02	95.30	15.18	4.76	11.59	7.31	1.35	3.11	0.46	1.92
B1873	164.11	19.36	71.95	12.44	3.52	10.33	6.52	1.07	2.59	0.33	1.95
B1908	318.88	35.13	128.90	19.76	5.72	13.72	10.26	1.87	4.47	0.56	3.4
B1943	22.31	3.18	16.02	3.91	1.23	3.63	4.74	1.01	2.78	0.44	2.86
B2032	20.4	2.98	13.80	3.77	1.3	4.52	4.92	1.03	2.8	0.41	2.67
B2166	18.62	2.59	12.73	3.21	1.09	2.86	3.77	0.78	2.25	0.29	1.95

Chapter 4

Table 1

SampleID	Ce	Pr	Nd	Sm	Eu	Gd	Dy	Ho	Er	Tm	Yb
B2299	146.52	17.37	70.10	12.15	3.23	7.06	5.82	0.99	2.25	0.27	1.69
B2318	144.18	16.99	63.37	11.08	3.25	9.12	5.71	0.96	2.27	0.31	1.66
B2319	248.28	28.49	102.43	16.58	4.97	14.05	8.3	1.42	3.43	0.42	2.4
B2364	106.91	12.32	45.48	8.32	2.54	6.34	4.25	0.75	1.73	0.18	1.02
B2406	277.75	31.61	119.24	18.84	5.14	11.54	8.99	1.46	3.6	0.43	2.52
B2443	177.51	21.09	82.31	13.22	3.46	8.83	6.67	1.06	2.67	0.31	1.86
B2520	14.06	2.13	11.38	3.01	1.1	3.43	4.91	1.01	3.09	0.43	2.75
B2580	317.97	36.44	129.74	20.79	5.89	16.96	9.87	1.66	4.02	0.48	3.23
B1644_6N HCl											
B1873_6N HCl											
B1908_6N HCl											
B703_6N HCl											

Chapter 4

Table 1

SampleID	Lu	Hf	Ta	Pb	Th	U	$^{176}Hf/^{177}Hf$	2 σ	$^{176}Hf/^{177}Hf$ IN	Et Hf
B193	0.26	8.71	6.69	2.38	8.12	2.04	0.282979	0.000003		6.87
B259	0.44	3.05	0.84	1.22	1.03	0.36	0.283149	0.000006	0.28311	12.87
B322	0.26	8.51	7.03	2.99	8.84	2.33				
B328	0.28	9.24	8.70	4.22	11.06	2.77				
B486	0.29	8.09	8.98	4.85	10.11	2.76	0.282995	0.000004	0.282992	7.41
B490	0.27	8.69	7.45	4.60	9.35	2.52				
B518	0.26	7.92	6.50	2.74	8.18	2.03				
B661	0.34	11.10	10.76	5.26	10.15	2.77	0.282976	0.000004		6.75
B703	0.45	11.15	14.25	7.22	13.06	5.32	0.28298	0.000003		6.88
B720	0.31	8.58	8.44	4.54	10.97	2.75				
B781	0.36	9.60	10.70	5.54	15.59	3.80				
B815	0.37	9.24	9.18	4.87	12.54	3.05				
B830	0.31	9.03	9.13	3.21	9.85	2.55	0.282996	0.000005	0.282994	7.47
B831	0.48	2.82	0.42	0.64	0.60	0.14				
B854	0.48	2.77	0.45	0.92	0.63	0.16				
B926	0.46	2.60	0.45	0.65	0.51	0.18	0.283224	0.000006	0.283176	15.52
B1036	0.26	9.60	8.22	3.23	8.84	2.38				
B1081	0.44	2.29	0.42	0.62	0.54	0.15				
B1160	0.37	10.26	11.11	5.13	11.81	3.09	0.282965914	0.000003		6.4
B1236	0.29	9.12	7.03	4.76	10.43	2.29				
B1297	0.30	9.16	7.46	3.61	7.53	2.07	0.282993	0.000006	0.282991	7.37
B1445	0.29	9.50	6.39	3.23	8.73	2.17				
B1568	0.33	9.40	11.26	5.63	13.12	3.37				
B1641	0.50	10.80	13.60	7.81	10.67	4.83	0.282983	0.000004		6.99
B1644	0.53	13.12	15.59	7.46	20.45	5.07	0.282985	0.000003		7.08
B1687	0.30	2.08	0.50	0.92	0.80	0.21				
B1720	0.32	5.71	4.20	2.64	5.46	1.49				
B1768	0.33	7.86	10.06	7.72	11.61	3.12				
B1873	0.28	8.22	7.94	4.11	9.01	2.35	0.283008	0.000005	0.283005	7.89
B1908	0.48	11.21	13.68	7.41	16.47	5.08	0.282987	0.000003		7.15
B1943	0.45	2.93	0.61	0.89	0.99	0.38	0.283213	0.000004		15.12
B2032	0.43	3.06	0.75	0.75	0.96	0.29	0.283181	0.000004	0.283143	14.01
B2166	0.31	2.22	0.53	0.90	0.71	0.69				

Chapter 4

Table 1

SampleID	Lu	Hf	Ta	Pb	Th	U	$^{176}Hf/^{177}Hf$	2 σ	$^{176}Hf/^{177}Hf$ IN	Et Hf
B2299	0.26	7.65	5.13	3.18	6.75	1.74	0.282975	0.000003		6.7
B2318	0.24	7.99	6.87	3.36	7.05	1.97	0.282969	0.000005	0.282966	6.49
B2319	0.37	8.89	12.65	5.35	14.16	3.72	0.282965	0.000004		6.35
B2364	0.20	4.77	4.34	2.21	4.72	1.30				
B2406	0.34	11.20	10.64	6.37	15.05	3.88	0.282973	0.000004		6.64
B2443	0.28	9.04	6.88	3.08	8.91	2.16				
B2520	0.44	2.40	0.33	0.88	0.45	0.24				
B2580	0.45	10.58	13.38	8.30	17.74	4.52	0.282989	0.000004	0.282985	7.2
B1644_6N HCl										
B1873_6N HCl										
B1908_6N HCl										
B703_6N HCl										

Chapter 4

Table 1

$^{143}Nd/^{144}Nd$	2 σ	$^{143}Nd/^{144}Nd$ IN	Et Nd	E0 Nd	$^{87}Sr/^{86}Sr$	2 σ	$^{87}Sr/^{86}Sr$ IN	$^{206}Pb/^{204}Pb$	2 σ
0.512876	0.000005	0.512855	4.98	4.65	0.703436	0.000005	0.703385		
0.51303	0.000005	0.512925	8.11	7.65	0.70351	0.000008	0.703399	19.255	0.001
	7.64672147	0.512925	5.598493						
			5.5984925						
0.512857	0.000005	0.512837	4.64	4.27	0.703285	0.000007	0.703209	20.324	0.001
	4.27202041		3.8818816						
0.512876	0.000004	0.512855	4.99	4.64	0.703616	0.000009	0.703543	19.965	
0.51287	0.000004	0.51285	4.9	4.53	0.703277	0.000005	0.703248	21.719	
	4.52561066		4.1354718						
0.512844	0.000006	0.512824	4.39	4.02	0.703434	0.000006	0.703373	20.147	0.001
	4.01843016		3.6282913						
0.513093	0.000005	0.512977	9.12	8.88	0.703387	0.000008	0.703191	18.938	0.001
	8.87565885		6.6128535						
0.512869	0.000005	0.512849	4.88	4.51	0.703382	0.000008	0.70331	20.137	
0.512852	0.000006	0.512831	4.52	4.17	0.703346	0.000007	0.703246	19.991	0.001
0.512866	0.000005	0.512845	4.79	4.45	0.703274	0.000007	0.703219	20.506	
0.512864	0.000005	0.512846	4.8	4.4	0.703264	0.000012	0.703231	21.062	
0.512853	0.000006	0.512833	4.55	4.19	0.703275	0.000008	0.703225	21.206	0.001
0.512867	0.000005	0.512849	4.86	4.46	0.703266	0.000005	0.703232	20.818	
0.513073	0.000005				0.703508	0.000008		18.985	0.001
0.513047		0.51294	8.39	7.98	0.703332	0.000008	0.703187	19.257	0.001

Chapter 4

Table 1

$^{143}Nd/^{144}Nd$	2 σ	$^{143}Nd/^{144}Nd$ IN	Et Nd	E0 Nd	$^{87}Sr/^{86}Sr$	2 σ	$^{87}Sr/^{86}Sr$ IN	$^{206}Pb/^{204}Pb$	2 σ
0.512873	0.000007	0.512853	4.94	4.59	0.703264	0.000006	0.703201	20.363	
0.512852		0.512831	4.52	4.17	0.703391	0.000008	0.703283	20.110	0.001
0.512858	0.000005	0.512839	4.68	4.3	0.703312	0.000007	0.703242	19.986	
0.512865	0.000005	0.512846	4.81	4.42	0.703411	0.000007	0.703331	20.496	
0.512854	0.000006	0.512835	4.6	4.21	0.703295	0.000007	0.703271	20.898	0.001
0.512878	0.000005				0.703302			21.893	
0.512859	0.000004				0.703322			21.255	
0.512873	0.000005				0.703329			21.399	
0.512867	0.000005				0.703339			21.777	

Chapter 4

Table 1

SampleID	$^{207}Pb/^{204}Pb$	2 σ	$^{208}Pb/^{204}Pb$	2 σ	$^{206}Pb/^{204}Pb$ IN	$^{207}Pb/^{204}Pb$ IN	$^{208}Pb/^{204}Pb$ IN	μ
B193								
B259	15.570	0.001	38.923	0.002	18.958	15.555	38.645	19
B322								
B328								
B486	15.619	0.000	39.736	0.001	20.148	15.610	39.524	38
B490								
B518								
B661	15.605		39.596		19.803	15.598	39.401	35
B703	15.683		40.810		21.484	15.673	40.620	51
B720								
B781								
B815								
B830	15.611	0.001	39.680	0.002	19.902	15.599	39.369	53
B831								
B854								
B926	15.541	0.001	38.473	0.003	18.658	15.528	38.218	18
B1036								
B1081								
B1160	15.611		39.716		19.952	15.603	39.483	40
B1236								
B1297	15.601	0.000	39.595	0.001	19.815	15.593	39.385	38
B1445								
B1568								
B1641	15.629		39.974		20.314	15.620	39.834	42
B1644	15.652		40.547		20.848	15.642	40.263	47
B1687								
B1720								
B1768								
B1873	15.661	0.001	40.303	0.003	21.026	15.652	40.075	39
B1908	15.642		40.393		20.602	15.632	40.163	47
B1943	15.555	0.001	38.724	0.003				
B2032	15.569	0.001	38.860	0.003	18.861	15.550	38.436	26
B2166								

Chapter 4

Table 1

SampleID	$^{207}Pb/^{204}Pb$	2 σ	$^{208}Pb/^{204}Pb$	2 σ	$^{206}Pb/^{204}Pb$ IN	$^{207}Pb/^{204}Pb$ IN	$^{208}Pb/^{204}Pb$ IN	μ
B2299	15.623		39.799		20.194	15.615	39.582	37
B2318	15.612	0.001	39.705	0.002	19.929	15.603	39.492	39
B2319	15.603		39.680		19.772	15.593	39.412	47
B2364								
B2406	15.626		39.903		20.307	15.618	39.662	41
B2443								
B2520								
B2580	15.646	0.001	40.206	0.002	20.727	15.638	39.986	37
B1644_6N HCl	15.690		41.321		21.674	15.680	41.031	48
B1873_6N HCl	15.657		40.400		21.075	15.649	40.172	39
B1908_6N HCl	15.665		41.084		21.180	15.655	40.851	48
B703_6N HCl	15.685		40.827		21.542	15.674	40.636	51

Chapter 4
Table 2

Olivine ID	Fo	Na2O	Al2O3	CoO	ZnO	P2O5	CaO
B1873-mt2-4-avg1	88.3	0.013	0.034	0.021	0.010	0.003	0.347
B1873-mt2-4-avg2	88.4	0.011	0.033	0.021	0.010	0.003	0.348
B1873-mt2-6-avg	88.8	0.014	0.041	0.020	0.008	0.008	0.326
B1873-mt2-12-avg	84.9	0.011	0.029	0.024	0.009	0.009	0.398
B1873-mt2-15-avg	88.0	0.011	0.030	0.020	0.007	0.007	0.415
B1873-mt2-18-avg1	84.6	0.011	0.032	0.024	0.009	0.005	0.427
B1873-mt2-18-avg2	84.3	0.010	0.031	0.024	0.009	0.006	0.412
B1873-mt2-18-avg3	84.3	0.010	0.029	0.024	0.009	0.005	0.409
B1873-mt2-20 avg1	88.6	0.012	0.038	0.020	0.007	0.003	0.341
B1873-mt2-20 avg2	88.3	0.013	0.036	0.020	0.007	0.003	0.342
B1873-mt2-27-avg1	86.9	0.012	0.032	0.021	0.008	0.003	0.378
B1873-mt2-27-avg2	86.5	0.010	0.032	0.021	0.008	0.003	0.378
B1873-mt2-23-avg1	86.2	0.011	0.031	0.023	0.008	0.004	0.413
B1873-mt2-23-avg2	86.2	0.010	0.030	0.022	0.008	0.004	0.411
B1873-mt1-6-avg1	84.7	0.009	0.032	0.023	0.009	0.003	0.382
B1873-mt1-6-avg2	84.5	0.009	0.032	0.024	0.009	0.004	0.383
B1873-mt1-10-avg1	87.8	0.011	0.034	0.021	0.008	0.009	0.375
B1873-mt1-10-avg2	87.7	0.011	0.031	0.021	0.008	0.010	0.437
B1873-mt1-14-avg	84.5	0.009	0.029	0.024	0.010	0.004	0.420
B1873-mt1-37-avg	87.9	0.011	0.033	0.021	0.008	0.009	0.390
B1873-mt1-38-avg1	84.7	0.010	0.029	0.023	0.010	0.003	0.460
B1873-mt1-38-avg2	84.7	0.010	0.031	0.023	0.010	0.004	0.452
B1873-mt1-38-avg3	84.8	0.010	0.030	0.023	0.010	0.004	0.454
B1873-mt1-38-avg4	85.1	0.010	0.029	0.023	0.010	0.004	0.448
B2299-mt2-1 avg	86.1	0.008	0.033	0.023	0.008	0.009	0.507
B2299-mt2-5 avg	87.8	0.008	0.029	0.021	0.007	0.005	0.504
B2299-mt2-7 avg	87.2	0.010	0.028	0.022	0.008	0.006	0.486
B2299-mt2-10 avg1	87.8	0.010	0.031	0.021	0.007	0.004	0.473
B2299-mt2-10 avg2	87.9	0.009	0.032	0.021	0.007	0.003	0.483
B2299-mt2-12 avg1	86.8	0.010	0.034	0.022	0.009	0.008	0.493
B2299-mt2-12 avg2	86.6	0.009	0.031	0.022	0.009	0.006	0.489
B2299-mt2-12 avg3	86.7	0.009	0.031	0.022	0.009	0.006	0.492
B2299-mt2-12 avg4	86.6	0.010	0.029	0.022	0.009	0.007	0.496
B2299-mt1-1 avg	86.5	0.012	0.028	0.021	0.010	0.007	0.482
B2299-mt1-6 avg	84.8	0.011	0.034	0.024	0.010	0.008	0.489
B2299-mt1-15 avg	84.8	0.010	0.033	0.024	0.009	0.010	0.485
B2299-mt1-21 avg	88.1	0.011	0.033	0.020	0.007	0.006	0.458
B2299-mt1-22 avg	87.5	0.010	0.044	0.021	0.007	0.007	0.440
B2299-mt1-23 avg	88.0	0.011	0.031	0.020	0.007	0.003	0.475
B2299-mt1-24 avg	84.8	0.010	0.032	0.024	0.009	0.008	0.473
B2299-mt1-27 avg	86.0	0.010	0.032	0.022	0.008	0.005	0.497
B2299-mt1-28 avg	87.7	0.011	0.029	0.020	0.007	0.005	0.479

Chapter 4
Table 2

Olivine ID	TiO2	NiO	MnO	Cr2O3	MgO	FeO	SiO2	Total
B1873-mt2-4-avg1	0.027	0.204	0.193	0.088	50.40	11.85	42.61	105.80
B1873-mt2-4-avg2	0.026	0.203	0.193	0.069	50.26	11.80	42.55	105.53
B1873-mt2-6-avg	0.022	0.243	0.176	0.104	49.83	11.21	42.06	104.06
B1873-mt2-12-avg	0.031	0.166	0.251	0.067	45.85	14.52	40.31	101.67
B1873-mt2-15-avg	0.026	0.191	0.207	0.072	48.31	11.77	41.05	102.11
B1873-mt2-18-avg1	0.024	0.163	0.255	0.035	45.73	14.81	40.47	101.99
B1873-mt2-18-avg2	0.026	0.162	0.257	0.032	45.03	15.00	39.85	100.85
B1873-mt2-18-avg3	0.027	0.162	0.256	0.047	45.17	14.95	39.96	101.07
B1873-mt2-20 avg1	0.025	0.225	0.181	0.093	48.99	11.20	41.30	102.43
B1873-mt2-20 avg2	0.022	0.226	0.181	0.088	47.69	11.22	40.21	100.05
B1873-mt2-27-avg1	0.024	0.203	0.205	0.042	46.44	12.52	39.79	99.68
B1873-mt2-27-avg2	0.024	0.202	0.210	0.049	45.74	12.73	39.30	98.70
B1873-mt2-23-avg1	0.038	0.161	0.232	0.068	47.22	13.43	40.98	102.62
B1873-mt2-23-avg2	0.042	0.161	0.233	0.092	47.10	13.48	40.92	102.51
B1873-mt1-6-avg1	0.045	0.172	0.249	0.060	44.98	14.50	39.54	100.00
B1873-mt1-6-avg2	0.038	0.172	0.252	0.039	44.99	14.66	39.54	100.15
B1873-mt1-10-avg1	0.029	0.204	0.197	0.059	47.36	11.72	40.14	100.17
B1873-mt1-10-avg2	0.044	0.182	0.214	0.153	47.56	11.92	40.44	101.03
B1873-mt1-14-avg	0.031	0.166	0.259	0.019	45.34	14.87	40.03	101.21
B1873-mt1-37-avg	0.030	0.199	0.200	0.063	47.82	11.69	40.41	100.89
B1873-mt1-38-avg1	0.037	0.161	0.264	0.035	45.10	14.48	39.81	100.41
B1873-mt1-38-avg2	0.037	0.161	0.267	0.033	45.13	14.56	39.80	100.51
B1873-mt1-38-avg3	0.045	0.162	0.265	0.077	45.43	14.53	40.02	101.06
B1873-mt1-38-avg4	0.034	0.163	0.257	0.031	46.09	14.42	40.52	102.04
B2299-mt2-1 avg	0.032	0.194	0.227	0.049	46.13	13.34	39.99	100.55
B2299-mt2-5 avg	0.039	0.187	0.197	0.068	46.46	11.53	39.43	98.49
B2299-mt2-7 avg	0.023	0.191	0.212	0.038	48.52	12.68	41.67	103.89
B2299-mt2-10 avg1	0.029	0.186	0.201	0.039	47.91	11.84	40.73	101.48
B2299-mt2-10 avg2	0.032	0.185	0.201	0.049	47.86	11.81	40.70	101.40
B2299-mt2-12 avg1	0.040	0.198	0.221	0.040	48.19	13.12	41.60	103.98
B2299-mt2-12 avg2	0.039	0.197	0.220	0.032	47.46	13.10	40.96	102.56
B2299-mt2-12 avg3	0.039	0.197	0.220	0.036	47.61	13.10	41.07	102.85
B2299-mt2-12 avg4	0.039	0.197	0.222	0.034	47.41	13.14	40.92	102.53
B2299-mt1-1 avg	0.023	0.189	0.238	0.054	46.49	12.90	40.16	100.62
B2299-mt1-6 avg	0.027	0.196	0.249	0.034	45.11	14.43	39.73	100.35
B2299-mt1-15 avg	0.023	0.191	0.252	0.034	45.13	14.48	39.75	100.43
B2299-mt1-21 avg	0.022	0.199	0.193	0.040	47.50	11.47	40.27	100.24
B2299-mt1-22 avg	0.023	0.216	0.202	0.053	47.49	12.11	40.39	101.02
B2299-mt1-23 avg	0.027	0.197	0.194	0.085	47.57	11.55	40.37	100.55
B2299-mt1-24 avg	0.025	0.193	0.250	0.039	45.23	14.42	39.86	100.58
B2299-mt1-27 avg	0.025	0.199	0.227	0.029	46.14	13.37	40.20	100.77
B2299-mt1-28 avg	0.025	0.196	0.197	0.044	47.05	11.76	40.21	100.03

Chapter 4
Table 2

Spinel ID	SiO2	TiO2	Al2O3	Cr2O3	V2O3	FeO	MnO
B1873-mt2-4-sp1	0.037	3.623	13.529	37.800	0.200	32.903	0.369
B1873-mt2-4-sp2	1.248	3.592	11.752	34.247	0.161	32.966	0.276
B1873-mt2-6-sp1	0.057	3.031	15.676	39.716	0.175	26.738	0.203
B1873-mt2-12-sp1	0.016	6.995	13.575	25.820	0.280	41.059	0.290
B1873-mt2-15-ol5	0.050	4.057	12.926	36.588	0.185	32.548	0.284
B1873-mt2-18-sp1	0.046	4.933	16.024	22.988	0.256	43.018	0.271
B1873-mt2-18-sp2	0.062	5.699	15.040	22.057	0.250	43.398	0.273
B1873-mt2-18-sp3	0.063	6.299	14.571	23.070	0.250	43.486	0.292
B1873-mt2-20-sp1	0.047	3.357	15.900	38.901	0.199	26.991	0.203
B1873-mt2-20-sp2	0.037	3.203	15.374	40.316	0.186	26.816	0.206
B1873-mt2-27-sp2	0.038	3.562	14.504	37.247	0.196	31.183	0.241
B1873-mt2-27-sp1	0.058	3.247	14.584	37.327	0.186	30.525	0.234
B1873-mt2-23-sp1	0.022	7.115	14.476	24.538	0.274	39.982	0.290
B1873-mt2-23-sp2	0.013	7.304	13.874	23.964	0.287	41.079	0.279
B1873-mt1-6-sp1	0.043	9.013	12.935	18.453	0.298	46.073	0.317
B1873-mt1-6-sp2	0.038	8.890	12.668	18.748	0.306	46.585	0.306
B1873-mt1-10-sp1	0.078	4.222	13.745	35.136	0.172	31.700	0.236
B1873-mt1-10-sp2	0.038	4.634	12.927	34.536	0.178	33.865	0.271
B1873-mt1-14-sp1	0.028	8.589	12.768	25.263	0.271	44.568	0.587
B1873-mt1-37-sp1	0.063	4.176	14.136	34.443	0.179	31.869	0.256
B1873-mt1-38-sp1	0.029	7.036	13.098	24.354	0.238	41.966	0.306
B1873-mt1-38-sp2	0.010	7.614	13.350	23.317	0.243	42.306	0.313
B1873-mt1-38-sp3	0.036	7.038	12.824	24.670	0.231	42.212	0.308
B1873-mt1-38-sp4	0.042	6.633	13.138	24.495	0.228	41.586	0.302
B2299-mt2-1 avg	0.048	5.594	15.067	23.345	0.239	41.954	0.263
B2299-mt2-5 avg	0.019	7.595	13.475	29.891	0.240	34.810	0.261
B2299-mt2-7 avg	0.024	4.253	10.738	38.594	0.186	32.326	0.248
B2299-mt2-10 avg1	0.035	6.948	13.958	29.946	0.242	33.922	0.269
B2299-mt2-10 avg2	0.045	7.848	13.771	29.646	0.241	34.448	0.270
B2299-mt2-12 avg1	0.023	14.070	10.399	16.660	0.305	43.916	0.316
B2299-mt2-12 avg2	0.062	8.576	11.696	25.565	0.220	38.664	0.303
B2299-mt2-12 avg3	0.052	12.427	10.601	21.305	0.260	42.009	0.316
B2299-mt2-12 avg4	0.053	11.107	11.625	23.782	0.258	39.902	0.355
B2299-mt1-1 avg	0.013	4.076	13.350	36.971	0.185	32.924	0.271
B2299-mt1-6 avg	0.057	4.267	13.602	26.301	0.225	42.564	0.272
B2299-mt1-15 avg	0.032	3.496	11.771	34.678	0.184	37.896	0.285
B2299-mt1-21 avg	0.032	3.786	13.450	37.602	0.193	31.044	0.231
B2299-mt1-22 avg	0.033	3.968	14.087	34.095	0.189	33.369	0.235
B2299-mt1-23 avg	0.028	4.053	13.081	37.593	0.185	31.858	0.232
B2299-mt1-24 avg	0.027	3.278	12.820	34.115	0.168	37.551	0.267
B2299-mt1-27 avg	0.014	3.864	13.986	35.319	0.174	34.215	0.266
B2299-mt1-28 avg	0.024	4.411	11.688	39.430	0.180	30.919	0.235

Chapter 4
Table 2

Spinel ID	MgO	NiO	ZnO	Total	FeO	Fe2O3	New total
B1873-mt2-4-sp1	9.597	0.133	0.085	98.275	21.922	12.204	99.498
B1873-mt2-4-sp2	11.641	0.162	0.066	96.111	19.495	14.971	97.611
B1873-mt2-6-sp1	13.760	0.188	0.059	99.602	15.940	12.000	100.804
B1873-mt2-12-sp1	11.399	0.171	0.068	99.672	22.817	20.273	101.703
B1873-mt2-15-ol5	11.459	0.162	0.072	98.330	19.508	14.492	99.782
B1873-mt2-18-sp1	10.535	0.170	0.064	98.302	22.339	22.981	100.605
B1873-mt2-18-sp2	10.765	0.187	0.062	97.793	22.368	23.373	100.135
B1873-mt2-18-sp3	10.042	0.162	0.057	98.291	24.081	21.565	100.452
B1873-mt2-20-sp1	13.759	0.173	0.063	99.594	16.263	11.923	100.788
B1873-mt2-20-sp2	13.911	0.166	0.054	100.268	16.025	11.993	101.469
B1873-mt2-27-sp2	12.545	0.155	0.087	99.758	18.128	14.509	101.211
B1873-mt2-27-sp1	12.378	0.160	0.092	98.790	17.818	14.121	100.204
B1873-mt2-23-sp1	11.611	0.175	0.075	98.558	22.370	19.573	100.519
B1873-mt2-23-sp2	11.409	0.188	0.084	98.480	22.721	20.402	100.524
B1873-mt1-6-sp1	10.879	0.206	0.066	98.282	24.911	23.519	100.638
B1873-mt1-6-sp2	11.098	0.196	0.066	98.901	24.651	24.377	101.343
B1873-mt1-10-sp1	12.726	0.185	0.073	98.273	17.901	15.336	99.810
B1873-mt1-10-sp2	12.009	0.161	0.077	98.697	19.322	16.162	100.316
B1873-mt1-14-sp1	6.632	0.130	0.112	98.947	30.821	15.278	100.478
B1873-mt1-37-sp1	12.961	0.175	0.068	98.326	17.564	15.898	99.918
B1873-mt1-38-sp1	10.822	0.186	0.092	98.126	23.140	20.922	100.222
B1873-mt1-38-sp2	11.132	0.194	0.088	98.568	23.333	21.086	100.681
B1873-mt1-38-sp3	10.876	0.189	0.090	98.477	23.139	21.197	100.600
B1873-mt1-38-sp4	10.684	0.187	0.088	97.385	22.780	20.900	99.479
B2299-mt2-1 avg	11.720	0.219	0.054	98.503	21.010	23.277	100.835
B2299-mt2-5 avg	13.144	0.206	0.079	99.720	20.597	15.796	101.303
B2299-mt2-7 avg	10.995	0.156	0.069	97.588	19.813	13.906	98.981
B2299-mt2-10 avg1	12.748	0.201	0.075	98.345	20.267	15.176	99.865
B2299-mt2-10 avg2	11.735	0.201	0.088	98.292	22.550	13.223	99.617
B2299-mt2-12 avg1	11.682	0.272	0.090	97.732	27.454	18.295	99.565
B2299-mt2-12 avg2	11.440	0.229	0.089	96.844	22.895	17.525	98.599
B2299-mt2-12 avg3	11.032	0.249	0.079	98.330	27.234	16.421	99.975
B2299-mt2-12 avg4	10.094	0.207	0.073	97.456	27.332	13.970	98.856
B2299-mt1-1 avg	11.556	0.158	0.088	99.591	19.804	14.581	101.052
B2299-mt1-6 avg	10.764	0.209	0.052	98.314	21.015	23.949	100.713
B2299-mt1-15 avg	10.327	0.164	0.084	98.918	20.783	19.019	100.823
B2299-mt1-21 avg	13.191	0.156	0.063	99.747	17.209	15.375	101.287
B2299-mt1-22 avg	12.794	0.189	0.068	99.028	17.842	17.256	100.757
B2299-mt1-23 avg	12.412	0.162	0.057	99.661	18.541	14.800	101.144
B2299-mt1-24 avg	10.623	0.169	0.078	99.097	20.369	19.095	101.010
B2299-mt1-27 avg	11.494	0.159	0.083	99.574	19.836	15.981	101.176
B2299-mt1-28 avg	12.905	0.155	0.056	100.003	17.989	14.371	101.442

Chapter 4
Table 2

Spinel ID	Mg#	Ti#	Cr#	Fe3#	Fe2+	Fe3+	Fe3+/Fetot
B1873-mt2-4-sp1	0.438	0.047	0.518	0.160	0.305	0.038	0.111
B1873-mt2-4-sp2	0.516	0.049	0.493	0.206	0.271	0.047	0.147
B1873-mt2-6-sp1	0.606	0.037	0.513	0.148	0.222	0.038	0.145
B1873-mt2-12-sp1	0.471	0.092	0.359	0.269	0.318	0.063	0.167
B1873-mt2-15-ol5	0.511	0.052	0.498	0.188	0.272	0.045	0.143
B1873-mt2-18-sp1	0.457	0.064	0.313	0.299	0.311	0.072	0.188
B1873-mt2-18-sp2	0.462	0.075	0.306	0.310	0.311	0.073	0.190
B1873-mt2-18-sp3	0.426	0.084	0.324	0.289	0.335	0.068	0.168
B1873-mt2-20-sp1	0.601	0.041	0.504	0.148	0.226	0.037	0.142
B1873-mt2-20-sp2	0.607	0.039	0.519	0.148	0.223	0.038	0.144
B1873-mt2-27-sp2	0.552	0.045	0.490	0.182	0.252	0.045	0.153
B1873-mt2-27-sp1	0.553	0.041	0.494	0.179	0.248	0.044	0.151
B1873-mt2-23-sp1	0.481	0.095	0.343	0.262	0.311	0.061	0.164
B1873-mt2-23-sp2	0.472	0.098	0.337	0.275	0.316	0.064	0.168
B1873-mt1-6-sp1	0.438	0.125	0.269	0.327	0.347	0.074	0.175
B1873-mt1-6-sp2	0.445	0.122	0.271	0.336	0.343	0.076	0.182
B1873-mt1-10-sp1	0.559	0.054	0.473	0.197	0.249	0.048	0.162
B1873-mt1-10-sp2	0.526	0.060	0.469	0.210	0.269	0.051	0.158
B1873-mt1-14-sp1	0.277	0.122	0.377	0.218	0.429	0.048	0.100
B1873-mt1-37-sp1	0.568	0.053	0.462	0.204	0.244	0.050	0.169
B1873-mt1-38-sp1	0.455	0.095	0.346	0.284	0.322	0.066	0.169
B1873-mt1-38-sp2	0.460	0.103	0.331	0.286	0.325	0.066	0.169
B1873-mt1-38-sp3	0.456	0.095	0.349	0.287	0.322	0.066	0.171
B1873-mt1-38-sp4	0.455	0.090	0.349	0.284	0.317	0.065	0.171
B2299-mt2-1 avg	0.499	0.073	0.319	0.304	0.292	0.073	0.200
B2299-mt2-5 avg	0.532	0.100	0.414	0.209	0.287	0.049	0.147
B2299-mt2-7 avg	0.497	0.056	0.537	0.185	0.276	0.044	0.136
B2299-mt2-10 avg1	0.529	0.092	0.417	0.202	0.282	0.048	0.144
B2299-mt2-10 avg2	0.481	0.106	0.422	0.180	0.314	0.041	0.117
B2299-mt2-12 avg1	0.431	0.212	0.265	0.278	0.382	0.057	0.130
B2299-mt2-12 avg2	0.471	0.120	0.377	0.247	0.319	0.055	0.147
B2299-mt2-12 avg3	0.419	0.183	0.330	0.243	0.379	0.051	0.119
B2299-mt2-12 avg4	0.397	0.163	0.366	0.206	0.380	0.044	0.103
B2299-mt1-1 avg	0.510	0.052	0.495	0.187	0.276	0.046	0.142
B2299-mt1-6 avg	0.477	0.055	0.358	0.312	0.292	0.075	0.204
B2299-mt1-15 avg	0.470	0.045	0.471	0.247	0.289	0.060	0.171
B2299-mt1-21 avg	0.577	0.047	0.496	0.194	0.240	0.048	0.167
B2299-mt1-22 avg	0.561	0.050	0.453	0.219	0.248	0.054	0.179
B2299-mt1-23 avg	0.544	0.051	0.501	0.189	0.258	0.046	0.152
B2299-mt1-24 avg	0.482	0.042	0.458	0.245	0.283	0.060	0.174
B2299-mt1-27 avg	0.508	0.049	0.471	0.204	0.276	0.050	0.153
B2299-mt1-28 avg	0.561	0.056	0.528	0.184	0.250	0.045	0.152

Spinel ID	Cr/(Cr+Al)	Fo	TC Wan	TC Coogan	Ni*(FeO/MgO)	Mn/FeO
B1873-mt2-4-sp1	0.652	88.3	1260	1262	377.08	126.41
B1873-mt2-4-sp2	0.662	88.4	1282	1283	375.19	126.79
B1873-mt2-6-sp1	0.630	88.8	1270	1272	429.19	121.96
B1873-mt2-12-sp1	0.561	84.9	1245	1247	414.51	133.67
B1873-mt2-15-ol5	0.655	88.0	1241	1243	365.91	135.99
B1873-mt2-18-sp1	0.490	84.6	1245	1248	414.03	133.21
B1873-mt2-18-sp2	0.496	84.3	1245	1248	423.46	132.66
B1873-mt2-18-sp3	0.515	84.3	1237	1240	422.61	132.71
B1873-mt2-20-sp1	0.621	88.6	1252	1254	404.23	125.15
B1873-mt2-20-sp2	0.638	88.3	1249	1251	417.62	125.18
B1873-mt2-27-sp2	0.633	86.9	1232	1234	430.65	126.72
B1873-mt2-27-sp1	0.632	86.5	1236	1238	442.31	127.79
B1873-mt2-23-sp1	0.532	86.2	1251	1253	358.75	133.70
B1873-mt2-23-sp2	0.537	86.2	1248	1250	362.31	133.70
B1873-mt1-6-sp1	0.489	84.7	1288	1290	435.35	133.03
B1873-mt1-6-sp2	0.498	84.5	1289	1292	440.70	133.26
B1873-mt1-10-sp1	0.632	87.8	1257	1259	396.00	130.44
B1873-mt1-10-sp2	0.642	87.7	1248	1250	357.76	139.00
B1873-mt1-14-sp1	0.570	84.5	1256	1258	428.44	134.69
B1873-mt1-37-sp1	0.620	87.9	1250	1252	381.60	132.21
B1873-mt1-38-sp1	0.555	84.7	1249	1251	405.68	141.02
B1873-mt1-38-sp2	0.540	84.7	1266	1269	409.29	142.07
B1873-mt1-38-sp3	0.563	84.8	1263	1265	407.08	141.37
B1873-mt1-38-sp4	0.556	85.1	1254	1257	399.88	138.05
B2299-mt2-1 avg	0.510	86.1	1256	1259	440.11	131.81
B2299-mt2-5 avg	0.598	87.8	1240	1242	364.90	132.31
B2299-mt2-7 avg	0.707	87.2	1253	1254	392.40	129.48
B2299-mt2-10 avg1	0.590	87.8	1247	1249	361.32	131.67
B2299-mt2-10 avg2	0.591	87.9	1254	1257	359.62	132.02
B2299-mt2-12 avg1	0.518	86.8	1347	1348	423.04	130.33
B2299-mt2-12 avg2	0.595	86.6	1282	1284	426.31	130.26
B2299-mt2-12 avg3	0.574	86.7	1311	1313	426.61	130.15
B2299-mt2-12 avg4	0.578	86.6	1276	1278	429.10	130.94
B2299-mt1-1 avg	0.650	86.5	1224	1226	411.86	143.11
B2299-mt1-6 avg	0.565	84.8	1278	1280	493.70	133.77
B2299-mt1-15 avg	0.664	84.8	1278	1280	480.40	135.03
B2299-mt1-21 avg	0.652	88.1	1250	1252	377.16	130.26
B2299-mt1-22 avg	0.619	87.5	1316	1317	433.69	128.95
B2299-mt1-23 avg	0.658	88.0	1242	1244	376.32	129.85
B2299-mt1-24 avg	0.641	84.8	1261	1263	484.64	134.21
B2299-mt1-27 avg	0.629	86.0	1245	1248	454.38	131.63
B2299-mt1-28 avg	0.694	87.7	1249	1251	385.04	129.90

Spinel ID	Al ppm	Fe ppm	Mn ppm	Mg ppm	Ca ppm	Ni ppm	Co ppm
B1873-mt2-4-sp1	181.05	92149.78	1498.40	303588.55	2483.29	1603.21	161.64
B1873-mt2-4-sp2	175.62	91757.38	1496.46	302775.00	2484.00	1597.71	164.79
B1873-mt2-6-sp1	215.30	87130.79	1366.85	300180.72	2330.45	1908.21	158.54
B1873-mt2-12-sp1	154.97	112910.55	1941.37	276178.30	2842.92	1308.45	186.05
B1873-mt2-15-ol5	158.67	91476.85	1600.16	291029.32	2964.83	1502.32	160.54
B1873-mt2-18-sp1	170.89	115142.53	1972.99	275480.33	3050.77	1278.36	189.31
B1873-mt2-18-sp2	161.65	116596.89	1989.62	271282.47	2945.59	1271.50	191.00
B1873-mt2-18-sp3	153.21	116260.03	1984.58	272133.50	2925.05	1276.62	190.93
B1873-mt2-20-sp1	199.17	87078.85	1401.79	295112.66	2436.23	1767.95	160.46
B1873-mt2-20-sp2	193.07	87197.19	1404.04	287270.54	2444.86	1775.54	156.05
B1873-mt2-27-sp2	166.86	97330.78	1586.51	279776.61	2703.21	1597.54	164.26
B1873-mt2-27-sp1	170.70	98967.55	1626.74	275522.29	2704.65	1589.10	166.54
B1873-mt2-23-sp1	165.34	104412.00	1795.66	284472.98	2955.08	1261.38	178.53
B1873-mt2-23-sp2	156.82	104762.07	1801.74	283762.61	2935.21	1266.48	176.07
B1873-mt1-6-sp1	168.29	112737.49	1929.10	270940.59	2733.76	1350.24	182.79
B1873-mt1-6-sp2	167.42	114001.86	1954.17	270996.83	2736.70	1351.94	185.10
B1873-mt1-10-sp1	178.21	91081.13	1528.24	285314.61	2680.85	1600.87	163.33
B1873-mt1-10-sp2	162.19	92696.68	1657.43	286494.19	3125.03	1426.96	163.83
B1873-mt1-14-sp1	155.19	115598.34	2002.71	273116.44	3003.91	1306.33	192.22
B1873-mt1-37-sp1	174.71	90911.35	1546.04	288094.47	2785.49	1560.60	161.54
B1873-mt1-38-sp1	151.36	112559.69	2041.79	271669.74	3289.42	1263.61	181.53
B1873-mt1-38-sp2	165.23	113164.39	2067.99	271841.28	3230.24	1268.84	182.05
B1873-mt1-38-sp3	159.79	112963.89	2054.13	273661.60	3243.22	1272.68	182.77
B1873-mt1-38-sp4	156.07	112079.99	1990.24	277664.73	3205.69	1278.46	181.88
B2299-mt2-1 avg	172.73	103743.42	1759.00	277909.82	3625.54	1521.48	184.20
B2299-mt2-5 avg	155.91	89652.41	1525.86	279890.69	3605.10	1470.17	162.88
B2299-mt2-7 avg	146.51	98562.16	1641.51	292312.13	3473.75	1501.85	175.42
B2299-mt2-10 avg1	165.75	92076.70	1559.43	288616.21	3380.99	1461.59	167.50
B2299-mt2-10 avg2	169.37	91850.86	1559.77	288324.30	3450.14	1456.84	166.80
B2299-mt2-12 avg1	179.71	102002.56	1710.04	290272.03	3521.05	1553.61	171.26
B2299-mt2-12 avg2	163.91	101805.32	1705.77	285900.75	3496.67	1545.01	169.56
B2299-mt2-12 avg3	165.92	101827.03	1704.77	286828.50	3517.23	1550.81	171.89
B2299-mt2-12 avg4	155.92	102142.88	1720.43	285607.95	3542.99	1548.39	172.60
B2299-mt1-1 avg	150.02	100320.23	1846.71	280070.34	3443.90	1483.85	163.95
B2299-mt1-6 avg	181.73	112169.81	1930.09	271773.61	3498.70	1543.68	189.52
B2299-mt1-15 avg	173.56	112562.11	1955.07	271852.81	3466.00	1497.29	187.17
B2299-mt1-21 avg	172.08	89189.45	1494.35	286161.00	3273.68	1561.65	154.03
B2299-mt1-22 avg	234.64	94165.32	1561.94	286096.03	3144.43	1700.45	165.73
B2299-mt1-23 avg	161.57	89815.79	1500.16	286587.96	3395.41	1549.64	159.64
B2299-mt1-24 avg	170.86	112140.18	1935.95	272476.57	3382.09	1519.68	188.80
B2299-mt1-27 avg	170.95	103976.90	1760.55	277973.04	3556.16	1567.64	175.63
B2299-mt1-28 avg	154.45	91445.18	1527.96	283409.78	3427.08	1540.01	160.19

Spinel ID	Cr ppm	Zn ppm	Ti ppm	xpxmn	xpxni	Fe2+/Fetot	Log10(fe 2+/Fe3+)
B1873-mt2-4-sp1	599.22	79.95	201.37	0.11	0.07	0.89	1.63
B1873-mt2-4-sp2	472.12	80.95	196.03	0.10	0.07	0.85	1.45
B1873-mt2-6-sp1	709.80	66.70	168.01	0.23	0.14	0.86	1.46
B1873-mt2-12-sp1	458.70	71.66	230.42	-0.08	0.12	0.83	1.36
B1873-mt2-15-ol5	490.73	59.45	197.99	-0.14	0.05	0.86	1.47
B1873-mt2-18-sp1	237.28	72.95	179.81	-0.07	0.12	0.81	1.28
B1873-mt2-18-sp2	216.20	75.81	195.51	-0.05	0.13	0.81	1.27
B1873-mt2-18-sp3	323.24	73.53	201.79	-0.05	0.13	0.83	1.36
B1873-mt2-20-sp1	634.43	57.56	190.28	0.15	0.11	0.86	1.47
B1873-mt2-20-sp2	600.72	56.21	163.53	0.15	0.12	0.86	1.46
B1873-mt2-27-sp2	290.49	64.91	177.70	0.11	0.14	0.85	1.42
B1873-mt2-27-sp1	332.83	64.53	180.07	0.08	0.16	0.85	1.43
B1873-mt2-23-sp1	465.43	65.34	282.70	-0.08	0.04	0.84	1.37
B1873-mt2-23-sp2	626.52	67.36	315.06	-0.08	0.05	0.83	1.36
B1873-mt1-6-sp1	409.03	71.64	340.47	-0.06	0.15	0.82	1.33
B1873-mt1-6-sp2	263.50	73.09	286.68	-0.07	0.15	0.82	1.30
B1873-mt1-10-sp1	402.71	67.12	214.56	0.01	0.09	0.84	1.38
B1873-mt1-10-sp2	1043.96	67.10	328.81	-0.22	0.04	0.84	1.40
B1873-mt1-14-sp1	128.57	80.30	229.61	-0.11	0.14	0.90	1.70
B1873-mt1-37-sp1	433.39	60.58	223.48	-0.04	0.07	0.83	1.35
B1873-mt1-38-sp1	236.14	82.00	278.92	-0.27	0.11	0.83	1.35
B1873-mt1-38-sp2	228.68	77.58	279.56	-0.30	0.11	0.83	1.35
B1873-mt1-38-sp3	527.91	79.71	333.85	-0.28	0.11	0.83	1.35
B1873-mt1-38-sp4	209.42	79.03	255.23	-0.20	0.10	0.83	1.35
B2299-mt2-1 avg	338.43	64.06	237.59	-0.03	0.15	0.80	1.24
B2299-mt2-5 avg	463.67	59.35	293.83	-0.04	0.05	0.85	1.45
B2299-mt2-7 avg	261.38	63.01	171.35	0.03	0.09	0.86	1.50
B2299-mt2-10 avg1	268.19	57.26	214.99	-0.03	0.05	0.86	1.46
B2299-mt2-10 avg2	333.14	59.91	237.49	-0.03	0.05	0.88	1.60
B2299-mt2-12 avg1	274.11	71.90	298.57	0.01	0.13	0.87	1.53
B2299-mt2-12 avg2	217.05	73.74	291.84	0.01	0.13	0.85	1.45
B2299-mt2-12 avg3	244.32	72.25	293.21	0.02	0.14	0.88	1.58
B2299-mt2-12 avg4	232.25	70.77	288.77	-0.01	0.14	0.90	1.68
B2299-mt1-1 avg	369.73	80.75	171.20	-0.33	0.12	0.86	1.47
B2299-mt1-6 avg	231.51	77.57	203.46	-0.08	0.23	0.80	1.22
B2299-mt1-15 avg	234.65	75.73	174.84	-0.11	0.21	0.83	1.35
B2299-mt1-21 avg	276.68	57.85	165.16	0.01	0.07	0.83	1.36
B2299-mt1-22 avg	359.75	60.01	170.54	0.05	0.14	0.82	1.32
B2299-mt1-23 avg	584.84	59.09	199.08	0.02	0.07	0.85	1.43
B2299-mt1-24 avg	268.66	72.01	188.63	-0.09	0.21	0.83	1.33
B2299-mt1-27 avg	197.87	67.59	187.97	-0.02	0.17	0.85	1.42
B2299-mt1-28 avg	298.19	59.19	186.58	0.02	0.08	0.85	1.42

Spinel ID	Dt	Fe2O3 liq	FeO	Fe2+liq	Fe3+liq	Fe2+/Fetot liq
B1873-mt2-4-sp1	26.92	0.45	11.45	0.165	0.006	0.967
B1873-mt2-4-sp2	23.15	0.65	11.22	0.164	0.008	0.953
B1873-mt2-6-sp1	25.07	0.48	10.78	0.156	0.006	0.963
B1873-mt2-12-sp1	29.94	0.68	13.91	0.202	0.008	0.960
B1873-mt2-15-ol5	30.76	0.47	11.34	0.164	0.006	0.965
B1873-mt2-18-sp1	29.97	0.77	14.12	0.206	0.010	0.955
B1873-mt2-18-sp2	29.86	0.78	14.29	0.209	0.010	0.955
B1873-mt2-18-sp3	31.72	0.68	14.34	0.208	0.009	0.961
B1873-mt2-20-sp1	28.43	0.42	10.82	0.156	0.005	0.967
B1873-mt2-20-sp2	28.99	0.41	10.84	0.156	0.005	0.968
B1873-mt2-27-sp2	32.83	0.44	12.12	0.174	0.006	0.969
B1873-mt2-27-sp1	31.96	0.44	12.33	0.177	0.006	0.970
B1873-mt2-23-sp1	28.72	0.68	12.82	0.187	0.009	0.956
B1873-mt2-23-sp2	29.36	0.69	12.85	0.188	0.009	0.956
B1873-mt1-6-sp1	22.24	1.06	13.55	0.202	0.013	0.938
B1873-mt1-6-sp2	22.02	1.11	13.67	0.204	0.014	0.936
B1873-mt1-10-sp1	27.41	0.56	11.21	0.163	0.007	0.959
B1873-mt1-10-sp2	29.21	0.55	11.43	0.166	0.007	0.960
B1873-mt1-14-sp1	27.64	0.55	14.37	0.207	0.007	0.968
B1873-mt1-37-sp1	28.97	0.55	11.20	0.163	0.007	0.959
B1873-mt1-38-sp1	29.16	0.72	13.83	0.202	0.009	0.957
B1873-mt1-38-sp2	25.74	0.82	13.82	0.203	0.010	0.952
B1873-mt1-38-sp3	26.37	0.80	13.81	0.202	0.010	0.953
B1873-mt1-38-sp4	28.01	0.75	13.75	0.201	0.009	0.955
B2299-mt2-1 avg	27.65	0.84	12.59	0.186	0.011	0.946
B2299-mt2-5 avg	30.97	0.51	11.07	0.161	0.006	0.962
B2299-mt2-7 avg	28.28	0.49	12.24	0.176	0.006	0.966
B2299-mt2-10 avg1	29.44	0.52	11.38	0.165	0.006	0.962
B2299-mt2-10 avg2	27.97	0.47	11.39	0.164	0.006	0.965
B2299-mt2-12 avg1	15.26	1.20	12.04	0.183	0.015	0.924
B2299-mt2-12 avg2	23.15	0.76	12.41	0.182	0.009	0.951
B2299-mt2-12 avg3	19.10	0.86	12.32	0.182	0.011	0.944
B2299-mt2-12 avg4	24.15	0.58	12.62	0.183	0.007	0.962
B2299-mt1-1 avg	34.88	0.42	12.53	0.180	0.005	0.972
B2299-mt1-6 avg	23.82	1.01	13.52	0.201	0.013	0.941
B2299-mt1-15 avg	23.70	0.80	13.76	0.202	0.010	0.952
B2299-mt1-21 avg	28.79	0.53	10.99	0.160	0.007	0.960
B2299-mt1-22 avg	18.56	0.93	11.28	0.169	0.012	0.935
B2299-mt1-23 avg	30.63	0.48	11.12	0.161	0.006	0.964
B2299-mt1-24 avg	26.65	0.72	13.78	0.201	0.009	0.957
B2299-mt1-27 avg	29.81	0.54	12.89	0.186	0.007	0.965
B2299-mt1-28 avg	29.11	0.49	11.32	0.164	0.006	0.964

Chapter 4

Table 3

Sample	Grain Number	SiO2	TiO2	Al2O3	Cr2O3	FeO*	MnO	MgO	CaO	Na2O	Total
B2299	Px 1	48.36	2.01	4.6	0.260	5.05	0.06	14.66	23.2	0.35	98.55
B2299	Px 1 - core average	48.11	1.93	4.58	0.215	5.04	0.06	14.69	23.12	0.35	98.10
B2299	Px 2	47.5	2.53	5.61	0.290	5.74	0.07	13.81	22.9	0.39	98.84
B2299	Px 2 - core average	47.58	2.41	5.65	0.227	5.74	0.07	13.76	22.88	0.39	98.71
B2299	Px 3	49.16	1.957	4.44	0.300	4.934	0.06	14.71	22.94	0.35	98.851
B2299	Px 3 - core average	49.14	1.89	4.39	0.287	4.85	0.06	14.76	22.92	0.34	98.63
B1644	Px 1	44.4	4.19	7.41	0.010	6.9	0.11	12.22	23.29	0.52	99.05
B1644	Px 1 - core average	46.00	3.53	6.21	0.008	6.55	0.11	12.85	23.43	0.49	99.18
B1644	Px 3	43.05	4.52	8.44	0.010	7.14	0.1	11.62	23.24	0.56	98.68
B1644	Px 3 - core average	43.30	4.33	8.28	0.010	7.13	0.10	11.69	23.26	0.57	98.67
B1445	Px 1	48.31	2.18	4.36	0.290	4.7	0.1	14.59	23.97	0.26	98.76
B1445	Px 1 - core average	44.64	3.77	6.84	0.045	6.51	0.08	12.61	23.52	0.35	98.37
B1445	Px 3	43.63	4.35	7.94	0.030	6.79	0.08	12.1	23.37	0.38	98.67

Chapter 4

Table 3

Sample	$Al^{IV}/[IV]_{Total}$	D_{H2O}	$H2O_{(Cpx)}$	$H2O_{liquid}$ (PPM)	$H2O_{liquid}$ (wt%)	Grain Number
B2299	0.080	0.024	709	29484	2.95	Px 1
B2299	0.078	0.024	709	29945	2.99	Px 1 - core average
B2299	0.098	0.030	510	17268	1.73	Px 2
B2299	0.097	0.029	510	17588	1.76	Px 2 - core average
B2299	0.076	0.023	632	27381	2.74	Px 3
B2299	0.075	0.023	632	27855	2.79	Px 3 - core average
B1644	0.143	0.042	263	6189	0.62	Px 1
B1644	0.118	0.035	263	7448	0.74	Px 1 - core average
B1644	0.161	0.048	382	8010	0.80	Px 3
B1644	0.156	0.046	452	9779	0.98	Px 3 - core average
B1445	0.081	0.025	452	18385	1.84	Px 1
B1445	0.134	0.040	432	10836	1.08	Px 1 - core average
B1445	0.155	0.046	432	9399	0.94	Px 3

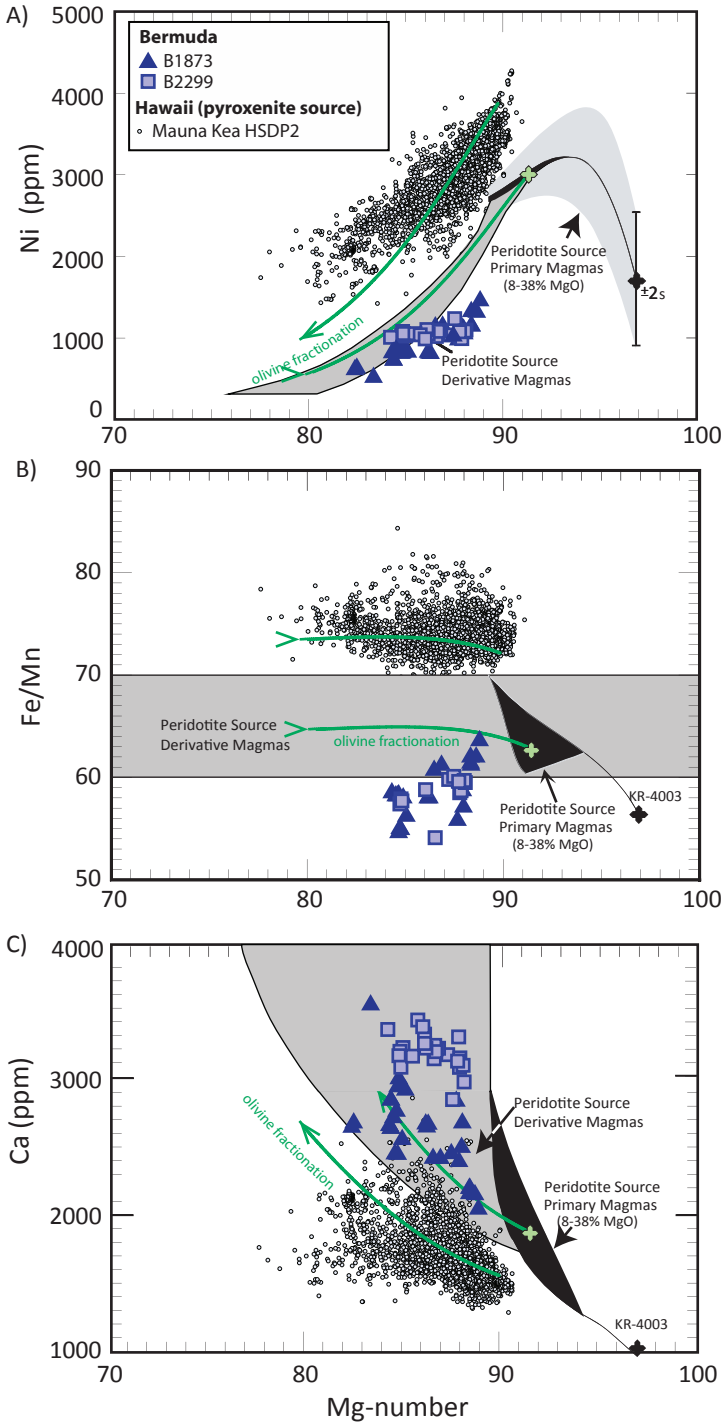

Supplementary Figure 4.1: Olivine chemistry A) Ni (ppm) B) Fe/Mn and C) Ca (ppm) concentrations versus Mg-number for Bermuda olivines. Olivine trace element chemistry falls within the region for magma derived from a peridotite source.

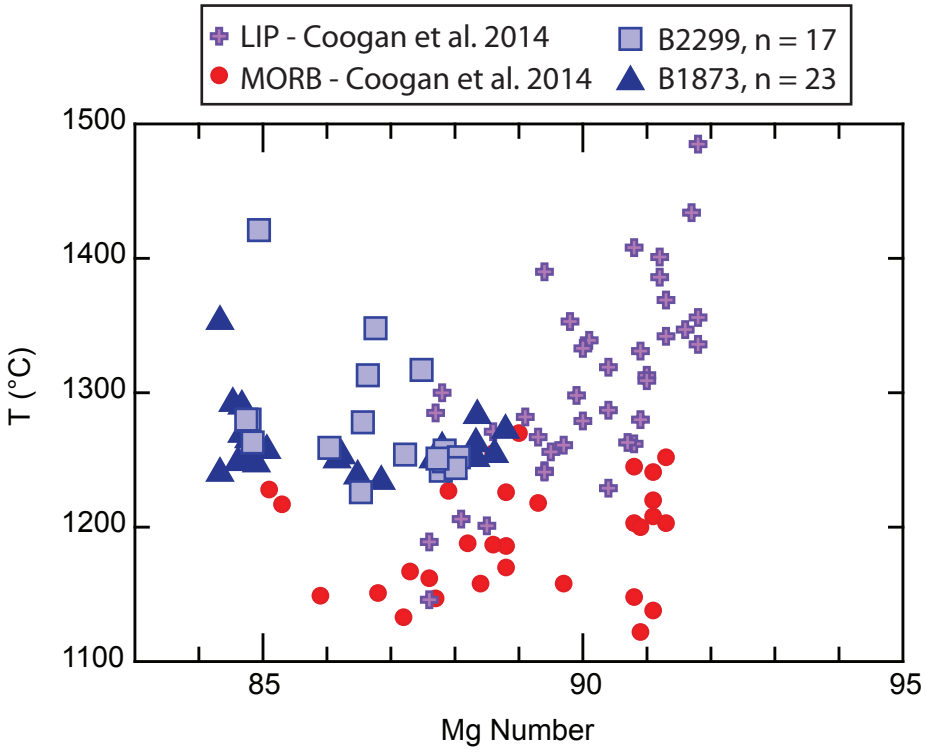

Supplementary Figure 4.2: Results from Al-in-olivine thermometry for Bermuda plotted against Mg-number. Also shown are olivines from Large Igneous Provinces (LIP) and Mid-Ocean Ridge Basalt (MORB) from Coogan et al., 2014.

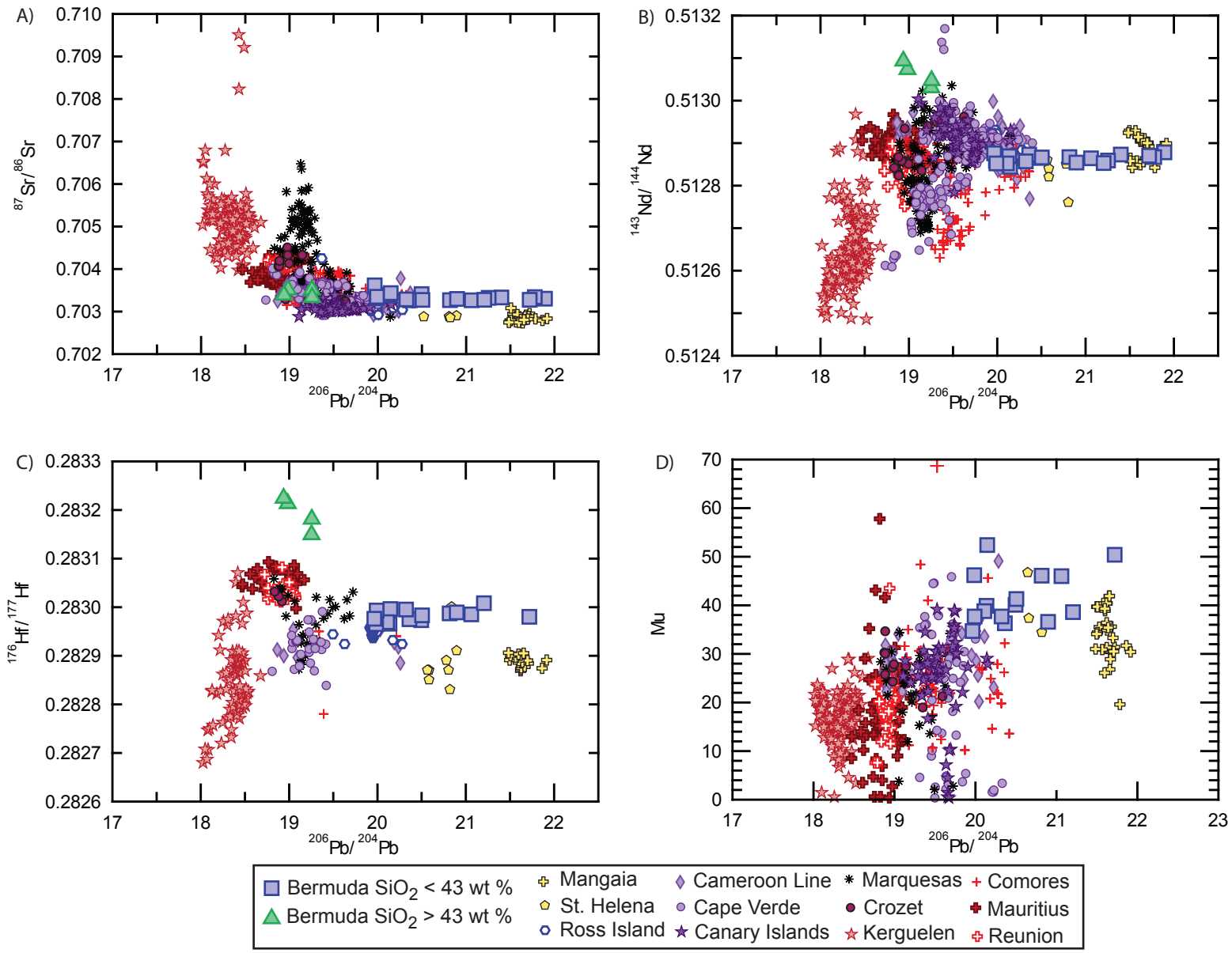

Supplementary Figure 4.3: Radiogenic isotopic data for Bermuda plotted with other ocean island basalts.

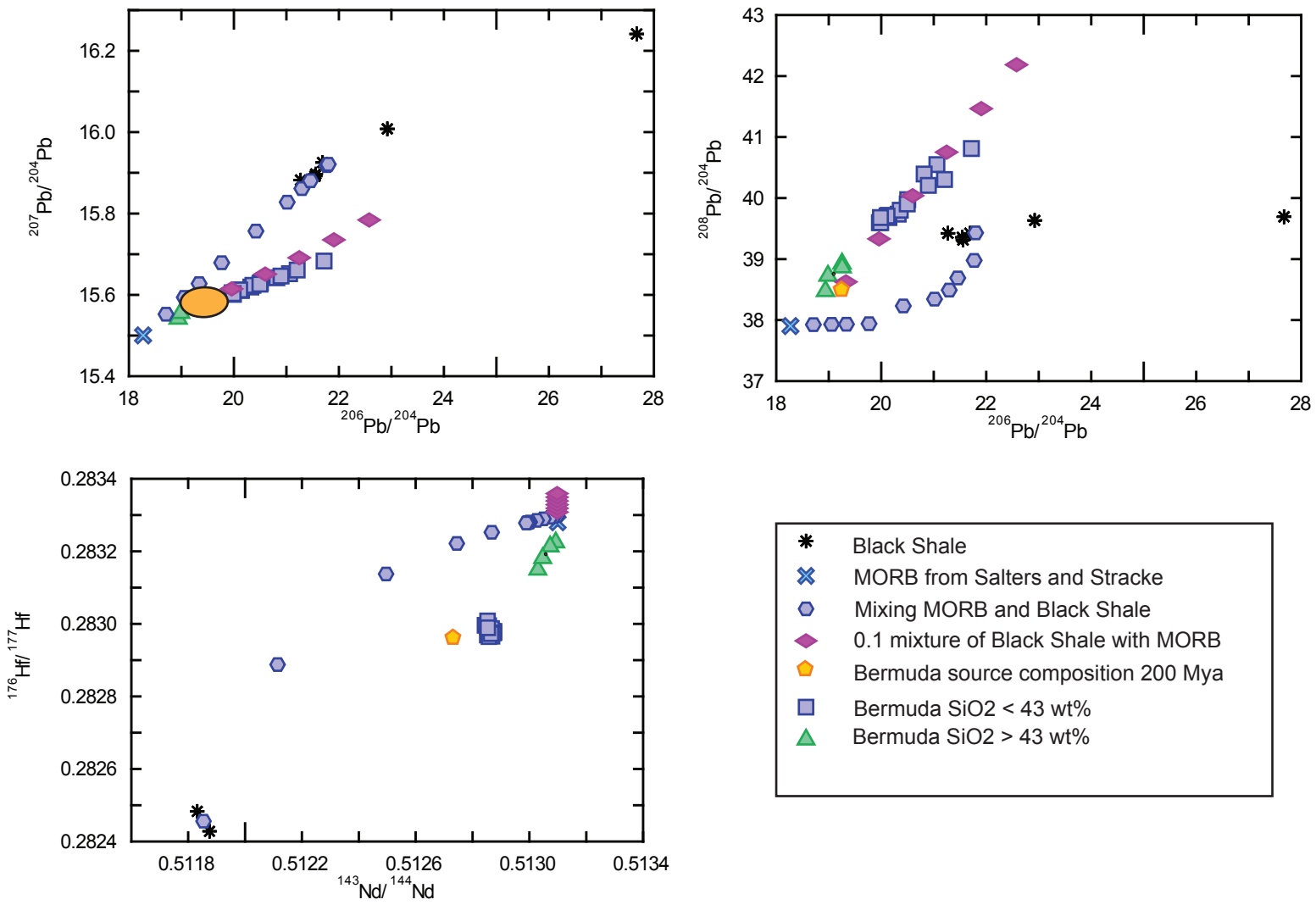

Supplementary Figure 4.4: Models showing isotopic evolution from mixing Mid-Ocean Ridge Basalt (MORB) and Black Shales. A mixure of 10% Black Shale with MORB was aged by 100 My increments to try to reproduce Bermdua compositions.

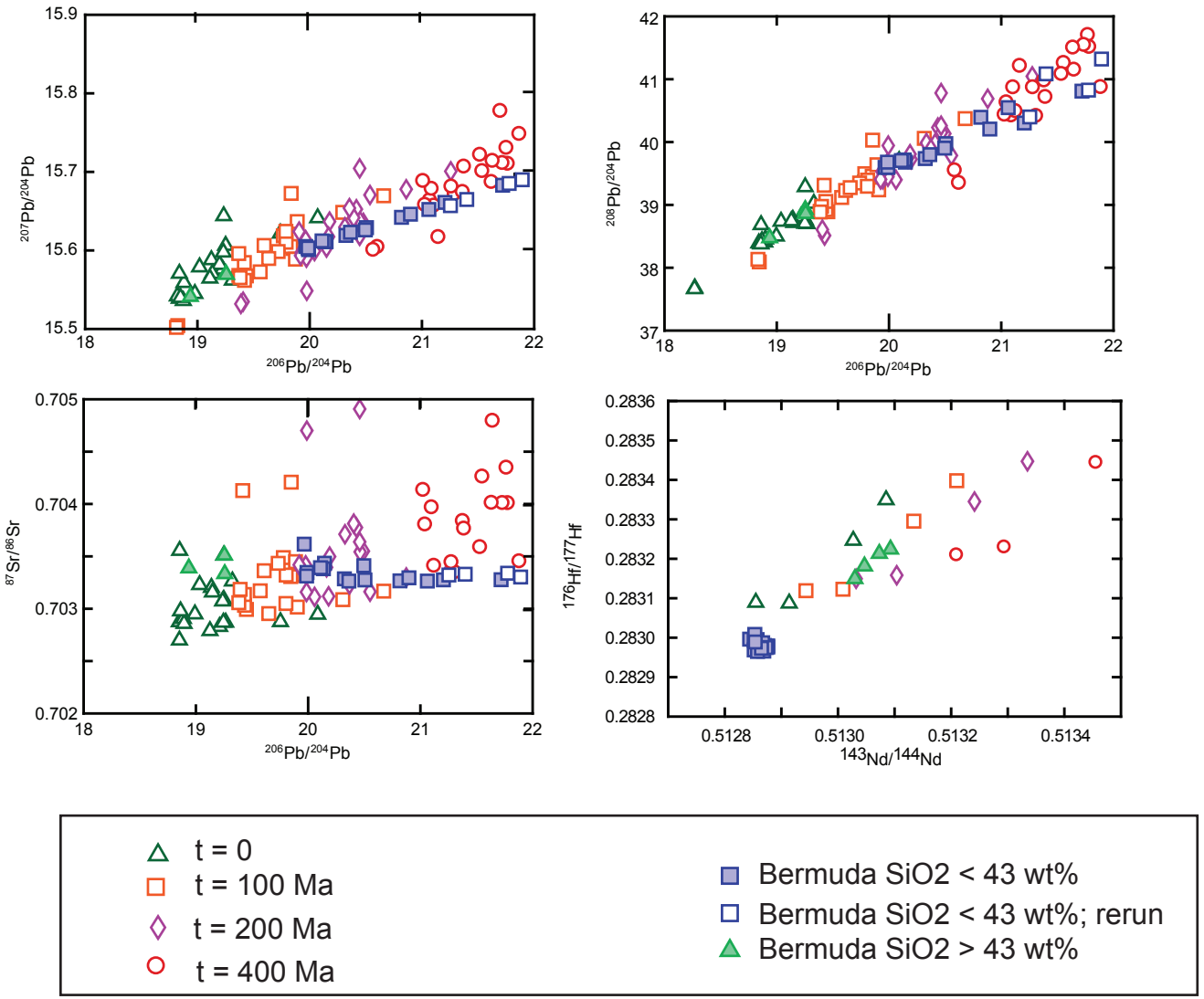

Supplementary Figure 4.5: Age projections of mid-ocean ridge basalt with high $^{206}Pb/^{204}Pb$.

Appendix A

Contrasting sediment melt and fluid signatures for magma components in the Aeolian Arc: Implications for numerical modeling of subduction systems

Denis Zamboni[1,2], Esteban Gazel[1], Jeffrey G. Ryan[3], Claudia Cannatelli[2,4], Federico Lucchi[5], Zachary D. Atlas[3], Jarek Trela[1], **Sarah E. Mazza[1]**, and Benedetto De Vivo[2]

[1] Department of Geosciences, Virginia Tech, Blacksburg, Virginia, USA
[2] Dipartimento di Scienze della Terra, dell'Ambiente e delle Risorse, Universita di Napoli Federico II, Napoli, Italy
[3] Department of Geology, University of South Florida, Tampa, Florida, USA
[4] Department of Geology and Andean Geothermal Centre of Excellence, Universidad de Chile, Santiago, Chile
[5] Dipartimento di Scienze Biologiche, Geologiche e Ambientali, Alma Mater Studiorum, Universita di Bologna, Bologna, Italy

Published May, 2016 in *Geochemistry, Geophysics, Geosystems*

Abstract

The complex geodynamic evolution of Aeolian Arc in the southern Tyrrhenian Sea resulted in melts with some of the most pronounced along the arc geochemical variation in incompatible trace elements and radiogenic isotopes worldwide, likely reflecting variations in arc magma source components. Here we elucidate the effects of subducted components on magma sources along different sections of the Aeolian Arc by evaluating systematics of elements depleted in the upper mantle but enriched in the subducting slab, focusing on a new set of B, Be, As, and Li measurements. Based on our new results, we suggest that both hydrous fluids and silicate melts were involved in element transport from the subducting slab to the mantle wedge. Hydrous fluids strongly influence the chemical composition of lavas in the central arc (Salina) while a melt component from subducted sediments probably plays a key role in metasomatic reactions in the mantle wedge below the peripheral islands (Stromboli). We also noted similarities in subducting components between the Aeolian Archipelago, the Phlegrean Fields, and other volcanic arcs/arc segments around the world (e.g., Sunda, Cascades, Mexican Volcanic Belt). We suggest that the presence of melt components in all these locations resulted from an increase in the mantle wedge temperature by inflow of hot asthenospheric material from tears/windows in the slab or from around the edges of the sinking slab.

Appendix B

Laboratory Techniques in Geology: Embedding Analytical Methods into the Undergraduate Curriculum

Baedke, S. J.[1], Johnson, E. A.[1], Kearns, L. E.[1], **Mazza, S. E.[2]**, Gazel, E.[2]

[1] James Madison University, Harrisonburg, VA, United States
[2]Virginia Polytechnic Institute and State University, Blacksburg, VA, United States

Poster presented at the American Geophysical Union Fall Meeting 2014

Abstract
Paid summer REU experiences successfully engage undergraduate students in research and encourage them to continue to graduate school and scientific careers. However these programs only accommodate a limited number of students due to funding constraints, faculty time commitments, and limited access to needed instrumentation. At JMU, the Department of Geology and Environmental Science has embedded undergraduate research into the curriculum. Each student fulfilling a BS in Geology or a BA in Earth Science completes 3 credits of research, including a 1-credit course on scientific communication, 2 credits of research or internship, followed by a presentation of that research. Our department has successfully acquired many analytical instruments and now has an XRD, SEM/EDS, FTIR, handheld Raman, AA, ion chromatograph, and an IRMS. To give as many students as possible an overview to the scientific uses and operation methods for these instruments, we revived a laboratory methods course that includes theory and practical use of instrumentation at JMU, plus XRF sample preparation and analysis training at Virginia Tech during a 1-day field trip. In addition to practical training, projects included analytical concepts such as evaluating analytical vs. natural uncertainty, determining error on multiple measurements, signal-to-noise ratio, and evaluating data quality. State funding through the 4-VA program helped pay for analytical supplies and support for students to complete research projects over the summer or during the next academic year using instrumentation from the course. This course exemplifies an alternative path to broadening participation in undergraduate research and creating stronger partnerships between PUI's and research universities.